MONASH University

The influence of azimuthal velocity and a parallel wall on vortex ring evolution

Christopher L Gargan-Shingles

BAeroEng/BSci

A thesis submitted for the degree of *Doctor of Philosophy* at

Monash University in 2017

Department of Mechanical and Aerospace Engineering

Copyright notice

Declaration

I hereby declare that this thesis contains no material which has been accepted for the award of any other degree or diploma at any university or equivalent institution and that, to the best of my knowledge and belief, this thesis contains no material previously published or written by another person, except where due reference is made in the text of the thesis.

This thesis contains extracts that were included in 2 original papers published in peer reviewed journals. These papers are as follows:

- C. Gargan-Shingles, M. Rudman, K. Ryan, 2015, The evolution of swirling axisymmetric vortex rings, *Physics of Fluids*, 27 (8)
- C. Gargan-Shingles, M. Rudman, K. Ryan, 2016, The linear stability of swirling vortex rings, *Physics of Fluids*, 28 (11)

The ideas, development, and writing up of all work included in the thesis were the principal responsibility of myself, the student, working within the Department of Mechanical and Aerospace Engineering under the supervision of Associate Professor Kris Ryan and Professor Murray Rudman.

Signature: ....████████████................

Name: .████████████

Date: ......30/05/2017...........................

Abstract

The flow dynamics of both confined and swirling vortex rings remain somewhat of a mystery to the scientific community. The influence that a vortex ring can wield on the boundary layer of a flat plate has application to the cooling of heated surfaces via synthetic jets. An improved understanding of both confined and swirling vortex rings is required in order to pursue this particular application any further.

The literature describes various properties of swirling vortex rings, however much of this previous work relies on imprecise initial vorticity distributions, and has largely neglected to classify the modes of swirling vortex ring instability. Confined vortex rings have been investigated within various domain designs, however their behaviour in an asymmetric domain, such as a next to a flat wall, is not well understood. In this thesis, numerical simulations were designed to investigate both swirling vortex rings, and vortex rings translating parallel to a surface.

The numerical algorithm applied for this work solves the Navier-Stokes equations to determine the fluid properties at each time step of the flow evolution. The code relies on the spectral element method of spatial discretization, breaking down a regular grid into polynomial basis functions. An operator splitting scheme is implemented for the third order time integration. For the full 3D simulations, computational load is reduced by transforming the third dimension into an array Fourier modes.

Vortex rings with a variety of ring aspect ratios and swirl magnitudes were numerically evolved in an axisymmetric domain, and their evolution monitored over time. The numerical relaxation process of swirling vortex rings was explored and identified. The development of the flow dynamics was discussed with reference to the governing equations, and the growth of a shear layer and corresponding Kelvin-

Helmholtz instability was observed. The strength of this shear layer was related to a logarithmic function of the ring aspect ratio and the swirl coefficient. The linear stability of these rings was also determined, and described within the Kelvin framework in a similar manner to that already developed for Batchelor vortex pairs. The stability characteristics were found to be remarkably similar to those for Batchelor vortex pairs, however the growth rates and amplified wavenumber were found to vary significantly for thicker rings due to the restrictions introduced by the ring geometry.

Near wall vortex rings with three different ring aspect ratios were implemented at three different wall separations, in order to determine the effect of the initial parameters on their evolution. The development of a swirling flow within the vortex core was observed, and the development of an instability noted, although it is different in nature to those identified for swirling vortex rings. A quantitative analysis of the effect of wall separation and ring aspect ratio on the velocity of fluid in the wall-normal direction was performed, and it was determined that thinner rings in closer initial proximity to the wall have larger wall-normal velocities. The effect of the flow dynamics on a scalar temperature field was also analysed, and it was shown that the heat flux from the wall peaks at a similar time to when the average wall-normal velocity is at a maximum.

This work has enhanced the scientific understanding of swirling vortex ring evolution, and allows future numerical work in this field to begin from a more realistic set of initial conditions. The stability of swirling vortex rings can now be discussed within the same framework as their non-swirling counterparts, allowing more in depth analyses to be performed. Most importantly, this work has identified that vortex rings represent excellent candidates for the cooling of electronics when applied parallel to the surface in question. Further work is required to find an ideal set of input parameters to maximise cooling efficiency.

Acknowledgements

Firstly, I would like to thank my supervisors, Associate Professor Kris Ryan and Professor Murray Rudman. I cannot imagine having more enthusiastic, helpful, and supportive guidance for my research. I appreciate all the time that you have both made for me, despite having innumerable other commitments both at the university and at home. I have no doubt that the world of research would have been a terrifying place if not for the enthusiasm and humour you both purvey.

I would also like to thank those who have provided me with insight and suggestions, despite not being directly involved my research. While technically a part of the CML group, I was always welcome in the group meetings, and will always be grateful for the guidance they provided. In particular, Professor Hugh Blackburn had a large impact on the direction of my work, with suggestions provided in both the lab meetings, and my mid-candidature review. I am also grateful towards my final submission seminar examiners, Doctor Justin Leontini and Professor Greg Sheard. The advice provided was invaluable in adding the polishing touches to the final document.

Professor Greg Sheard also provided the numerical code which made this entire thesis possible, and has also always been available if I had questions regarding the use of the code. For this, I am very appreciative. I would also like to acknowledge the facilities provided by the Department of Mechanical and Aerospace Engineering, and Monash University. The computational and physical facilities used to complete this thesis were state of the art, and the influence this had on the final outcome cannot be overstated.

"Roads? Where we're going, we don't need roads."

Dr Emmett Brown

x

Contents

Nomenclature

Table 1-1 – List of symbols used in this thesis. Symbols are presented in alphabetical order, along with their description. Refer to local context where multiple parameters share the same symbol.

Symbol	Parameter
A	Cross-sectional area
A	Eigenvalue operator
a	Core radius
α, β, γ	Coefficients for the backwards-multistep scheme
α	Angle of nozzle exterior
α	Vortex ring global tilt angle
b	Wall separation parameter
b	Kelvin instability mode branch identifier
c	Centre of vortex ring in y-direction
C	Constant for numerical vorticity distribution
D	Piston diameter
dl	Segment of vortex line
ds	Line integral specifier
dS	Surface integral specifier
δ^*	Displacement thickness
δ	Boundary layer thickness
δ	Shear layer thickness
F	Force applied
f	Oscillation frequency
F_p	Net pressure force
G	Velocity gradient tensor
Γ	Circulation
H	Distance below vortex ring
i	Imaginary number
i, j, k	Basis directions
k	Axial wavenumber
κ	Normalised wavenumber
κ	Diffusion coefficient
L	Operator in the numerical method
L	Piston stroke

Table 1-1 – continued

Symbol	Parameter
L	Distance from vortex line
λ_2	Lambda 2 operator
m	Mass
m	Azimuthal wavenumber
μ	Stability multiplier
μ	Dynamic viscosity
n	Number of waves
N	Anti-symmetric part of the velocity gradient tensor
N	Non-linear advection operator
∇	Divergence operator
ν	Kinematic viscosity
ϖ	Complex eigenvalues
ω	Vorticity
ω	Perturbation rotation rate
p	Pressure
φ	Angle from positive x-axis
ϕ	Scalar field
ψ	Streamfunction
q	Point label
R	Ring radius
r, ϑ, z	Polar co-ordinate directions
Re	Reynolds number
Re_p	Piston Reynolds number
Re_s	Shear layer Reynolds number
ρ	Density
S	Symmetric part of the velocity gradient tensor
s	Distance from vortex core
SR	Stroke ratio
σ	Real growth rate
t	Time
T	Matrix transpose operator
T	Period
τ	Shear stress
u	Velocity
U	Translational velocity of vortex ring
U_f	Free-stream velocity
U_p	Piston velocity mean
Δu	Shear layer velocity differential
V	Volume
W	Swirl magnitude
x	Distance along plate
x, y, z	Cartesian co-ordinate directions

Chapter 1

Introduction

Vortex rings are an elegant example of a closed vortex structure, existing as an essential feature of various fluidic motions, both natural and man-made. They occur in the wakes of flying and swimming creatures, from birds (Kokshaysky, 1979) and butterflies (Fuchiwaki *et al.*, 2013), to squid (Anderson and Grosenbaugh, 2005) and jellyfish (Mohseni, 2006). They develop in the downwash of fixed wing aircraft (Lundgren *et al.*, 1992) and helicopters (Ahlin and Brown, 2009), and form in the chambers of fuel injection systems (Begg *et al.*, 2009, Kaplanski *et al.*, 2010), having a significant influence on combustion efficiency (Ishizuka *et al.*, 2013). They are created as a by-product of underwater drilling (Chahine and Genoux, 1983), and develop within the human heart (Kheradvar and Gharib, 2007).

The unique properties of vortex rings are numerous and varied; they possess a self-induced velocity (Thomson, 1867), transport quiescent fluid via an entrainment bubble (Maxworthy, 1972), and develop wavy instabilities in a predictable fashion (Widnall and Sullivan, 1973). It is unsurprising that they have attracted the attention of engineers, who have sought to harness their potential. They have been trialled as a means to fight oil well fires (Akhmetov *et al.*, 1980), as efficient transport systems for solid particles (Yagami and Uchiyama, 2011), and in the production of zero-net-

mass-flux jets (Glezer and Amitay, 2002). These synthetic jets have shown excellent prospects for a number of applications, including the replacement of conventional jets (Mallinson *et al.*, 1999), delaying boundary layer separation (Amitay *et al.*, 1997), and efficiently cooling electrical systems (Pavlova and Amitay, 2006).

This thesis explores three separate but related aspects of vortex ring behaviour, which are not fully understood.

- The manner in which the addition of an azimuthal velocity component modifies the evolution of a vortex ring under axisymmetric conditions.
- The development of the linear phase of instability for equilibrated vortex rings.
- The flow structures generated by a flat plate aligned parallel with the propagation axis of a vortex ring.

1.1 Fundamental concepts

In order to describe the current understanding of vortex ring behaviour, a consistent nomenclature is required to define vortex ring systems.

1.1.1. Co-ordinate system

Two different co-ordinate systems are used when describing vortex ring systems. The basis directions of the Cartesian co-ordinate system are x, y, and z, such that the position of any point can be described in vector form as

$$\boldsymbol{x} = \boldsymbol{i}x + \boldsymbol{j}y + \boldsymbol{k}z \,.$$

1-1

In the cylindrical co-ordinate system, r, θ, and z form the basis directions, and the vector definition of position becomes

$$\boldsymbol{x} = \boldsymbol{i}r + \boldsymbol{j}\theta + \boldsymbol{k}z \,.$$

1-2

The cylindrical co-ordinates r and θ are defined as the radial and azimuthal directions, respectively.

1.1.2. Velocity

The movement of a fluid is described by the flow velocity $\boldsymbol{u}$. This vector is described by three component directions through

$$\boldsymbol{u} = \boldsymbol{i}u_x + \boldsymbol{j}u_y + \boldsymbol{k}u_z \ , \qquad\qquad 1\text{-}3$$

for the Cartesian co-ordinate system, and through

$$\boldsymbol{u} = \boldsymbol{i}u_r + \boldsymbol{j}u_\theta + \boldsymbol{k}u_z \ , \qquad\qquad 1\text{-}4$$

for the cylindrical co-ordinate system. If the divergence of the velocity field is zero, such that

$$\nabla \cdot \boldsymbol{u} = 0 \ , \qquad\qquad 1\text{-}5$$

then the flow is incompressible, and density is constant throughout the domain. The assumption of incompressibility is made for the entire scope of this thesis, as at the relatively low velocities present in vortex ring flows, the flow is effectively incompressible.

1.1.3. Vorticity

An important concept for understanding the flow field of a vortex ring is the vorticity, $\boldsymbol{\omega}$. The vorticity field is Galilean invariant, and is defined as the curl of the flow velocity $\boldsymbol{u}$,

$$\boldsymbol{\omega} = \nabla \times \boldsymbol{u} \ . \qquad\qquad 1\text{-}6$$

This vorticity can be expressed in the Cartesian co-ordinate system as

$$\boldsymbol{\omega} = \boldsymbol{i}\omega_x + \boldsymbol{j}\omega_y + \boldsymbol{k}\omega_z \,, \qquad\qquad 1\text{-}7$$

where the components are given by

$$\omega_r = \frac{\partial u_z}{\partial y} - \frac{\partial u_y}{\partial z} \,,\; \omega_y = \frac{\partial u_x}{\partial z} - \frac{\partial u_z}{\partial x},\; \omega_z = \frac{\partial u_y}{\partial x} - \frac{\partial u_x}{\partial y} \,. \qquad 1\text{-}8$$

Similarly, in the cylindrical co-ordinate system,

$$\boldsymbol{\omega} = \boldsymbol{i}\omega_r + \boldsymbol{j}\omega_\theta + \boldsymbol{k}\omega_z \,, \qquad\qquad 1\text{-}9$$

with components given by

$$\omega_r = \frac{1}{r}\frac{\partial u_z}{\partial \theta} - \frac{\partial u_\theta}{\partial z},\; \omega_\theta = \frac{\partial u_r}{\partial z} - \frac{\partial u_z}{\partial r},\; \omega_z = \frac{1}{r}\left(\frac{\partial}{\partial r}(ru_\theta) - \frac{\partial u_r}{\partial \theta}\right). \qquad 1\text{-}10$$

1.2 Fluid and flow properties

1.2.1. Density

The definition of fluid density is identical to that for a solid, assuming that the fluid has a uniform density across the domain in which it resides. The density in such a scenario is given by

$$\rho = \frac{m}{V} \,, \qquad\qquad 1\text{-}11$$

where m is the mass of the fluid within a domain of volume V.

For the purposes of the flows considered in this thesis, the fluid density is assumed to be uniform. In addition, the governing equations are typically non-dimensionalised before any analysis is undertaken. It is the ratio of the various terms

that is important in dictating the behaviour of the flow field, and as such, the actual magnitude of the fluid density is unimportant. Therefore, the density has been scaled out of the governing equations.

1.2.2. Shear force

Shearing forces occur when fluid layers flowing at different velocities interact. The fluid close to the layer interface experiences applied forces in two different directions, deforming the local fluid and inducing a shear. The shear stress τ provides a measure of the amount of shear within a flow field, and is given by

$$\tau = \frac{F}{A},$$
1-12

where F is the force applied parallel to the cross-section of fluid, with the cross-sectional area parallel to the flow denoted as A. A localised region of fluid that experiences large magnitudes of the shear force is known as a shear layer.

1.2.3. Viscosity

The ability of a fluid to resist shearing is quantified by the viscosity. The viscosity is effectively a macroscopic representation of the microscale forces occurring between the different particles of a fluid. Mathematically, the viscosity μ is related to shear stress through the equation

$$\tau = \mu \frac{\partial u}{\partial y},$$
1-13

where $\partial u / \partial y$ is the local velocity gradient perpendicular to the direction of motion. Fluids that have a constant viscosity, regardless of flow velocity or applied forces, are known as Newtonian fluids.

In flows where the density is uniform, it is also convenient to define the kinematic viscosity ν, which relates the viscosity and density through the equation

$$\nu = \frac{\mu}{\rho}.$$

1-14

1.2.4. Pressure

The pressure exerted on any particular boundary of a fluid region is given by

$$p = \frac{F}{A},$$

1-15

where F is the force applied perpendicular to the fluid boundary, with the cross-sectional area normal to the flow denoted as A. The force on a region, however, is due to the net pressure force, summed across all boundaries of the region. Mathematically, this is given by

$$\boldsymbol{F}_p = -\nabla p .$$

1-16

This equation describes fluid motion from high pressure low pressure regions.

1.3 Additional concepts

1.3.1. Circulation

The circulation of a region of fluid provides a measure of the strength of the rotation in that region. It can be related to either a line integral of the velocity around a closed curve, given by

$$\Gamma = \oint \boldsymbol{u}. \mathrm{d}\boldsymbol{s} ,$$

1-17

or to a surface integral of vorticity, through

$$\Gamma = \int \int \boldsymbol{\omega} . \, \mathrm{d}\boldsymbol{S} \ .$$

The circulation is only relevant for the fluid within the boundary of the integration, and so the choice of integration domain is important in determining the correct value of the circulation.

1.3.2. Stream function

The stream function provides a means for predicting the path of the flow for two-dimensional flows. The stream function $\boldsymbol{\Psi}$ can be determined at each point in the flow by solving the equation

$$\boldsymbol{u} = \nabla \times (0 \, , 0 \, , \boldsymbol{\Psi}) \ .$$

1-19

In Cartesian coordinates, the components are

$$u_x = \frac{\partial \Psi}{\partial y} \text{ and } u_y = -\frac{\partial \Psi}{\partial x} \ ,$$

1-20

while in cylindrical coordinates, the components are

$$u_z = \frac{1}{r}\frac{\partial \Psi}{\partial r} \text{ and } u_r = -\frac{1}{r}\frac{\partial \Psi}{\partial z} \ .$$

1-21

Lines drawn through the flow along points of constant stream function represent the streamlines of the flow, which are tangent to the flow velocity vector in that instant.

1.3.3. Reynolds number

The Reynolds number is a non-dimensional parameter that relates the relative magnitude of inertial and viscous forces. Flows with a low Reynolds number show

little to no turbulent characteristics and are dominated by viscous diffusion. Increasing the Reynolds number reduces the influence of viscous diffusion and enhances the development of turbulent structures (Reynolds, 1883).

A convenient definition for flows in which rotation dominates over strain, such as vortex ring flows, is given by

$$Re = \frac{\Gamma}{\nu},$$
<div align="right">1-22</div>

where Γ is the circulation within a relevant region, and ν is the kinematic viscosity.

1.3.4. Navier-Stokes equations

The behaviour of a fluid is completely described by the Navier-Stokes equations. The momentum equation can be written in non-dimensional form as

$$\frac{\partial \boldsymbol{u}}{\partial t} = (-\boldsymbol{u}.\nabla)\boldsymbol{u} - \nabla p + \frac{1}{Re}(\nabla^2 \boldsymbol{u}),$$
<div align="right">1-23</div>

and together with Equation 1-5, this completes the Navier-Stokes equations for an incompressible Newtonian fluid. A number of further simplifications are required in order to solve these equations analytically for generalised fluid flows. Typically, numerical methods are required to solve for flows at high Reynolds numbers, or in relatively complex domains.

1.3.5. Boundary layers

Viscosity has the effect of reducing the velocity of a fluid in the vicinity of a solid surface. The thickness of this boundary layer region is typically defined as the distance from the bounding surface to the point in the flow where the velocity has reached 99% of the free stream velocity. The thickness of a boundary layer is well understood for the case of a steady continuous Newtonian flow parallel to a flat plate,

8

where the boundary layer thickness δ for a laminar flow is given by

$$\delta = \frac{5.0x}{Re^{1/5}}.$$

1-24

In this definition, the length scale x used for the Reynolds number is the distance along the plate the flow has travelled.

Viscous flows can be modelled using inviscid analysis by replacing the non-slip surface with a free-flip surface at a distance δ^* from the original position of the surface. This displacement thickness is defined for incompressible flows as

$$\delta^* = \int_0^\infty 1 - \frac{u_x(y)}{U_f}.\,\mathrm{d}y.$$

1-25

This definition requires knowledge of the value of the free-stream velocity U_f at all points in the flow.

1.4 Vortex definition

1.4.1. Vortex geometry

A number of terms in the Navier-Stokes equations are only relevant in regions of high rotation; a region with a high magnitude of rotation within a small area is denoted as a vortex. The simplest vortex geometry is that of a 2D vortex in an isolated plane, as shown in Figure 1-1a. The vorticity is confined entirely within the plane of rotation. The distance from the vortex centre to some point in the plane is defined using the variable s. The angle around the core from the positive x-axis is denoted as Φ. The fluid within the high rotation region is the vortex core, and this region is bounded by the core radius, denoted as a. The definition of core radius depends largely on the vorticity distribution in the region, in addition to the vortex identification method used, and will be defined as required.
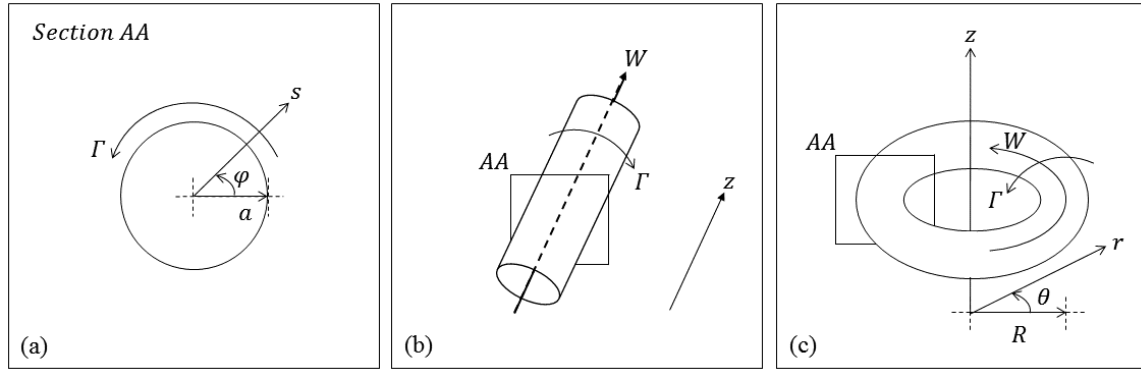
Figure 1-1 – Schematic of a vortex cross-section (a), along with two vortex geometries: a straight vortex (b), and a vortex ring (c). Section AA is a cut out of the geometries in (b) and (c). The referenced variables are circulation (Γ), distance from core centre (s), core radius (a), core angle (φ), axial velocity or swirl magnitude (W), and ring radius (R).

1.4.2. The λ_2 field

To investigate vortex dominated flows, it is necessary to define the location, strength, and spatial extent of each vortex. In practice, this is often difficult. The λ_2 field provides a convenient method of identifying regions of high rotation.

This parameter, λ_2, is defined as the second eigenvalue of the tensor $S^2 + N^2$, which is composed of the symmetric (S) and anti-symmetric (N) parts of the velocity gradient tensor G. Mathematically, these three operators are defined as

$$S = \frac{J + J^T}{2} \text{ and } N = \frac{J - J^T}{2},$$
<div align="right">1-26</div>

$$G = \nabla u = \begin{bmatrix} \partial u_x / \partial x & \partial u_y / \partial x & \partial u_z / \partial x \\ \partial u_x / \partial y & \partial u_y / \partial y & \partial u_z / \partial y \\ \partial u_x / \partial z & \partial u_y / \partial z & \partial u_z / \partial z \end{bmatrix}.$$
<div align="right">1-27</div>

Here, T is used to indicate the transpose operation on a matrix.

A negative value of λ_2 indicates that rotational effects dominate strain driven processes. That point is therefore likely to be within the core of a vortex (Jeong and Hussain, 1995).

1.4.3. Straight vortex

The logical extension to the case of a planar vortex is to project it into the out-of-plane direction. This is known as a straight or tubular vortex, and is typically assumed to be of infinite length during analysis. Such vortices can also exist with a non-zero axial velocity component. A schematic of this type of vortex is provided in Figure 1-1b.

Multiple straight vortices with aligned axes of rotation are often considered in scientific investigations, and the separation parameter between any pair of straight vortices is typically expressed as a/b, where b is the distance between the centres of the two cores.

1.4.4. Vortex ring

The extrusion of the vortex cross-section into the azimuthal direction produces a torus shaped vortex, known as a vortex ring. The geometry of a vortex ring as defined for this thesis is provided in Figure 1-1c. The axis of the vortex ring is aligned with the z-direction, and is denoted as the propagation direction. The centre of the vortex ring is positioned at $r = 0$. Velocity in the azimuthal direction is denoted as u_θ, and is referred to as the swirling component of velocity. The distance from the centre of the vortex (as defined in Figure 1-1a) remains as s.

The size of a vortex ring is defined using the ring aspect ratio Λ, which is the ratio of the core radius a to the ring radius R,

$$\Lambda = \frac{a}{R}.$$

1-28

This definition has been chosen in order to maintain consistency with the separation parameter used in the analogous problem of the Batchelor vortex pair, however note that the inverse ring aspect ratio is also sometimes used in the literature. The centre of the ring is located at $s = R$.

1.5 General vortex ring properties

1.5.1. Formation

The production of circular vortex rings is achieved in a laboratory setting by imparting linear momentum to a region of fluid, through an orifice with axial symmetry, into a tank of quiescent fluid (Batchelor, 1967). The boundary layer at the edge of the opening separates due to the shear layer that develops, and rolls-up to form the core of the vortex ring (Gharib *et al.*, 1998). The vorticity distribution of this vortex core is effectively Gaussian for very thin rings (Weigand and Gharib, 1997). The experimental setup for a piston produced vortex ring, and a visualisation of the post-formation flow field, is provided in Figure 1-2.

Studies in which the vortex rings are produced experimentally, using a piston-type setup, typically define the Reynolds number using the apparatus parameters as the length and velocity scales, through

$$Re_p = \frac{U_p D}{\nu},$$

1-29

where U_p is the mean piston velocity, and D is the diameter of the orifice through which the piston forces the fluid. The velocity over time profile of a piston is known as the velocity program. The primary non-dimensional parameter used to define the formation of piston produced vortex rings is the stroke ratio SR, defined as

$$SR = \frac{L}{D},$$

1-30

where L is the stroke length, and D is the diameter of the orifice. These variables are indicated in Figure 1-2a. The stroke ratio is sometimes referred to as the formation time, due to its large influence on the formation properties of the vortex ring (Gharib *et al.*, 1998). The cross-sectional profile of an experimentally produced vortex ring is provided in Figure 1-2b.
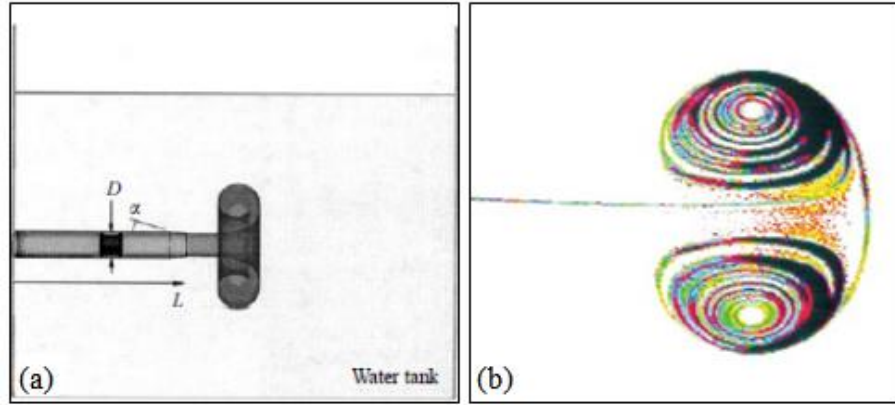
Figure 1-2 – (a) An example schematic of the production of a vortex ring, where L is the length of the piston stroke, D is the diameter of the piston, and α is the angle of the exterior of the nozzle. (b) Visualisation of an experimental vortex ring at the formation time. Reproduced from Gharib *et al.* (1998), with the permission of Cambridge University Press.

There exists a limiting value for the stroke ratio, above which the resulting vortex rings do not entrain all of the ejected fluid (Gharib *et al.*, 1998). The peak circulation possible for a vortex ring occurs when the stroke ratio is within the range $3.6 < SR < 4.5$; the exact value tends to increase with Reynolds number, with a lower piston acceleration, and with a nozzle angle α (as defined in Figure 1-2a) nearer to zero (Gharib *et al.*, 1998).

The formation process has the potential to produce both laminar and turbulent vortex rings. The Reynolds number associated with the transition from a laminar formation to a turbulent formation varies with the stroke ratio; the value is $Re \approx 10\,000$ for a ring with $SR = 1.0$, while for $SR = 4.0$, the transition occurs at $Re \approx 20\,000$ (Glezer, 1988). Vortex rings that are formed in the laminar regime can be described using similarity laws, assuming that the reference frame is attached to the translating vortex ring, and an appropriate definition of the time origin is used (Hettel *et al.*, 2007, Danaila and Helie, 2008). This property allows the Reynolds number to be controlled in numerical simulations via modifications to the viscosity of the fluid, without violating the governing equations.

1.5.2. Numerical vorticity distribution

The production of a vortex ring from a piston can be modelled numerically using a time and space varying inlet condition, ignoring the flow dynamics within the piston chamber (Danaila *et al.*, 2009). Typically, a hyperbolic tangent function is used for the inlet velocity profile; this arrangement is acceptable for qualitative analyses, as it approximates the shape of experimental jet profiles (Danaila *et al.*, 2009).

However, the use of numerical simulation also enables the implementation of an initial flow field, with the ring already formed. This negates the need to model the piston induced formation process. There are a variety of vorticity profiles that have been used to describe the vorticity distribution of a vortex core, in both numerical and analytical analyses. The simplest of these is the Rankine vortex (Thomson, 1880), which has constant azimuthal vorticity within the core. Mathematically, this can be expressed as

$$\left.\begin{array}{ll} \omega_z = C & , \quad s \leq a \\ \omega_z = 0 & , \quad s > a \end{array}\right\}, \qquad\qquad 1\text{-}31$$

where C is some constant equal to the magnitude of the vorticity. This is not a realistic vorticity profile, but simplifies many forms of analysis, allowing first order approximations.

The Norbury-Fraenkel vortex (Fraenkel, 1972, Norbury, 1973) features a linear azimuthal distribution within the core, such that

$$\left.\begin{array}{ll} \omega_z = C(a - s) & , \quad s \leq a \\ \omega_z = 0 & , \quad s > a \end{array}\right\}, \qquad\qquad 1\text{-}32$$

where C is some constant equal to the peak vorticity. This improves upon the constant vorticity approximation, whilst still simplifying analytic derivations.

A more realistic profile is the Gaussian vortex, which has a Gaussian distribution of vorticity within the core (Moore and Saffman, 1973, Saffman, 1978). The vorticity in this case can be expressed as

$$\omega_z = C \exp(-(s/a)^2) \, , \qquad\qquad 1\text{-}33$$

where C is some constant equal to the peak vorticity in the distribution. This provides a closer analogy to the measured distribution of vorticity, and is an exact solution of the Navier-Stokes equations for infinitely thin rings, or isolated straight vortices (Shariff *et al.*, 1994). All vortices asymptotically approach the Gaussian distribution over time (Le Dizes and Laporte, 2002). A straight vortex with a Gaussian distribution of vorticity in the core, and a Gaussian distribution of axial velocity, is known as a Batchelor vortex. A Batchelor vortex with zero axial velocity is sometimes known simply as a Gaussian vortex (Lacaze *et al.*, 2007).

For vortex rings with finite thickness, the Gaussian distribution does not satisfy the Navier-Stokes equations (Shariff *et al.*, 1994). To correct the vorticity distribution, a Gaussian vortex ring can be numerically "relaxed" until it reaches a quasi-steady state, where it once again satisfies the Navier-Stokes equations and only viscous forces are acting (Shariff *et al.*, 1994). Performing this relaxation at a high Reynolds number allows the ring to remain close to its initial size and circulation (Shariff *et al.*, 1994). The azimuthal vorticity contours of the relaxed state resemble those of piston produced vortex rings, and the thicker the ring, the further from the Gaussian distribution the result progresses (Archer *et al.*, 2008).

This result of this process is presented in Figure 1-3, where the modification from a perfect Gaussian is evident in the vorticity contours. The quality of the relaxation can be determined by considering the relationship between the azimuthal vorticity and the streamfunction at each point in the flow. The condensing of a scatter plot of this data into a single curve, as shown in Figure 1-4, signals that the relaxation process has completed (Shariff *et al.*, 1994). This relaxation process and the resulting azimuthal vorticity distribution of the vortex ring has been well established for non-

swirling rings, although the evolution time required for relaxation is inconsistent across publications (Shariff *et al.*, 1994, Le Dizes and Verga, 2002, Archer *et al.*, 2008). The relaxed vorticity distribution for swirling Gaussian vortex rings is currently unknown.
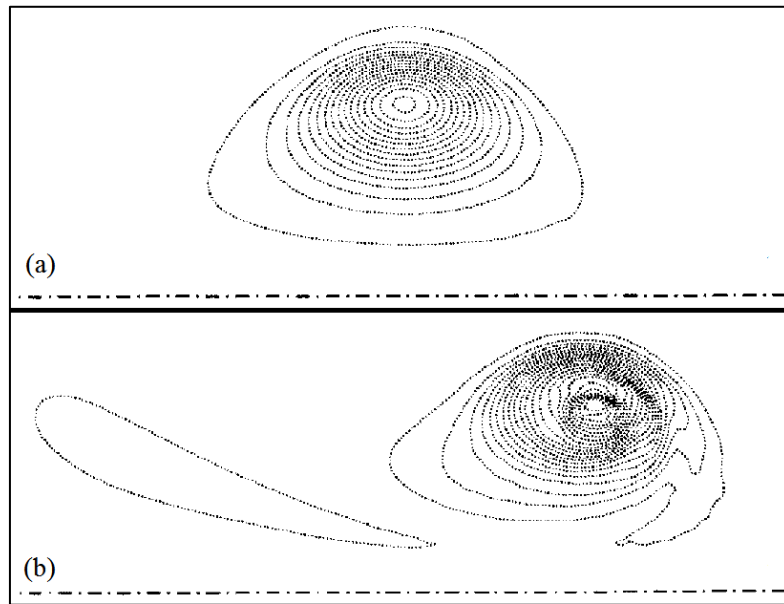
Figure 1-3 –Azimuthal vorticity of the cross-section of the vortex core of a ring, (a) in the process of relaxing, and (b) having completed the relaxation process. The dash-dot lines show the axis of the vortex ring. Reproduced from Shariff *et al.* (1994), with the permission of Cambridge University Press.
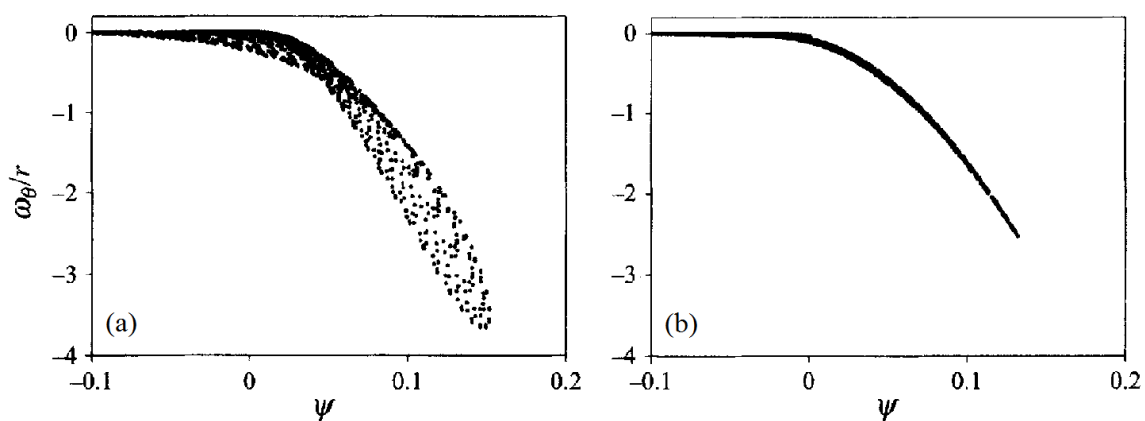
Figure 1-4 – A quantitative representation of the change in the flow field due to the relaxation process. The scatter plots show vorticity (normalised by *r*-position) versus streamfunction for all grid points in the field of a vortex ring, for (a) Gaussian initial conditions, and (b) the equilibrated condition. The relaxation is evident in the compression of the initially spread out points into a single smooth curve. Reproduced from Shariff *et al.* (1994), with the permission of Cambridge University Press.

Given that the analysis of numerical vortex rings need not rely on piston generated initial conditions, the definition of the Reynolds number can be modified to use more relevant flow parameters, namely the circulation based definition provided in Equation 1-22. This definition ties the Reynolds number to a property of the vortex ring itself (the circulation of the core), rather than to the apparatus used to create it.

1.5.3. Velocity field

For a simple line vortex, the influence on a point some distance from the vortex line is given by the Biot-Savart law (Batchelor, 1967). This relation sums the contribution from each infinitesimal segment of these filaments to determine the velocity at a chosen point. The velocity at a point q, which is a distance L from a segment of the vortex core of infinitesimal length dl, is given by

$$u_x = \frac{\Gamma}{4\pi} \oint \frac{dl \times \boldsymbol{L}}{|L|^3}.$$

1-34

This equation is effectively a simplification of the vorticity Navier-Stokes equations, which are obtained by taking the curl of Equation 1-23. This equation is shown schematically in Figure 1-5.
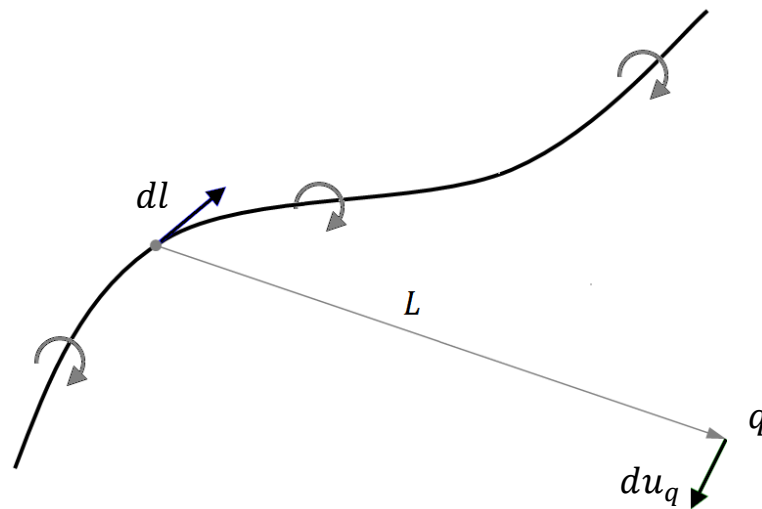
Figure 1-5 – Schematic of the Biot-Savart approximation for the vortex line segment. The velocity induced at point q depends on the sum of the influence of all the infinitesimal line segments dL.

The velocity field induced by a vortex ring is complicated by the curvature of the geometry. The flow field induced by an infinitely thin vortex ring may be exactly defined through the use of the Biot-Savart law, with the exception of the points along the singularity line. However, for a finite thickness vortex ring, the equation is applicable only for the velocity field far from the rotational region. In these cases, it can be used to approximate the spatial extent of the influence of a vortex ring.

1.5.4. Translational velocity and viscous diffusion

The velocity field of an isolated vortex ring induces a translational velocity on the ring itself (Thomson, 1867). An empirical relation for this velocity was derived by Lamb (1879), and is similar to the form of the Biot-Savart law from Equation 1-34. The translational velocity U is expressed as

$$U = \frac{\Gamma}{4\pi R}\left[\ln\left(\frac{8}{\Lambda}\right) - \alpha\right],$$
1-35

where α is a constant that depends on the core vorticity distribution. A thin vortex ring with constant core vorticity has $\alpha = 0.5$ (Lamb, 1879). However, a thin vortex ring with a Gaussian distribution of vorticity has been shown to have a value closer to $\alpha = 0.558$ (Saffman, 1970). A correction for ring thickness, up to $\Lambda = 0.4$, was suggested by Archer *et al.* (2008), who empirically determined that

$$\alpha = 1.12 \times \Lambda^2 + 5.0 \times \Lambda^4 + 0.558 \,.$$
1-36

The exact translational velocity of a vortex ring varies over time, as vortex rings change in size as they evolve. Vortex rings with a finite Reynolds number will grow in size over time, due to viscous diffusion. The size of the vortex core at a particular time t is a function of the initial core radius a_0 and the viscosity v, and can be found using the equation of Saffman (1970), where

$$a^2 = a_0^2 + 4vt \,.$$
1-37

1.6 Vortex ring with azimuthal velocity

In a modification analogous to the addition of an axial velocity to Gaussian vortex, an azimuthal velocity component can be added to the core of a vortex ring. This is the W component shown referred to in Figure 1-1c. Vortex rings with a non-zero W component are typically denoted as "swirling" rings, and are essential building blocks of turbulent flows (Virk *et al.*, 1994). They give excellent first approximations to the downwash of helicopter blades (Ahlin and Brown, 2009), and have helped elucidate various types of vortex breakdown (Ooi *et al.*, 2001, Shariff and Leonard, 1992, Panda and McLaughlin, 1994). A localized azimuthal velocity can develop in a vortex ring without swirl as a consequence of the growth of wavy instabilities (Naitoh *et al.*, 2002), or the presence of a confining wall (Chang *et al.*, 1997).

The magnitude of the swirling flow of a vortex ring is quantified in this thesis by considering the maximum of the non-dimensional azimuthal velocity within the vortex core. Mathematically, the swirl magnitude W is given by

$$W = \max[u_\theta] \Big|_{R-a}^{R+a}$$

1-38

This is equivalent to the definition used to quantify the axial velocity component of a Batchelor vortex (Lacaze *et al.*, 2007).

1.6.1. Analytical studies

The early considerations of swirling vortex rings focussed on analytical proofs of their existence. Moffatt (1988) compared the evolution of a viscous vortex ring flow field to the process of magnetic relaxation, and obtained steady solutions of the Euler equations. This analysis showed that vortex rings with a volume flux within the vortex core were able to form with a steady structure. Turkington (1989) independently performed a similar analysis, without the magnetism analogy, and found that steady flows occurred when the swirl was less than a certain critical magnitude.

1.6.2. Effect on propagation velocity

The modification of the propagation velocity of vortex rings due to swirl has also been investigated. Thin-cored vortex rings were predicted to have a reduction in translational velocity with the addition of an azimuthal velocity component (Widnall *et al.*, 1970, Moore and Saffman, 1972). This was confirmed via a later numerical study of polarised rings, which are a sub-class of swirling rings (Virk *et al.*, 1994). That study assumes a Gaussian distribution of vorticity, although the reduction in translational velocity has also been observed in a numerical study of a piston generated swirling vortex ring (Ooi *et al.*, 2001).

1.6.3. Axial vortex

Various studies have demonstrated the development of a straight vortex (see Section 1.4.3), which forms along the axis of a swirling vortex ring during the early evolution. It was initially noted in numerical studies of axisymmetric rings with relatively weak swirls, by Virk *et al.* (1994) for $\Lambda = 0.2$ at $Re = 800$, and by Ooi *et al.* (2001), for $\Lambda \approx 0.5$ at $Re = 4\ 020$ (see Figure 1-6). The axial vortex has also been observed in an experimental study for rings with swirl up to a magnitude of $W = 3.0$, with $Re = 2\ 000$ and $\Lambda \approx 0.5$ (Naitoh *et al.*, 2014). The diversity in these three studies suggests that the development of an axial vortex is independent of ring size, swirl magnitude, and initial vorticity distribution.

1.6.4. Leading edge shear layer

The development of oppositely signed vorticity at the leading edge of a swirling vortex ring (henceforth known as the leading edge shear layer) has also been identified. Virk *et al.* (1994) and Ooi *et al.* (2001) again agreed with each other, identifying the appearance of a thin leading edge shear layer, near the $r = 0$ axis (see Figure 1-6b). A much stronger leading edge shear layer was observed by Cheng *et al.* (2010), who analyzed a range of vortex rings with $0.2 < \Lambda < 0.5$ and $0.4 < W < 2.0$, at $Re = 800$. This study featured a full 3D numerical domain, however used a

Gaussian profile as the initial vorticity distribution, and did not relax the rings before commencing the analysis. Therefore, as explained in Section 1.5.2, the initial flow field used is not a solution of the Navier-Stokes equations.
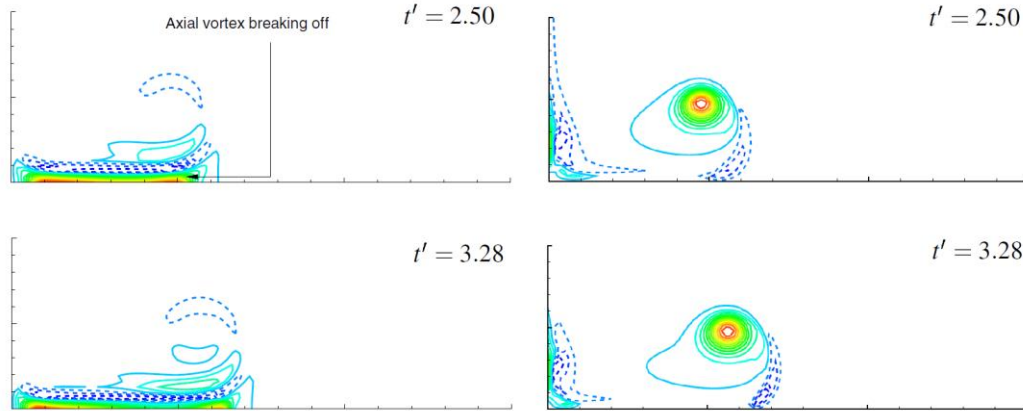
Figure 1-6 – Development of the axial vortex (left frames, showing azimuthal velocity), and the leading edge oppositely signed vorticity region (right frames, showing azimuthal vorticity). Reproduced from Ooi *et al.* (2001), with the permission of the corresponding author.
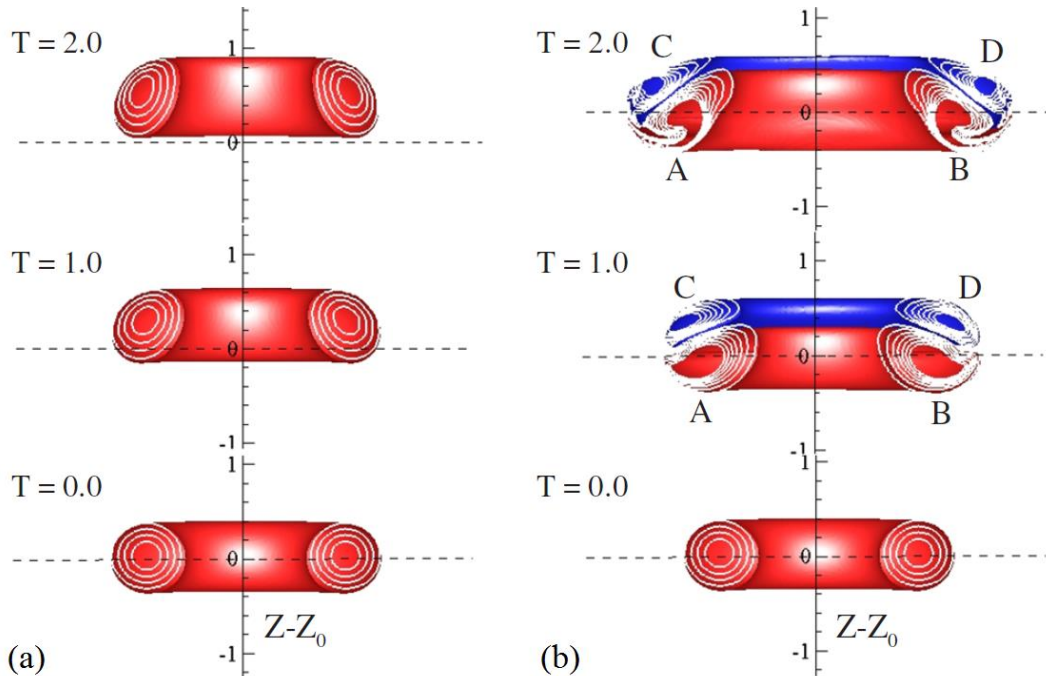
Figure 1-7 – Iso-surfaces of positive and negative azimuthal vorticity, for (a) a non-swirling vortex ring, and (b) a swirling vortex ring. The development of the oppositely signed vorticity region can be observed in the field of the swirling vortex ring. Reproduced from Cheng *et al.* (2010), with the permission of AIP Publishing.

Regardless, Cheng *et al.* (2010) found that the leading edge shear layer developed into a secondary vortex ring (see the blue contours in Figure 1-7), possessing a higher concentration of vorticity compared to the original ring, but with a lower total circulation. They explain this phenomenon by noting that the centrifugal force induced by the swirl drives the fluid towards the outer edge of the ring, producing a pair of oppositely signed vortices. One of these vortices increases the strength of the original ring, while the other produces a ring of opposite sign. The total circulation remains constant. Additionally, they observed that the strength of the swirl determines the influence that the secondary ring has on the evolution of the primary ring, and that the secondary ring always forms upstream of the original ring.

In the experimental work of Naitoh *et al.* (2014), temporary development of the expected leading edge shear layer occurred, but the layer diffused soon after (see Figure 1-8). This is surprising, given the swirl magnitude and Reynolds number are similar to those used by Cheng *et al.* (2010). In place of the shear layer, they observed the subsequent occurrence of an asymmetric "peeling off" action present on the rings, dragging fluid from the leading edge of the vortex ring axis, around the exterior of the ring, and into the wake. The reason for this difference is unknown.

(a) *t* = 1.0 s   (b)   *t* = 1.3s
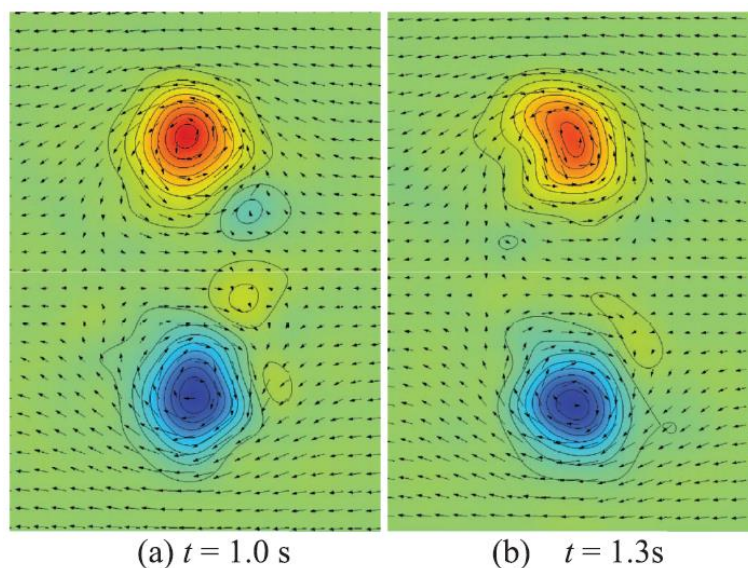
Figure 1-8 – Velocity vectors with coloured azimuthal vorticity contours in a cross section of the vortex ring. The oppositely signed vorticity region can be observed to form and then diffuse soon after. Reproduced from Naitoh *et al.* (2014), with the permission of AIP Publishing.

1.7 Linear stability of vortex rings

The stability of isolated vortex rings has been considered by various authors. Vortex rings are known to be susceptible to sinuous instabilities in a manner analogous to Gaussian vortices in a strain field (Widnall and Sullivan, 1973, Widnall *et al.*, 1974, Saffman, 1978). The addition of axial velocity to a Gaussian vortex pair (resulting in a Batchelor vortex pair) has been shown to modify the identity of the most amplified instability (Lacaze *et al.*, 2007). Swirling vortex rings develop wavy instabilities in a similar manner to non-swirling rings (Lifschitz *et al.*, 1996, Hu *et al.*, 2001), so it is likely that the same instability mechanisms apply. The core structure of the instabilities present on swirling rings has not been elucidated.

1.7.1. Bachelor vortex pair instability

Vortices (either Batchelor vortex pairs, or vortex rings) are unstable to resonant combinations of Kelvin modes (Crow, 1970, Widnall *et al.*, 1970, Widnall and Sullivan, 1973, Archer *et al.*, 2008). Such vortices have been studied extensively since the time of Thomson (1880), and the primary instability mechanisms summarised by Saffman (1992) and Kerswell (2002). The instability of the base field can be described through a normal mode analysis, where the form of a perturbation in the velocity $\boldsymbol{u}$ for a vortex pair can be expressed as

$$\boldsymbol{u}' = \boldsymbol{u}(s) \exp(i[kz + m\phi - \varpi t]) \, , \qquad \text{1-39}$$

where s is the distance from the centre of the core, k is the axial wavenumber, and m is the wavenumber around the vortex core (see Figure 1-9a and Figure 1-9c). For a vortex ring, the perturbation equation is

$$\boldsymbol{u}' = \boldsymbol{u}(s) \exp(i[k\theta + m\phi - \varpi t]) \, , \qquad \text{1-40}$$

where k is the azimuthal wavenumber, and m is the same as in the vortex pair case (see Figure 1-9b and Figure 1-9c).
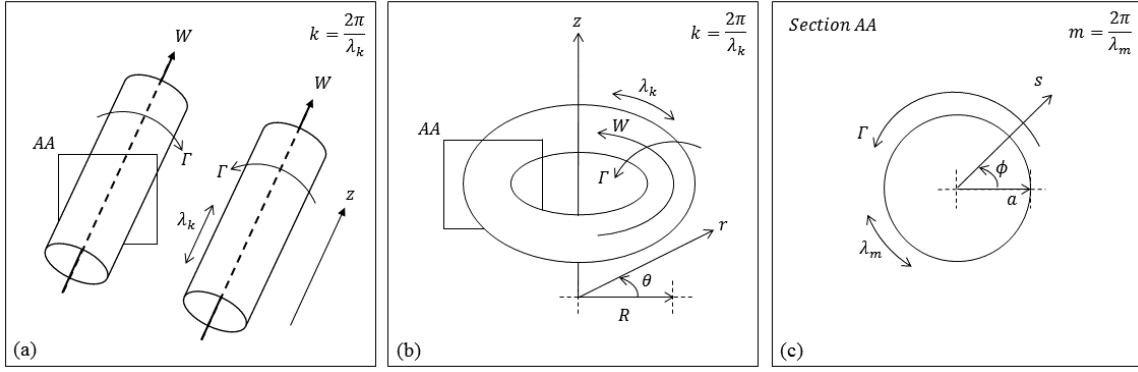
Figure 1-9 – Schematic of the geometric and stability definitions for (a) a Batchelor vortex, and (b) a swirling vortex ring. The cross-section of the vortex core, which is the same for both cases, is given in (c). The wavelengths λ_k and λ_m are the wavelengths corresponding to the wavenumbers k and m, respectively, for wavy instabilities that may develop.

In both cases, ϖ represents the complex eigenvalues of the solution, and can be expressed as a function of the real growth rate σ and oscillation frequency f, through

$$\varpi = f + \mathrm{i}\sigma, \qquad\qquad 1\text{-}41$$

The real growth rate is inhibited by viscous damping, leading to a critical Reynolds number, below which instabilities are not observed. Conversely, for large Reynolds numbers, vortices undergo a transition to turbulence, before the Kelvin instabilities can form.

In order to be consistent in referencing the two different geometries, the wavenumber k is designated as the out-of-plane wavenumber. For a vortex pair, this is the wavenumber along the length of the infinite vortex, and can take arbitrary values, while for a vortex ring, this wavenumber is around the azimuth, and is periodic. The wavenumber m is designated as the in-plane wavenumber (around the vortex core) regardless of the geometry.

Instabilities of this type are typically defined by the value of the in-plane wavenumber, and are collectively known as Kelvin modes. Each value of m can have multiple mode shapes (see Figure 1-10), known as different branches of the mode, and typically the various branches of a single mode have similar characteristics.

1.7.2. Form of instability

An isolated Batchelor vortex immersed in a strain field exhibits instability through the normal mode resonance of two Kelvin modes. Typically, some combination of m and $m+2$ is the most amplified (Tsai and Widnall, 1976, Moore and Saffman, 1975). Although it has been referred to here as a resonant Kelvin instability, this instability mechanism is essentially the elliptic instability, which has also been investigated by numerous authors (Leweke and Williamson, 1998, Eloy and Le Dizes, 1999, Lacaze *et al.*, 2007). However, other combinations of m are possible such as the curvature instability (introduced in Section 1.7.5). For a Gaussian vortex pair (*i.e.* with no axial velocity), the [–1 , +1] resonant pair is most amplified (Tsai and Widnall, 1976).

(a) mode 1: $(-1,1,1)$ (b) mode 2: $(-1,1,2)$ (c) mode 3: $(-1,1,3)$ (d) mode 4: $(0,-2,1)$ (e) mode 5: $(0,-2,2)$

(f) mode 6: $(0,-2,3)$ (g) mode 7: $(-1,-3,1)$ (h) mode 8: $(-1,-3,2)$ (i) mode 9: $(-2,-4,1)$ (j) mode 10: $(-1,1,[1,2])$
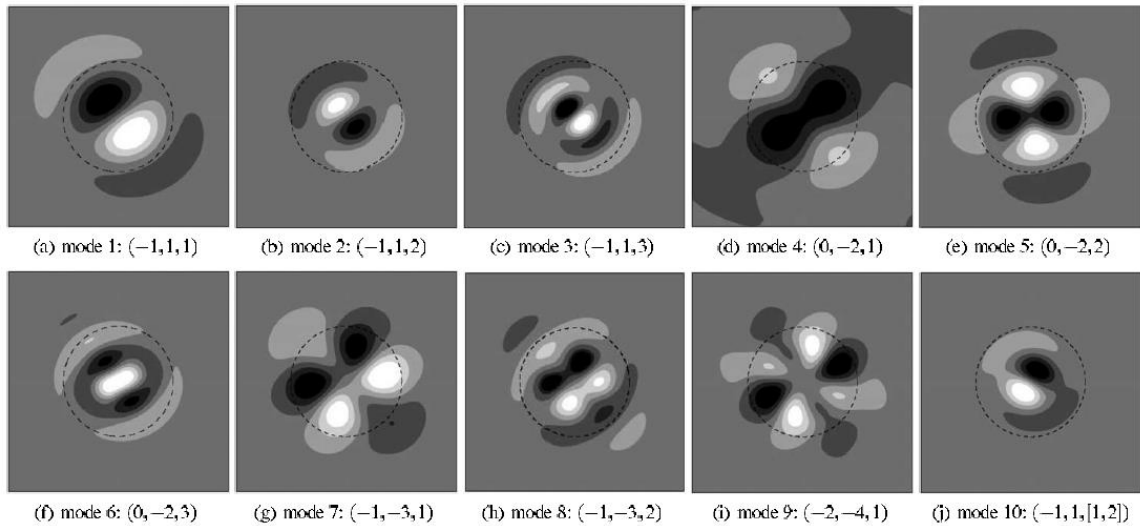
Figure 1-10 – Axial vorticity perturbation fields resulting from resonant Kelvin mode instabilities for various mode combinations and their branches. The notation for each mode is given as (m, $m+2$, [b_1 b_2]), where b_1 and b_2 are the branch numbers of each mode. If $b_1 = b_2$, then only one value is provided. Reproduced from Roy *et al.* (2008), with the permission of AIP Publishing.

Points in the wavenumber domain where the rotational frequency for the branches of the two modes intersect indicate regions where maximum amplification occurs (Tsai and Widnall, 1976). Figure 1-11 presents the rotational frequency for three branches of the first bending mode (+1) instability, as a function of the normalised wavenumber. The (-1) mode is mirrored about the *x*-axis of the plot; the intersection points between these two modes therefore occurs along the horizontal axis (corresponding to a zero global rotation rate of the perturbation). Combinations of mode branches that induce perturbations with a self-induced rotation rate of zero produce the most amplified instability (Moore and Saffman, 1975, Tsai and Widnall, 1976). The intersection points will exhibit the peak growth rate in their immediate vicinity, however the rotation rate does not need to exactly match that of an intersection point to induce growth. This implies vortex cores are actually unstable to a band of wavenumbers around an intersection frequency, although the growth rate will be lower when the frequency is offset from the intersection point (Tsai and Widnall, 1976).
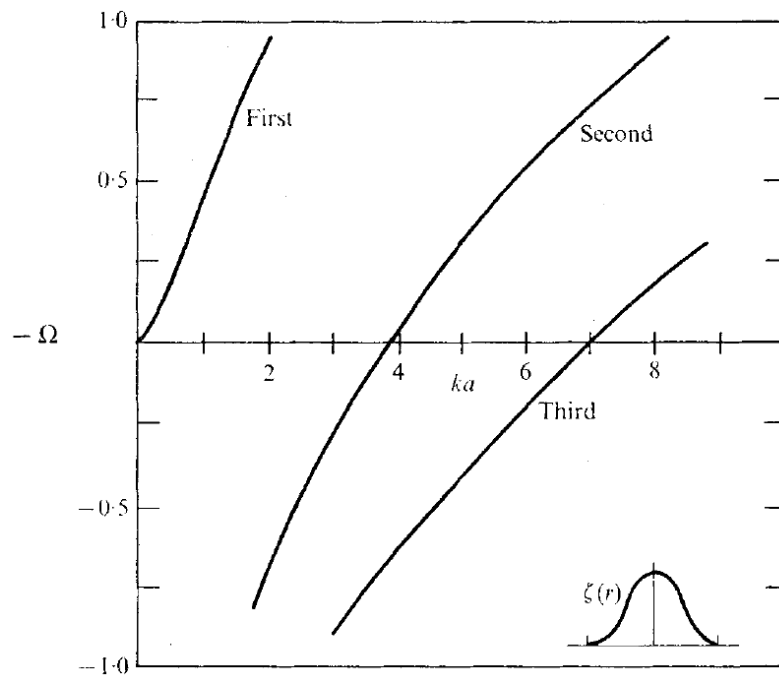
Figure 1-11 – Dispersion relations for bending modes on a Cartesian vortex with a Gaussian distribution of vorticity. The vertical axis represents the global rotation rate of a perturbation. Reproduced from Widnall *et al.* (1974), with the permission of Cambridge University Press. For a more current example, see Sipp and Jacquin (2003).

26

The addition of an axial velocity component to the Gaussian pair vortex core (forming a Batchelor vortex pair) breaks the symmetry between the bending modes, damping the [–1 , +1] modes and maximally amplifying a different combination of [m , m+2] (Lacaze *et al.*, 2007). Thus, the addition of an axial flow will result in a particular intersection point, associated with non-zero rotation rate, producing the most amplified instability (Moore and Saffman, 1975). The different unstable combinations of [m , m+2] will coexist in different regions of the κ-W plane, which has been shown (see Figure 1-12) for both co- and counter-rotating Batchelor vortex pairs (Lacaze *et al.*, 2007, Roy *et al.*, 2008, Ryan *et al.*, 2012).
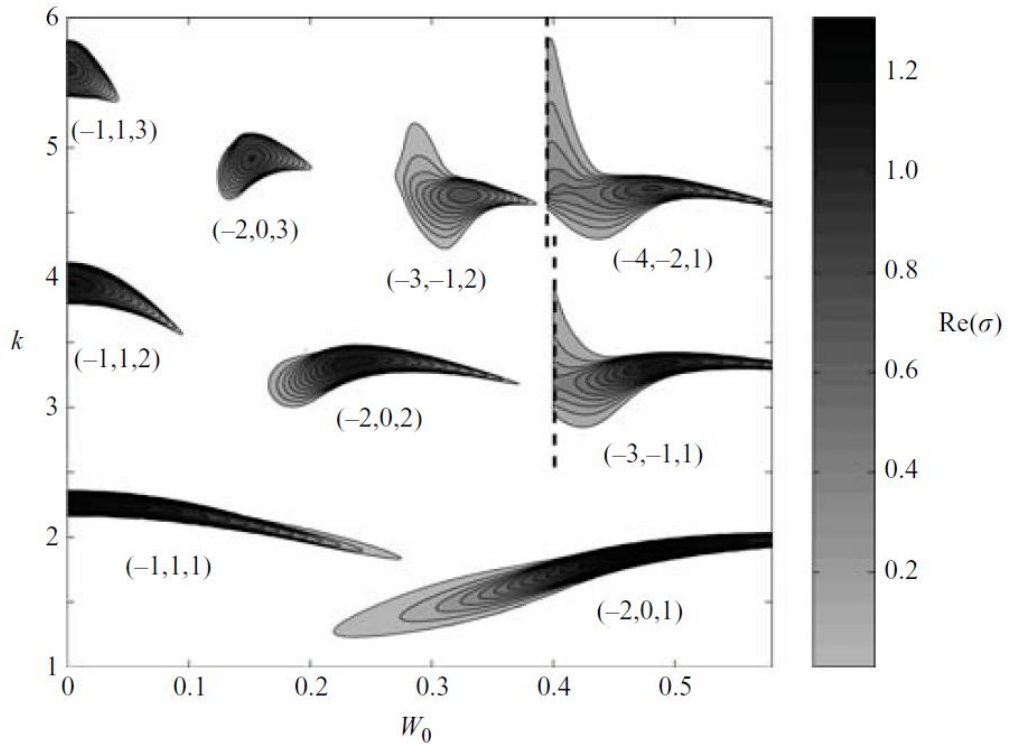
Figure 1-12 – Instability regions of the principal mode combinations in the (W_0, κ) plane, at a Reynolds number of 20 000. The vertical axis is equivalent to κ, while the growth rate $Re(\sigma)$ is equivalent to σ as defined in Equation 1-41. Reproduced from Lacaze *et al.* (2007), with the permission of Cambridge University Press.

1.7.3. Vortex rings

Vortex rings are subject to similar instability mechanisms, but have an additional constraint that k can only take certain discrete values, as an integer number of waves must be present. The value of k varies across the ring as a function of the distance r from the vortex ring axis. The wavenumber at the centre of the core k_c can be expressed as

$$k_c = \frac{n}{R},$$

1-42

where n is a positive integer and R is the ring radius. The normalised wavenumber can then be defined as a function of the ring aspect ratio,

$$\kappa_c = n\Lambda .$$

1-43

A vortex ring in an incompressible inviscid fluid is almost always unstable (Widnall and Sullivan, 1973). With the introduction of a finite viscosity, the number of waves induced by an instability can vary over time, as shown by both theoretical vortex models (Thomson, 1880) and numerical analyses (Shariff *et al.*, 1994). The value of κ for which an instability is amplified can be approximated using a modified asymptotic theory for a vortex ring with a uniform distribution of vorticity in the core (Widnall *et al.*, 1974). The effect of curvature on stability is only a local effect for vortex rings with this vorticity distribution (Widnall and Tsai, 1977). The largest correction required to this approximation is a viscous correction. Small non-zero rotation of the perturbations, the assumption of a thin core, and the various definitions of core radius, have all been found to have negligible effect on the instability (Saffman, 1978).

Typically, theoretical analysis accurately predicts the number of waves that form on an unstable vortex ring, while overestimating the magnitude of the experimentally observed growth rate, even after applying the viscous correction (Dazin *et al.*, 2006).

The predicted growth rates are also consistently higher than the computed growth rates for numerically simulated vortex rings; physical effects such as the growing vortex core are not accounted for in the analyses. Results from all methods generally agree on the wavenumber of the most amplified mode (Lifschitz *et al.*, 1996).

Experimental investigations will always have multiple modes present, and varying ring sizes. Real vortex rings with vary in size over time (through the action of viscous diffusion via Equation 1-37), continuously modifying the growth and identity of the most amplified instability. Asymptotic approaches predict the maximum possible growth rate for all perturbations, while simulations typically consider only a single mode (Lifschitz *et al.*, 1996). It is therefore understandable that experimentally derived results rarely align perfectly with predictions.

1.7.4. Swirling vortex rings

The development of instabilities on swirling vortex rings is expected to follow the Kelvin framework outlined for vortex pairs and non-swirling vortex rings. The parameter ranges over which instability of Batchelor vortices has been studied incorporate small values of W (i.e. 0.0 to 0.5), and κ values in the range of 1.0 to 6.0. Lacaze *et al.* (2007) considered very thin counter-rotating Batchelor vortex pairs (core radius to separation ratio of 0.01) with Reynolds numbers of 5 000 and 20 000, and found that only the strength of the most amplified resonant modes varied with Reynolds number, not the position of each within the parameter space. Roy *et al.* (2008) considered both co-rotating and counter-rotating Batchelor vortex pairs (core radius to separation ratio of 0.14 to 0.18), with Reynolds numbers of 14 000 and 31 400, and noted that the region of instability varied slightly as the thickness of the pair was varied. It is therefore likely that the ring aspect ratio will influence the growth regions for the case of swirling vortex rings.

The growth and behaviour of the [–1 , +1] resonant mode pair for non-swirling vortex rings has been presented previously (Archer *et al.*, 2008, Shariff *et al.*, 1994, Widnall and Tsai, 1977), however it appears that other combinations of [*m* , *m+2*] for a vortex

ring are either more difficult to identify, or have not been considered or published. The stability of vortex rings with swirl (for which alternate modes would be expected to grow) has been considered in multiple studies (Lifschitz *et al.*, 1996, Hu *et al.*, 2001, Naitoh *et al.*, 2002, Hattori and Fukumoto, 2012, Cheng *et al.*, 2010), however the resulting modes have not been consistently discussed with regards to the Kelvin framework.

Swirling rings have been shown via numerical simulations to develop both the zeroth and first branch of the [–1 , +1] instability, during the linear growth phase (Hu *et al.*, 2001). The growth rate for the first branch combination is similar to that of the non-swirling case, while the zeroth branch does not have any zero crossing for a vortex ring without swirl (Hu *et al.*, 2001). In the same study, on a much thicker ring, multiple resonant pairs were amplified simultaneously, due to the large variation in k over the vortex core; this prevented the identification of any of the individual modes involved.

It is expected that modes for a swirling vortex ring will be analogous to those that develop on Batchelor vortex pairs, however, a consolidated mapping of instability modes in a κ-W parameter space is not yet available for swirling vortex rings. In addition, much of the work on swirling rings has been performed using unrealistic azimuthal vorticity distributions. Additional research is required to bring the understanding of swirling vortex ring instability growth up to the level that exists for Batchelor vortices. Enhancing the understanding of the relationship between swirling vortex ring instabilities, and that of vortex pairs and non-swirling rings, will enable the use of instabilities to suit individual applications.

1.7.5. Curvature instability

An additional type of instability, known as the curvature instability, has also been predicted to develop on vortex rings (Hattori and Fukumoto, 2003). This instability involves a resonance between Kelvin modes of m and $m+1$, and has been determined to be a first order effect (Fukumoto and Hattori, 2005). The curvature instability

may be stronger than the elliptic instability, but only in cases with a sufficiently strong swirling component of velocity (Blanco-Rodriguez and Le Dizes, 2016). For Reynolds numbers on the order of 10^4, only very thin rings ($\Lambda < 0.125$) are expected to support its growth (Fukumoto and Hattori, 2005). Additionally, the use of an equilibrated Gaussian as an initial condition prevents the exponential growth rate of this instability (Fukumoto and Hattori, 2005). These compounding factors make it unlikely that the curvature instability will be observed in the results of this thesis.

1.8 Near-wall evolution of vortex rings

1.8.1. Relation to synthetic jets

A zero-net-mass-flux or synthetic jet is produced by the oscillation of a piston within a closed domain, producing an array of vortex rings which may coalesce into a coherent jet, depending on the exact frequency of oscillation (Glezer and Amitay, 2002). The use of synthetic jets as replacements for conventional cooling devices has already shown potential in the impingement of a jet directly onto a heated surface (Pavlova and Amitay, 2006). The use of synthetic jets as a cooling mechanism parallel to a surface requires further research.

The complete behavior of jets interacting with a solid parallel surface is likely to be described by a combination of the physics governing a vortex ring translating parallel to a flat surface, and the behavior of multiple vortex rings interacting in an unbounded domain (Ghosh and Baeder, 2012). The interaction between a vortex ring and a flat featureless wall therefore provides a first principles approximation to the physics of asymmetrically bounded synthetic jets.

1.8.2. Straight vortices

The effect of aligning the translational axis of a vortex ring parallel to a wall has received limited attention in the literature; however the behavior of a wall-

influenced vortex ring can be predicted from the near-wall behavior of straight vortices. These vortices move parallel to the surface due to the inviscid interaction between the physical vortex and its mirror image behind the wall (Doligalski and Walker, 1978). A recirculation region forms upstream of the vortex core (relative to the direction of travel) due to an adverse pressure gradient near the surface (Doligalski and Walker, 1978). This results in a localized increase in the thickness of the boundary layer (see Figure 1-13), which manifests as a narrow spire of oppositely signed vorticity (Peridier *et al.*, 1991). The generated vorticity wraps around the primary vortex core (Doligalski *et al.*, 1994), reducing its strength (Visbal, 1991). This boundary layer expulsion occurs for any boundary layer flow in which there is a persistent adverse pressure gradient (Elliot *et al.*, 1983). A large free stream velocity differential between the wall and the fluid reduces the response of the boundary layer to this effect (Degani and Walker, 1992).
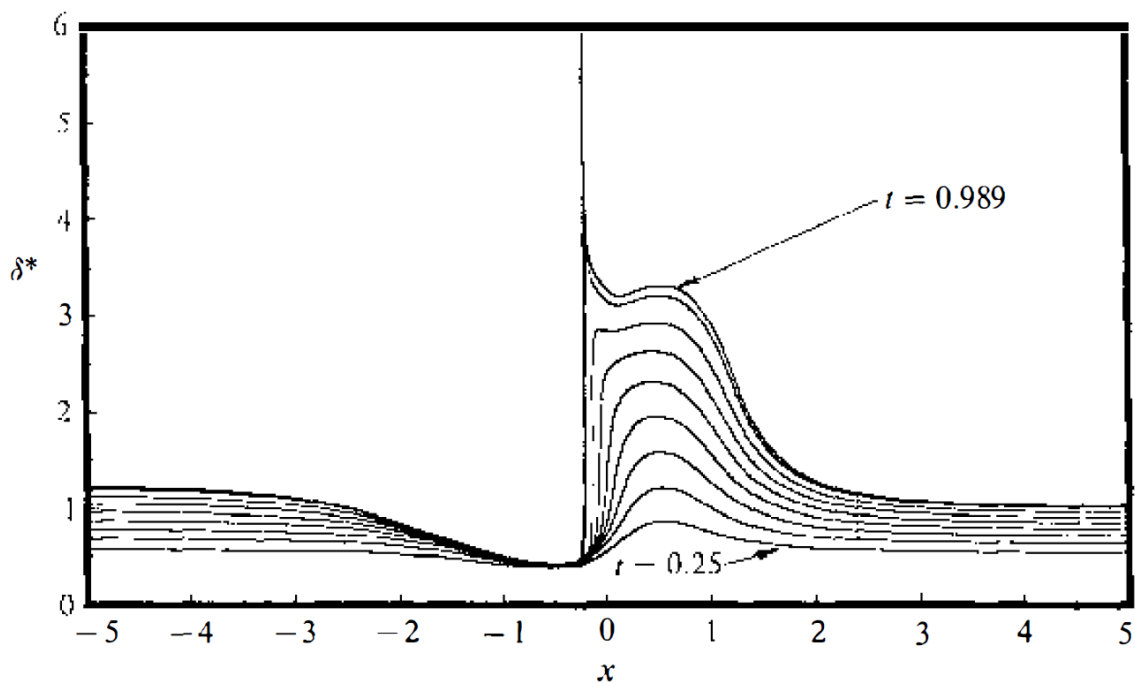
Figure 1-13 – Time evolution of the displacement boundary layer thickness for separation due to a near-wall vortex. The $x = 0$ position indicates the position of the centre of the vortex core. The vortex has anticlockwise rotation. Reproduced from Doligalski *et al.* (1994), with the permission of Annual Reviews.

1.8.3. Direct impact

The direct impact of a vortex ring with a wall, where the translational axis is perpendicular to the wall surface, has also been observed to result in ejection of boundary layer material (Walker, 1978). This occurs due to the development of an adverse pressure gradient on the wall adjacent to the core of the impacting ring (Yamada *et al.*, 1985). For very small distances between the vortex ring generator and the wall, the abrupt ejection of oppositely signed vorticity coalesces into a secondary vortex ring (Orlandi and Verzicco, 1993b), while the primary ring rebounds off the wall (Harvey and Perry, 1971). A sufficiently large Reynolds number enables the development of additional vortex structures, including tertiary rings (Cerra Jr and Smith, 1983). The additional rings are convected around the original core, into the center of the primary ring, while any additional structures typically move away from the wall entirely (Cerra Jr and Smith, 1983). These collisions enhance transport and mixing of the near-wall fluid (Verzicco and Orlandi, 1996).

1.8.4. Oblique collisions

Oblique collisions of a vortex ring with a wall, where the angle between the wall surface and translational axis is between 0° and 90°, have also been observed. Typically, oblique collisions compress the near-wall core (Lim, 1989), developing oppositely signed vorticity and reducing the strength of the core (Verzicco and Orlandi, 1994). This is accompanied by unsteady boundary layer separation (Ersoy and Walker, 1987), and the development of fluid structures at the opposite side of the ring (Verzicco and Orlandi, 1994). These structures, developed from within the boundary layer, are carried towards the far side of the ring via a pressure differential, and form at much lower Reynolds numbers than required in a direct collision (Verzicco and Orlandi, 1994). These dynamics vary considerably from those observed for the analogous case of the oblique impact of a vortex pair (as opposed to a ring), where very limited secondary structures are able to develop (Verzicco and Orlandi, 1994).

1.8.5. Parallel interaction

Prior studies have not considered a vortex core translating parallel to a non-slip wall. However, the findings of the normal and oblique impact cases do provide some insight to the expected behavior of a near-wall vortex ring. The development of a recirculation region and subsequent boundary layer eruption is expected for the near-wall core, accompanied by the movement of fluid structures from the boundary layer to the far side of the vortex ring. The region of the ring nearest the wall will weaken due to the development of oppositely signed vorticity, while the nearby sections of core are likely to develop azimuthal velocity (swirl) due to the fluid circulation that develops. Additionally, a vortex ring aligned axially with a non-slip flat plate experiences opposing self-induced velocity fields, as the self-induced velocity of the vortex ring (Lamb, 1879) opposes the velocity induced by the mirror image (Milne-Thomson, 1962). This should produce a forward velocity differential across the vortex ring, bending the vortex ring about its primary axis, and directing its motion towards the wall.

Previous studies of confined vortex rings (as outlined in Section 1.8.3 and Section 1.8.4) have failed to confirm these expected behaviors, as the focus has typically been on domains with either two-fold or four-fold symmetry. The case of a single plate parallel to the motion vector has not been considered, however elliptical vortex rings have been investigated moving parallel to, and in-between, twin no-slip plates at low Reynolds numbers (Chang *et al.*, 1997). Results from this work are presented in Figure 1-14 and Figure 1-15. The interaction between the elliptical vortex rings and the flat plates produces secondary vortex tubes near the surface of each plate, while helical axial waves move the surface fluid away from the flat plates and into the center of the domain (Chang *et al.*, 1997). The relation between this mechanism and that of the boundary layer spires of the vortex tube case has not been explored. In addition, the vortex ring separates into a vortex pair early in the evolution, restricting the development of asymmetric phenomena (Chang *et al.*, 1997).
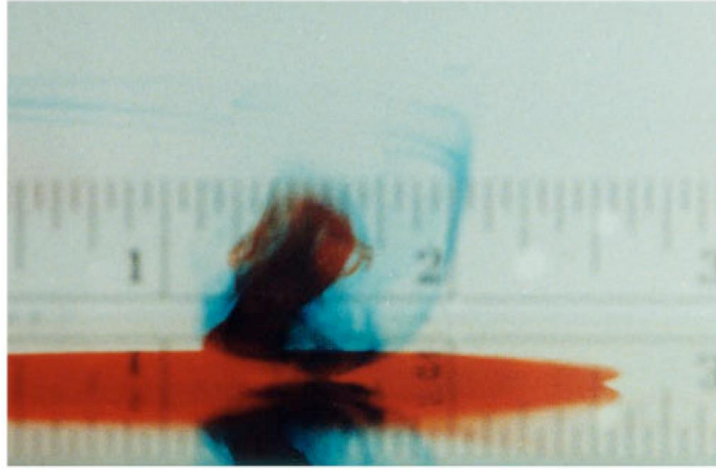
Figure 1-14 – Image from experimental work, showing near wall fluid (red), being drawn into the core of the vortex ring (blue). Reproduced from Chang *et al.* (1997), with the permission of AIP Publishing.
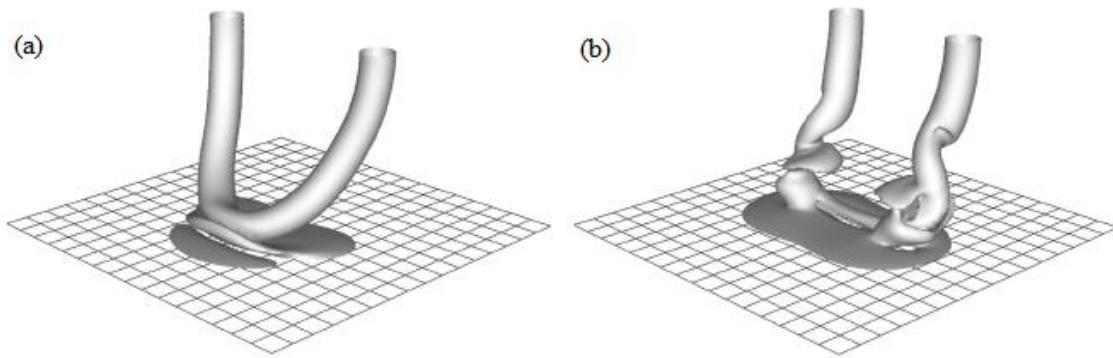
Figure 1-15 – Iso-surfaces of vorticity magnitude near the surface of the wall as the ring evolves over time. The image at (b) is at a later time than the image at (a). Reproduced from Chang *et al.* (1997), with the permission of AIP Publishing.

1.8.6. Confined formation

In a study of the formation of a vortex ring within a square tube, it was found that confinement only slightly deforms the vortex core shape, and does not significantly alter the formation process (Stewart *et al.*, 2012, Stewart and Vlachos, 2012). A recently developed theoretical model for a confined axisymmetric vortex ring confirms that confinement has limited influence on the formation process, as shown in Figure 1-16 (Danaila *et al.*, 2015). Domains with diameter greater than 3 times the ring diameter did not affect the ring at any stage of development (Danaila *et al.*, 2015). The confinement does, however, result in the development of secondary vortex structure behind the primary core (Stewart and Vlachos, 2012).
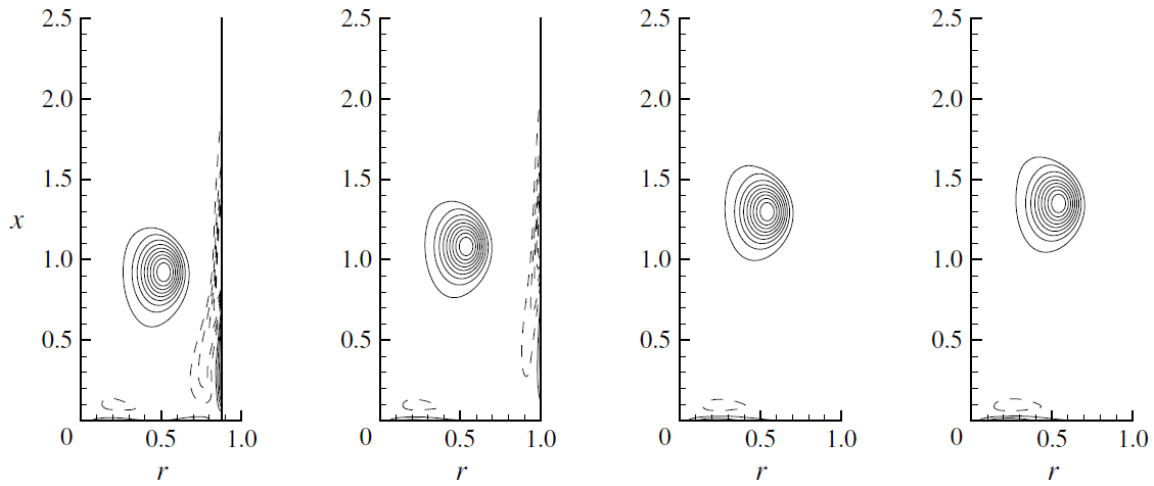
Figure 1-16 – Comparison of the azimuthal vorticity for the near-wall core of a vortex ring, at $t = 5$ for four different wall confinement values. The confinement of each ring decreases from right to left, with the rightmost ring subject to very limited confinement. Reproduced from Danaila *et al.* (2015), with the permission of Cambridge University Press.

The initial velocity of the vortex ring is slightly larger in more tightly confined domains, due to the interaction with the oppositely signed vorticity layer during formation (Stewart and Vlachos, 2012). The formation of a vortex ring from an eccentric port into an asymmetric domain is also "strikingly similar" to that of an isolated ring (Gharakhani and Ghoniem, 1998). The close proximity of the nearest wall of the domain eventually interferes, producing vortices within the ring itself with axially aligned spin axes (Gharakhani and Ghoniem, 1998). The section of the ring closest to the bounding domain initially has an increased translational velocity, although the remainder of the ring catches up after a short amount of time (Gharakhani and Ghoniem, 1998).

The translation of vortex rings through pipes is effectively an axisymmetric form of the parallel-wall interaction. An example of this is the development of vortex rings within human arteries, formed due to flow separation at the entrance of aneurysms (Salsac *et al.*, 2006). As an artery bulges outwards, a vortex ring is generated that persists within the region, influencing the artery wall (Sheard, 2009). Depending on the model used, the ring can travel through the expanded pipe vessel before

impacting on the downstream wall of the aneurism (Boustead, 2012). It has been suggested that these rings can transition to turbulence in some cases (Egelhoff *et al.*, 1999). The vortex ring is not typically the object of interest in studies of aneurisms, and so the influence on the vortex ring due to these interactions is unknown.

1.8.7. Instability development

The growth of instabilities on vortex rings impacting solid geometry is relatively similar to those observed for isolated rings, with azimuthal instabilities developing on both the primary and secondary vortex rings due to resonant Kelvin modes (Cerra Jr and Smith, 1983). These act to decrease the azimuthal coherence of the rings over time, an effect that intensifies with increasing Reynolds number (Cerra Jr and Smith, 1983). The secondary ring has a larger variation in the product of the eigenvalues of the strain tensor across the ring, and hence a larger growth rate of instability (Orlandi and Verzicco, 1993b). The presence of the additional rings in the system induced instability into a ring that would otherwise be stable in an isolated system (Swearingen *et al.*, 1995). For the case of oblique rings impacting a wall, it has been shown that the stability of the ring is enhanced as the angle of impact is increased away from the direct impact case (Verzicco and Orlandi, 1994, Chen *et al.*, 1997). This is due to the pressure differential resulting in the development of a strong axial flow inside the core of the vortex ring (Orlandi and Verzicco, 1993a), increasing the helicity density. Regions with high helicity densities have a tendency to reduce dissipation and small scale energy transfer (Melander and Hussain, 1994), suppressing the formation of azimuthal instabilities, which also act on the small scale (Verzicco and Orlandi, 1996).

1.9 Research Aims

The preceding review of the literature has identified a number of gaps in the current understanding of both swirling vortex rings, and near-wall vortex rings. These gaps are highlighted in the following sub-sections, along with a description as to how this thesis will address each of them.

1.9.1. Numerical relaxation of swirling vortex rings

In the consideration of vortex rings with swirl, previous studies have taken the core azimuthal vorticity to have a Gaussian distribution in the core cross-section, and analysed properties from this state (see Cheng *et al.* (2010) for example). However, a finite Gaussian vortex must be allowed to relax to a state which satisfies the governing equations, in order to compare with experimental work (Shariff *et al.*, 1994). Such a state is yet to be established for a swirling vortex ring, and it is not known what resemblance such a state would have to an experimentally produced ring. This work aims to investigate the influence of the governing equations on the relaxation process, and determine the similarities between the relaxed Gaussian and a piston produced vortex ring after its formation time. Given the use of a Gaussian profile is widespread (Widnall and Tsai, 1977, Shariff *et al.*, 1994, Cheng *et al.*, 2010, Batchelor, 1967, Archer *et al.*, 2008), knowledge about its usefulness in approximating swirling vortex rings is valuable.

1.9.2. Development of secondary vortex ring

The expulsion of a secondary vortex ring from within the leading edge shear layer, has been previously noted by Ooi *et al.* (2001) and shown by Cheng *et al.* (2010). However, the role that shear layer instabilities have in forming this oppositely signed ring has not been discussed. These regions are subject to shear layer instabilities, which have previously been observed in the early formation wake structures of piston produced vortex rings (Glezer, 1988, Lim, 1997). The wavelength of the most amplified instability should be similar in magnitude to the width of the shear layer (Rayleigh, 1880). However, this instability mechanism is inviscid, so instability modes with small growth rates will be damped out by the presence of viscosity (Michalke, 1964). It is therefore anticipated that the shear layer instability will be more likely to grow at high Reynolds numbers. This work aims to determine the effect of the initial ring parameters on the development of the secondary vortex rings, given a relatively large Reynolds number.

1.9.3. Primary instability mechanisms for swirling vortex rings

Swirling vortex rings are known to be susceptible to wavy instabilities (Lifschitz *et al.*, 1996, Hu *et al.*, 2001), however their relation to specific Kelvin modes has not been determined. It is predicted that even a small azimuthal component of velocity through the core of a vortex ring will alter the most amplified Kelvin mode coupling, as well as altering the number of waves seen in the induced resonant Kelvin mode instability. As of yet, the instabilities resulting from the addition of an equivalent velocity component to a vortex ring (producing a swirling vortex ring) have not been described within the Kelvin framework (Hu *et al.*, 2001). In addition, the influence of Λ and W on the most amplified Kelvin mode couplings seen on vortex rings is yet to be determined. This work aims to identify the instability modes as a function of Λ and W, and to identify these modes as those already understood for the case of a Batchelor vortex pair.

1.9.4. Growth rate of swirling vortex ring instabilities

The growth rates of the primary modes of instability have been extensively predicted both for non-swirling vortex rings (Widnall *et al.*, 1974, Shariff *et al.*, 1994, Archer *et al.*, 2008), and for Batchelor vortex pairs (Lacaze *et al.*, 2007, Roy *et al.*, 2008, Ryan *et al.*, 2012). Some attempt has been made to identify the growth rates for swirling rings (Lifschitz *et al.*, 1996), however these have not been linked to specific Kelvin modes. Varying the separation between a Gaussian vortex pair modifies the growth rates of the instabilities (Lacaze *et al.*, 2007), and it is expected that a similar phenomenon will be observed by varying the aspect ratio for vortex rings. This work seeks to determine the impact that both Λ and W have on the growth rates of the identified Kelvin modes.

1.9.5. Evolutionary characteristics of a near-wall vortex ring

Predictions can be made about the behaviour of vortex rings moving parallel to a flat plate, based on investigations of oblique collisions and fully confined domains.

It is expected that the vortex ring will tilt due to opposing induced velocity effects (Doligalski and Walker, 1978), and that a boundary layer spire will form due to the interaction between the near wall core, and the wall (Peridier *et al.*, 1991). This work seeks to determine the exact evolutionary process of near wall vortex rings, and to confirm the above predictions. The interaction between vortices and a non-slip surface is relevant for all forms of complex wall turbulence. Developing a full description of the behavior of near-wall vortex rings is paramount in building understanding of wall related turbulence (Robinson, 1997).

1.9.6. Wall normal velocity variance with ring parameters

The effect of varying ring size and initial wall separation on the fluid mixing of the interaction can be measured by considering the wall-normal velocity in the vicinity of the vortex ring. The development of this parameter over time gives an indication of when there is a peak in boundary layer fluid moving normal to the wall. This work aims to quantify the magnitude of the wall-normal velocity, and determine the efficiency of using vortex rings to induce such an effect.

1.9.7. Effect on temperature field and influence of multiple rings

The focus of this work is primarily on the dynamics of vortex rings. However, the eventual application of this work is to the heat transfer potential of synthetic jets angled parallel to flat surface. Therefore, a qualitative investigation into the effect of the near-wall interaction on a scalar temperature field, and a brief look at how an array of near-wall vortex rings behaves, is also included. This is discussed in more depth in Chapter 6.

Chapter 2

Methodology

Computational fluid dynamics techniques are used to simulate and investigate the stability and behaviour of vortex rings throughout this thesis. The methodology is described in three major sections:

i)   an overview of the algorithm used to solve the Navier-Stokes equations;

ii)   a discussion of the techniques employed to ensure convergence to the correct solution; and

iii) a description of the post-processing used to extract the results.

2.1 Numerical algorithm

The code employed in this project was first published in Sheard *et al.* (2007), and the 2D axisymmetric solver was published in Sheard and Ryan (2007). The algorithm (VIPER) uses the spectral element method, is theoretically the most efficient method for a smooth flow (Karniadakis and Sherwin, 1999). The code discretises elements with a 2D tensor product of a polynomial basis set, which are defined on points provided by Gauss-Legendre-Lobatto quadrature. This quadrature includes points on the element edges to ensure C_0 continuity between adjacent elements. Given this numerical scheme is well established, it did not seem necessary to divert the flow of the thesis by considering alternative schemes.

The Navier-Stokes equations (Equation 1-5 and Equation 1-23) are recast as a set of integral equations, by applying a form of the Galerkin method. These integral equations are approximated using Gaussian quadrature within each element, producing a set of ordinary differential equations that are then solved. The convergence achieved by this method is typically exponential.

2.1.1. Time stepping

Time-integration is performed using an operator splitting scheme, based on a class of backwards-multistep schemes developed by Karniadakis *et al.* (1991). The basic idea, for an equation of the form

$$\frac{\partial u}{\partial t} = Lu \,,$$

2-1

with L as some operator that can be written as a sum of m pieces, is that updating u from one time step to the next is a simple matter of summing the contribution of each operator on u separately. This is performed through backwards differentiation, where the time derivative at the next time step is evaluated, and an appropriate backwards order scheme (combination of L operators) is applied to find the solution for the velocity field at this time step.

VIPER uses the three-step time splitting scheme proposed by Karniadakis *et al.* (1991), although this is effectively four steps if the pressure field is not known in advance. The first sub-step explicitly solves the advection term of the Navier-Stokes equations for $\boldsymbol{u}$,

$$\frac{\bar{\boldsymbol{u}} - \sum_{q=0}^{J-1} \alpha_q \boldsymbol{u}^{n-q}}{\Delta t} = \sum_{q=0}^{J-1} \beta_q \boldsymbol{N}(\boldsymbol{u}^{n-q}) \,.$$

2-2

where $\boldsymbol{N}$ is the non-linear advection operator. The second sup-step requires knowledge of the kinematic pressure P, which can be approximated through

$$\nabla^2 P^{n+1} = \frac{\nabla \cdot \overline{\boldsymbol{u}}}{\varDelta t}.$$

2-3

The second intermediate velocity field can then be obtained by enforcing continuity. Mathematically, this sub-step is given by

$$\overline{\overline{\boldsymbol{u}}} = \overline{\boldsymbol{u}} - \varDelta t \, \nabla P^{n+1}.$$

2-4

The final velocity field is obtained from the third sub-step, where the Helmholtz equation

$$\frac{\gamma \boldsymbol{u}^{n+1} - \overline{\overline{\boldsymbol{u}}}}{\varDelta t} = \nu \nabla^2 \boldsymbol{u}^{n+1},$$

2-5

is solved for the final velocity field using the desired boundary conditions. In these equations, α, β, and γ are coefficients related to the specific to the scheme (refer to Karniadakis *et al.* (1991) for values).

2.1.2. Stability analysis

To undertake a global stability analysis, the velocity and pressure fields of a steady base flow field are decomposed into a 2D base flow $(\overline{\boldsymbol{U}}, \bar{p})$ and a small 3D disturbance $(\boldsymbol{u}', p')$.

Substituting these into the Navier-Stokes equations and neglecting terms that are non-linear in the perturbation yields the linearized Navier-Stokes equations,

$$\frac{\partial u'}{\partial t} = -(\overline{U} \cdot \nabla)u' - (u' \cdot \nabla)\overline{U} - \nabla p' + \frac{1}{Re}(\nabla^2 u'),$$

2-6

$$\nabla \cdot u' = 0.$$

The only difference is in the advection term, which now has two separate terms. However, the disturbance can also be integrated in time, independently of the base flow, by an almost identical solution algorithm.

The stability problem can be reduced to a two-parameter system that depends on the spanwise mode number β at a given Reynolds number Re. The disturbance field is decomposed into a Fourier series expansion in the spanwise direction,

$$u'(x,y,z,t) = \int_{-\infty}^{\infty} u(x,y,t)e^{i\beta z}d\beta \,.$$

2-7

The modes with a different spanwise mode number can be decoupled because of the linearity of Equation 2-6, giving

$$u'(x,y,z,t) = \begin{Bmatrix} u(x,y,t)e^{i\beta z} \\ v(x,y,t)e^{i\beta z} \\ w(x,y,t)e^{i\beta z} \end{Bmatrix} \,,$$
$$p'(x,y,z,t) = \{p(x,y,t)e^{i\beta z}\} \,.$$

2-8

Numerically, the stability properties for a given Re and a set β are obtained by integrating the perturbation field (for a single value of β) forward in time, with suitably chosen initial conditions. The growth of the field can then be monitored. Perturbation fields with different values of β can be computed independently, as they only couple with the base field.

The growth of an instability can be characterised by a multiplier μ,

$$\mu = e^{\varpi T} \,,$$

2-9

where ϖ is the complex growth rate of the mode and T is the period over which it is calculated. These multipliers correspond to the eigenvalues of an operator A, which is defined such that

$$u_{n+1} = A(u_n).$$

<div align="right">2-10</div>

where n and $n + 1$ define the values at sequential integer values of T. This parameter measures the linear change in a perturbation over a period T, through the expression

$$F(t + T) = |\mu|F(t),$$

<div align="right">2-11</div>

where the function $F(t)$ is associated with the flow field. Hence, a multiplier with a magnitude of greater than one corresponds to a growing instability.

Flows do not have to be strictly periodic for the stability analysis to be successful, as steady flows can be considered periodic with an arbitrary period T. This property is applied for the stability analyses performed in this thesis, where the base flow fields are not periodic. The code used in this study uses a block-power method based on a modified Arnoldi iteration to determine the leading eigenvalue of the system (Barkley and Henderson, 1996).

2.1.3. Fourier components

3D flow fields can be obtained where the out-of-plane direction is represented by a Fourier series approximation. The Fourier modes are only coupled during the advection step of the time-stepping procedure, as the pressure and diffusion steps can be decoupled before being computed.

2.1.4. Scaling factors

Results discussed in this thesis are presented in their non-dimensional form in order to aid comparisons between different scenarios. The different scaling ratios are presented in Table 2-1. The "0" subscript indicates the value prior to the axisymmetric relaxation phase, while the "i" subscript indicates the value at the axisymmetric relaxation time.

Table 2-1 – List of parameters and their non-dimensional scaling for cases initialised from both the initial fields, and the relaxation times.

	Axisymmetric	Full 3D
Length scale	a_0	a_i
Time scale	$\dfrac{2\pi a_0^2}{\Gamma_0}$	$\dfrac{2\pi a_i^2}{\Gamma_i}$
Velocity scale	$\dfrac{\Gamma_0}{2\pi a_0}$	$\dfrac{\Gamma_i}{2\pi a_i}$
Vorticity scale	$\dfrac{\Gamma_0}{2\pi a_0^2}$	$\dfrac{\Gamma_i}{2\pi a_i^2}$
Pressure scale	p_0	p_i
Density scale	$\dfrac{p_o a_0^2}{4\pi^2 \Gamma_0}$	$\dfrac{p_i a_i^2}{4\pi^2 \Gamma_i}$

2.2 Numerical parameters

2.2.1. Axisymmetric evolution of Gaussian initial conditions

As discussed in Section 1.9.1, the implementation of Gaussian initial conditions for the vortex rings necessitates a period of axisymmetric relaxation. The assumption of axisymmetry is retained for the evolution stage of the investigation. A cross-section of the vortex ring is initialised in the zr-plane (using a cylindrical co-ordinate system), and the remainder of the ring is simulated by enforcing axisymmetry in the governing equations.

Vortex rings with different ring aspect ratios are considered by holding the core radius constant with a unit value, and setting the ring radius as required. The initial ring radius required to develop the initial velocity field can be obtained via rearrangement of Equation 1-28. The magnitude of swirl is varied by modifying the peak azimuthal velocity as desired, as defined by Equation 1-38.

2.2.1.1.   *Mesh and domain*

The domain is cylindrical, $400a_0$ in length and $400a_0$ in diameter. The boundaries of the domain are sufficiently far away so as to have negligible influence. The grid resolution required to resolve the flow features diminishes with distance from the vortex ring. Therefore, a refined region of the mesh is used in the immediate vicinity of the ring, where the element size is $0.25a_0$, in both the *z*- and *r*-directions. This refined region forms a smaller cylinder at the centre of the domain, with a length of $40a_0$ and a diameter of $30a_0$. Outside of this refined region, the elements are stretched to the boundary of the domain, such that a single element in this region has a side length in the z-direction of $180a_0$. The nodes of the mesh are shown as the black data points in Figure 2-1.

The data is approximated by 11th order polynomials within each element, resulting in a total of 40 boundary points and 81 internal points at which flow conditions are determined. An example of the locations of these points for a single element is provided in Figure 2-2. The mesh is comprised of a total of 9882 elements, and 10 106 nodes.
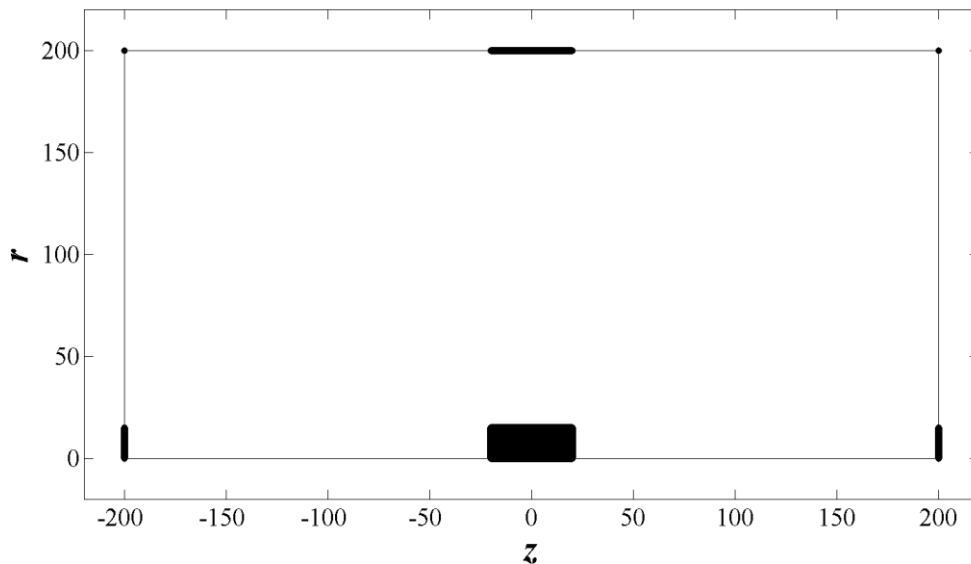
Figure 2-1 – Schematic of the node locations and domain boundaries. Each node has been represented by a small filled circle. The region with a high concentration of nodes is the refined region.
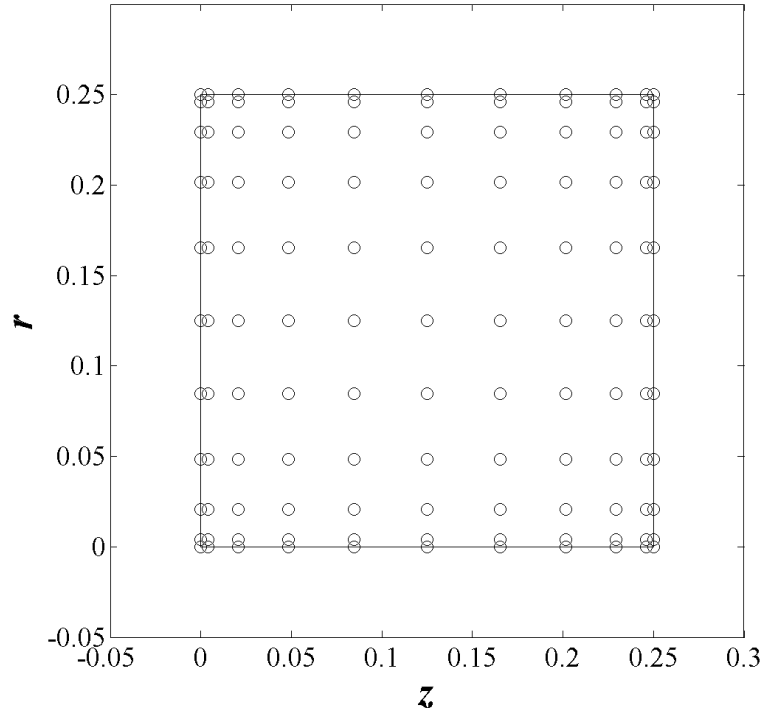
Figure 2-2 – Schematic of the calculation locations for a single element in the domain.

2.2.1.2.   Initial conditions

The initial azimuthal vorticity distribution in the core is defined initially by a Gaussian. It is specified in cylindrical polar co-ordinates in terms of the distance s from the centre of the core, using

$$\omega_\theta = 2\exp(-s^2),$$
2-12

where

$$s^2 = (r - R_0)^2 + z^2.$$
2-13

In order to implement this vorticity distribution, the corresponding velocity fields are required. The two velocities in the plane are related via the stream function, through the equations

$$u_r = \frac{\partial \psi}{\partial z} \vec{r},$$

2-14

and

$$u_z = \frac{1}{r} \frac{\partial (r\psi)}{\partial r} \vec{z}.$$

2-15

The azimuthal vorticity is related to the velocity components through the equation

$$\omega_\theta = \frac{\partial u_r}{\partial z} - \frac{\partial u_z}{\partial r}.$$

2-16

Taking the *z*-derivative of Equation 2-14, the *r*-derivative of Equation 2-15, and substituting these into Equation 2-16, yields

$$\omega_\theta = \frac{\partial^2 \psi}{\partial z^2} - \frac{\partial}{\partial r} \left(\frac{1}{r} \frac{\partial (r\psi)}{\partial r} \right),$$

2-17

which can be expressed using Equation 2-12 as

$$2 \exp(-s^2) = \frac{\partial^2 \psi}{\partial z^2} - \frac{\partial}{\partial r} \left(\frac{1}{r} \frac{\partial (r\psi)}{\partial r} \right).$$

2-18

Equation 2-18 is solved numerically for the stream function of the flow field, which provides a description of the required velocity components through Equation 2-14 and Equation 2-15. The stream function is solved using a 4th order accurate finite difference method in MATLAB.

An azimuthal velocity component is implemented using a Gaussian distribution, in the same manner as Cheng *et al.* (2010), using

$$u_\theta = W_0 \exp(-s^2).$$

2-19

The Gaussian vortex initial condition is not steady, and sheds vorticity over time, experiencing a gradual change in translational velocity. A constant background velocity is added to the domain, keeping the vortex ring close to the centre of the refined region, although allowing it to move relative to the domain. The background velocity magnitude for each case is determined using Equation 1-36, and modified as required using a low resolution test simulation.

2.2.1.3.   *Boundary conditions*
The inlet (the right boundary) is defined using Dirichlet velocity boundary conditions, where the velocity is parallel to the axis of symmetry, with a magnitude of the background velocity in the negative z-direction. The outlet (left boundary) is initialised with a homogenous Neumann velocity boundary condition, such that the velocity gradient across the boundary is zero in all directions.

The outside boundary of the cylinder, at $r = 200a_0$, is not a bounding wall, and permits the flow of fluid across the boundary of the domain. This boundary is initialised with the same boundary condition as that of the outlet. The z-axis is initialised with a symmetry boundary, being the $r = 0$ position of the axisymmetric domain.

2.2.1.4.   *Grid resolution study*
A comprehensive grid resolution study was performed to verify mesh independence, and to ensure agreement with theory and previously published numerical data. The circulation, core size, and peak azimuthal vorticity are compared over a number of different grid sizes, and then a Richardson extrapolation is used to predict the mesh-independent value. The variation between this value and the value for the chosen mesh ($0.250\,a_0$) was found to be less than 1%. These results are presented in Table 2-2.

Table 2-2 – Results from the grid resolution study for the axisymmetric evolution case. R.E.V stands for the Richardson Extrapolated Value, while the % column gives the percentage difference between the R.E.V. and the chosen case of 0.250.

	4.000	2.000	1.000	0.500	0.250	R.E.V.	%
Γ/Γ_0	2.287	1.237	0.903	0.845	0.840	0.839	0.100
a/a_0	2.507	1.640	1.342	1.211	1.190	1.185	0.459
Max ω_θ	6.178	2.566	2.587	2.415	2.415	2.421	0.288

Table 2-3 – Comparison of the values found in the current study with those of Archer *et al.* (2008)

	This study	Archer	Difference
a/R_0	0.355	0.360	1.418%
R/R_0	1.039	1.038	0.137%
Γ/Γ_0	0.908	0.911	0.284%

An additional simulation was performed to compare to Case A2 in Archer *et al.* (2008). The parameters used to compare between the two cases are provided in Table 2-3, where a, R, and Γ are less than 1.5% different. One further case compared the change in the core size to that predicted by Equation 1-37. The predicted evolved core size of a non-swirling ring has a difference of just 0.59% to the value obtained by the simulation. These differences include any error introduced by the data extraction method, which is discussed in Section 2.3.

2.2.2. Axisymmetric evolution of piston initial conditions

2.2.2.1. Mesh and domain

A piston driven vortex ring is also simulated, and the assumption of axisymmetry is retained. The mesh and domain utilised for the piston produced vortex ring are based on the mesh shown in Figure 2-1, with two minor modifications. Firstly, the refined region (the inner cylinder) is shifted to the left edge of the domain, to align with the initial location of the vortex ring. The initial time $t = 0$ is taken as the formation time of the vortex ring, as defined by Gharib *et al.* (1998). In terms of the core radius at the formation time, the refined region mesh has a side length of

$0.278a_0$. The domain size is $366a_0$ in the z-direction and $183a_0$ in the r-direction. The refined region extends to around $56a_0$ in the z-direction and $14a_0$ in the r-direction. In addition, the mesh is doubled in resolution in the z-direction within a_0 of the inlet boundary, to help resolve the early stages of the ring formation. A schematic of the new mesh and domain is provided in Figure 2-3.

2.2.2.2.   Initial conditions

The vortex ring is produced by the boundary conditions, therefore the initial flow field is simply a domain full of quiescent fluid. Due to the input conditions, it is unfeasible to include a background flow in the piston simulations.

2.2.2.3.   Boundary conditions

The boundary conditions are similar to those in use for the Gaussian initial conditions. In this case, however, the right boundary is given a homogenous Neumann velocity boundary condition, along with the outside boundary, for all velocity components. The z-axis remains as the symmetry axis.
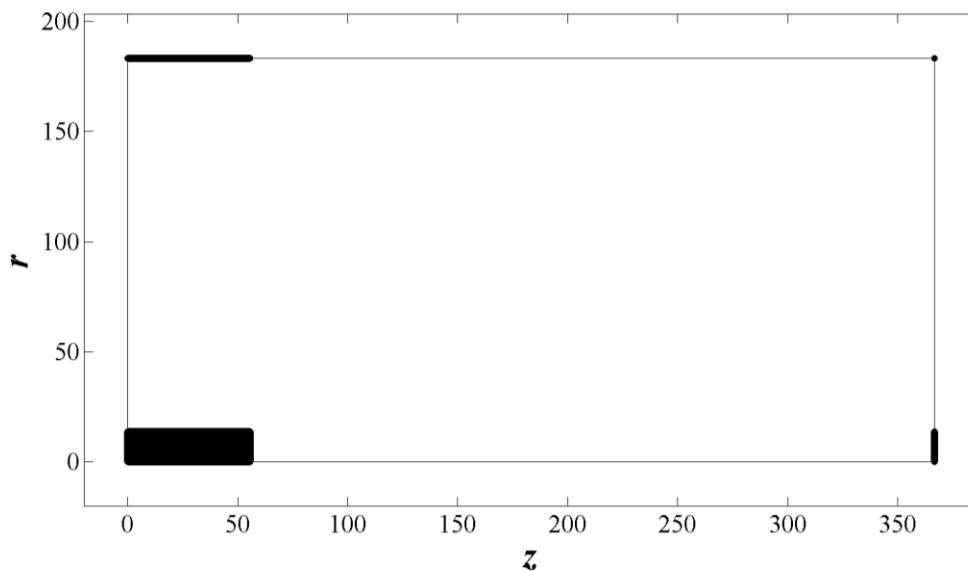
Figure 2-3 – Schematic of the mesh and domain used for the piston simulation. Each node has been represented by a small black circle. The region with a high concentration of nodes is the refined region.

In order to properly simulate the motion of a piston, the left boundary is given a Dirichlet velocity boundary conditions that varies with position along the boundary, and over time. The velocity of the piston is defined by a trapezoidal function, such that the combined acceleration and deceleration period equates to 5% of the total piston movement time, see Figure 2-4. The z-component of velocity, u_z, has a profile in the r-direction defined by the approximate piston radius, R, and the maximum piston velocity, U_0, through the equation

$$u_z = \frac{U_0}{2}\left[1 - \tanh\left(\frac{25}{4}\left(\frac{r}{R} - \frac{R}{r}\right)\right)\right].$$

2-20

This equation is presented visually in Figure 2-5. The piston motion time T is defined such that that the piston has an approximate effective stroke ratio of 2.5 (as defined in Equation 1-30), which allows the majority of the generated circulation to roll-up into the vortex ring core (Gharib *et al.*, 1998).
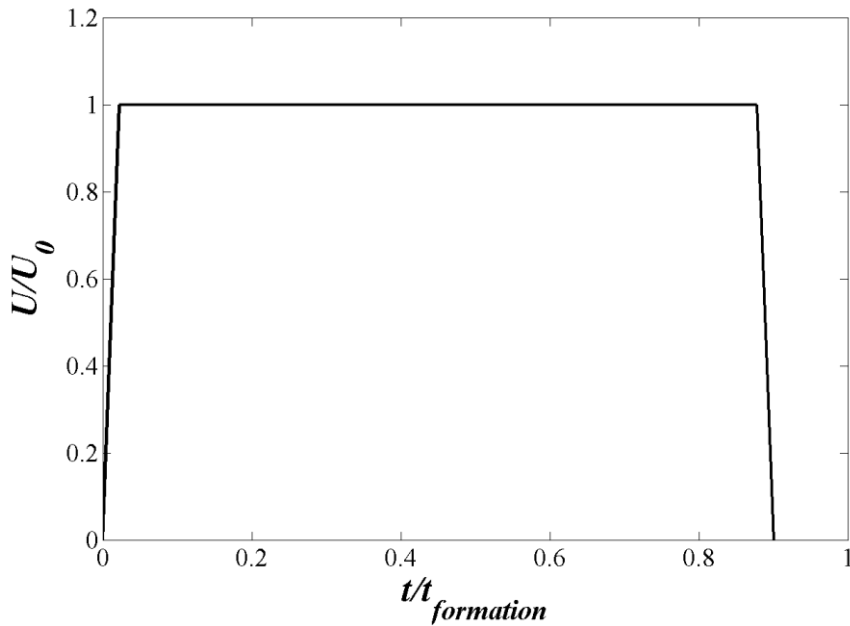
Figure 2-4 - Piston velocity profile. The time is normalised by the formation time (defined in Equation 1-30), while the velocity is normalised by the peak piston velocity.
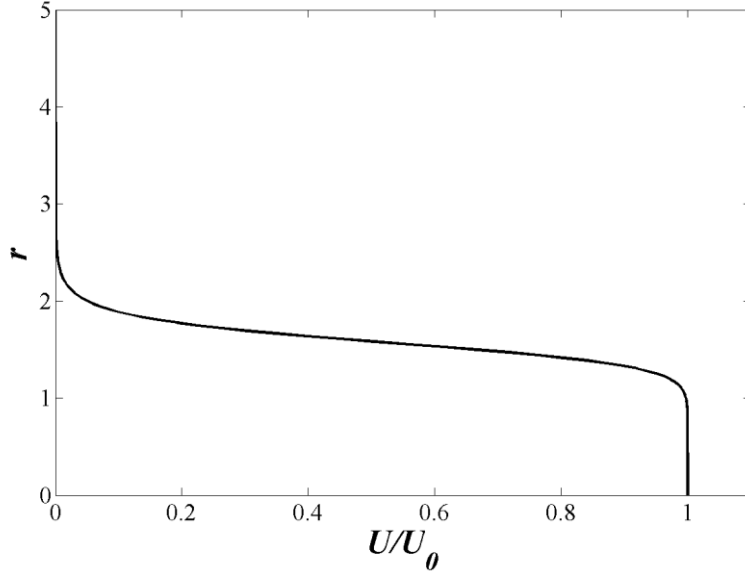
Figure 2-5 – Schematic of the velocity produced as a function of *r* for the simulated piston, as provided by Equation 2-20.

Swirl is introduced by setting a velocity in the θ-direction, which is related to the z-velocity component through the relation

$$u_\theta = \frac{u_z r}{4.8}.$$

2-21

The denominator provides a swirl magnitude of approximately $W_0 = 0.5$ in the resulting vortex ring flow field.

2.2.2.4. Grid resolution study

A new grid resolution study is performed, using the piston initial conditions. The results are summarised in Table 2-4. All values are sampled at the formation time, as defined by Equation 1-30. At a mesh spacing of $0.21a_0$, all three tested variables are within 1% of the Richardson extrapolated value. At a mesh spacing of $0.42a_0$, only the circulation is outside of this mark, at a difference of 1.3%. Using the same element sizing as for the Gaussian case, which equates to $0.278a_0$ based on the formation time properties, lies between these two values, and provides the required accuracy for fewer computational resources than the $0.21a_0$ case.

Table 2-4 – Grid resolution data from the piston produced vortex ring simulation. The step sizes are given in terms of a_0.

Step size	3.36	1.68	0.84	0.42	0.21
$\Gamma/\Gamma_{\text{R.E.V.}}$	0.788	1.207	1.036	1.013	1.004
$a/a_{\text{R.E.V.}}$	1.474	1.342	1.055	1.001	0.999
$W/W_{\text{R.E.V.}}$	0.725	1.055	1.005	1.000	1.000

2.2.3. Linear stability analysis

The base fields for the linear stability analyses are obtained from the relaxed flow fields developed through the process outlined in Section 2.2.1. The mesh is modified slightly before performing the linear stability analysis, by halving the length of the refined region in the z-direction. The boundary conditions are identical to those used in the evolution of the base flow.

2.2.3.1. *Grid resolution study*

To demonstrate that the solutions obtained by the algorithm are accurate, the growth rates are compared to a previous numerical study by Archer *et al*. (2008), who found good agreement with the earlier viscous predictions of Shariff *et al*. (1994). The growth rates presented in Table 2-5 are similar to within 12%. This discrepancy is not unexpected, given the differences in methodology between the two studies. Archer *et al*. (2008) did not focus on a single mode, and instead determined an average growth rate of the most amplified mode around their sampling time, allowing the investigated mode to vary. Here, the growth rate is obtained through an asymptotic analysis of a frozen base field for a single unstable mode; this isolates the individual growth rates of modes. Nonetheless, the similarity between the results provides confidence that the algorithm used is correct for this application.

Table 2-5 – Comparison of growth rate σ for two different ring aspect ratios Λ with values provided in the literature. The other given parameters are circulation Γ, number of waves n of the most amplified mode, and the percentage difference between the studies.

	Equilibration Time		Stability Sampling Time				
	Λ	Γ/Γ_o	Λ	Γ/Γ_o	n	σ	Diff. (%)
Current Study	0.344	0.909	0.344	0.903	6	0.087	
Archer *et al.* (2008)	0.347	0.911	-	0.904	6	0.082	6.10
Current Study	0.234	0.992	0.251	0.988	10	0.114	
Archer *et al.* (2008)	0.227	0.995	-	0.995	10	0.130	12.3

2.2.4. Modelling near wall vortex rings

Fully 3D simulations are used to model the vortex ring/wall interaction. The third dimension is modelled using the Cartesian Fourier expansion technique introduced in Section 2.1.3 . A non-slip wall is implemented at $x = 0$, and the vortex rings are initialised on the negative-x side of the wall.

2.2.4.1.   *Mesh and domain*

The region of the xy-plane bounded by $-14a_i \leq x \leq -2a_i$ and $-12a_i \leq y \leq 12a_i$ is meshed using elements with side lengths of a_i in both the x- and y-directions. Within the region $-5a_i \leq x \leq 0$, the elements are compressed to $a_i/16$ in length in the x-direction, in order to properly resolve boundary layer phenomena. In between these two regions is a transition region, containing 3 elements that increase in size, avoiding an abrupt increase in element size between the boundary layer region and the refined region. The elements are stretched to the boundaries of the domain outside of the refined region, and the entirety of the xy-plane has a length of $80a_i$ in the y-direction and $40a_i$ in the x-direction. This geometry is presented in Figure 2-6. The z-direction is modelled using a Fourier expansion. The planes are separated by a distance of $0.25a_i$, with a total of 801 planes used in each simulation, giving a z-range of $200a_i$. The arrangement of these planes, and the orientation of the domain, is given in Figure 2-7.
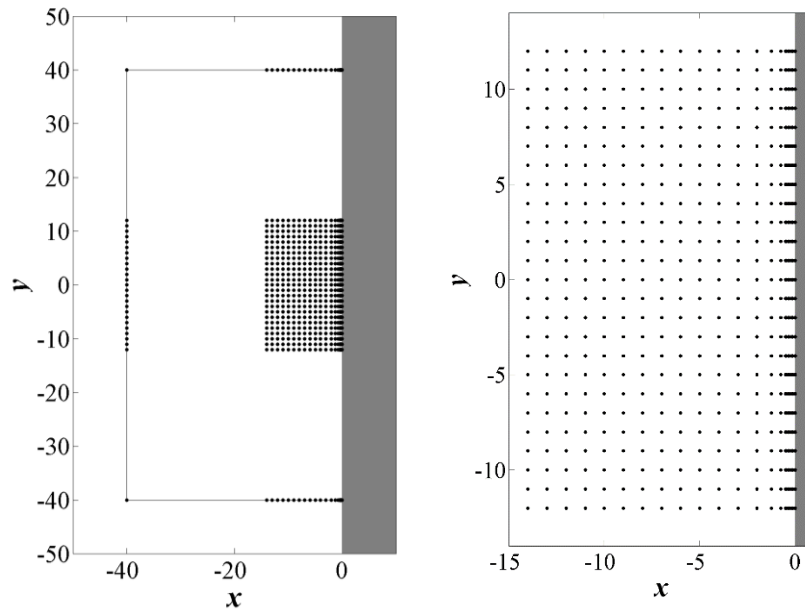
Figure 2-6 – Design of the overall mesh in the *xy*-plane for the full 3D domain, showing (left) the entire plane, and (right) a zoomed view of the refined region. The grey shaded region indicates the position of the wall, however the wall does not physically have a depth in the *x*-direction.
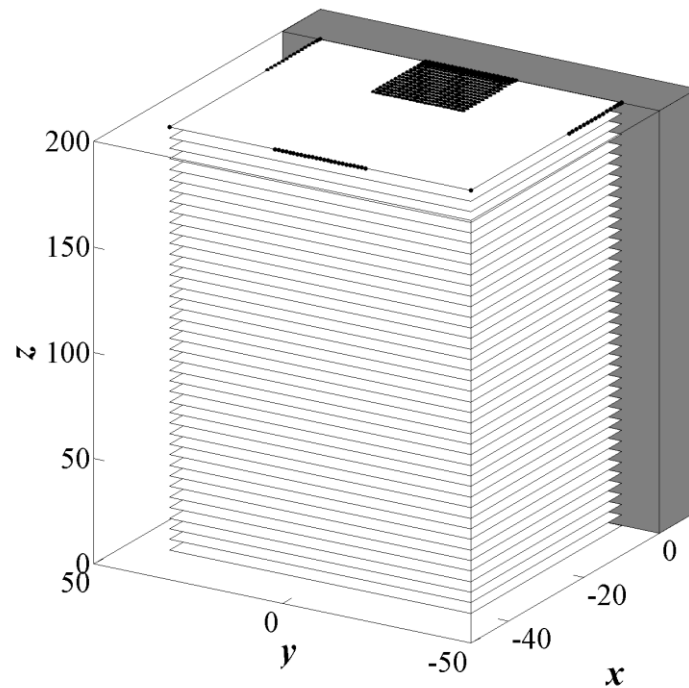
Figure 2-7 – Visualisation of the 3D mesh and domain. The mesh points have been shown on the top plane. The grey shaded region indicates the position of the wall, however the wall does not physically have a depth in the *x*-direction. The planes have been displayed as having a separation of 5a_i, however the actual plane spacing is 0.25a_i.

2.2.4.2.　　　Initial conditions

The relaxed flow fields from three of the axisymmetric cases are interpolated into a Cartesian mesh, then projected into Fourier space and saved as the initial flow field for the 3D cases. The $r = 0$ axis of the axisymmetric case is placed at the required distance from the wall to give the desired separation. However, the flow field obtained via this method does not exactly satisfy continuity; the initial flow field is not divergence free. In the first calculation step, the algorithm must modify the flow. A comparison between the initial and corrected streamlines (in the xz-plane) is provided in Figure 2-8. The form of the corrected streamlines compares well with the work of Danaila *et al.* (2015), who analytically predicted the streamline contours for a confined vortex ring.

Figure 2-8 – Comparison of the initial (left) and corrected (right) streamlines for the vortex ring core nearest to the wall, in the $y = 0$ plane (the axis of symmetry).

2.2.4.3. Boundary conditions

The boundary along $x = 0$, which serves as the bounding wall for these simulations, is initialised with a Dirichlet velocity boundary condition, such that the velocity in all directions at the wall is zero. The free-stream boundaries, which consist of the $x = -40a_i$, $y = -40\,a_i$, and $y = +40\,a_i$ planes, are Neumann velocity boundary conditions, such that flow may cross the b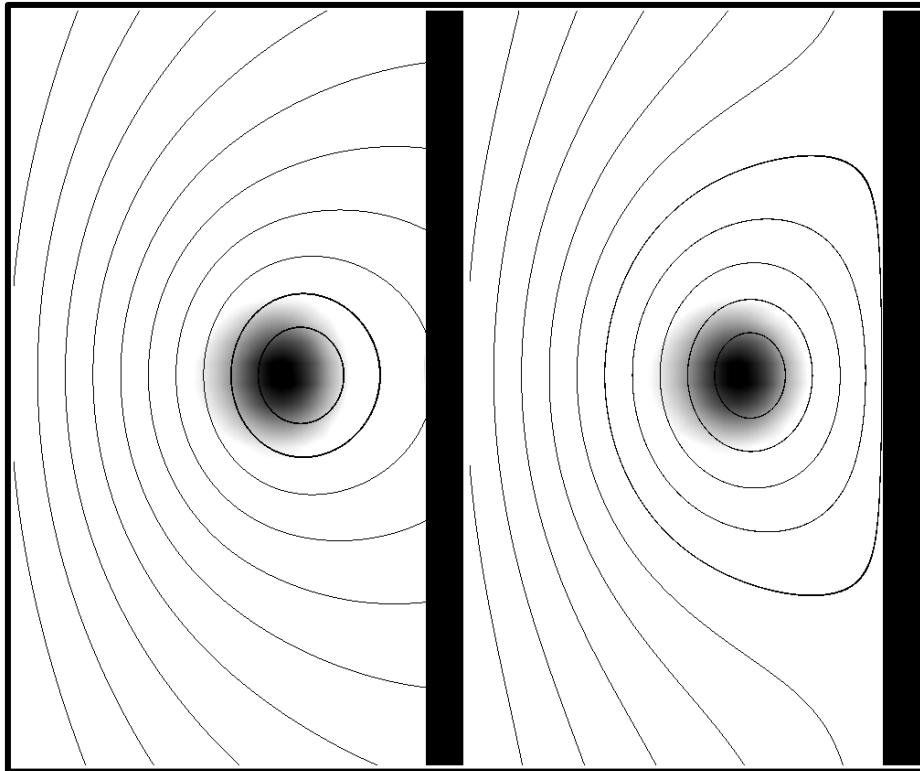oundary, but not change over the boundary. Finally, the top and bottom boundaries of the domain, corresponding to $z = 0$ and $z = 200$, are defined with a periodic boundary condition. This is done by enforcing that all velocity components and velocity derivatives are equal on these two planes.

2.2.4.4. Domain length in z-direction

A consequence of the use of periodic boundary conditions in the z-direction is that the algorithm is actually calculating the flow field for an infinite array of vortex rings. The magnitude of the effect of the neighbouring rings on the vortex ring in question can be approximated by considering the Biot-Savart law from Equation 1-34. To quantify the effect of a single vortex ring, consider the velocity along the centre line of the vortex ring. At some distance H above or below the vortex ring (but still on the centre line), the induced velocity is given by

$$u = \frac{\Gamma}{2} \frac{R^2}{(R^2 + H^2)^{\frac{3}{2}}}.$$

2-22

The influence on a ring due to an infinite series of rings (excluding the influence on itself) can be expressed as an infinite series sum, through

$$u = \Gamma \sum_{j=1}^{\infty} \frac{R^2}{(R^2 + j^2H^2)^{\frac{3}{2}}}.$$

2-23

The ratio of the velocity magnitude induced by the infinite array of rings (at integer multiples of the distance H above and below the ring) to the velocity induced by the ring itself ($\Gamma/2R$), at the centre of the ring, is given by

$$ratio = 2 \sum_{j=1}^{\infty} (1 + j^2 H^2)^{-\frac{3}{2}}. \qquad\qquad \text{2-24}$$

Equation 2-24 is presented in Figure 2-9 as a percentage. The induced velocity with a ring separation of $H = 3R_0$ is less than 10% of that induced at the vortex ring centre. The induced velocity at $6R_0$ is less than 1% of that at the vortex ring centre. Therefore, the domains used in this study are large enough to reduce the effect of the infinite array to negligible levels.

An additional consideration of the periodic boundary conditions is the wake recycling that can occur. This wake recycling is the key factor to take into consideration when defining the z-domain size. Using Equation 1-35, the maximum non-dimensional velocity of any of the rings analysed is on the order of 0.5. Therefore, the domain should be at least twice as long as the length of time of simulation. These assumptions are tested in the grid resolution study.
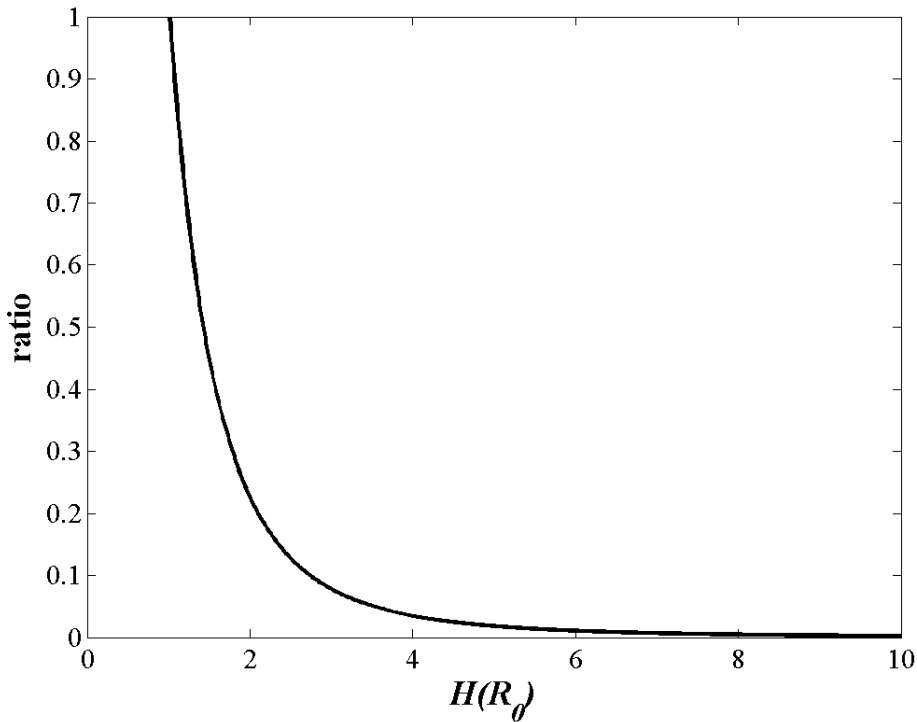

Figure 2-9 – Ratio of the induced velocity by a second vortex ring, at a distance of H either above or below the original ring, to the velocity induced by the original ring itself. H is expressed in units of R_0.

2.2.4.5. *Grid resolution study and domain analysis*

Six independent tests were performed to investigate the grid resolution requirements. The parameters used in these tests are provided in Table 2-6. The ring is evolved using the standard time step for 30 dimensionless time units, for all cases. At this time, the flow field has experienced significant interaction with the wall, but retains its toroidal shape, which can be analysed using typical vortex ring methods. The circulation has been extracted from the $\theta = 0$, $\theta = \pi/2$, $\theta = \pi$ planes, where θ is measured from the positive x-axis. The circulation is also sampled at a shifted $\theta = 0$, where the plane is centred on $y = a_i$ rather than $y = 0$. A full breakdown of the results from the grid resolution study is provided in Appendix A. The mesh and domain chosen produce a solution within 2% of the grid independent solution for all measured parameters, at $t = 30$.

Table 2-6 – Grid resolution trials for the near-wall simulations. All values are expressed in terms of the equilibrated core radius, a_i.

Test	X_R , Y_R	X_r , Y_r	Δ_{xy}	Δ_b	X_t	Δ_z	Z_R	Transition
A	40 , 40	Varies	0.50	-	0.00	0.25	40	-
B	40 , 40	14 , 14	Varies	-	0.00	0.25	40	-
C	40 , 40	14 , 14	0.50	Varies	0.50	0.25	40	-
D	40 , 40	14 , 14	0.50	1/32	Varies	0.25	40	-
E	40 , 40	14 , 14	0.50	1/16	0.50	Varies	40	-
F	40 , 40	14 , 14	1	1/16	0.50	0.25	Varies	-
G	40 , 40	14 , 24	1	1/32	0.50	0.25	200	4 steps

2.3 Data analysis and post-processing

2.3.1. Axisymmetric evolution of vortex rings

2.3.1.1.   *Data extraction*

The instantaneous translational velocity of the vortex ring is used to modify the z-velocity field of each output time step, to ensure the analysed flow fields are in the frame of reference of the vortex ring. The velocity fields are converted to an array of cubic splines over a regular grid in the vicinity of the vortex core. This reduces the volume of data being manipulated, and removes the C_1 discontinuities that are introduced by the code at the element boundaries.

2.3.1.2.   *Ring properties*

The properties of the vortex core are obtained based on the methods used in Archer *et al.* (2008). The azimuthal vorticity is determined via Equation 2-16, where the two velocity derivatives are obtained through differentiation of the cubic spline coefficients. This vorticity field is then integrated using Gaussian quadrature over a region $\pm 4a_0$ from the vortex core to reduce inclusion of wake vorticity, which can skew the data (Archer *et al.*, 2008). For the initial conditions, the use of this sampling domain predicts the size of the core to within 0.22% of a_0.

The circulation is obtained from the relation

$$\Gamma = \int \omega_\theta \mathrm{d}r\mathrm{d}z ,$$

2-25

while the first and second radial moments of azimuthal vorticity are given by

$$R = \frac{1}{\Gamma} \int r\omega_\theta \mathrm{d}r\mathrm{d}z ,$$

2-26

$$R_2^2 = \frac{1}{\Gamma} \int r^2\omega_\theta \mathrm{d}r\mathrm{d}z ,$$

2-27

noting that the first radial moment of azimuthal vorticity corresponds to the radius

of the vortex ring. The size of the vortex core can be estimated from these two radial moments, through

$$a^2 = 2(R_2^2 - R^2) .$$

2-28

The swirl magnitude is determined by sampling the peak azimuthal velocity within the core region at each time step.

2.3.1.3.   *Relaxation time*

The relaxation time of swirling vortex rings is determined based on the method of Shariff *et al.* (1994). The streamfunction at each point in the domain is determined using Equation 2-14 and Equation 2-15. The first of these integrals is simply

$$\Psi_r = - \int u_r dz .$$

2-29

The second equation has the form of a linear first order ODE,

$$\Psi_z = \frac{1}{e^r} \int e^r \, ru_z dr .$$

2-30

The total streamfunction can then be determined from

$$\Psi = \Psi_r + \Psi_z .$$

2-31

These values are then compared to the ratio of the azimuthal vorticity to the radius for each point. The key to this method is to identify the time at which the array of points thins down to a single cohesive curve, as shown earlier in Figure 1-4.

2.3.2. Linear stability analysis of vortex rings

The azimuthal velocity and vorticity fields for each stability analysis are extracted, and images of these variables in the core cross-section are output to image files. The full 3D shape of the mode is also output to an image file, while the real and imaginary

parts of the growth rate are output to a data file. The images and associated growth rate values are used to identify the most amplified mode in each case.

2.3.3. Near-wall evolution of vortex rings

2.3.3.1.   Removal of spurious Nyquist frequencies

The use of Fourier modes to simulate the z-direction in the 3D domain is computationally efficient, however it can lead to aliasing in the results due to un-resolved high frequencies (due to truncation of the infinite Fourier series). These are removed in post-processing by passing each position in the xy-plane through a low-pass filter, reducing the influence of higher frequency while ensuring that the loss of original data is negligible. The masking function m is related to the frequency space f through Equation 2-32,

$$m = \frac{1}{2}\left(1 - \tanh\left(s \times \left(\frac{f}{K} - \frac{K}{f}\right)\right)\right). \qquad \text{2-32}$$

For these simulations, a cut-off frequency of 1.75 with a steepness factor of 12.5 produces the desired results.

2.3.3.2.   Ring properties

The properties of the vortex ring are extracted using the same equations as for the axisymmetric analysis, as introduced in Section 2.3.1.2. However, as these equations are only applicable within a single θ-plane, first the centre of the vortex ring must be found so that azimuthal planes can be extracted. Analysis for this case is in the reference frame as the stationary wall, so no modifications are required for the velocity field.

The flow field is symmetric about the x-axis, so the centre of the ring in the y-direction will remain in the centre of the domain. The position of the vortex ring in the translational direction (i.e. the z-direction) and wall-normal direction (i.e. the

x-direction) are determined by considering the *y*-vorticity in the *y* = 0 plane. The plane is split in half, between the two vortex cores, and the ring radius of each side is determined. The position of the split is altered such that the two values are equal, and the process is repeated. This method is iterated until the values converge.

However, the interaction between the vortex ring and the wall will alter the shape of the ring away from a perfect torus. The angle of the plane extracted for each point around the ring is therefore modified based on the direction of the vortex core at that position, see Figure 2-10. This modification is based on the dominant direction of the vorticity vector at that location. This is also accomplished using an iterative process, which involves monitoring the standard deviation of the vorticity magnitude while slightly varying the angle of the plane, around both the *z*- and *r*-axis (assuming this is based on a cylindrical co-ordinate system with the origin at the centre of the ring).
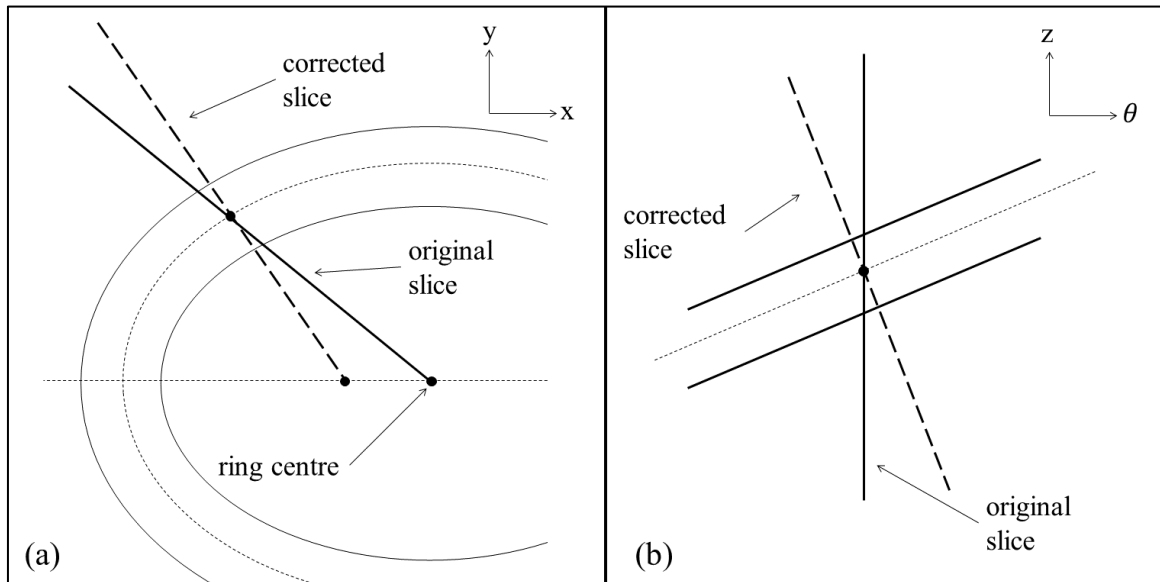

Figure 2-10 – Schematic of the required modifications to extract the azimuthal properties of the vortex core, due to (a) ring stretching in the *xy*-plane, and (b) the tilting of the ring out of the *xy*-plane.

Once the correct plane for the angle in question has been determined, the ring properties can be calculated for this plane. The ring radius that is obtained from this analysis is adjusted slightly, such that it correctly measures the distance from the centre of the core to the centre of the ring.

2.3.3.3. *Boundary layer information*

The true boundary layer thickness, which is given by Equation 1-25, requires knowledge of the free-stream velocity profile. This is not obtainable for the case of a vortex ring near a wall. Instead, a modified relation is derived. By considering only the velocity within the region $-a_0 < x < 0$, the shape of the boundary layer is approximated using the relation

$$\delta^* = \int_0^{a_i} 1 - \frac{u(x, y, z)}{u_{max}} \cdot dy \, .$$

2-33

This relation does not give the true boundary layer thickness, but rather provides a means with which to compare the boundary layer profiles of different scenarios.

Chapter 3

The evolution of swirling axisymmetric vortex rings

The focus of this chapter is on the aims related to the impact of Gaussian initial conditions on the evolution of swirling vortex rings (Section 1.9.1), and to the development of secondary vortex rings from the expected leading edge shear layer (Section 1.9.2). The abstract, results, and conclusions presented in this chapter form the basis of a peer-reviewed article, entitled "*The evolution of swirling axisymmetric vortex rings*", published in Physics of Fluids in August of 2015, by this author. The original content of the article has been retained, however the figure and equation numbering has been updated to reflect the overall layout of this thesis. The final section of the results, Section 3.3, was not included in the published work.

3.1 Introduction

In order to minimise the viscous effects, and encourage the growth of the shear layer instability, the Reynolds number used throughout this chapter is $Re = 10\,000$. The formation and early evolution of swirling rings has been well studied at low Reynolds numbers, however there is a lack of understanding of their evolutionary characteristics at high Reynolds numbers. This value will also result in negligible influence from viscous dissipation, allowing the progression of the shear layer instabilities to be described simply in terms of advection. Despite the large Reynolds number, an equivalent non-swirling ring produced by a piston would be well within the laminar regime (Glezer, 1988), so turbulence has not been considered.

The ring aspect ratios considered are within the range $0.2 < \Lambda_0 < 0.5$ to aid in the subsequent observations, as thicker rings have a more drastic and obvious relaxation process. The swirl distribution is also initially Gaussian, with magnitudes $0.0 < W_0 < 0.5$. These are similar to the smallest swirl magnitudes considered in Cheng *et al.* (2010), to inhibit any transition to turbulence, and prevent the shear layer from greatly altering the underlying shape of the original ring. Simulations are performed for 96 combinations of initial parameters, using 16 values of Λ_0 and 6 values of W_0. The cases are numbered 1 through 96 for indexing purposes, as provided in Table 3-1. Each simulation is run for 75 dimensionless time units, aside from cases 48 and 96, which are run for 300 dimensionless time units.

Two piston generated vortex are also numerically evolved in order to provide a comparison between the types of initial conditions, one with a swirling component of velocity, and one without. At the formation time, the vortex rings have approximate values of $Re_p = 10\,000$, $\Lambda_0 = 0.32$, and $W_0 = 0.5$ ($W_0 = 0$ for the non-swirling ring). This corresponds to Case 87 (Case 7) for the Gaussian cases.

The swirling vortex rings are numerically evolved within an axisymmetric domain, to reduce the computational resources required for the investigation. Given the low swirl magnitudes used, and the prediction of an initially laminar ring, this is not expected to greatly impact upon the obtained results. The rings are monitored over time to determine how their vorticity distributions compare to that of piston produced rings after a suitable relaxation period. The development of instabilities on the leading edge shear layer is also monitored, to provide a better understanding of how this particular phenomena influences vortex ring evolution.

Table 3-1 – List of case numbers with corresponding parameters within the parameter space.

		W_0					
		0.00	0.10	0.20	0.30	0.40	0.50
	0.20	1	17	33	49	65	81
	0.22	2	18	34	50	66	82
	0.24	3	19	35	51	67	83
	0.26	4	20	36	52	68	84
	0.28	5	21	37	53	69	85
	0.30	6	22	38	54	70	86
	0.32	7	23	39	55	71	87
Λ_0	0.34	8	24	40	56	72	88
	0.36	9	25	41	57	73	89
	0.38	10	26	42	58	74	90
	0.40	11	27	43	59	75	91
	0.42	12	28	44	60	76	92
	0.44	13	29	45	61	77	93
	0.46	14	30	46	62	78	94
	0.48	15	31	47	63	79	95
	0.50	16	32	48	64	80	96

3.2 Results

3.2.1. General evolution

A brief summary of the full evolution of the ring is presented first, and analysed in more detail in the following sections. Initially, as the ring begins its motion (from left to right, in all figures), the swirl and vorticity distributions in the *zr*-plane are distorted from their initial Gaussian contours into more complex (but still closed) curves. The changing dynamics result in an axial vortex region separating from the core (A in Figure 3-1), entraining ω_θ (B in Figure 3-1) that would, in non-swirling rings, be shed downstream into the far wake. A shear layer, consisting of azimuthal vorticity of the opposite sign to that in the vortex core, is observed growing in magnitude at the leading edge of the vortex core, near the axis of the vortex ring (C in Figure 3-1). Over time, the shear layer convects around the vortex core, over the outer edge of the ring (D in Figure 3-1).
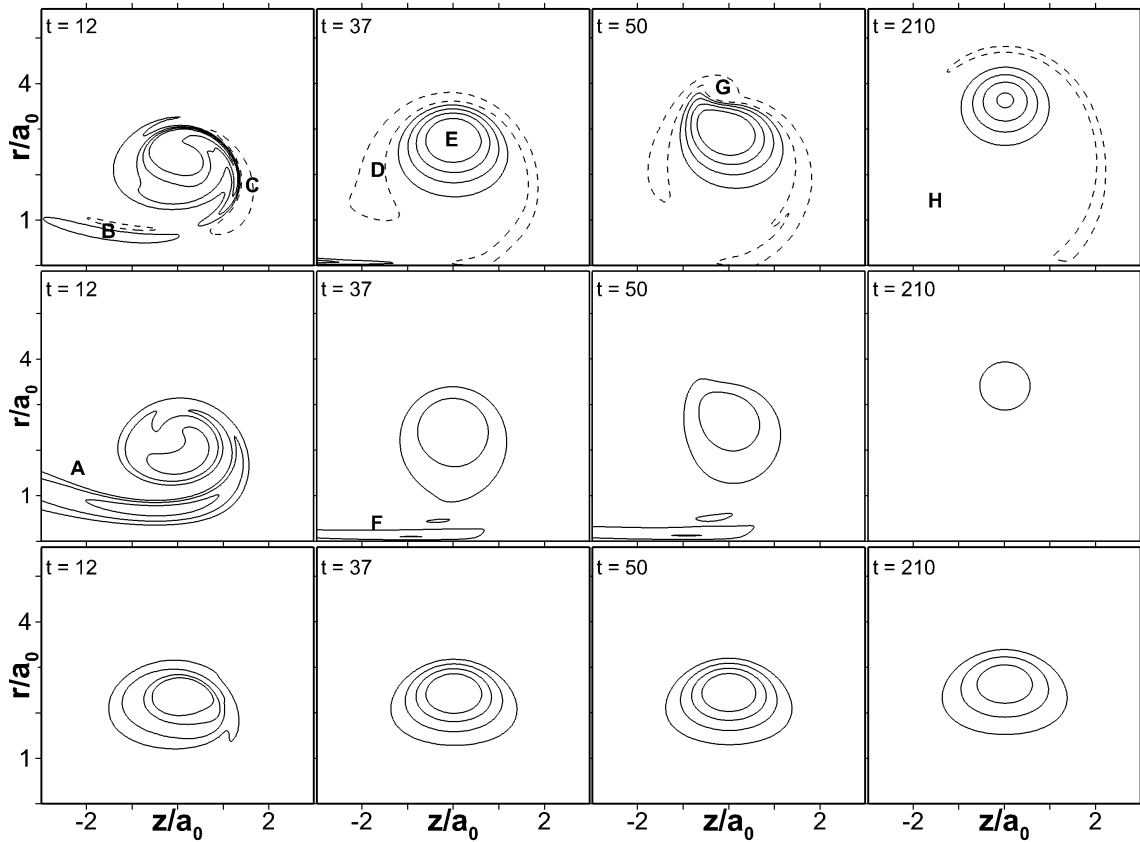
Figure 3-1 - Summary of the evolution of the swirling ring, shown by contours of ω_θ (top line) and u_θ (middle line) for $\Lambda_0 = 0.5$ and $W_0 = 0.5$. Comparison provided with ω_θ (bottom line) for a non-swirling ring with $\Lambda_0 = 0.5$. Contours of ω_θ are (-0.1, 0.4, 0.8, 1.2, 1.6). Contours of u_θ are (0.1, 0.2, 0.4). Dashed line indicates negative contours.

The positive ω_θ contours reach an elliptical shape, indicating that the vortex core has relaxed from its initial Gaussian shape to a vorticity distribution expected from a piston produced vortex ring (E in Figure 3-1). The amount of ω_θ being shed from the core reduces as the influence of the initial Gaussian distribution decays, and most of the ω_θ component of the axial vortex is convected downstream into the far wake, while the azimuthal velocity component remains (F in Figure 3-1). For certain cases, a shear layer instability develops from within the leading edge shear layer, resulting in an oppositely signed vortex ring forming and being convected around the original ring (G in Figure 3-1).

This growth and shedding process can be repeated multiple times, depending on the chosen ring parameters, until the strength of the shear layer is reduced and the instability decays. The vortex core settles into a viscous diffusion dominated state, and the profile of the vortex ring remains relatively constant (H in Figure 3-1). The piston generated vortex ring follows a very similar evolution, and reaches a qualitatively similar final state. Results from the piston simulation will be identified where applicable. The evolutionary process of a non-swirling ring is shown for comparison in the bottom line of Figure 3-1.

3.2.2. Growth of axial vortex and shear layer

The initial Gaussian distribution of azimuthal vorticity does not satisfy the equilibrium equations, so the vorticity distribution must relax to a suitable state. This relaxation process dominates the early stages of evolution. The initial variation in the distribution of ω_θ within the vortex core is not heavily influenced by the presence of swirl, with the core shape and position of peak ω_θ for a non-swirling ring (solid line in Figure 3-2a) being qualitatively similar to that for a swirling ring (dashed line in Figure 3-2a). That is, the swirl is decoupled from ω_θ at this early time. Conversely, the warping of the core shape influences the initial evolution of the swirl field. Figure 3-2b shows that the swirl contours are stretched in the streamwise direction.
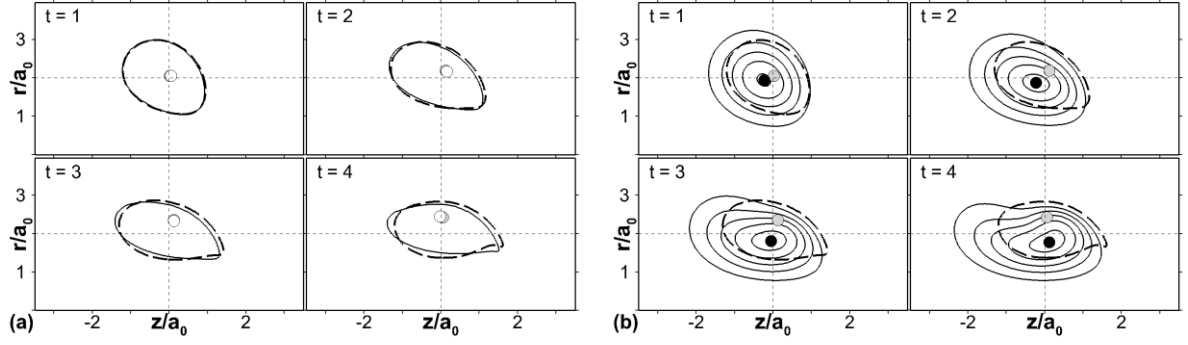
Figure 3-2 - (a) Comparison of the approximate core radius for a non-swirling ring ($\Lambda_0 = 0.5$ and $W_0 = 0.0$) (solid line, white circle indicating position of maximum) with that of a swirling ring ($\Lambda_0 = 0.5$ and $W_0 = 0.5$) (thick dashed line, grey circle indicating position of maximum) for the early vortex core evolution. (b) Comparison of the approximate core radius for a swirling ring (thick dashed line, grey circle indicating position of maximum) and the corresponding contours of u_θ, with contours separated by 0.10 (solid lines, black circle indicating position of maximum).

This variation in the swirl contours can be explained through examination of the governing equations. As the Reynolds number is large, viscous terms are negligible. Approximating the change in the flow field to be a result of the advection terms only, the azimuthal momentum equation reduces to

$$\frac{\partial u_\theta}{\partial t} \approx -u_r \frac{\partial u_\theta}{\partial r} - u_z \frac{\partial u_\theta}{\partial z} + \frac{u_\theta u_r}{r} \qquad \text{3-1}$$

The terms on the right-hand side (RHS) of Equation 3-1 act to increase u_θ at the leading edge of the vortex ring, and reduce u_θ at the trailing edge (Figure 3-3a). The $-u_z \, \partial u_\theta / \partial z$ term is initially dominant, given the large magnitude of positive u_z near the axis of the ring, and $\partial u_\theta / \partial z$ being positive at the leading edge, and negative at the trailing edge. This term thus acts to increase the magnitude of u_θ at the leading edge, near the axis of the vortex ring. The swirl field stretches in the z-direction, and the resulting contraction of the core in the r-direction over time causes a subsequent increase in the magnitude of the $-u_r \, \partial u_\theta / \partial r$ term. Figure 3-3b shows the variation of the terms between $t = 1$ and $t = 3$. The third term in the equation, $u_r u_\theta / r$, is negligible in comparison to the other two terms, due to the inherent flow configuration of the initial conditions.
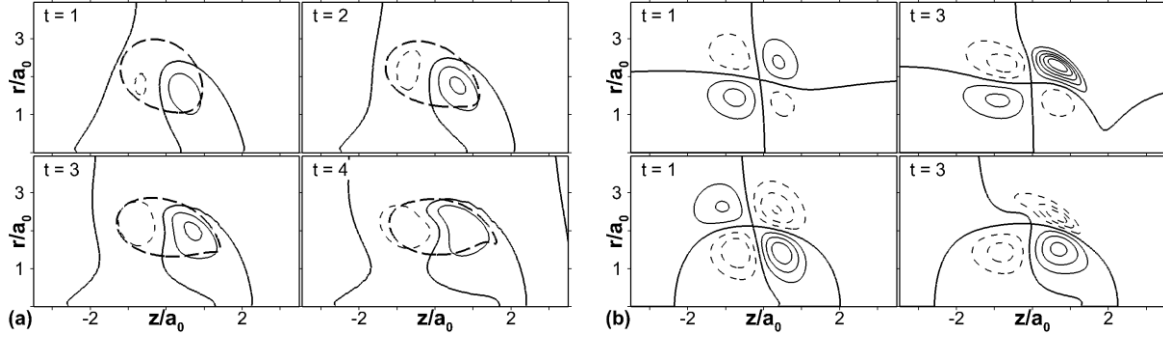
Figure 3-3 - (a) Early evolution of the swirl acceleration distribution, defined by Equation 3-1, for a ring with $\Lambda_0 = 0.5$ and $W_0 = 0.5$. Contours separated by 0.10. Zero line shown in bold. Dashed lines indicated negative values. The thick dashed line gives an approximation of the core size. (b) Contours of the first two terms of the RHS of equation (14). Top row: $-u_r\, \partial u_\theta/\partial r$; Second row: $-u_z\, \partial u_\theta/\partial z$; Contours separated by 0.05. Zero line shown in bold.

As the first two terms in Equation 3-1 act to increase the swirl magnitude in two distinct regions of the vortex core, the swirl field begins to separate into two peaks over the period $t = 5$ to $t = 8$ (top row of frames in Figure 3-4). One peak is within the original vortex core, with a second peak nearer to the axis and leading edge. The tail section of fluid continues to grow and move towards the axis, while being stretched downstream into the wake.

The change in the azimuthal vorticity is inherently linked to the swirl through the governing equations, so the evolving swirl field eventually influences the vorticity. Taking the curl of the momentum equations and neglecting the viscous terms allows the equation for azimuthal vorticity to be written as

$$\frac{\partial \omega_\theta}{\partial t} \approx \frac{u_\theta}{r}\frac{\partial u_\theta}{\partial z}.$$

$$3\text{-}2$$

Equation 3-2 defines the explicit role that u_θ has on influencing the change in ω_θ over time, and is overlaid on the contours of ω_θ in Figure 3-5. Initially, the change in ω_θ is confined to the region of the flow where ω_θ is finite and positive. The dynamics of the flow act to decrease ω_θ near the leading edge of the core (where $\partial u_\theta/\partial z$ is negative), and increase ω_θ near the trailing edge (where $\partial u_\theta/\partial z$ is positive), with a slight bias towards the axis of the ring due to the $1/r$ term.
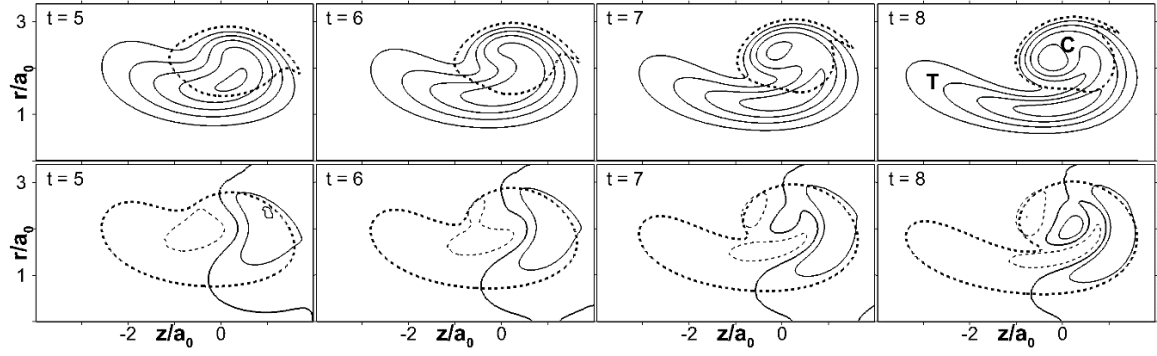
74

Figure 3-4 - Continued evolution of the swirl velocity (top row, overlayed with approximate core size) and the swirl acceleration (overlayed with the $u_\theta = 0.1$ contour) for a ring $\Lambda_0 = 0.5$ and $W_0 = 0.5$. C and T indicate the core and tail regions, respectively. Contours of u_θ separated by 0.10. Contours of swirl acceleration separated by 0.20. Zero line shown in bold. Thin dashed lines indicate negative values.
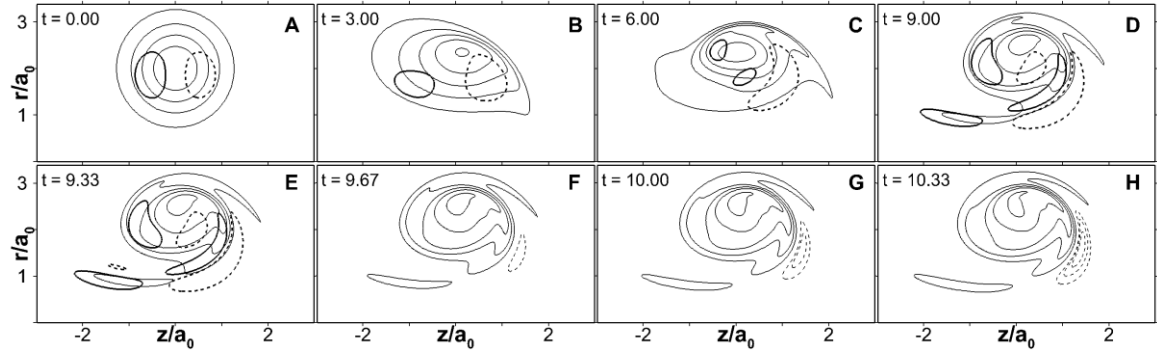

Figure 3-5 - Evolution of the azimuthal vorticity contours, showing the development of the negative vorticity region, for a ring with $\Lambda_0 = 0.5$ and $W_0 = 0.5$. Contours of ω_θ (thin lines) overlaid with $\partial\omega_\theta/\partial t$ (bold lines). Positive ω_θ contours start at 0.2 and increase by 0.4. Negative ω_θ contours start at -0.02 and decrease by 0.06. $\partial\omega_\theta/\partial t$ contours are ±0.3. Dashed lines indicate negative values. Overlay removed from final three frames for clarity.

At $t = 9$, a region containing positive ω_θ begins to evolve between the vortex core and the axis of the vortex ring. This is due to the fact that azimuthal vorticity shed by the core relaxation process is entrained by the newly developed swirl region moving toward the axis. In the case of a non-swirling vortex ring, the vorticity shed due to relaxation is advected into the far wake.

The evolution of the swirl field has a secondary effect. Due to the growth of u_θ near the leading edge, and the curvature of the swirl field in this region, $\partial u_\theta/\partial z$ becomes negative forward of the core, outside the highly positive azimuthal vorticity region (Figure 3-5D). This region, in which u_θ is positive and r is relatively small, results in the growth of negative azimuthal vorticity at the leading edge (Figure 3-5H).

The contraction of the tail region toward the axis increases u_θ due to conservation of angular momentum. At approximately $t = 30$, the tail region, which is now effectively an axial vortex, is the main contributor towards the growth of negative ω_θ at the leading edge. The large swirl magnitude and small r-position of the tail, combined with the sharp decrease in swirl at the leading edge, greatly influences ω_θ through Equation 3-2. This increase in negative ω_θ is shown in Figure 3-6a, and the motion of the tail toward the axis is shown using u_θ contours in Figure 3-6b.

By this time, the negative ω_θ has been convected and stretched around the vortex core due to the rotation induced by the core. A similar process is observed for all tested rings with a non-zero swirl. The presence of an axial vortex at the ring axis and a negative azimuthal vorticity region at the leading edge have been observed in previous studies, such as Virk, *et al.*[12] (for a polarized ring), Ooi, *et al.*[14] (for a numerical piston produced ring), and Naitoh, *et al.*[26] (for an experimentally produced ring).
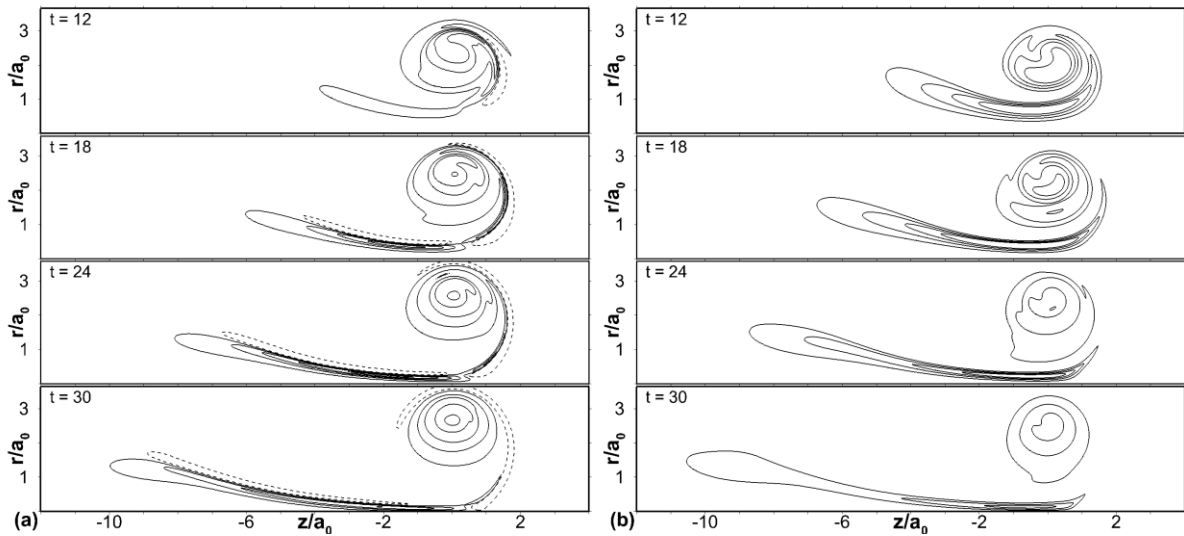
Figure 3-6 - The development of the negative ω_θ region and the motion of the vortex tail towards the axis. Contours of ω_θ (a) and u_θ (b) for a ring with $\Lambda_0 = 0.5$ and $W_0 = 0.5$. Contours of ω_θ start at -0.25 (dotted line) and increase by 0.5. Contours of u_θ start at 0.01 and increase by 0.01.

3.2.3. Core relaxation time

The swirl at the axis continues to be fed over time by the evolution of the azimuthal circulation of the vortex ring, however the amount of positive ω_θ shed by the ring steadily decreases from around $t = 24$ onwards for the $\Lambda_0 = 0.5$ and $W_0 = 0.5$ ring (see Figure 3-7a). Consequently, as the fluid in the axial vortex is gradually convected into wake, the angular momentum at the axis remains constant, while the azimuthal circulation in the region begins to decrease. The cessation of vorticity shedding is consistent with the core freeing itself from its Gaussian initial conditions, and for non-swirling rings this occurs with a corresponding reduction in strain rate fluctuations within the core, providing an easy method of determining the relaxation time (Lacaze *et al.*, 2007). For swirling vortex rings, the development of instabilities within the shear layer results in continued fluctuations in the core strain rate beyond this time (see Section 3.2.4). Due to these fluctuations, the equilibration of the core is not a true relaxation time; however in this context we are using it to mean the time at which its evolution is no longer dependent on its Gaussian initial condition, and will do so for the purposes of this paper.

As demonstrated by Figure 1 in Shariff *et al.* (1994), plotting the ratio of the azimuthal vorticity to the radius versus the Stokes streamfunction for a number of grid points produces a spread curve which collapses to a single line as the vortex core reaches its equilibrated state. Following a similar method for the vortex rings considered here allows an estimation of the relaxation time to be made for the swirling vortex rings. This estimation is obtained by fitting quadratic functions to the collapsing curves for negative streamfunction values, and monitoring the change in the residual over time. An estimation of the variation in relaxation time for a sample of rings with varying swirl values and sizes is shown in Figure 3-7b. It can be seen that the relaxation time always increases with the inverse of Λ_0, and is relatively similar for all ring sizes when swirl is absent. The general influence of swirl is to spread the relaxation times of the varying ring sizes, with each ring ratio showing a slightly different trend with increasing swirl. Relaxation times for the remaining initial ring parameters will be presented in Section 3.2.5.
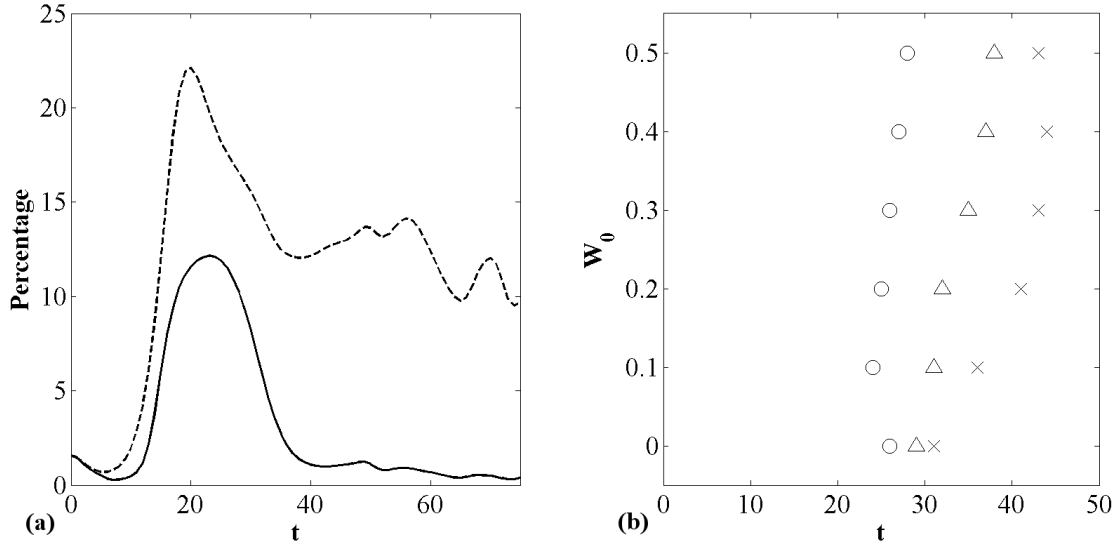
Figure 3-7 - (a) Percentage of azimuthal circulation (solid line) and an integral measure of swirl (dashed line) contained within $a_0/2$ of the $r = 0$ axis, within a logging domain of $\pm 2a$ from $z = 0$. (b) Relaxation time of the vortex core for ring sizes of $\Lambda_0 = 0.22$ (x), $\Lambda_0 = 0.32$ (Δ), $\Lambda_0 = 0.50$ (o).

The evolution of the relationship between the Stokes streamfunction and the azimuthal vorticity divided by the radius at each point has been shown at various times of the $\Lambda_0 = 0.5$, $W_0 = 0.0$ ring in the top row of Figure 3-8. The evolution from the initial broad distribution of points ($t = 0$), through a fluctuating distribution ($t = 10$), to the collapsed distribution ($t = 30$ and $t = 40$) is evident. The bottom row of Figure 3-8 shows the same snapshots in time, but for a ring with $W_0 = 0.5$. The initial distribution and fluctuation are similar, although the curve takes noticeably longer to collapse, and has a different form to the non-swirling case. The growth of the instabilities after this time in the shear layer of swirling rings results in a renewed distortion of the curve.

3.2.4. Comparison with piston generated vortex ring and post-relaxation evolution

The flow fields of the numerically evolved Gaussian rings at the relaxation time are similar to those evolved by piston produced rings. Figure 3-9a presents a comparison between the flow fields for a non-swirling Gaussian ring, and a non-swirling piston

produced ring shortly into its evolution, for $\Lambda_0 = 0.32$. Although the piston case has an additional arm of positive vorticity, the core shapes have similar elliptic profiles at similar evolution times. The vorticity arm is gradually advected downstream from the piston produced vortex core over time. Figure 3-9b shows the comparison between the flow fields for a swirling Gaussian ring of $\Lambda_0 = 0.32$ and $W_0 = 0.50$, and a swirling piston produced ring, with approximately similar size and swirl magnitude.
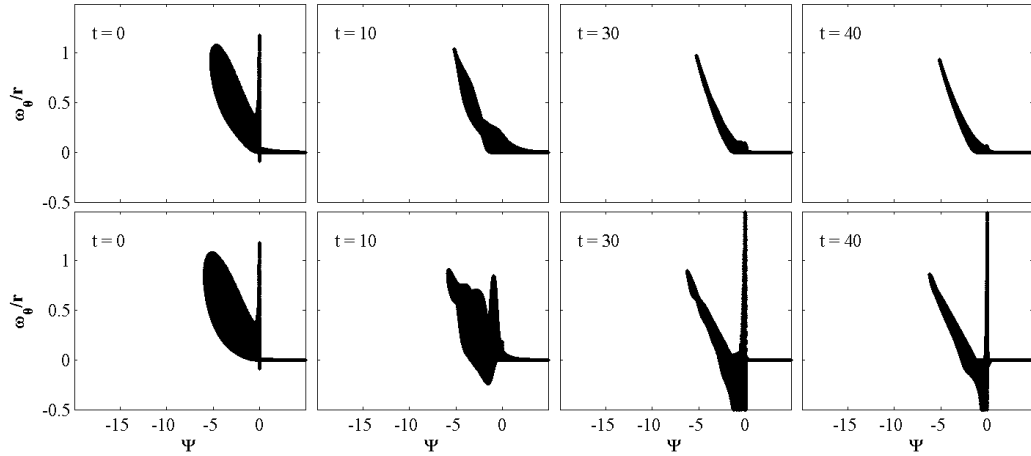

Figure 3-8 - Evolution of the streamfunction plots for non-swirling (top row) and swirling (bottom row) rings with $\Lambda_0 = 0.5$, over time, showing how the array of points settles to a compact shape as the core relaxes. Each curve is made up of individual points located within $5a_0$ of the vortex core in the z-direction, and between 0 and 10 in the r-direction.
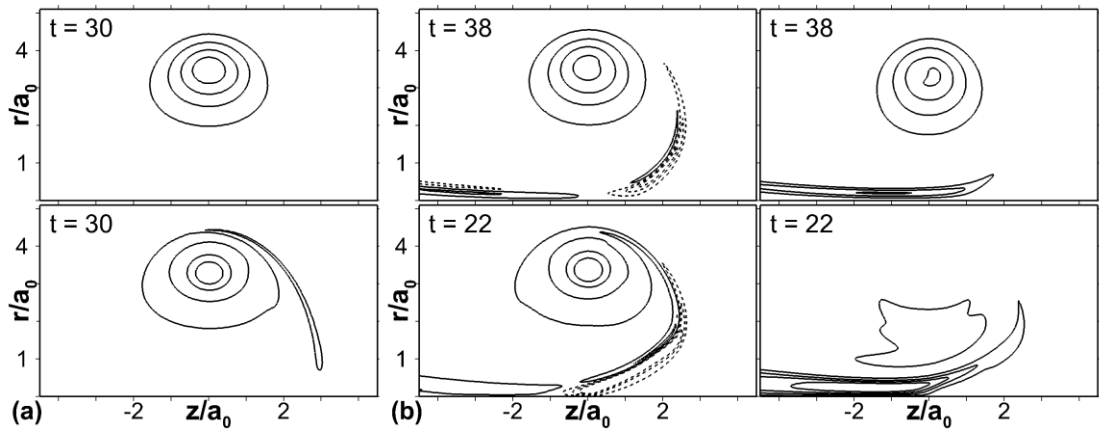
Figure 3-9 - Comparison between evolved Gaussian cores (top line) and piston produced cores (bottom line) for $\Lambda_0 = 0.32$. (a) $t = 30$ of non-swirling Gaussian core compared to $t = 30$ of non-swirling piston core. Contours of ω_θ start at 0.25 and increase by 0.5. (b) $t = 38$ of $W_0 = 0.50$ Gaussian core compared to $t = 22$ of $W_0 = 0.50$ piston core. First column: Contours of ω_θ; contours start at 0.25 and increase/decrease by 0.5. Dashed lines indicate the negative contours. Second column: Contours of u_θ; contours start at 0.05 and increase by 0.10.

The most notable difference between the two cases lies in the shape of the swirl field present within the core of the vortex ring. The swirl contours for the Gaussian initial condition case retain much of their initial circular shape, even after core relaxation has completed. In contrast, the swirl contained within the core of the piston produced ring seems to be concentrated within the lower half of the core, and has a relatively constant magnitude in this region. In addition, the Gaussian initial condition introduces a noticeable delay in the evolution of the ring for the swirling case.

Despite these two differences, the rings do have similar general properties, in that the two cases both feature a strong axial vortex, a negative ω_θ region at the leading edge, and a swirling region within the core. This suggests that the two different rings will experience similar evolutions from this time, given that the negative ω_θ region dominates the evolution, and the axial vortex provides the driving force for maintaining the strength of the negative ω_θ region.

The negative ω_θ region, after it has been convected around the core, forms a shear layer, and so is subject to the Kelvin-Helmholtz instability. The behaviour of this instability is similar for both initial conditions, and this is shown explicitly in Figure 3-10, where the top row of frames shows the development of the instability for the Gaussian initial conditions, and the bottom row of frames for the piston initial condition. If the shear layer (A in Figure 3-10) is of sufficient strength, this instability can grow to the point where a roll up of the vorticity occurs (B in Figure 3-10), and a secondary vortex ring of the opposite sign is formed. The secondary vortex ring is then itself convected around the original ring (C in Figure 3-10), and shed from the system (D in Figure 3-10). Despite the different initial conditions of the two rings, the underlying ejection process is the same; instability within the shear layer rolls up into a secondary ring, which is shed from the system. If the shear layer is not of sufficient strength to significantly grow the instability, the shear layer is convected around the ring and into the wake, without detaching into a clear secondary ring.
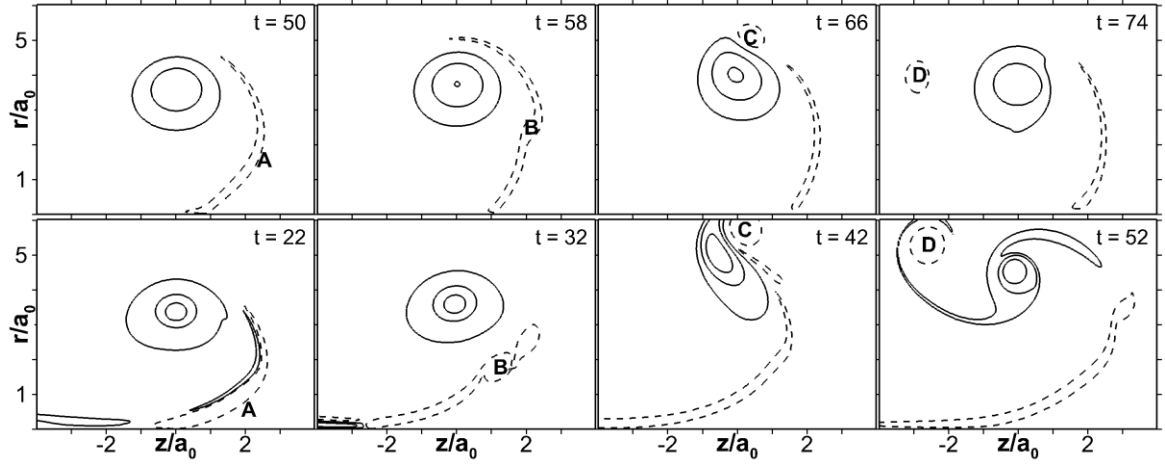
Figure 3-10 - Progression of the ejection process of negative vorticity Contours of ω_θ for $\Lambda_0 = 0.32$, $W_0 = 0.5$. Top row: Flow fields for the Gaussian core vortex ring. Contours shown are -0.25, 0.10, 1.10, 2.10. Bottom row: Flow fields for the piston generated vortex ring simulation. The previous ejection can be seen in the first frame. Contours shown are -0.10, 0.10, 1.10, 2.10.

3.2.5. Shear layer strength

The formation time of the secondary ring is defined here as the time at which the peak in negative ω_θ begins moving away from the ring axis. This formation first relies on the influence of the Gaussian initial conditions becoming negligible; that is, the vortex core must reach its relaxed state. In addition, the positive vorticity entrained near the ring axis must be convected into the wake, and the shear Reynolds number within the leading edge shear layer must reach a peak. In Figure 3-11, it can be seen that for all cases, the secondary ring does not form until these three conditions have been met. This implies that the growth of the Kelvin-Helmholtz instability and the formation of the secondary ring are intrinsically linked to the evolution of the vortex core.

Given that a Kelvin-Helmholtz instability has been identified, there should exist a cut-off Reynolds number, similar to what is observed for the Cartesian form of the instability. Here, a shear layer Reynolds number is introduced for this purpose, and expresses the strength of the shear layers in the flow through

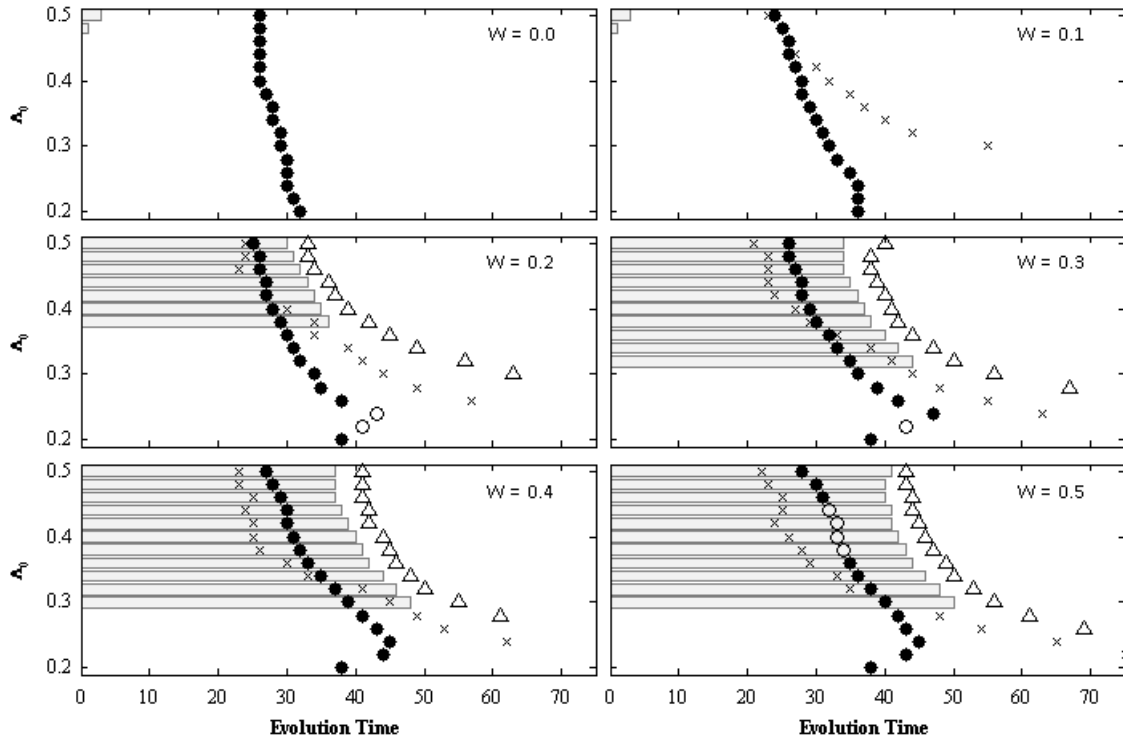$$Re_s = \frac{\delta\,\Delta u}{\nu} \qquad\qquad 3\text{-}3$$

81

Figure 3-11 - Dimensionless time for various stages in the vortex ring evolution. The formation of the secondary vortex ring (△ symbols) only occurs once the core has relaxed (● and ○ symbols) shear Reynolds number has peaked (× symbols), and the vorticity entrained near the ring axis has been convected into the wake (the shaded bar represents the period of time until there is consistently less than 1% of the total azimuthal circulation within $a_0/2$ of $r = 0$ and $\pm a_0$ of $z = 0$). Note that the ○ symbols indicate cases for which the relaxation values found were outliers, so these values have been interpolated from the general trend.

where δ is the displacement thickness of the shear layer and Δu is the velocity differential across the thickness. The thickness of the shear layers is measured through the maximum magnitude of negative ω_θ within the layer, perpendicular to the local vorticity contours.

The magnitude of the initial peak in shear layer intensity can be defined using Re_s, and doing so reveals a direct relationship with the initial conditions of the vortex ring. As presented in Figure 3-12, plotting the peak in Re_s against $\log_e(W_0 \Lambda_0^3)$ yields a collapse of the data into a single curve. The resultant dynamics of each case are related to the initial parameters of the simulation. Cases with $\log_e(W_0 \Lambda_0^3) < -6$ do not show growth of the shear layer at the leading edge of the vortex ring. For cases with $-6 < \log_e(W_0 \Lambda_0^3) < -4.9$ (corresponding to $0 < Re_s < 100$), the shear layer

forms, but it is typically not strong enough to form the secondary ring, as indicated by the crosses in Figure 3-12. For cases with $\log_e(W_0\Lambda_0^3) > -4.9$ (corresponding to $Re_s > 100$), the shear layer forms and produces the secondary ring, as shown by the filled circles in Figure 3-12.

The exception to the above rules appears to be cases with a low swirl magnitude, of $W_0 = 0.1$ or less, which do not produce the instability for any of the tested ring sizes. The axial vortex has a slower growth in these cases due to the weaker swirl magnitude in the system, and also weakens faster due to the inherent higher translational velocity present in low swirl cases. This suggests that it is a rapid weakening of the shear layer after the peak in shear layer Reynolds number that prevents the instability growth. These cases are indicated by the open circles in Figure 3-12.
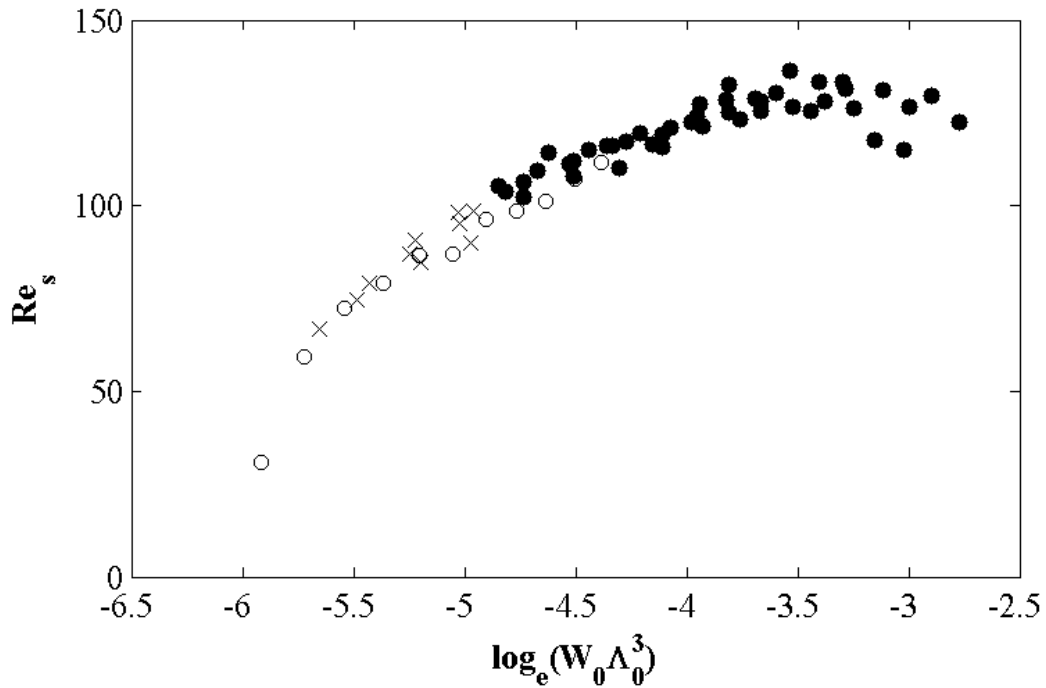

Figure 3-12 - Variation in the magnitude of the initial peak of Re_s with Λ_0 and W_0. ● indicates cases in which roll up of the KHI was observed, ×'s indicate cases in which roll up did not occur for $W_0 > 0.1$, and ○ indicates cases where roll up did not occur for $W_0 = 0.1$. Cases in which the shear layer was too weak to form are not represented on this figure.

The drop off seen for $\log_e(W_0 \Lambda_0^3) > -3.5$ is likely due to the time differential between the initial peak in shear layer intensity, and the final relaxation of the core. For these cases, such as $\Lambda_0 = 0.5$ and $W_0 = 0.5$ in Figure 3-11, the shear layer strength peaks while the core is still undergoing significant relaxation from its initial Gaussian form, preventing the shear layer from growing to its full potential. The highly unsteady relaxation of these rings may also result in a significant amount of swirl being shed into the wake before the shear layer can fully form. Rings in this region may be unsuitable for simulation using Gaussian initial conditions due to this difference to piston produced rings; however this requires further investigation.

3.2.6. Quasi-steady state

The growth and roll up of the Kelvin-Helmholtz instability continues to influence the evolution of the swirling rings past the initial growth period. The convection of the secondary vortex rings around the original core can be tracked. Here, a rotation angle is defined, as the angle made between the z-axis and the line connecting the positions of the peak positive ω_θ of both the primary and secondary cores. The variation with time of the strain rate ε (defined here as the magnitude of the stress tensor) at the position of peak positive ω_θ is shown in Figure 3-13 for the ring with $\Lambda_0 = 0.32$ and $W_0 = 0.5$. The rotation angle is shown overlaid on top of the strain rate, which exhibits a local maxima in time as the secondary ring forms ($t = 58$ in Figure 3-10), and when the secondary ring is at a rotation angle of 90° ($t = 66$ in Figure 3-10). The peaks in the strain rate occur due to the forces on the original vortex core induced by the secondary ring being in direct opposition to the induced velocity provided by the original ring itself. When the secondary ring is convected into the wake, the original shear layer is weakened.

The shear layer retains the ability to produce and shed additional vortex rings, providing the strength of the shear layer is sufficient to continue to generate them. This depends in turn on the strength of the axial vortex at the axis of the vortex ring, which contributes to the shear layer strength through Equation 3-3.
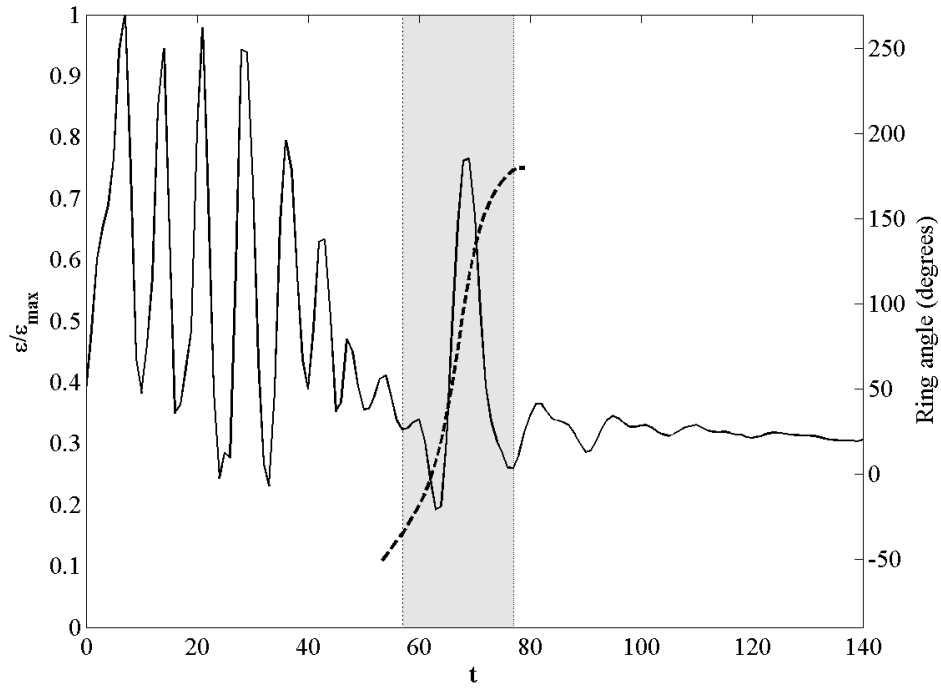
Figure 3-13 - History of the strain rate over time (thin line) overlayed with the rotation angle of the secondary ring (dashed line), for the $\Lambda_0 = 0.32$, $W_0 = 0.5$ Gaussian ring. Only one secondary vortex ring is produced for this case. Shaded region indicates the convection period for the secondary ring.

Figure 3-14 shows the ring with $\Lambda_0 = 0.5$ and $W_0 = 0.5$, which has a similar strain rate and rotation angle relation to the ring shown in Figure 3-13, but features multiple ejections. These ejections continue until the shear layer is too weak to generate any further secondary vortex rings. Typically, this occurs when the axial vortex has weakened to the point where it can no longer maintain the shear layer at the required strength ($Re_s > 100$). At this time, on the order of $t = 145$ for the $\Lambda_0 = 0.32$ and $W_0 = 0.5$ ring, and $t = 210$ for the $\Lambda_0 = 0.5$ and $W_0 = 0.5$ ring, the variation in the strain rate within the core has steadied, and no additional secondary rings are being generated (see the settling of the strain rate in Figure 3-13 and Figure 3-14).
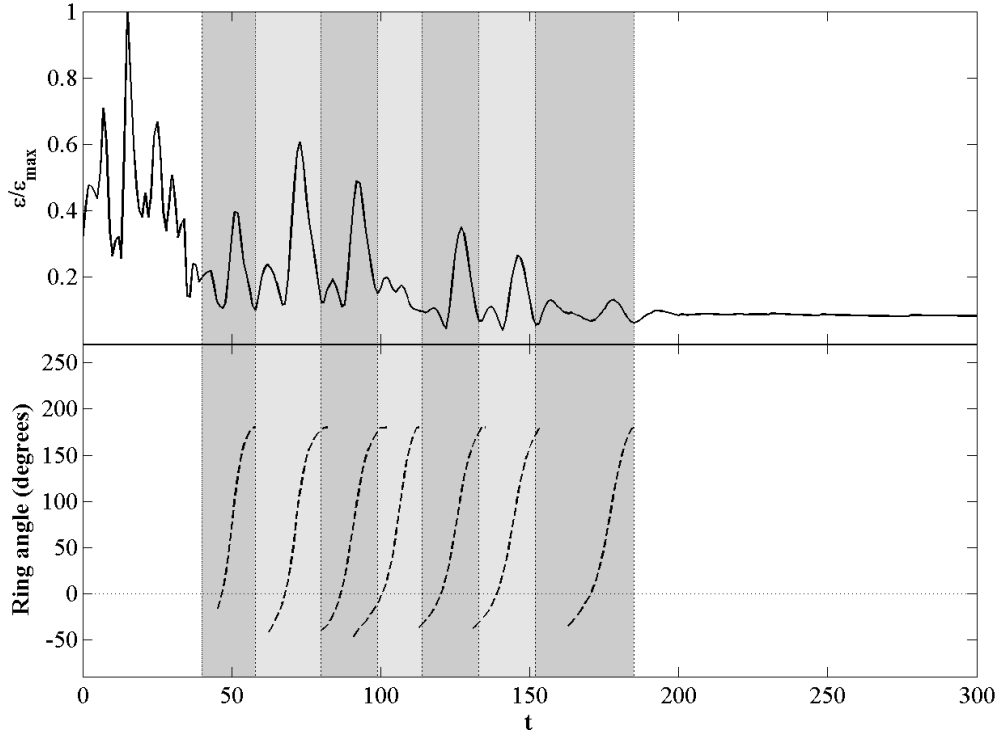
Figure 3-14 - History of the strain rate over time (top frame) with the corresponding rotation angle of the secondary ring (bottom frame), for the $\Lambda_0 = 0.5$, $W_0 = 0.5$ Gaussian ring. The shaded regions indicate convection periods. The horizontal dotted line indicates zero degrees, where the two cores are at the same r-coordinate, and the secondary ring is upstream of the primary ring.

The flow fields at this quasi-steady state ($\Lambda_0 = 0.32$, $W_0 = 0.5$ at $t = 145$) are presented in the top row of Figure 3-15. This final state has a similar form to that of a viscously diffused non-swirling ring, with two key differences; it retains the weak shear layer at the leading edge of the core, reaching from the axis to the outside of the ring; and it continues to push very small amounts of swirling fluid into the tail region. The piston produced ring settles to a similar state, the final flow fields of which are shown in the bottom row of Figure 3-15. The two vortex rings have similar streamlines, and the same major flow features regarding ω_θ and u_θ, however there are slight differences in the shape and positioning of the major features. The shear layer itself is slightly weaker and smaller than that of the Gaussian case. Following this period, both rings evolve in a slowing varying quasi-steady manner, where the primary evolutionary mechanism is the diffusion of vorticity.
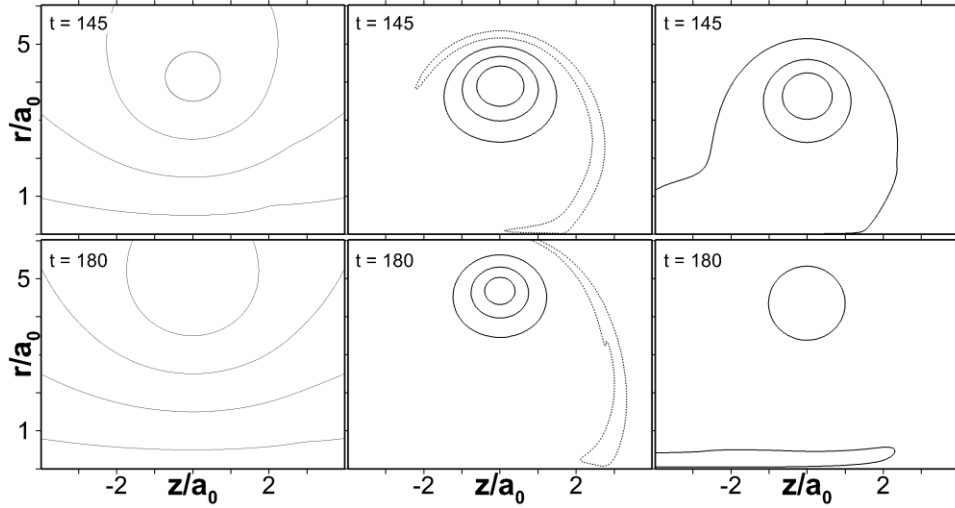
Figure 3-15 - Comparison between steady state flow fields for the Gaussian (top line at $t = 145$) and piston (bottom line at $t = 180$) cases. From left to right: *streamlines*; ω_θ; u_θ. Streamlines separated by 0.1. Positive contours of ω_θ start at 0.25 and are separated by 0.50, negative contour of ω_θ is -0.05. Contours of u_θ separated by 0.10, starting at 0.01. Dashed lines indicate negative values.

3.3 3D Considerations

In order to provide a comparison for the axisymmetric results, two simulations are performed with the condition of axisymmetry removed. The first uses the same mesh as the axisymmetric case, but with the axisymmetry removed and replaced with an azimuthal Fourier expansion. The other uses a highly resolved mesh in the *xy*-plane, and models the *z*-direction with a Fourier expansion. Random noise is applied to the initial flow field of Case 96, with a magnitude 10^4 smaller than the core radius, in order to encourage the growth of non-axisymmetric modes. Performing either of these simulations without any initial noise achieves identical evolution to the axisymmetric case. Note that the ring is not evolved axisymmetrically before considering these 3D simulations.

The development of the Kelvin-Helmholtz instability in the first simulation is presented using contours of ω_z in a slice through the vortex ring, in Figure 3-16. The secondary ring development follows the same evolution as discussed for the axisymmetric cases; the axial vortex develops a shear layer at the leading edge, which develops an instability and experiences a roll-up. The timing is identical to that of

the axisymmetric case. There is, however, two key differences to the cases with axisymmetry enforced. As seen in the iso-contours of the λ_2 field in Figure 3-17, the rear of the axial vortex itself rolls up into a secondary vortex ring-like structure. In addition, the leading edge secondary vortex ring that develops is not a perfect vortex ring, and is instead split at two locations around its circumference. This is likely evidence of an instability forming; the ring eventually diverges from its axisymmetric counterpart, breaking apart asymmetrically.
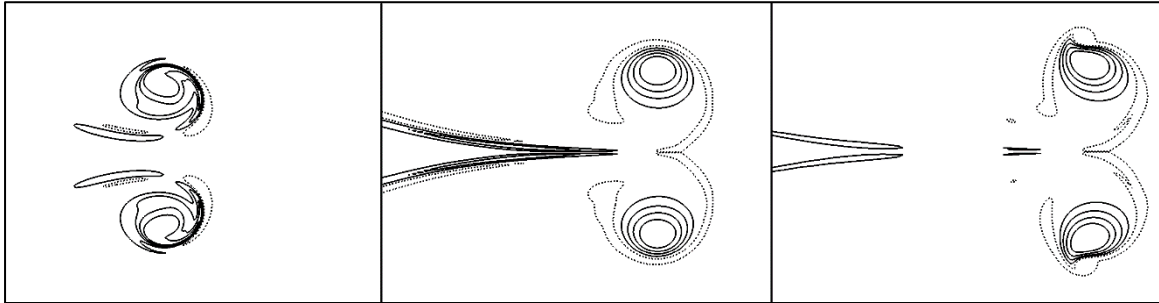

Figure 3-16 – Contours of ω_θ, showing the evolution of the vortex ring at the same times as those presented in Figure 3-1: $t = 12$, $t = 37$, and $t = 50$. Contours level are (-0.1, 0.4, 0.8, 1.2, 1.6).

Attempting to reproduce the analysis on the Cartesian grid produces an interesting result, as the splitting of the secondary ring identified in the cylindrical grid is not retained, as shown in Figure 3-18. The expected development of the secondary ring occurs, and a slight four-fold instability is observed in the axial vortex. This may be related to the four-fold instability observed by (Rojanaratanangkule, 2015) for a vortex ring within a swirling fluid, although the magnitude of their instability is much greater, and also impacts the leading edge shear layer. However, given that both this analysis and the study by (Rojanaratanangkule, 2015) are performed on Cartesian grids, it can be conjectured that the instability occurs due to the numerical mesh, rather than as an intrinsic property of swirling vortex ring evolution.
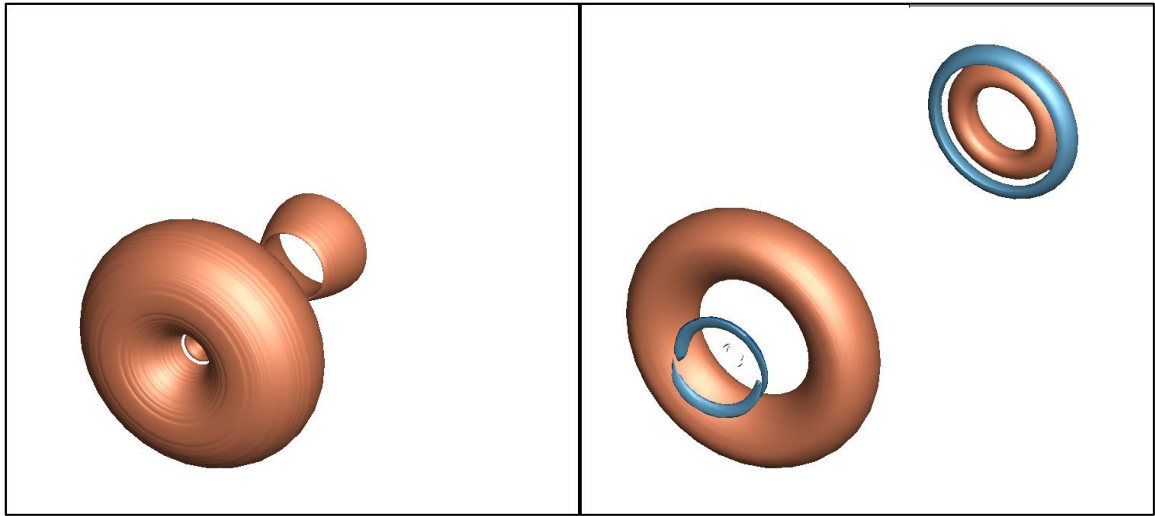
Figure 3-17 – Iso-contours of λ_2 = -1, at t = 18 (left) and t = 40 (right), showing the split in the leading edge seconday vortex ring that develops. Iso-contours are overlaid with coloured contours of ω_θ. Contour levels are [-0.01, 0.01]. Blue indicates negative contours.

Figure 3-18 – Iso-contours of λ_2 = -1 for the case performed on the Cartesian grid, at (left) t = 37 and (right) t = 61. Aside from the expected development of the secondary ring, a subtle four-fold instability can be observed occuring in the wake of the ring. Iso-contours are overlaid with coloured contours of ω_z. Contour levels are [-0.06 -0.02 0.02 0.06]. Blue indicates negative contours.

3.4 Conclusions

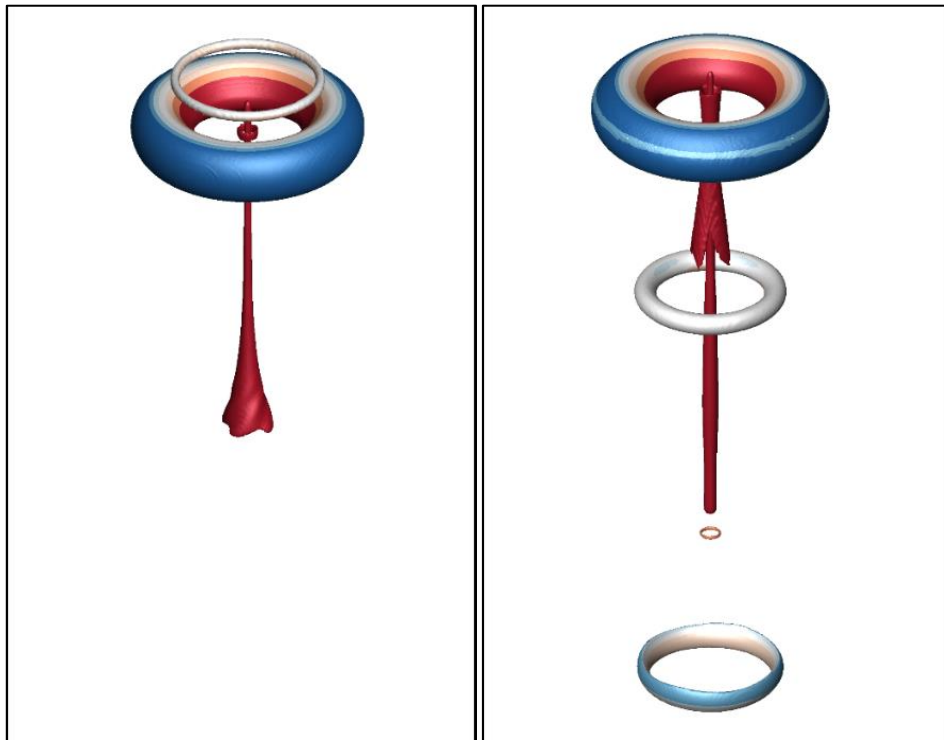Through numerical simulations, the evolution of axisymmetric swirling Gaussian vortex rings was explored with explicit reference to the governing equations. It was shown that these rings evolve towards an equilibrium core vorticity distribution in a similar manner to non-swirling Gaussian vortex rings, although the resulting vorticity contours of the flow field differ. The time required for this equilibration process to complete (or the relaxation time) was generally found to increase with increasing initial swirl magnitude and decreasing initial ring aspect ratio. The swirling component of the flow was shown to result in the formation of a shear layer at the leading edge of the vortex core. The shear layer was found to be inviscidly unstable, resulting in a roll up of negative azimuthal vorticity into secondary vortex rings for shear layers of sufficient strength. The threshold for the production of secondary rings was shown to be $Re_s > 100$ and $W_0 > 0.1$.

The evolution process of the axisymmetric Gaussian ring was found to have similar stages to that of a piston generated ring. The form of the Gaussian ring after the relaxation time was similar to that of the piston generated ring, and for all cases the equilibrium state was reached before any secondary ring shedding was observed. Predictions of the expected behaviour, including the peak shear layer strength and relaxation time, can be made based on the initial ring aspect ratio and swirl magnitude of the rings. This work suggests that Gaussian initial conditions can produce swirling rings that are qualitatively similar to that produced by a piston, however the vortex cores must be allowed to reach their relaxed elliptical state before instability growth rates or evolutionary properties are considered. The results show that there is some question as to whether this is still applicable for rings with $\log_e(W_0 \Lambda_0^3) > -3.5$. Future research is required to determine the applicability of the results for these rings, as well as the overall range of Reynolds numbers at which these flow dynamics hold.

Chapter 4

The linear stability of swirling vortex rings

This chapter focusses on the aims related to the identification of the primary instability mechanisms for swirling vortex rings (Section 1.9.3) and to the variation in the growth rates of unstable modes due to the ring parameters (Section 1.9.4). The abstract, results, and conclusions presented in this chapter form the basis of a peer-reviewed article, entitled *"The linear stability of swirling vortex rings"*, published in Physics of Fluids in November of 2016, by this author. The original content of the article has been retained, however the figure and equation numbering has been updated to reflect the overall layout of this thesis.

4.1 Introduction

The flow field at the equilibration time for each of the rings analysed in the previous section is taken as the initial condition for a separate linear stability analysis. 12 different wavenumbers are analysed for each of the equilibrated flow fields, producing between 4 and 15 waves on each ring. Not all of these stability analyses converge, due to slowly growing modes and computational time constraints. The converged cases cover a significant portion of the parameter space, as shown in Figure 4-1. The axisymmetric domain is retained for the base flow field, however the instabilities that develop are not restricted to being axisymmetric in nature.
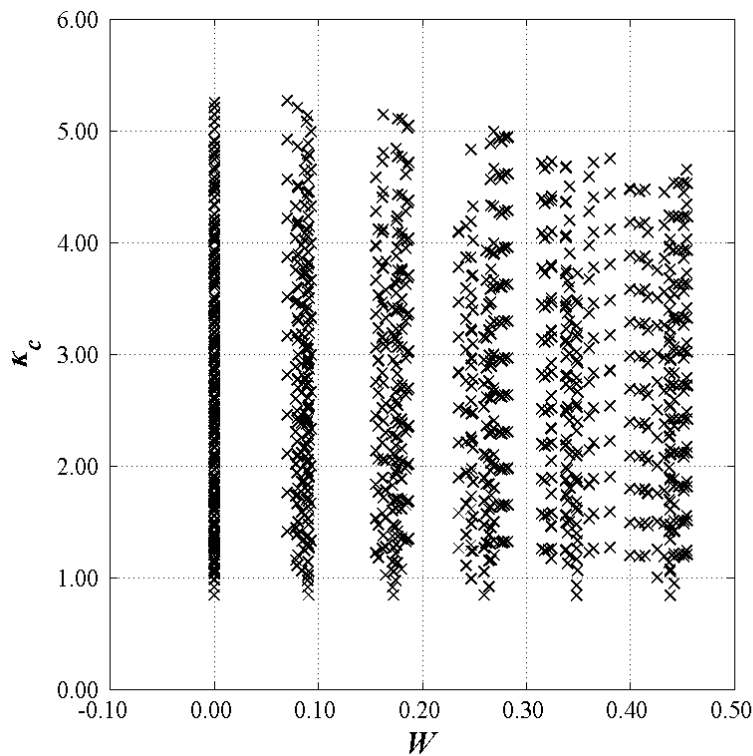

Figure 4-1 - Positions of the converged cases in the parameter space, consisting of the out-of-plane wavenumber at the core centre (κ_c) and the swirl magnitude W.

4.2 Results

4.2.1. Similarities with the Cartesian case

4.2.1.1.   *Comparison of the mode shapes*

The most amplified resonant Kelvin mode pair in each case is identified by considering the values of m across the vortex core. These observations are confirmed through comparison of the perturbation fields for u_θ and ω_θ in the r-z plane, with those presented in the literature (see Roy *et al.* (2008)). A further cross-check is performed by monitoring the value of the oscillation frequency f for the different modes of each ring, to identify any obvious inconsistencies with the values of similar modes. This is particularly useful in the identification of modes for vortex rings with $W = 0$, where $f = 0$ only for the primary modes (Lacaze *et al.*, 2007). For a given set of input parameters, if the mode shape is unclear and the growth rate is significantly below the peak growth rate, then the mode is neglected in the subsequent analyses. These neglected modes make up approximately 30% of the converged cases.

Figure 4-2 presents an example of the mode shapes for each of the unique mode combinations identified. Each row of the figure represents a different base mode, and each column a different branch combination. The first row of Figure 4-2 represents the different branch combinations of the [–1 , +1] resonant mode. The three primary combinations, given by [1 , 1], [2 , 2], and [3 , 3], have similar mode shapes, but can be distinguished by the number of oscillations of the mode in the *s*-direction. The two secondary combinations, [1 , 2] and [2 , 3], show properties of their constituent branches. The second row of Figure 4-2 presents the equivalent perturbation fields for the [–2 , 0] resonant modes. The shape of these modes varies slightly over a wavelength, which has previously been discussed in detail for Batchelor vortex pairs (Roy *et al.*, 2008). The [–3 , –1] resonant modes are typically more difficult to identify due to their increased complexity, however the modes presented in the third row of Figure 4-2 typify their predicted form.
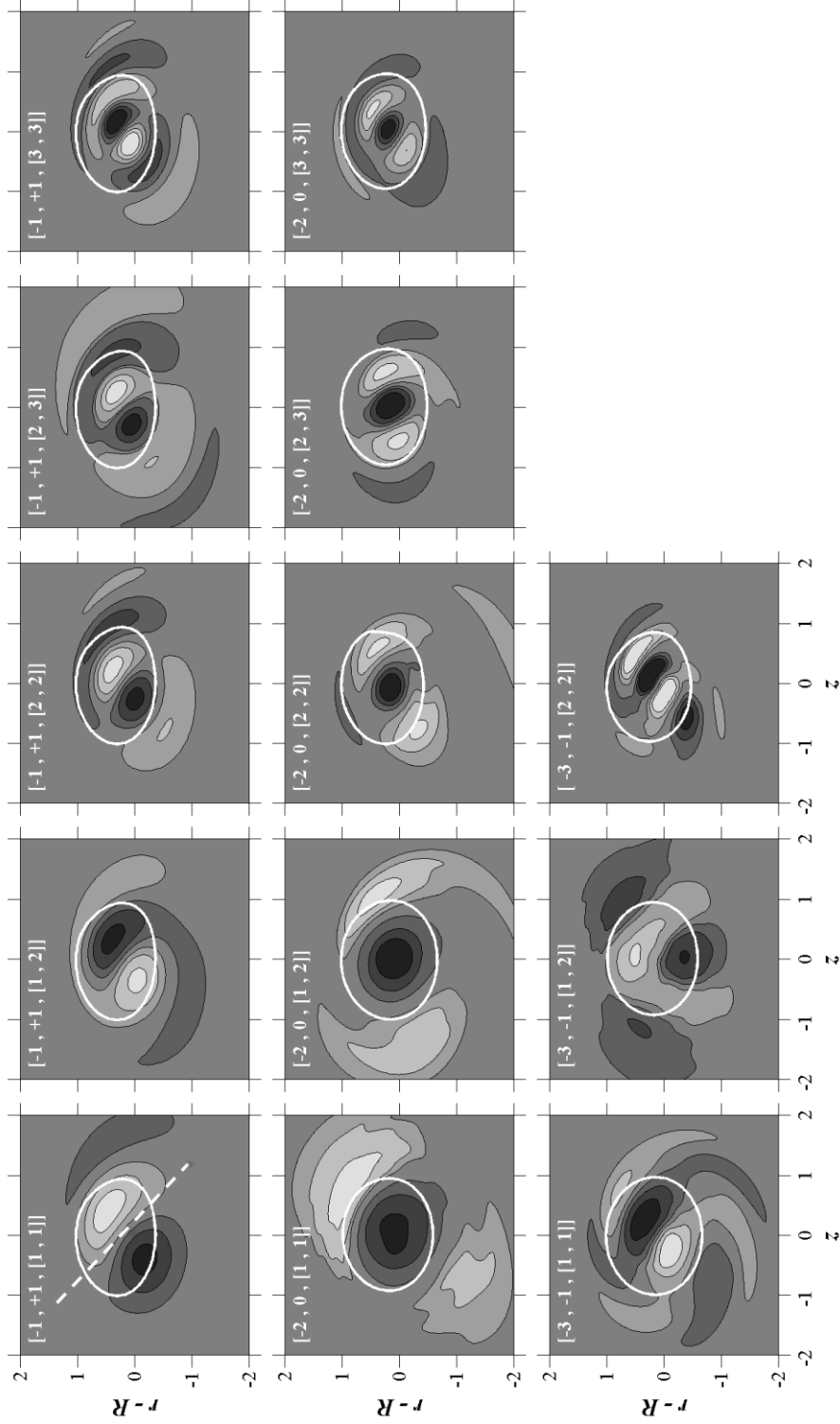
Figure 4-2 – Contours of azimuthal velocity perturbations for the identified branches of the [–1 , +1] (top row), [–2 , 0] (middle row), and [–3 , –1] (bottom row) modes. The white solid lines indicate a contour of vorticity at a position of (0 , a) in the (z , r - R) plane, centred on the peak azimuthal vorticity of the vortex core. The initial radius of the ring influences the shape of the core at equilibration; higher ring radii lead to more circular cores. The contour levels have been chosen such that the perturbation shape of each mode is readily identifiable, and as such magnitudes should not be compared across frames.

The mode shapes presented here show subtle differences to those observed for Batchelor vortex pairs. Most obvious is the break in symmetry experienced by the [–1 , +1] resonant modes. The dashed line in the top left frame of Figure 4-2 shows the axis about which the [–1 , +1] instability is typically symmetrical for the Batchelor vortex pair, however, this symmetry has been lost with the introduction of ring curvature. The difference is due to the variation in the geometry of the vortex ring compared to that of the Batchelor vortex pair; in particular, that the wavenumber of an instability with n waves varies across the core of a vortex ring due to the varying distance from the ring axis. Therefore, even the most amplified instability will have varying growth conditions over the cross-section of the core. This will be discussed further in Section 4.2.2.2 of the results. It is expected that sufficiently large vortex rings will produce modes with greater similarity to the Batchelor vortex pair case, due to the reduced curvature and hence the reduced wavenumber variation.

4.2.1.2. Interaction between mode branches

The variation in the most amplified mode with κ_c can be observed by examining the growth rate of different modes for a given ring. The growth rates for a typical vortex ring with $\Lambda = 0.35$ and $W = 0.00$ are presented in Figure 4-3, as a function of κ_c which is restricted to an integer multiple of Λ as defined by Equation 1-43. The data exhibits three separate peaks, which correspond to the first three branches of the [–1 , +1] mode, as evidenced by the perturbation fields presented in Figure 4-4. Frames A-D ($n = 4$ to $n = 7$) are clear examples of the [–1 , +1, [1 , 1]] instability, with only the angle between the primary peaks of the instability varying as a function of wavenumber. Frames F-I ($n = 9$ to $n = 12$) show the characteristics of the second primary branch combination of mode [–1 , +1], while frames K-L ($n = 14$ and $n = 15$) typify the third primary branch combination of this mode. The remaining frames of Figure 4-3, corresponding to $n = 8$ and $n = 13$, show characteristics of the branch combinations [–1 , +1, [1 , 2]] and [–1 , +1, [2 , 3]].
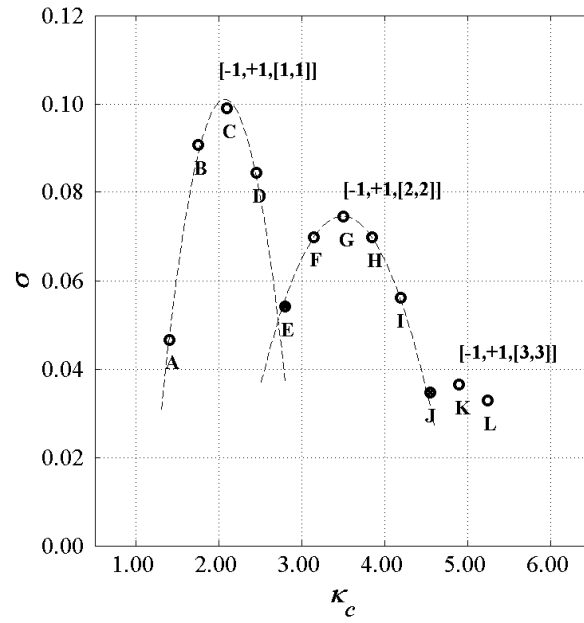
Figure 4-3 - Growth rates σ for the instabilities occurring on the 12 different out-of-plane wavenumbers κ_c for a ring with ring aspect ratio of $\Lambda = 0.35$ and swirl magnitude of $W = 0.00$. The first two peaks have been fitted with quadratics, using $n = 4$ to $n = 7$ and $n = 9$ to $n = 12$ respectively. The filled circles indicate a secondary branch combination, as opposed to a primary branch combination.

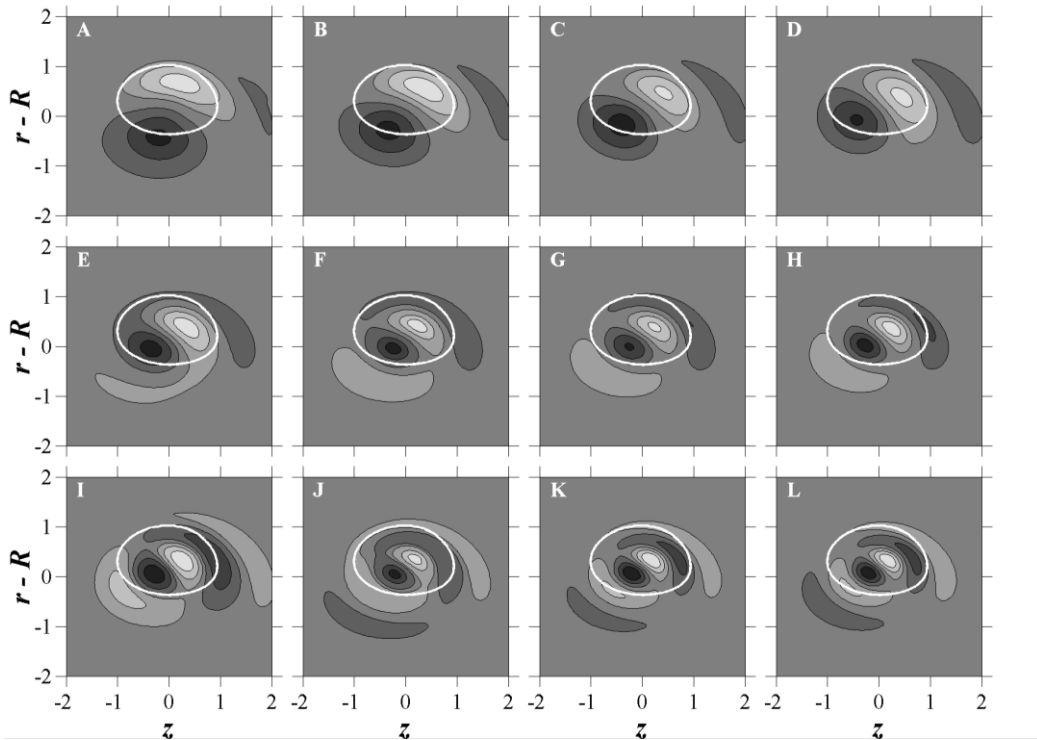Figure 4-4 - Perturbation fields of azimuthal velocity for a ring with ring aspect ratio of $\Lambda = 0.35$ and swirl magnitude of $W = 0.00$. Each frame represents a different number of waves n, with $4 \leq n \leq 15$, ordered from top left to bottom right. The contour levels have been chosen such that the perturbation shape of each mode readily identifiable, and as such magnitudes should not be compared across frames.

These modes are positioned in between the peaks of the surrounding branches, and it is therefore anticipated that the resultant modes will be a combination of the two nearby primary modes. The physical manifestation of these modes is qualitatively similar to the shape of the equivalent modes as observed for Batchelor vortex pairs.

4.2.1.3.   *Interaction between modes*

The branches of different primary modes can also interact. Figure 4-5 presents the growth curves for a ring with $\Lambda = 0.33$ and $W = 0.28$, while Figure 4-6 provides perturbation fields for each data point in Figure 4-5. The addition of an azimuthal velocity damps the growth of the $[-1,+1]$ resonant mode pair, and will amplify the growth of a different combination of $[m,m+2]$. The first instability, corresponding to $n = 4$ and $\kappa_c = 1.32$, does not exhibit a perturbation field that is identifiable as any of the typical Kelvin mode pairs. The lack of complexity within the core suggests that this may in fact be an example of the Crow instability, which scales with R rather than a, and occurs at low values of κ_c (Crow, 1970). The other four identified modes have been designated as follows: $[-1,+1,[1,1]]$ for $n = 5$ to $n = 7$, which is still the most amplified mode for these cases, despite being damped by the addition of swirl; $[-2,0,[2,2]]$ for $n = 9$ and $n = 10$, evidenced by the number of oscillations within the core; $[-2,0,[3,3]]$ for $n = 12$, again by the number of oscillations in the core; and $[-3,-1,[2,2]]$ for $n = 14$ and $n = 15$, due to the development of the positive and negative symmetry. The remaining cases, for $n = 8, 11, 13$, show characteristics of being hybrid combinations of the surrounding modes.
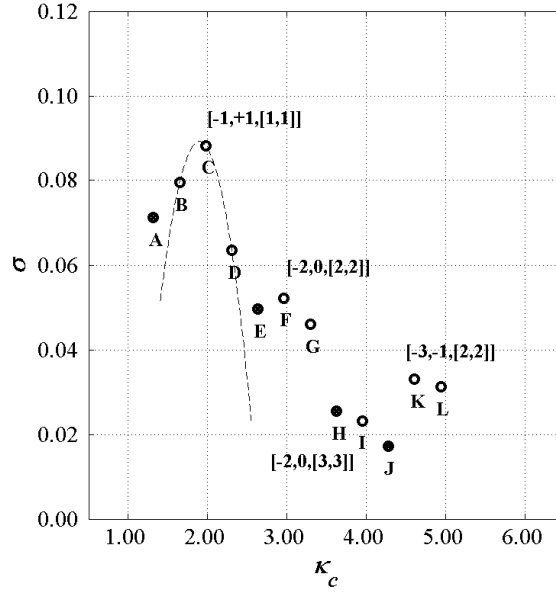
Figure 4-5 - Growth rates σ for the instabilities occurring on the 12 different out-of-plane wavenumbers κ_c for a ring with ring aspect ratio of $\Lambda = 0.33$ and swirl magnitude of $W = 0.28$. The first peak has been fitted with a quadratic, using points B-D. The filled circles indicate a hybrid or secondary branch combination, as opposed to a primary branch combination.

Figure 4-6 - Perturbation fields of azimuthal velocity for a ring with ring aspect ratio of $\Lambda = 0.33$ and swirl magnitude of $W = 0.28$. Each frame represents a different number of waves n, with $4 \le n \le 15$, ordered from top left to bottom right. The contour levels have been chosen such that the perturbation shape of each mode readily identifiable, and as such magnitudes should not be compared across frames.

4.2.2. Influence of ring size

4.2.2.1.   Relationship between Λ and κ

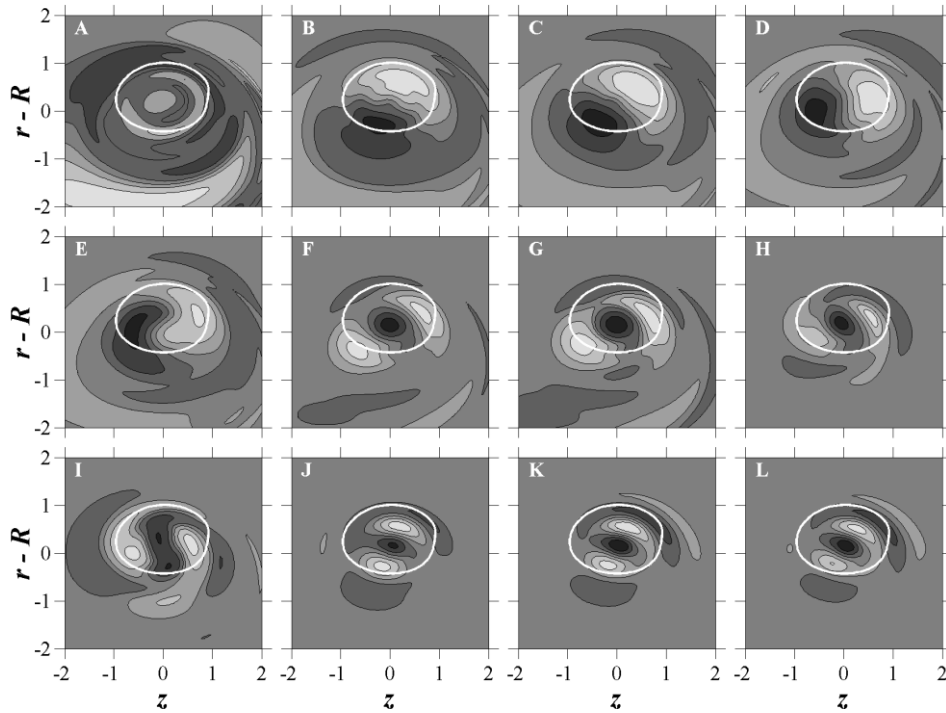The most amplified instability mode for each case does not necessarily experience supportive growth conditions across the entire cross-section of the vortex core. The curvature of the ring induces a variation in the wavenumber over the cross-section of the core. The value of the wavenumber k varies with the distance from the weighted centre of the core in the R direction, which can be expressed as a function of the core radius a through a modification of Equation 1-42,

$$k = \frac{n}{R + pa} \qquad\qquad \text{4-1}$$

where p is a real number bounded by $(-1/\Lambda, +\infty)$. Applying the same modification to Equation 1-43 yields

$$\kappa = \frac{n\Lambda}{1 \pm p\Lambda} \qquad\qquad \text{4-2}$$

To illustrate this effect, three specific values of κ are considered: κ_{inner} (for $p = -1$), κ_c (for $p = 0$), and κ_{outer} (for $p = +1$). Physically, κ_{inner} and κ_{outer} define the normalised wavenumber at one core radius from the centre of the core, in the radial direction. The three variables are shown schematically in Figure 4-7, for an ideal ring with an 8 wave instability around its circumference. The ratio of κ_{outer} to κ_{inner} is dependent only on the ring aspect ratio, and can be expressed as

$$\kappa_{var} = \frac{\kappa_{outer}}{\kappa_{inner}} = \frac{1 - \Lambda}{1 + \Lambda} \qquad\qquad \text{4-3}$$

The variable κ_{var} is presented graphically in Figure 4-8a. The cases in this study have a limited range of κ_{var}, between 0.49 and 0.67, as indicated by the shaded region. Smaller values of κ_{var} indicate a larger variation in wavenumber across the core.
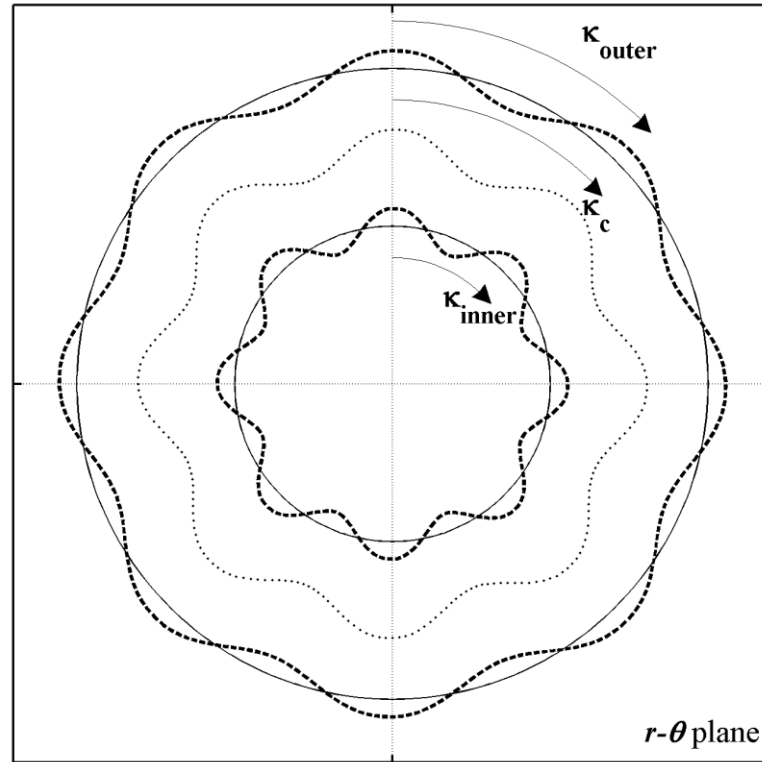
Figure 4-7 - View down the *z*-axis of a vortex ring with $n = 8$, showing the variation in the normalised out-of-plane wavenumber κ with the distance from the axis of symmetry.
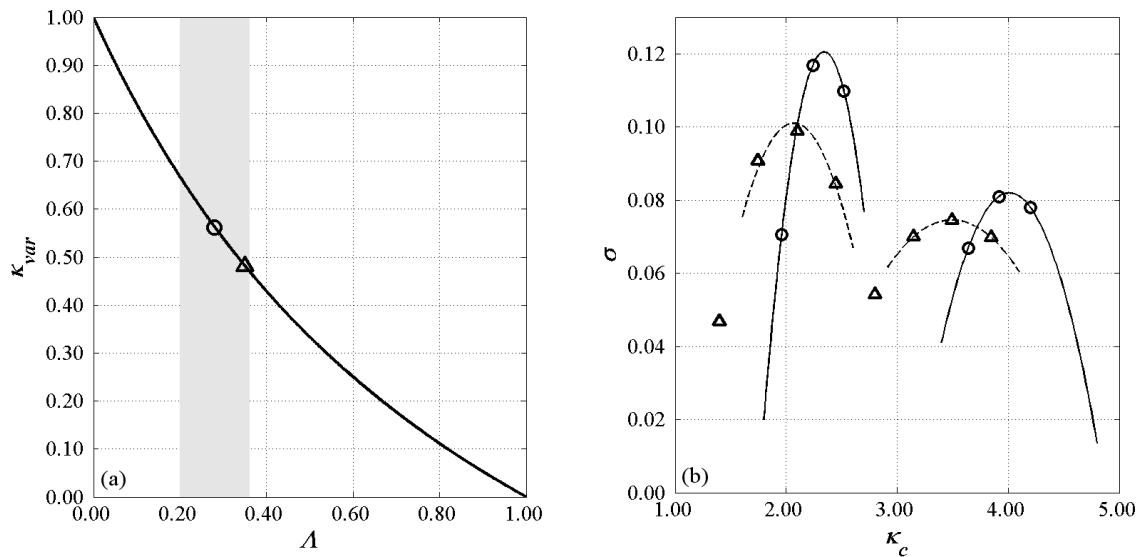
Figure 4-8 - (a) The wavenumber variation parameter κ as a function of Λ. The shaded region indicates the range of Λ for the vortex rings in this study, while two particular cases are indicated with the symbols [o] ($\Lambda = 0.280$, $W = 0.00$) and [Δ] ($\Lambda = 0.350$, $W = 0.00$). (b) Comparison of the different ring sizes and the growth peaks for the first two primary branches of the [-1 , $+1$] instability. Growth peaks have been fitted with quadratics for visualisation purposes only.

Stability discussions are typically undertaken with reference to κ_c. This is adequate for a Batchelor vortex pair, for which there is no variation in wavenumber as a function of core radius, however κ_c does not provide the full picture for an unstable vortex ring. If the most amplified mode for a given ring is that for which the optimal κ value is at the ring centre, then the mode will have sub-optimal growth conditions on both the innermost and outermost regions of the core. Similarly, even if a mode has sub-optimal growth conditions in the centre of the vortex core, it may be amplified at the extremity of the vortex core. It is hypothesised that the peak growth rate for thicker rings should be lower as there is a larger variation in κ across the core region, leading to sub-optimal mode support across the vortex core. In addition, thicker rings should exhibit a wider range modes growing around the peak growth region, compared to thinner rings. This is because the variation in κ across the vortex core ensures some region of the vortex core supports enhanced perturbation growth. Figure 4-8b compares the peak sizes for two different non-swirling rings, with κ_{var} values as indicated in Figure 4-8a, for the first two primary branches of the [–1 , +1] instability. The thinner ring produces tall and focussed peaks, while the thicker ring, for which κ_{var} is further from 1, induces slower growth, and in turn, a lower peak height. The larger variation in κ for the thicker ring enables typically less amplified modes to sustain growth on the core, while inhibiting the growth of the most amplified mode.

4.2.2.2.   *Variation in peak σ and κ_c with Λ*

The shape of the most amplified mode is dependent on the value of κ_c with the largest growth rate, however the value of κ_c corresponding to the peak growth rate is also dependent on the ring size. The peak growth κ_c for the [–1 , +1, [1 , 1]] mode for each of the non-swirling cases is presented in Figure 4-9a as a function of Λ. Those values of Λ for which insufficient data was available to accurately locate the peak have been excluded. The discrete values that κ_c must take for a finite sized vortex ring implies that thicker rings (with larger separation in the values of κ_c) are less likely to experience the maximum possible growth rate of the instability. Cases with similar thicknesses are unstable to the same value of n, which is the reason for

the grouping of the points on the graph. A similar method also reveals the relationship between σ and Λ, and is presented in Figure 4-9b. The peak in each group of points indicates which case is closest to producing the maximum possible growth rate for that particular mode.

The growth rates of each case that produce one of the first three branches of the [–1 , +1] mode instability are presented in Figure 4-10a. The difference in κ_{var} across the cases alters peak height, position (in κ_c), and width, explaining the large spread in the positions of the data points. Three individual peaks have been identified using solid lines for the position of the first branch. These differences can be qualitatively corrected by using κ_{var} as a normalisation factor. Vortex rings with a larger spread of κ values (smaller κ_{var}) will have reduced growth rates compared to vortex rings with a smaller spread of κ_{var}. Increasing the ring aspect ratio (resulting in a larger spread of κ values) also moves the peak growth position on the vortex core towards the axis, as modes which have a larger growth rate corresponding to κ_{inner} have a larger region of core to develop than modes favoured by κ_{outer}. This suggests that the most sustained growth within the core no longer occurs at a wavenumber of κ_c, and is instead governed by some value of κ closer to κ_{inner}.
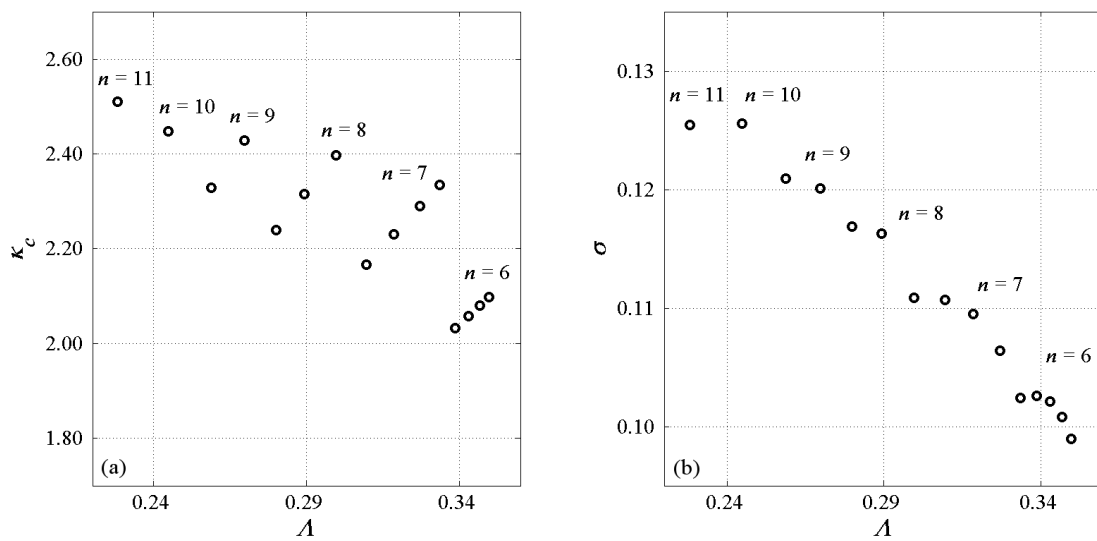

Figure 4-9 - Plot of the (a) peak wavenumber at the core centre κ_c and (b) the peak growth rate σ as a function of the ring aspect ratio Λ.
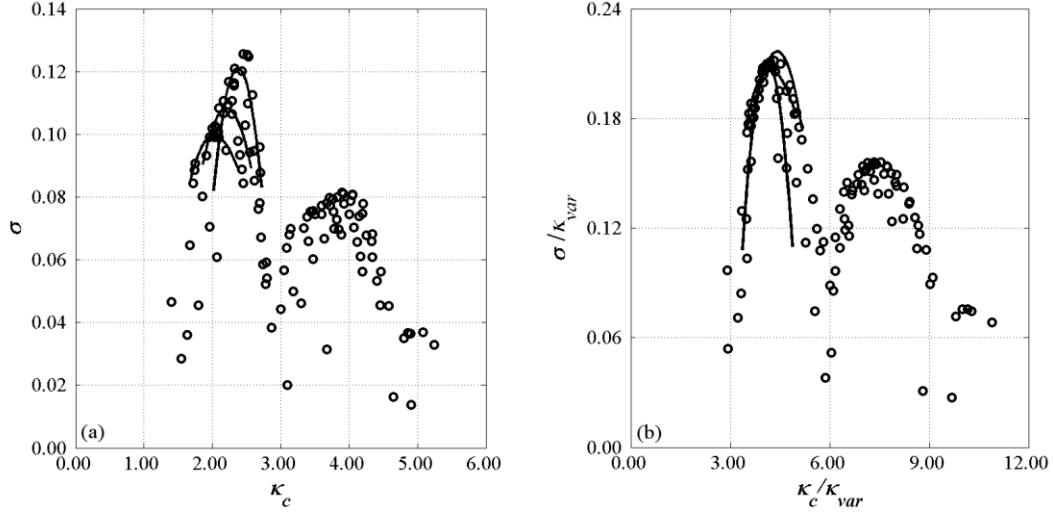
Figure 4-10 - Plot of the growth rate σ for the primary modes of the non-swirling cases as a function of the out-of-plane wavenumber at the core centre κ_c. Shown (a) without the wavenumber variation (κ_{var}) scaling and (b) with the scaling (right). The black curves on each plot represent the positions of the peak of three different cases.

Therefore, dividing both κ_c and σ by κ_{var} provides an approximate method to align the three peaks from Figure 4-10a to Figure 4-10b. The variation in the width of the σ versus κ_c curves has not been affected by this change. It is worth noting here that, while attempts were made to normalise the data using an appropriate combination of coefficients and exponents of Λ, no successful combination was found.

4.2.2.3.   Variation in mode shape with κ_c

The basic shape of the perturbation fields for given values of κ_c and W are qualitatively similar, regardless of the ring thickness. Frames A-D of Figure 4-11 present the perturbation fields for four different vortex rings with similar κ_c values, but different combinations of Λ and n. The specific parameters of each ring are provided in Table 4-1. The growth rates for the modes vary considerably, due to the very different values of κ_{var} across these four cases, however the perturbation fields are similar. Frames E-H of Figure 4-11 give the perturbation fields for four different vortex rings with varying values of κ_c, but with similar values of κ_c/κ_{var}. Here, the values of σ/κ_{var} are similar for the four cases, indicating that the normalisation has brought the cases into qualitative agreement. However, the shape of the instability modes does not appear to rely on this normalised variable κ_c/κ_{var}. Cases D and G,

104

which have only a 3% variation in the value of κ_c/κ_{var}, have a noticeable difference in the angle of the perturbation field between the two cases. This observation, and the similarity in cases A-D, and in cases E-F, implies that the value of κ_c remains the dominant factor in determining the visual characteristics of the mode.
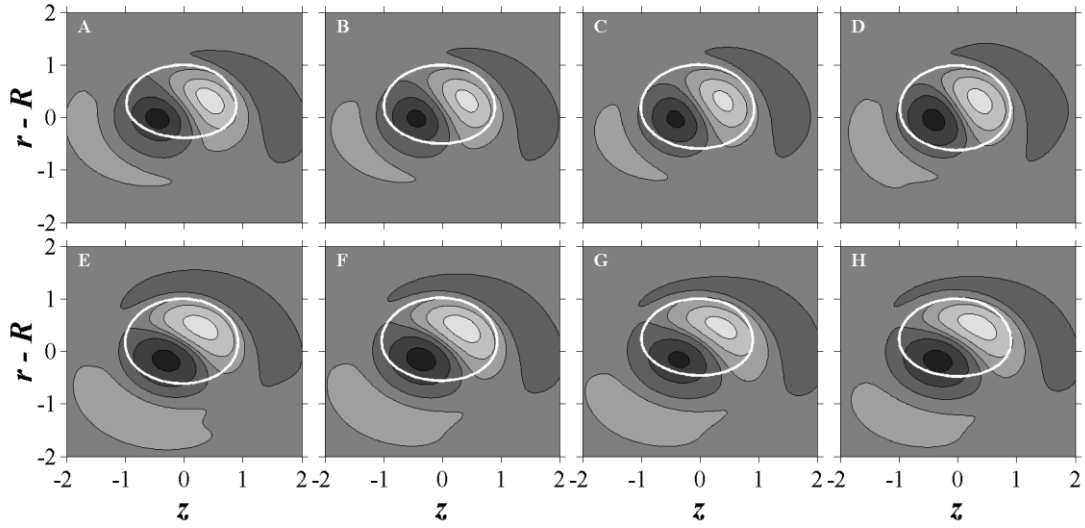

Figure 4-11 – Perturbation fields of azimuthal velocity, showing the influence of the ring curvature on the shape of the [-1,1] instability mode. Parameters for the presented cases are given in Table 4-1. The contour levels have been chosen such that the perturbation shape of each mode is readily identifiable, and as such magnitudes should not be compared across frames.

	n	Λ	κ_{var}	κ_c	$\mathbf{Re}\,(\sigma)$	$\kappa_c\,/\,\kappa_{var}$	$\mathbf{Re}\,(\sigma)\,/\,\kappa_{var}$
A	8	0.339	0.494	2.710	0.067	5.486	0.136
B	9	0.300	0.539	2.696	0.078	5.003	0.145
C	10	0.270	0.575	2.698	0.088	4.691	0.153
D	11	0.245	0.607	2.693	0.096	4.438	0.158
E	9	0.259	0.589	2.329	0.121	3.955	0.205
F	8	0.289	0.551	2.315	0.116	4.200	0.211
G	7	0.319	0.517	2.230	0.109	4.316	0.212
H	7	0.310	0.527	2.167	0.111	4.109	0.210

Table 4-1 – The parameters for the vortex rings given in Figure 4-11, with the number of instability waves n, the ring aspect ratio Λ, the wavenumber variation parameter κ, out-of-plane wavenumber at the core centre κ_c, and growth rate σ.

4.2.3. Mode map from normalized data

The normalisation of κ_c and σ using κ_{var} provides a convenient method of unifying the data from the various different cases, although it remains inexact due to the inability to account for the change in the width of the peaks. It is, however, still possible to produce a mode map indicating the approximate growth regions of each resonant Kelvin mode pair. In order to permit comparison to existing literature, the growth regions for each instability have been presented in a similar manner to that of Roy *et al.* (2008) and Lacaze *et al.* (2007). Figure 4-12 presents the observed growth regions for the primary branches of the [–1 , +1], [–2 , 0], and [–3 , –1] modes, as a function of both κ_c/κ_{var} and W. The distribution of the raw data is not uniform, and so the data has been interpolated using cubic splines in order to produce a smoother mode map. These relative positions are qualitatively similar to those presented in Lacaze *et al.* (2007), even though the axes have been scaled to account for the variation in ring aspect ratios, and the resolution within the domain is much lower.

The peaks for the [–1 , +1] modes occur along the $W = 0$ axis. The peak growth rate of the [–2 , 0, [1 , 1]] mode occurs on the edge of the parameter space at high W, and would presumably occur at larger values of W if these vortex rings with higher swirls were included. The [–3 , –1] modes also exhibit regions of positive growth, however their growth rates are much smaller than the other two resonant mode pairs, suggesting that either this mode is influenced more heavily by the ring curvature, or is simply more difficult to identify. A number of cases, with large Λ, high W, and low κ_c, showed significant growth rates, however did not exhibit any recognisable Kelvin mode perturbation fields. Instead, the most amplified region of the instability for these cases was within the outer shear layer of the equilibrated flow fields. The existence of this instability has been noted for the sake of completeness, however has not been included as a distinct region in Figure 4-12.
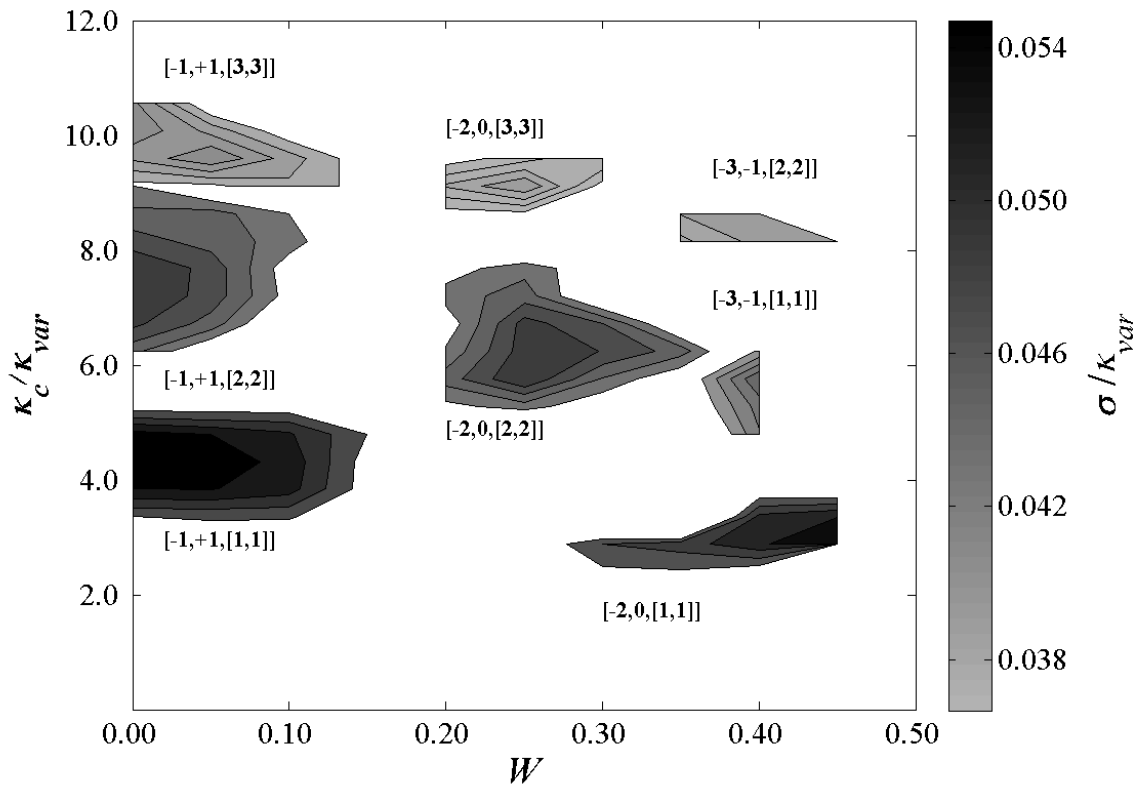
Figure 4-12 - Mode map of the instability islands for swirling vortex rings, using the wavenumber variation parameter κ_{var} as a normalisation factor for both the out-of-plane wavenumber κ_c and the growth rate σ. The swirl magnitude W is unchanged. Only the top 50% of each island is shown, so that the growth islands are clearly separated. The growth rate magnitude provided by the contour map is indicative only, but is within reasonable error bounds (related to the variation in peak width between the extreme cases). The widths of the peaks shown are effectively an average width across all the ring aspect ratios sampled

4.3 Conclusions

A linear stability analysis was applied to numerically equilibrated swirling vortex rings with ring aspect ratios between 0.2 and 0.5, and azimuthal velocity magnitudes between 0.0 and 0.5. The subsequent instabilities induced by resonant Kelvin mode pairs were found to closely follow the growth patterns predicted and observed in previous publications for Batchelor vortex pairs. The variation in the most amplified wavenumber at different radii from the ring axis was shown to be a function of the ring aspect ratio; thicker rings have a greater variation and hence support the growth of instabilities further from the peak growth wavenumber for a particular mode. The shape of the cross-section of the most amplified mode was found to be solely a function of the azimuthal wavenumber at the weighted core centre. The value of the azimuthal wavenumber corresponding to peak growth, and the magnitude of this peak growth, were found to vary instead as a function of the wavenumber variation parameter. Normalisation of the azimuthal wavenumber and growth rate using the wavenumber variation parameter allowed the development of a mode map, showing the approximate values of swirl magnitude and normalised wavenumber at which each individual mode is the most amplified.

This work suggests that the development of instabilities on swirling vortex rings are caused by the same fundamental physics which apply to the Batchelor vortex pair case. It has also been shown that the addition of swirl to an initially non-swirling vortex ring will alter the instabilities that form, in much the same way that the addition of an axial velocity to a Batchelor vortex pair modifies the instabilities. From this work, it can be deduced that an induced swirling flow will alter the instability modes of the vortex ring, damping the development of [–1, +1] modes and aiding the growth of [–2 , 0] and [–3, –1] modes, to further enhance fluid mixing. Additional research is required to fully complete the parameter space for the instability growth of swirling vortex rings. The behaviour of these instabilities at different Reynolds numbers and larger swirl magnitudes has potential for future investigation, in order to further the understanding of vortex ring stability.

Chapter 5

The behaviour of near-wall vortex rings

I n this chapter, the focus turns to the aims related to evolutionary traits of swirling vortex rings (Section 1.9.5), and the influence of ring parameters on wall-normal velocity (Section 1.9.6). The results presented in this chapter consist of original work, parts of which were presented at the 11th European Fluid Mechanics Conference in Seville, Spain, in September of 2016. However, the results in this chapter have not previously been published.

5.1 Introduction

This section explores the dynamics that occur during the interaction of a non-swirling vortex ring with an axially aligned no-slip wall. The focus is on the mixing between the boundary layer and the free-stream flow, to determine whether vortex rings are a candidate to enhance cooling of heated surfaces. The evolution of the ring may be divided into different stages, beginning from the initial ring distortion due to the presence of the wall, and ending with the horse-shoe shaped vortex tube that remains after the near-wall core has dissipated.

Three different rings were considered, with aspect ratios of $\Lambda_i = 0.26$ (Ring 1), $\Lambda_i = 0.33$ (Ring 2), and $\Lambda_i = 0.37$ (Ring 3). These were chosen to show the influence of ring aspect ratio, using selected equilibrated cases from Chapter 3. Implementing these rings too close to the wall artificially distorts the ring structure of the initial conditions, while placing the rings too far away delays the interaction, allowing the ring to grow excessively due to viscous diffusion. Striking a balance between these two factors, three different initial wall separations were implemented for each ring, with magnitudes of $b_i = 2.0$ (Case A), $b_i = 2.5$ (Case B), and $b_i = 3.0$ (Case C).

For the chosen separations, the circulation loss from the near wall core due to the new domain is less than 1% for all cases. The separations are normalized by the core radius at initialization, or a_i. The parameters for each ring are provided in Table 5-1 for clarity. The viscosity in each case is modified such that $Re = 1\,000$ for each case at initialization. The Reynolds number is closer to a magnitude that is associated with micro-scale circuitry. In addition, a larger Reynolds number would require greater resolution to resolve finer length scales, which in turn would require greater computational resources than those available.

In describing the flow field of a near-wall vortex ring, different azimuthal planes of the vortex ring referred to. The azimuthal direction is defined in the range $-180^\circ < \theta \leq 180^\circ$, with $\theta = 0^\circ$ the closest point to the wall., for a vortex ring travelling towards the observer. All rotations in the xy-plane are defined as though

viewed on a ring travelling towards the observer, and all rings propagate in the positive z-direction. Positive angles and rotations are defined in the anti-clockwise direction. In this chapter, the term "near-wall core" is used to describe the ring region contained within the range $-45° \leq \theta \leq 45°$. Figure 5-1 provides an overview of these definitions. In addition, the parameter z_c is introduced, which refers to the position of the vorticity centroid of the ring in the z-direction.

Table 5-1 – Parameters used to defined each case. This notation is used in place of referring to an aspect ratio and wall separation repeatedly in the chapter.

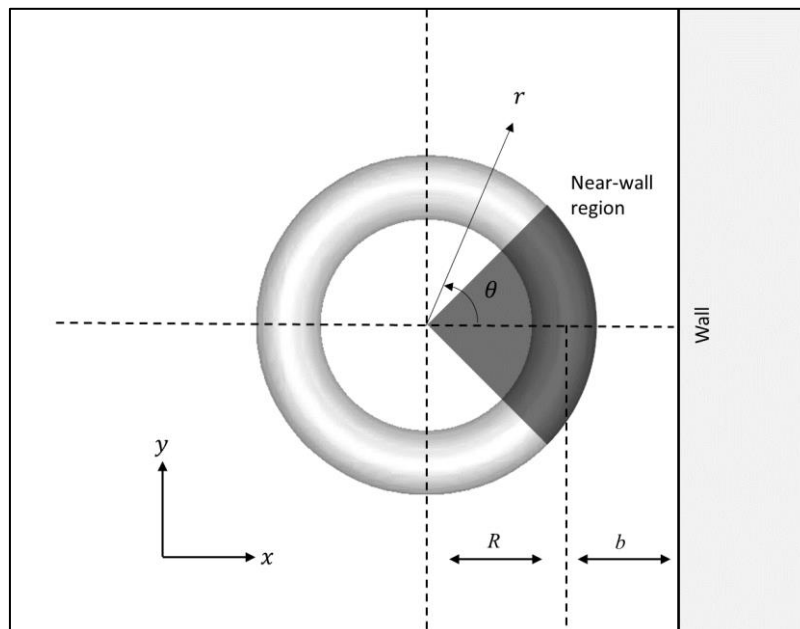|	$\Lambda_i = 0.26$	$\Lambda_i = 0.33$	$\Lambda_i = 0.37$
$b_i = 2.0$	Ring 1A	Ring 2A	Ring 3A
$b_i = 2.5$	Ring 1B	Ring 2B	Ring 3B
$b_i = 3.0$	Ring 1C	Ring 2C	Ring 3C

Figure 5-1 – Schematic of the definition of the azimuthal direction, θ, in the 3D Cartesian domain of the near-wall vortex ring. The z-direction is positive in the out-of-page direction. The near-wall region of the vortex ring (shown as the shaded region in the figure) is defined as $-45° \leq \theta \leq 45°$.

In addition to the correction to the flow field introduced in Section 2.2.4.2, the vortex ring must also adjust to the presence of the wall. The impact of this process is shown in Figure 5-2, which presents the average velocity in the wall-normal direction in a plane located at $x = -0.1$. The modified Gaussian profile of the core flattens on the wall side over time, reducing the average velocity in the x-direction in the vicinity of the ring. The inviscid effect of the wall minimizes the x-velocity near the wall boundary, rapidly altering the local profile of the near-wall vorticity, and inducing lower velocity in the x-direction in this plane. The equilibration from the value at initialization can be seen to occur over approximately the first 4 dimensionless time units, and no more than the first 6 time units, for all simulations in the parameter space. A number of studies have shown that confinement of a vortex ring during formation does not greatly alter the eventual behavior of the ring (Stewart and Vlachos, 2012, Stewart *et al.*, 2012, Danaila *et al.*, 2015). Therefore, the need for equilibration from a non-confined ring in this case should not drastically alter the subsequent evolution.
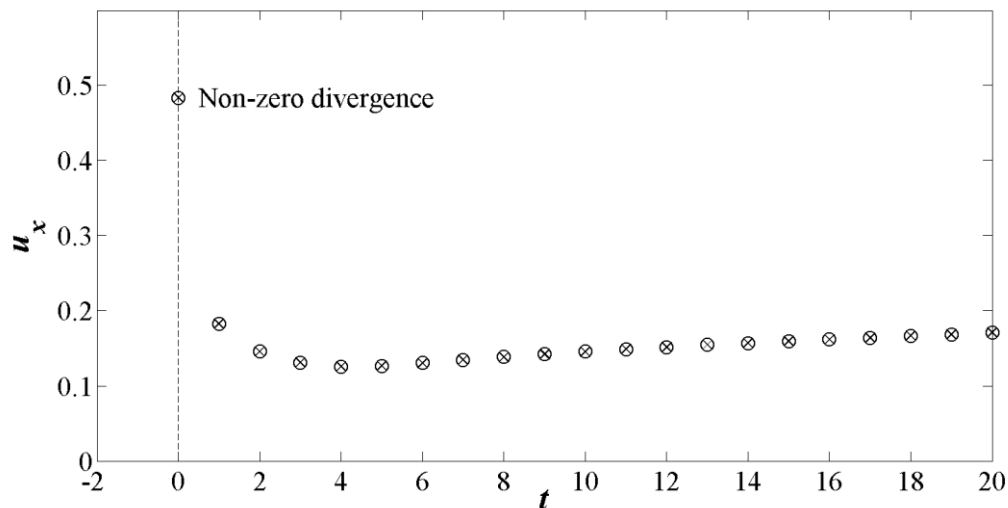

Figure 5-2 - Plot of the average positive u_x, over a 20×20 plane located at $x = -0.1$, for Ring 1A. The change in this value from the initial axisymmetric state to the near-wall state can be seen occurring over the first few time steps.

5.2 Results

5.2.1. Overview of evolution

The general evolution of the vortex ring is explored through a qualitative discussion in this section to provide a basic understanding of the processes involved. The evolution is investigated in more detail in the following sections. The early evolution of the vortex ring is dominated by inviscid effects. The presence of the wall slows the forward motion of the vortex ring, an effect that is inversely proportional to distance from the wall. This results in a continuous variation in the translational velocity across the ring, with the near-wall core travelling the slowest. The variation in this translational velocity as a function of θ in the near-wall section of ring bends the vortex core downstream (negative z-direction, see frames A-C in Figure 5-3). This bending interacts with the ring circulation, instigating the development of two localized swirling flows within the vortex core in the xy-plane, through localised precession of the vortex core (see the coloured contours in frames C and D of Figure 5-3). The rotation is clockwise (as viewed on an approaching ring) for $\theta < 0^\circ$, and anti-clockwise for $\theta > 0^\circ$. This process moves fluid away from $\theta = 0^\circ$ for $r > R$, and towards $\theta = 0^\circ$ for $r < R$.
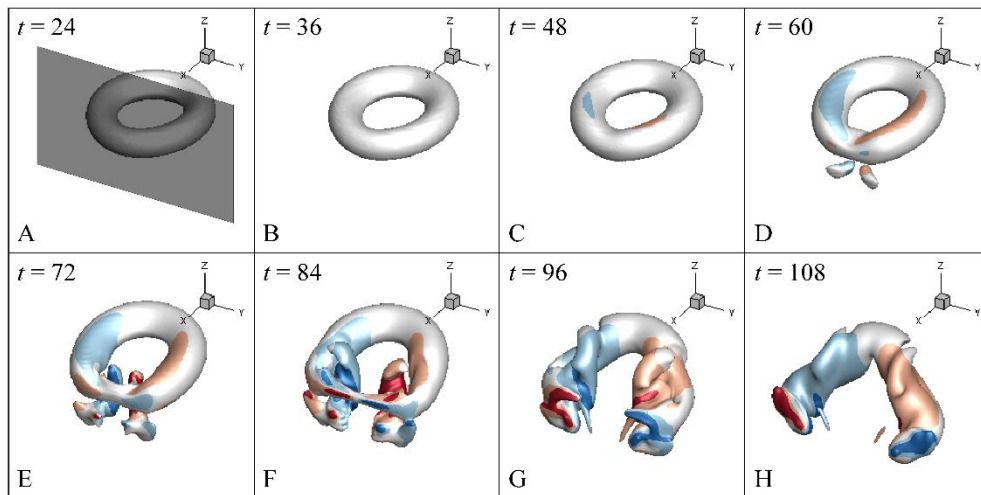

Figure 5-3 – Ring 1C - Demonstration of the overall variation in the ring shape over the course of the near-wall evolution. Contours of z-vorticity [-3,-1,1,3] are overlaid on a $\lambda_2 = $ -1 iso-contour. Red represents clockwise rotation (viewed from the top down), blue represents clockwise rotation. The shaded region in the first frame shows a section of the wall for reference.

Two counter-rotating z-vortices are ejected from these localised swirling regions and move towards the center of the ring, one from each side of the $y = 0$ axis. This occurs through a similar mechanism to that discussed in Chapter 3 (for vortex rings with a constant magnitude of swirl throughout the ring). Over a similar timeframe to the onset of the isolated swirl, perturbations develop in the core-normal vorticity (previously the azimuthal vorticity before the bending occurred). These perturbations are induced by a different instability mechanism to the Kelvin-mode coupling instability discussed in Chapter 4. In addition to bending the vortex ring, the inviscid influence of the bounding wall tilts the propagation vector of the ring towards the wall, reducing its momentum in the z-direction and moving the ring closer to the wall.

A boundary layer region along the surface of the wall develops due to the presence of the ring. The circulation of the ring induces an adverse pressure gradient in a localised region of this boundary layer, downstream of the vortex ring, drawing the boundary layer vorticity away from the wall and into the ring center. This is visible in the λ_2 field as twin vortex arms reaching out from the wall (see frames D, E, and F of Figure 5-3), however it is actually single structure of fluid with significant y-vorticity (at least initially). The velocity field of the vortex ring pulls this vorticity into the center of the vortex ring, where it interacts with the two counter-rotating vortices ejected by the vortex core, forming one coherent structure joining the boundary layer and the vortex ring. The kinetic energy of the near-wall core region dissipates over time, as it works to develop the boundary layer and draw in boundary layer fluid (see frame G of Figure 5-3). Once this occurs, a horseshoe shaped vortex structure remains (see frame H of Figure 5-3). The two ends of the horseshoe act as low pressure supply lines to continue transporting fluid away from the wall. Eventually, all resemblance to the original torus shape is lost, leaving behind an arrangement of vortex tubes within the boundary layer of the domain. All rings investigated in this study follow a similar evolutionary process.

5.2.2. Inviscid interaction

The wall separation and Reynolds number chosen here allow the early stages of the evolution to progress with minimal interference from viscous effects. As an example, Figure 5-4 shows both the advection (top row) and viscous (bottom row) terms of the y-component of the Navier-Stokes equations, in the $y = 0$ plane, for Ring 1C. This ring, as the thinnest and furthest from the wall, is used as the base case against which the other rings are compared. The near-wall vortex core moves towards the wall over time, as indicated on the figure by the position of the core center in the $\theta = 0^{\circ}$ plane. The viscous terms are only significant in strength within the boundary layer, so have little influence on the vortex ring in these early stages.

The presence of the wall at $x = 0$ enforces a condition of zero velocity on this plane. The inviscid dynamics of the vortex ring (i.e. assuming a free-slip wall) can be modelled by a mirrored vortex ring, placed an equal distance behind the wall. Figure 5-5 shows the positioning of such a mirrored ring, in relation to the real ring and the position of the wall. To simplify the explanation further, a Biot-Savart approximation (Equation 1-34) is applied, assuming a pair of vortex lines parallel to a non-slip boundary. The influence of the velocity due to the nearest mirrored vortex is shown in the lower part of Figure 5-5, however the furthest mirrored vortex will also provide a small inverse influence.

Although this method is a gross simplification of the true geometry, it is sufficient to explain the behavior of the system. Specifically, it reveals that the velocity induced is non-linear with distance, resulting in the bending of the vortex ring, particularly in the near-wall region. The bend in the ring at $t = 8$ for Ring 1C is shown in Figure 5-6a. The displacement of the $\theta = 0^{\circ}$ position in the z-direction (compared to the $\theta = 180^{\circ}$ position) at $t = 8$ is around $0.2a_i$, but grows to $0.9a_i$ by $t = 32$, as shown in Figure 5-6b. The discrepancy in the z-position between the near- and far-wall vortex ring regions also tilts the propagation direction of the ring towards the wall. This is discussed further in Section 5.2.5.
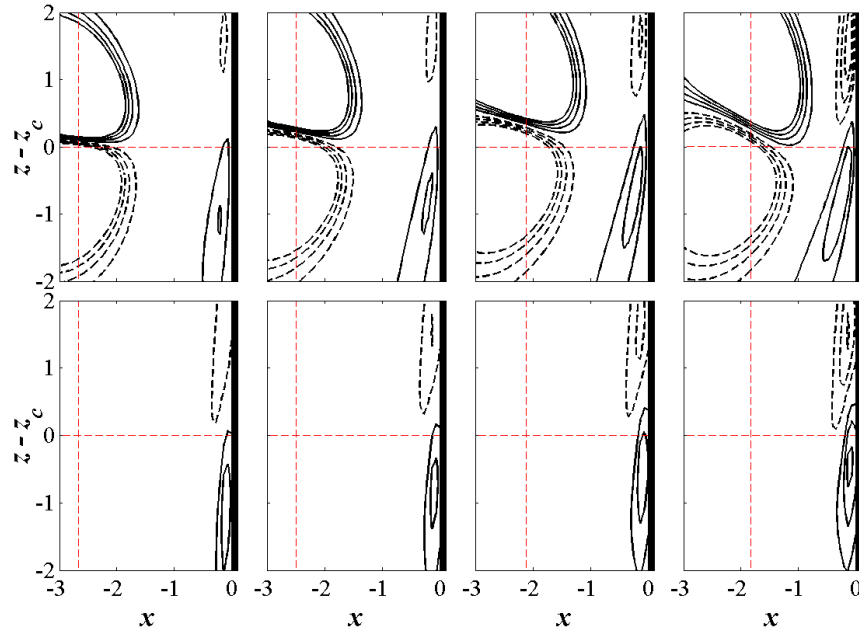
116

Figure 5-4 - Comparison of the *y*-component of advective (top row) and diffusive (bottom row) terms of the Helmholtz vorticity equations, at four different times for Ring 1C. Contours are [-0.020 -0.015 -0.010 -0.005 0.005 0.010 0.015 0.020]. Dashed black lines indicated negative contours. The wall is located at $x = 0$, and is indicated in the figure by the solid black region. The centre of the near-wall core in both the *x*- and *z*-directions is indicated by the red dotted lines.
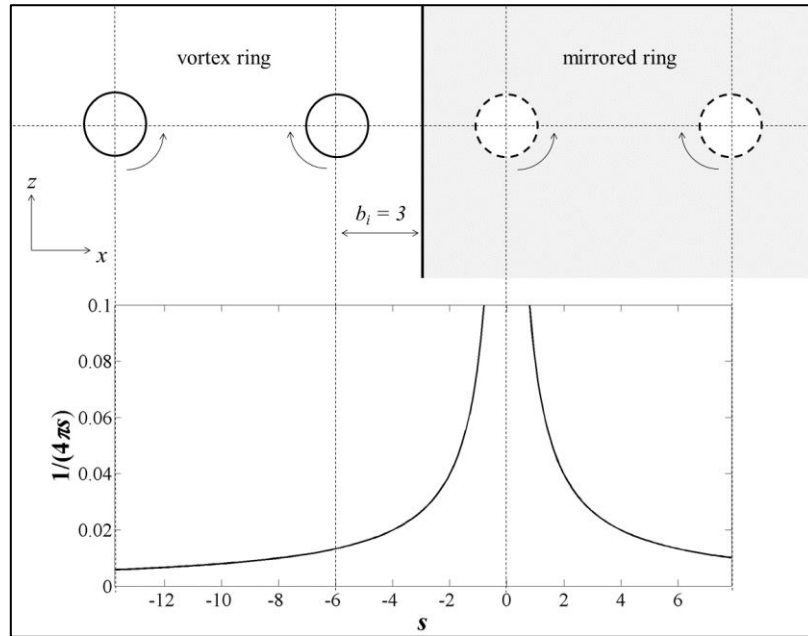

Figure 5-5 – Schematic showing the vortex ring and wall, including a mirrored vortex ring behind the wall, for Ring 1C. This mirrored ring provides identical inviscid dynamics to those of the wall, allowing the early evolution to be described in terms of the effect of this second ring. The Biot-Savart model is obtained using a 2D analogue of the system; *i.e.* each of the displayed cores are 2D, with no 3D ring geometry. The velocity variation induced due to the wall approximates the shown curve, noting that *s* is measured from the centre of the near-wall mirrored core.
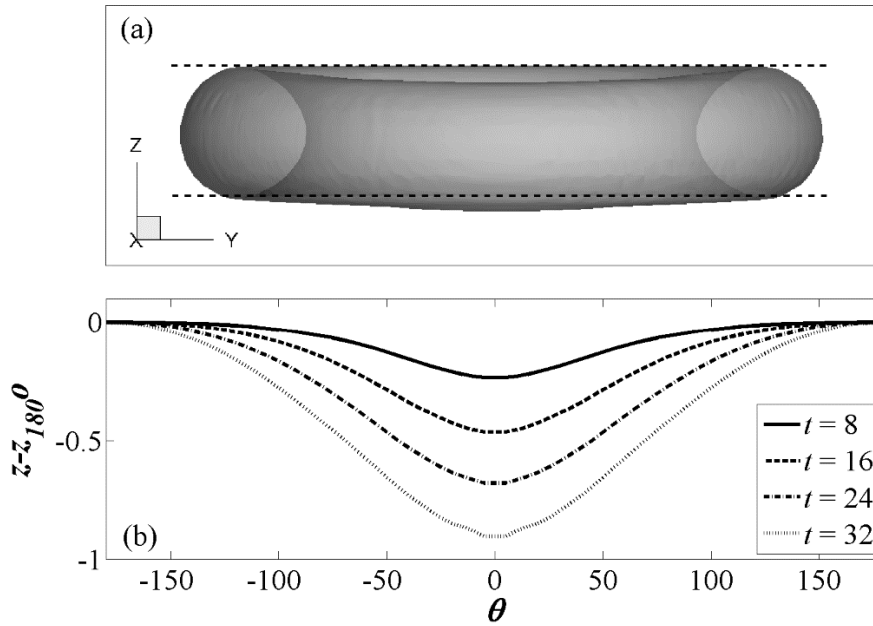
Figure 5-6 – (a) Graphical representation of the localised bending at $t = 8$ for Ring 1C, using an iso-contour of the λ_2 field. The image has been taken normal to the wall plane (such that the vortex ring is being viewed through the wall). The dotted lines represent the upper and lower bounds of the unbent vortex ring. (b) The displacement of the core centroid in the z-direction as a function of azimuthal position, compared to the position of the ring centre at $\theta = 180°$, for four different times for Ring 1C. The solid line corresponds to the instant shown in (a).

5.2.3. Localised regions of swirl

The bending of the vortex ring is accompanied by the development of twin isolated regions of z-vorticity (described here as swirling velocity), positioned within the vortex core, either side of the y-axis (see frames C and D of Figure 5-4). The development of the swirling flow field has several potential explanations, and it is useful to compare these to identify their relative influence. Viscous dissipation can be ruled out as having a significant impact; the development of the rotating velocity field occurs on a much faster timescale. A high pressure region driving fluid into the core of the vortex ring could also induce a swirling velocity component into the xy-plane. However, at the early times at which the swirling velocity is first observed, the pressure differential along the wall (shown in Figure 5-7a) is not sufficient to significantly contribute the observed swirling flow.

118

The bulk motion of the vortex ring in the wall-normal direction displaces existing fluid in the region (satisfying continuity in the local control volume), ejecting fluid away from the wall and around the vortex ring. This process is likely to have some influence on the observed flow phenomena, however observations of the flow field suggest that a different process has a greater influence on the development of the z-vorticity. The localised bending of the vortex core may also induce swirl.

Figure 5-7b provides the velocity vectors tangent to an xy-plane passing through the center of the vortex core at $\theta = 45°$, which is near the peak gradient of the bend. The rotation appears to be centered on the bent region of the ring, suggesting that the development of this velocity is directly related to the bending process. Figure 5-8a shows the initial vortex ring rotation in the $y = 0$ plane (positive ω_y). The bending induced by the presence of the wall can be viewed as being caused by a pair of opposite forces that are offset, causing torques in the x-direction acting to push the near-wall core downwards, as shown in Figure 5-8b. The rotation on the left is negative ω_x, while the rotation on the right is positive ω_x.
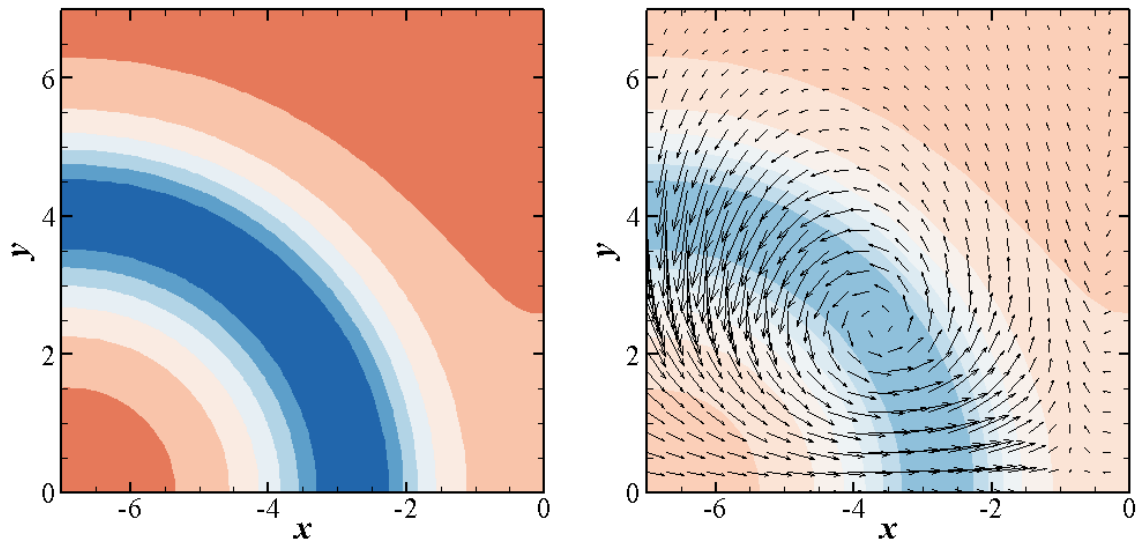

Figure 5-7 – An xy-plane through the centre of the core (as measured at $\theta = 45°$) of Ring 1C, showing (a) pressure contours, where blue represents low pressure, red represents high pressure, and (b) velocity vectors induced tangent to this plane, overlaid on the pressure contours from (a), which have been faded slightly to aid visibility.
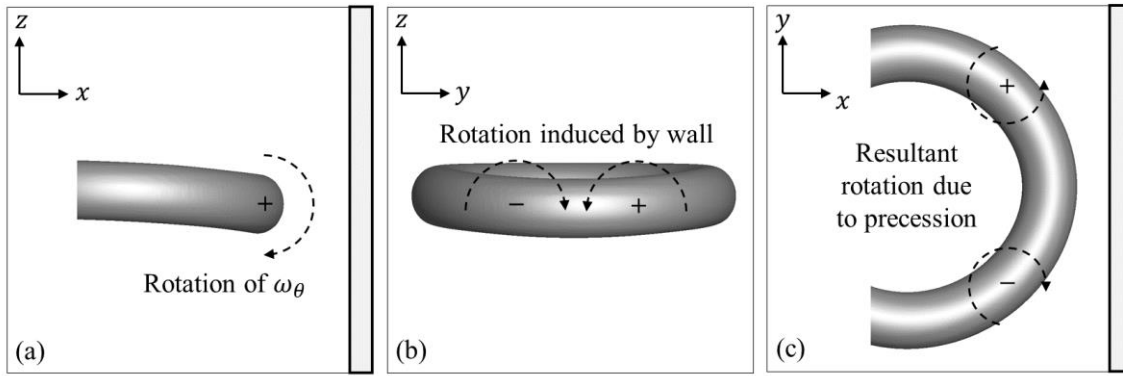
Figure 5-8 – Relationship between the three torque directions. (a) The azimuthal vorticity of the vortex core is modified by (b) the bending due to the wall, resulting in the development of (c) twin localised swirling velocity fields through precession. All vectors are drawn in the plane of their respective images.

The interaction between these vortex components can be considered in terms of the governing equations. The z-component of the inviscid Helmholtz vorticity equation governs the rate of change of ω_z, which is responsible for the swirling velocity in the xy-plane. The equation is given by

$$\frac{D\omega_z}{Dt} = -\left(\omega_x \frac{\partial u_z}{\partial x} + \omega_y \frac{\partial u_z}{\partial y} + \omega_z \frac{\partial u_z}{\partial z}\right).$$ 5-1

The sign of each of the terms in the equation is given in Table 5-2, and explained in detail here. The sign of ω_x can be seen in Figure 5-8b; it is negative for $y < 0$, and positive for $y > 0$. The sign of ω_x, which can be approximated by ω_θ in the near wall region, can be seen in Figure 5-8a; it is positive over the entire near-wall region.

For the velocity derivatives, consider a ring in a cylindrical co-ordinate system, propagating in the positive z-direction. With this arrangement, u_z is positive on the interior of the ring ($r < R$) and negative on the exterior of the ring ($r > R$). An observer moving from the inside of the core ($r = R$-a) to the outside of the core ($r = R$+a) will see a monotonic decrease in u_z. Returning to Cartesian co-ordinates, moving from the inside of the core in the positive x-direction (*i.e.* towards the wall) will result in a negative value for $\partial u_z/\partial x$. Likewise, moving from the inside of the core in the

positive y-direction will result in a negative value for $\partial u_z/\partial y$, and the negative y-direction will result in a positive value for $\partial u_z/\partial y$.

Therefore, for $y < 0$, the first two products (referring to $\omega_x \, \partial u_z/\partial x$ and $\omega_y \, \partial u_z/\partial y$) are positive, contributing to the development of negative ω_z (due to the negative sign). Likewise, for $y > 0$, the first two produces are negative, contributing to the development of positive ω_z. The rotation induced due to these terms is shown in Figure 5-8c. It is analogous to precession observed in solid body dynamics, induced by the reorientation of the axis of a spinning object.

The third product term in Equation 5-1 ($\omega_z \, \partial u_z/\partial z$) breaks the symmetry of the developed swirl within the cross-section of the vortex core. To aid in the visualization of its effect, Figure 5-9 provides line contours of u_z overlaid on coloured contours of developed ω_z, for Ring IC at $t = 8$, for a cross-section of the core. Viewing the slice in the positive θ-direction, the $\partial u_z/\partial y$ increases the ω_z field in the upper left ($r < R$, $z > z_c$) and lower right ($r > R$, $z < z_c$) corners, and opposes it in the other two corners. The developed swirling velocity is strongest at the points with the most significant bending, at around $\theta \pm 45^\circ$.

Table 5-2 – The sign (positive or negative) of each of the terms in Equation 5-1.

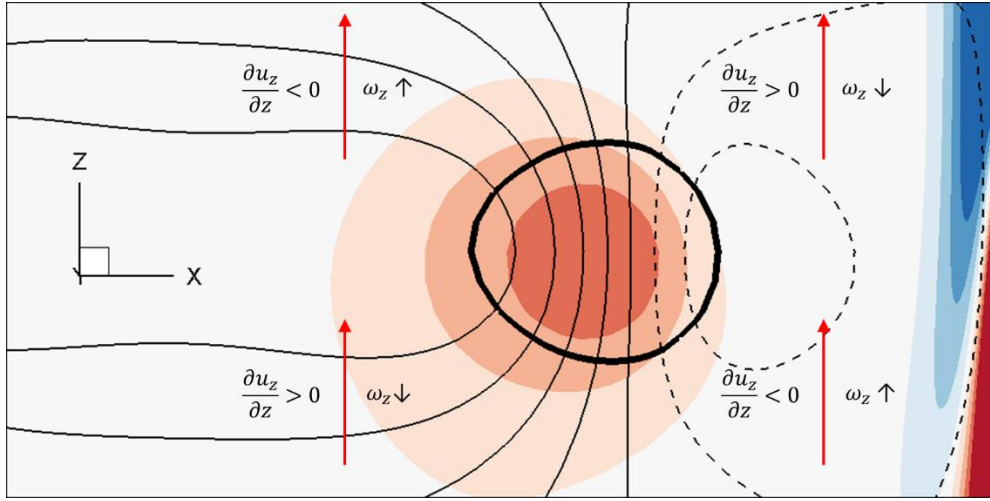|	$y < 0$	$y > 0$		Region	$\partial u_z/\partial z$
ω_x	–	+		$z < z_c, r < R$	+
$\partial u_z/\partial x$	–	–		$z < z_c, r > R$	–
ω_y	+	+		$z > z_c, r < R$	–
$\partial u_z/\partial y$	+	–		$z > z_c, r > R$	+
ω_z	–	+			

Figure 5-9 – The sign of $\partial u_z/\partial z$ around the vortex core, and the resultant increase or decrease in ω_z, for Ring 1C at $t = 8$, in a plane located at $y = 2$. The velocity component u_z is given by the thin contour lines of [-0.2, -0.1, 0.2, 0.4, 0.6, 0.8]. Dashed lines indicated negative contours. The vortex core is represented by the thick line, which is a contour of $\lambda_2 = -10$. The coloured contours show ω_z, with contour levels of [-0.06, -0.04, -0.02, 0.02, 0.04, 0.06]. Blue indicates negative contours.

Evidence of this effect, and the developing swirl, is provided in Figure 5-10. Here, slices have been taken at 3 different angles of θ, and tilted such that they are perpendicular to the local vortex rotation, using the process described in Section 2.3.3.2. Each row contains a different angle (10°, 25°, 45°, and 135°), while the columns contain different time steps. The velocity in each slice agrees with the schematic provided in Figure 5-8c and the flow vectors in Figure 5-7b, with velocity moving towards the wall on the interior of the ring (negative θ-direction) and away from the wall on the outside of the ring. The rotation of the centerline of the swirl field away from the vertical (due to the $\omega_z\,\partial u_z/\partial z$ term in Equation 5-1) is visible in these slices, and is most notable in the $t = 24$ contours at $\theta = 25°$ and $\theta = 45°$. Figure 5-10 also reveals that the induced velocity is stronger at 45°, near the peak gradient in the ring bend, than it is at 25°. A swirling velocity component can be seen forming at 135° at $t = 24$ (the appearance of the dark blue contours), as the bending reaches to this angle by this time (see Figure 5-6), although the magnitude is much lower than near the wall. No azimuthal velocity is observed along the centerline of the ring (at 0° and 180°), as bending does not occur at these locations. Note that the general blue background of the contour fields is due to the bulk motion of the ring.
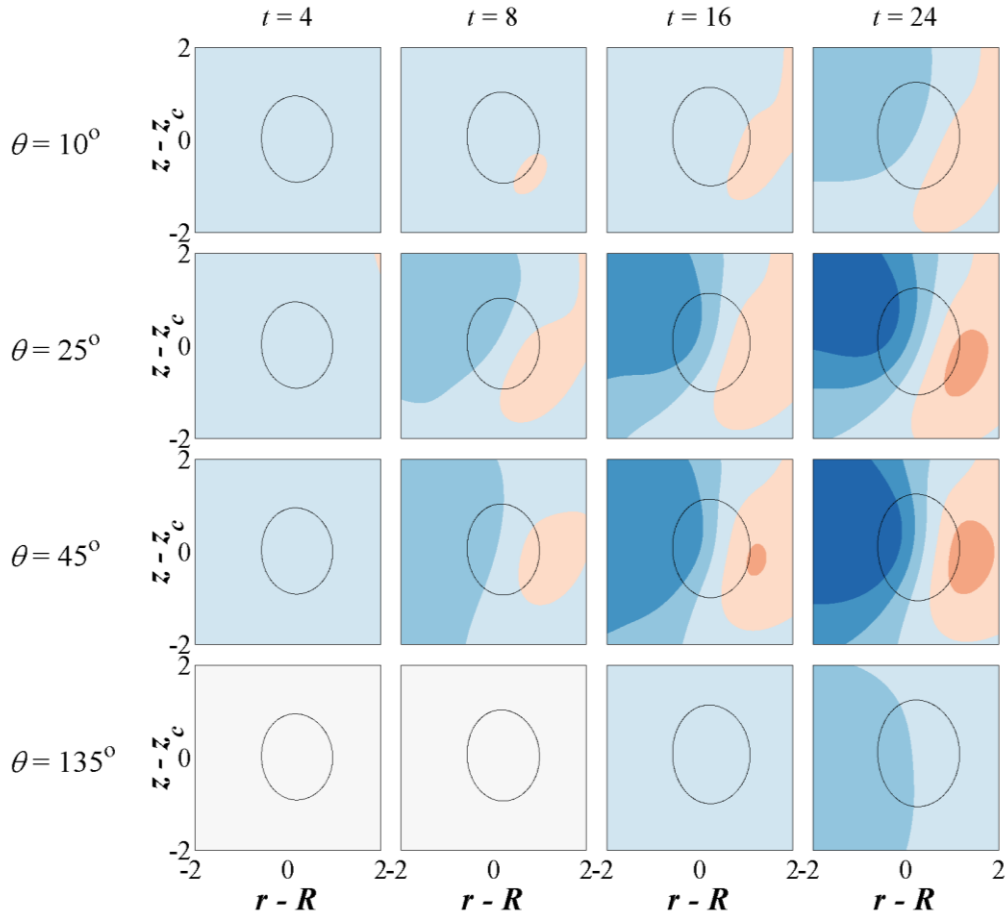
Figure 5-10 – Contours of the swirling velocity, overlaid with a contour of ω_θ that passes through $z\text{-}z_c = a$, for Ring 1C. Each row presents a different angle ($\theta = 10°$, $25°$, $45°$, $135°$). Red contours indicate azimuthal velocity in the positive θ-direction, blue contours indicate azimuthal velocity in the negative θ-direction. Contours are $u_\theta = [-0.09, -0.05, -0.01, 0.01, 0.05, 0.09]$.

The swirling flow does not remain isolated to the vortex core, as some of this fluid is shed towards the center of the vortex ring. This process occurs via the same mechanism as discussed in Chapter 3, whereby the swirling fluid is forced inwards from the core due to the rotation of the vortex core. However, unlike in Chapter 3 where the uniform swirl forms a single axial vortex along the z-axis, here two axial vortices form, rotating in opposite directions, due to the reflective wall-normal symmetry of the physics. Figure 5-11a shows contours of z-vorticity in the xy-plane, for $t = 8$, $t = 16$, and $t = 24$, for Ring 1C. The early time (black contours) shows that z-vorticity is confined to the bending region, however over time, a region of this fluid moves towards the axis (blue contours, red contours). Figure 5-11b presents the λ_2 field, showing the twin axial vortices in the center of the ring, for Ring 3C at $t = 60$.
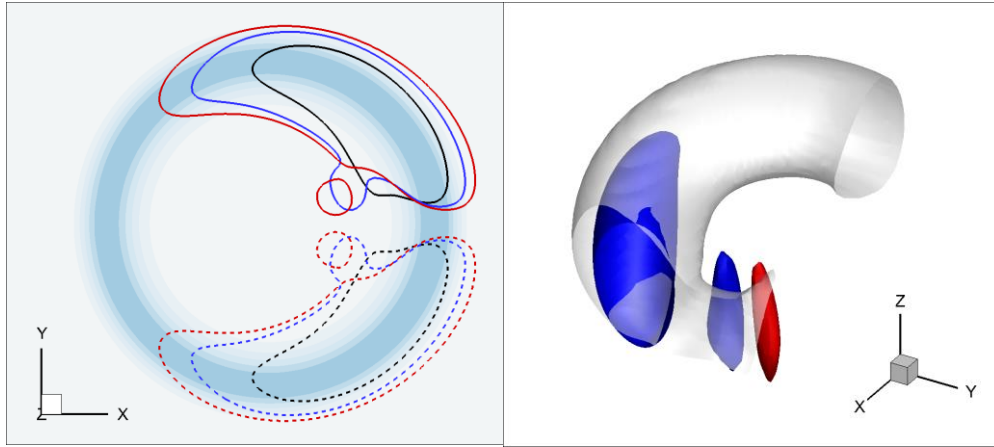
Figure 5-11 – (a) The z-vorticity field in an xy-plane at $z = z_c$, for Ring 1C for $t = 8$ (black), $t = 16$ (blue), $t = 24$ (red). The twin axial vortices can be seen moving toward the centre of the ring. Contour levels are [-0.025 0.025]. Background shows ring position through the λ_2 field. (b) Representation of the twin axial vortices developing in the centre of the ring, at $t = 60$ for Ring 3C. The ring has been cut at $x = -1.0$ and $y = 0.75$ to show the vortices. Blue indicates clockwise rotation in the top-down xy-plane, red indicates anti-clockwise.

5.2.4. Stability characteristics

The growth of resonant Kelvin mode pairs is a key instability mechanism for isolated vortex rings. In order to test for similar instabilities for the near-wall vortex rings, perturbations in the azimuthal vorticity field are analyzed. The azimuthal vorticity is averaged on 72 evenly spaced planes for the vortex ring, and subtracted from each plane to give the perturbation fields. Figure 5-12 provides examples of these fields for Ring 1C, for 0º, 25º, 45º, and 135º.

The vorticity perturbations vary in magnitude with azimuthal position, reaching a maximum of around 5% of the peak azimuthal vorticity in the core at the 0º angle. The shape of the vorticity perturbation at 0º and 25º is similar to those identified for swirling vortex rings, and resemble the [0 , -2] resonant Kelvin mode pair (see Section 4.2.1.1). This is despite zero swirl developing at the 0º angle. The perturbation fields at 45º are similar to those expected for non-swirling rings, that of the [-1 , +1] resonant Kelvin mode pair. This is despite of the fact that 45º has significant magnitude of swirl.
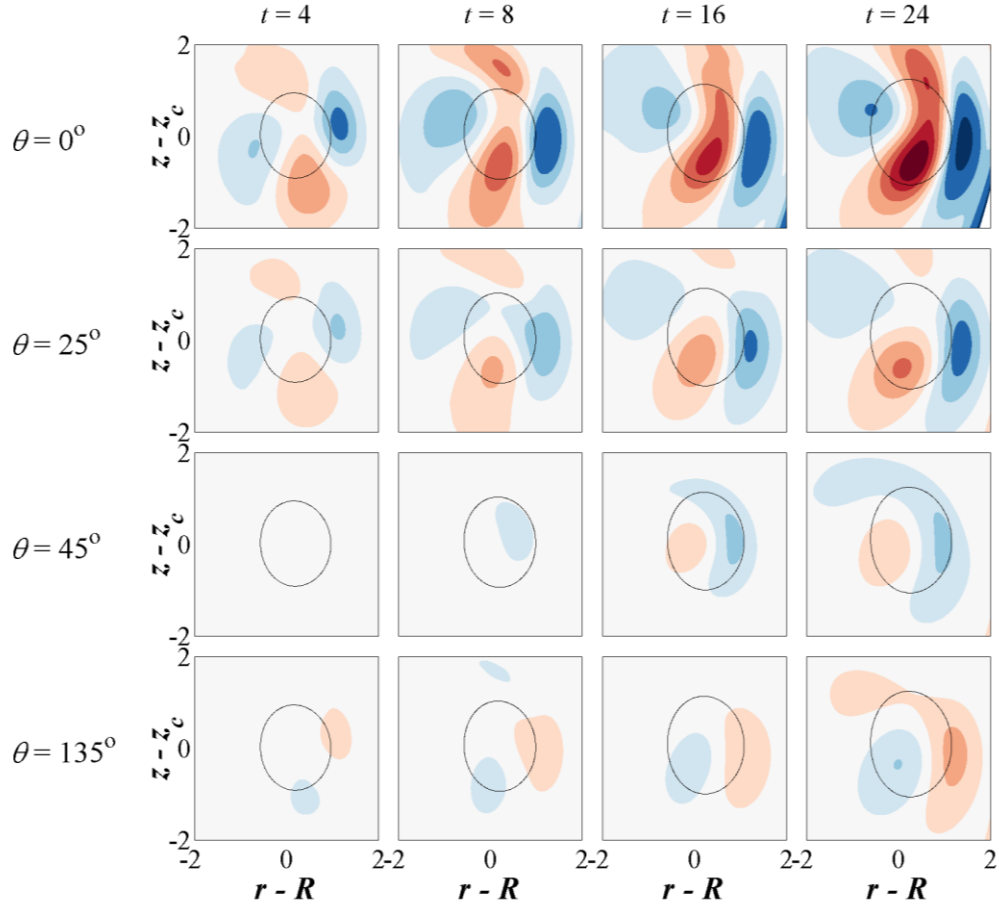
124

Figure 5-12 - Contours of azimuthal vorticity perturbation, overlaid with a measure of the edge of the core, for Ring 1C. Each row presents a different angle (θ = 0º, 25º, 45º, 135º). Red contours indicate an increase in azimuthal vorticity relative to the averaged plane, blue contours indicate a decrease. Contours are ω_θ = [-0.09 -0.07 -0.05 -0.03 -0.01 0.01 0.03 0.05 0.07 0.09].

The differences observed with these instabilities suggest that there is an entirely different instability mechanism at work, despite the vorticity variation in each slice having the appearance of a resonant Kelvin mode instability. Observing the 3D form of the vortex ring, as presented in Figure 5-13 for ring 1C at t = 15, reinforces this contention, as the visualization shows no similarity to the expected form of a resonant Kelvin mode instability. The wavenumber for the instability is around κ = 0.5, which is outside of the region of previously observed coupled Kelvin mode instabilities. The observed perturbations are therefore likely to be induced by a different instability mechanism, which is yet to be explored.
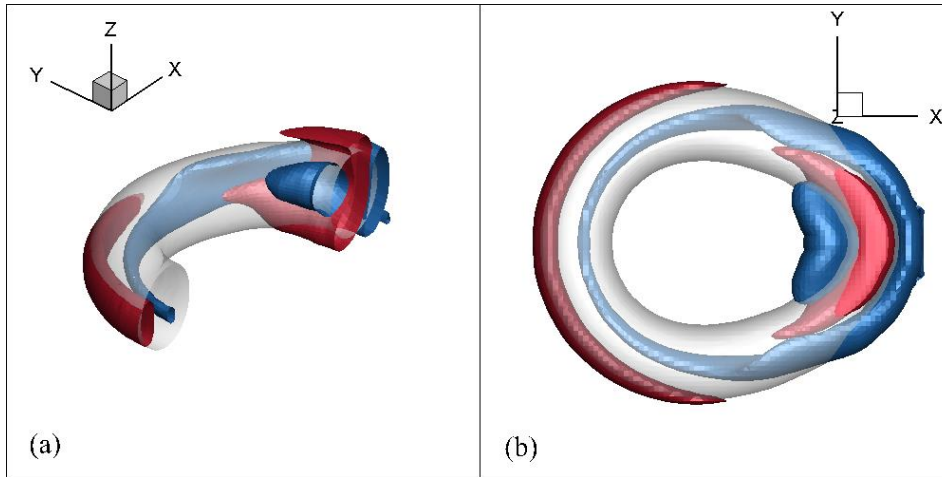
Figure 5-13 – Three-dimensional image of the vorticity perturbations of Ring 1C. (a) Isometric view (with $y < 0$ removed) with the wall is located in the upper right hand corner of the image (opposite of the previous isometric images). (b) Top down view, with the wall located at the right hand side of the image. Contours are $\omega_\theta = [-0.09\ 0.09]$.

5.2.5. Development of tilt angle

The difference between the z-positions of the near-wall and far-wall sides of the vortex ring continues to increase over time. The rate of increase of this tilt angle depends on the initial wall separation of the ring, as the tilting is directly related to wall proximity. Figure 5-14 presents the evolution of the tilt angle for the three different ring sizes (one frame for each), and the three different wall separations (identified by the different line styles). In this figure, the time axis has been normalized by the initial wall separation b_i, which brings the three different cases for each ring size into approximate alignment.

The success of this normalization method suggests that each ring follows a particular evolutionary path, and that increasing the initial wall separation delays the time at which the ring reaches a particular tilt angle. The separation distance is key to describing the tilt angle evolution, as the induced variation in the propagation velocity (simplified using the Biot-Savart law in Section 5.2.2) is a consistent phenomenon across all rings.
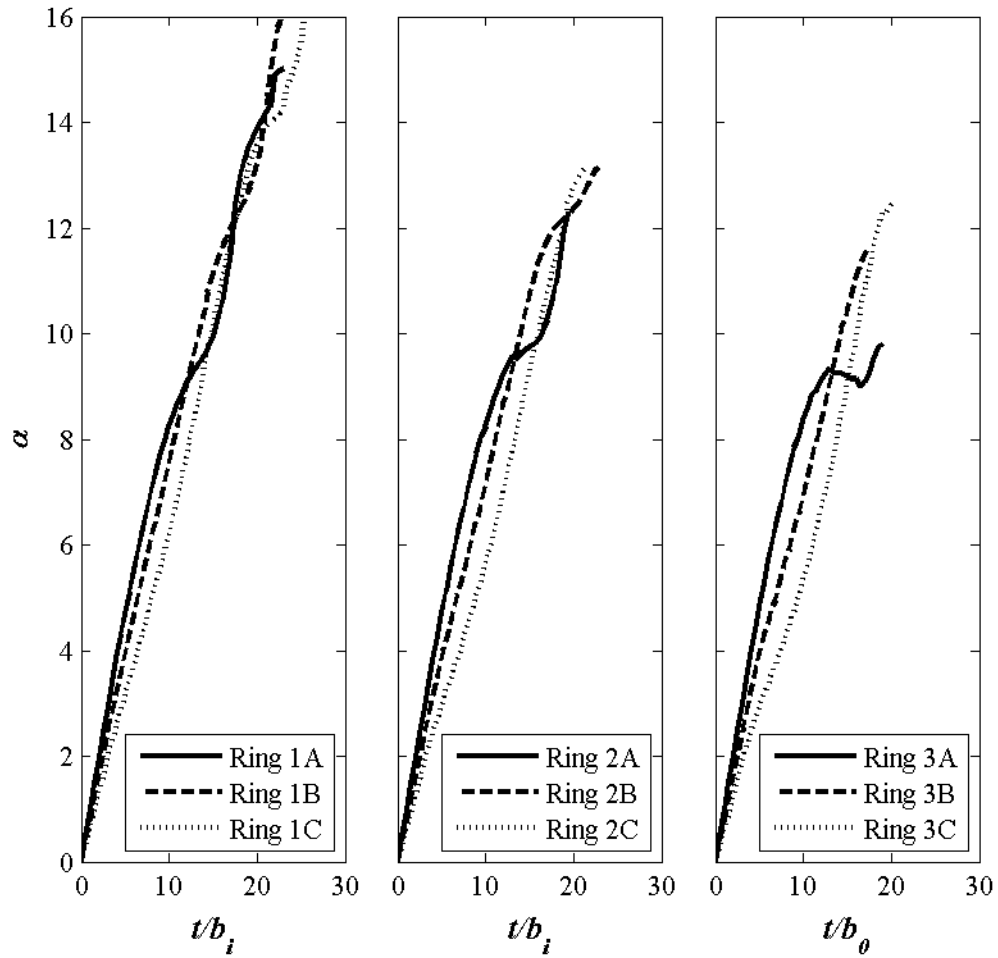
126

Figure 5-14 – Tilt angle as a function of time. The three frames represent the three different ring sizes ($\Lambda_i = 0.26$, $\Lambda_i = 0.33$, $\Lambda_i = 0.37$), each showing $b_i = 2.0$ (thick line), $b_i = 2.5$ (dashed line), and $b_i = 3.0$ (dotted line). The normalisation of the time axis using the initial wall separation has brought the different cases for each ring into alignment.

This normalization provides a convenient method of predicting the behavior of a particular ring. The peak magnitude of the tilt angle, measured at the time when the core near the wall has dissipated (as has occurred in Figure 5-3G), also varies, with the thinnest ring reaching a larger ultimate tilt angle than the two thicker rings. In all cases, a closer initial wall separation results in less tilt, potentially due to viscous effects in the near wall region.

The similarity in the evolution of different cases is also shown by Figure 5-15, which presents the relationship between two modified variables: the product of the tilt angle and the initial wall separation αb_i, against the ring centre separation

normalised by the initial ring centre separation c/c_i. The cases appear to all follow the same path on this plot, deviating only when the influence of the wall becomes significant. Each case branches off at a slightly different point, with Ring 1C remaining on the primary path for the majority of its evolution.
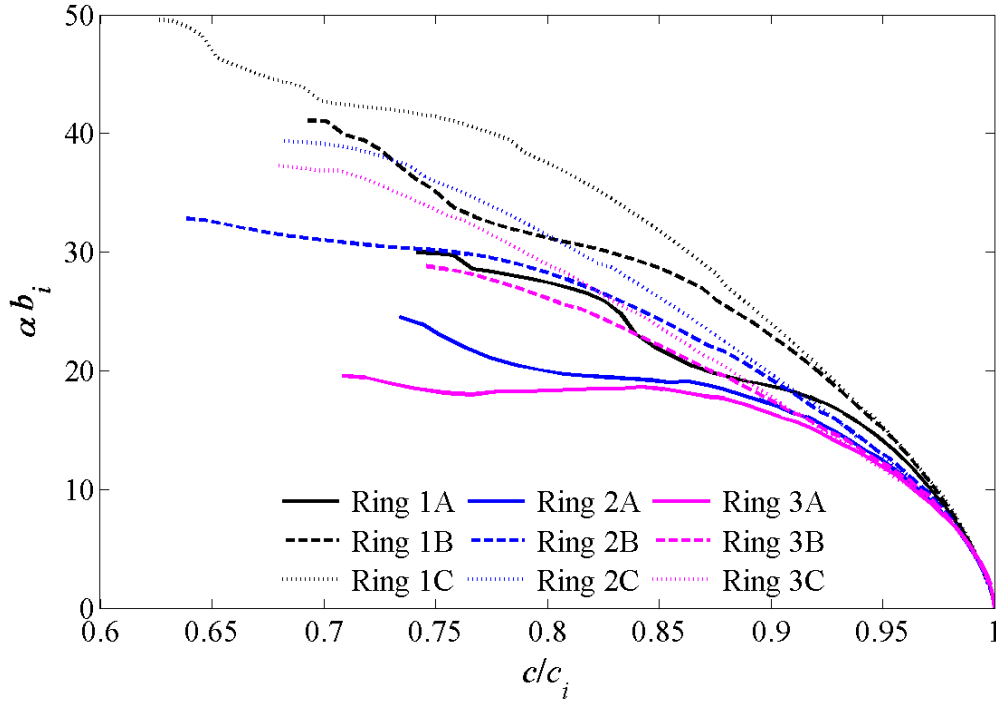

Figure 5-15 – The evolution of the tilt angle of the vortex rings, presented here multiplied by the initial wall separation of the near-wall core. The horizontal axis is a normalised position of the centre of the vortex ring, c, based on its initial position, c_i. The rings are differentiated by the line colour; Ring 1 (black), Ring 2 (blue), Ring 3 (magenta). The initial wall separations are differentiated by the line style; $b_i = 2.0$ (solid), $b_i = 2.5$ (dashed), $b_i = 3.0$ (dotted).

Figure 5-16 shows the variation over time of both the translational velocity and the bulk wall-normal velocity of the vortex ring, measured as the displacement of the ring center over time. As the evolution progresses, there is a steady decrease in the z-velocity (translational) over time, corresponding to a steady increase in the x-velocity (wall-normal). The change in the z-velocity is an order of magnitude larger than the change in the x-velocity, suggesting that a large proportion of the momentum is lost due to viscous effects. In addition, the decrease in the z-velocity for Ring 3B and Ring 3C is not linear, indicating that the thickness of these rings may be interfering with the tilting process.
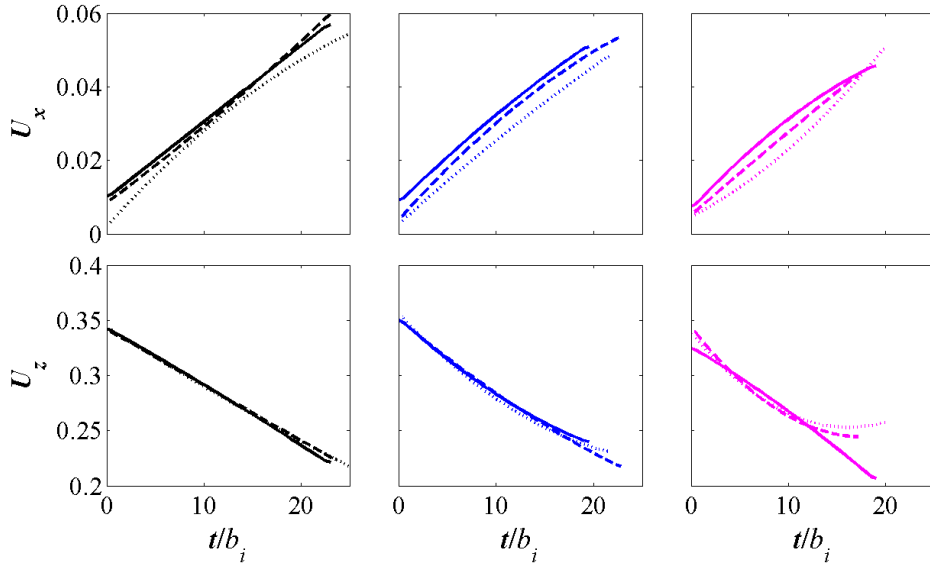
Figure 5-16 – The bulk velocity of the vortex ring in the *x*-direction (top row) and the *z*-direction (bottom row). The rings are differentiated by the line colour; Ring 1 (black), Ring 2 (blue), Ring 3 (magenta). The initial wall separations are differentiated by the line style; $b_i = 2.0$ (solid), $b_i = 2.5$ (dashed), $b_i = 3.0$ (dotted).

5.2.6. Boundary layer effects

During the early development of the vortex ring, the diffusive terms are negligible. The advection terms in Figure 5-4 show the mechanism responsible for slowing and drawing the ring towards the wall. The vorticity increases downstream of the ring, and towards the wall. The flow dynamics close to the wall are diffusion dominated for all of the times provided, but grow in strength at the same rate as the advection terms.

Analyzing the thickness of the boundary layer of the wall reveals the development of the expected boundary layer spire, and confirms the fact that increasing the initial wall separation only delays the evolution of the vortex rings. Here, as the free-stream velocity profile becomes exceedingly complex, the approximation of Equation 2-33 (Section 2.3.3.3) is used. A graphical representation of this relation is presented in the left hand column of Figure 5-17, for rings 1A, 2A, and 3A. The $z = 0$ position in each case is aligned with the center of the near-wall core of the vortex ring. Each of the shaded regions shown represents an approximation of the boundary layer profile for a different time step.
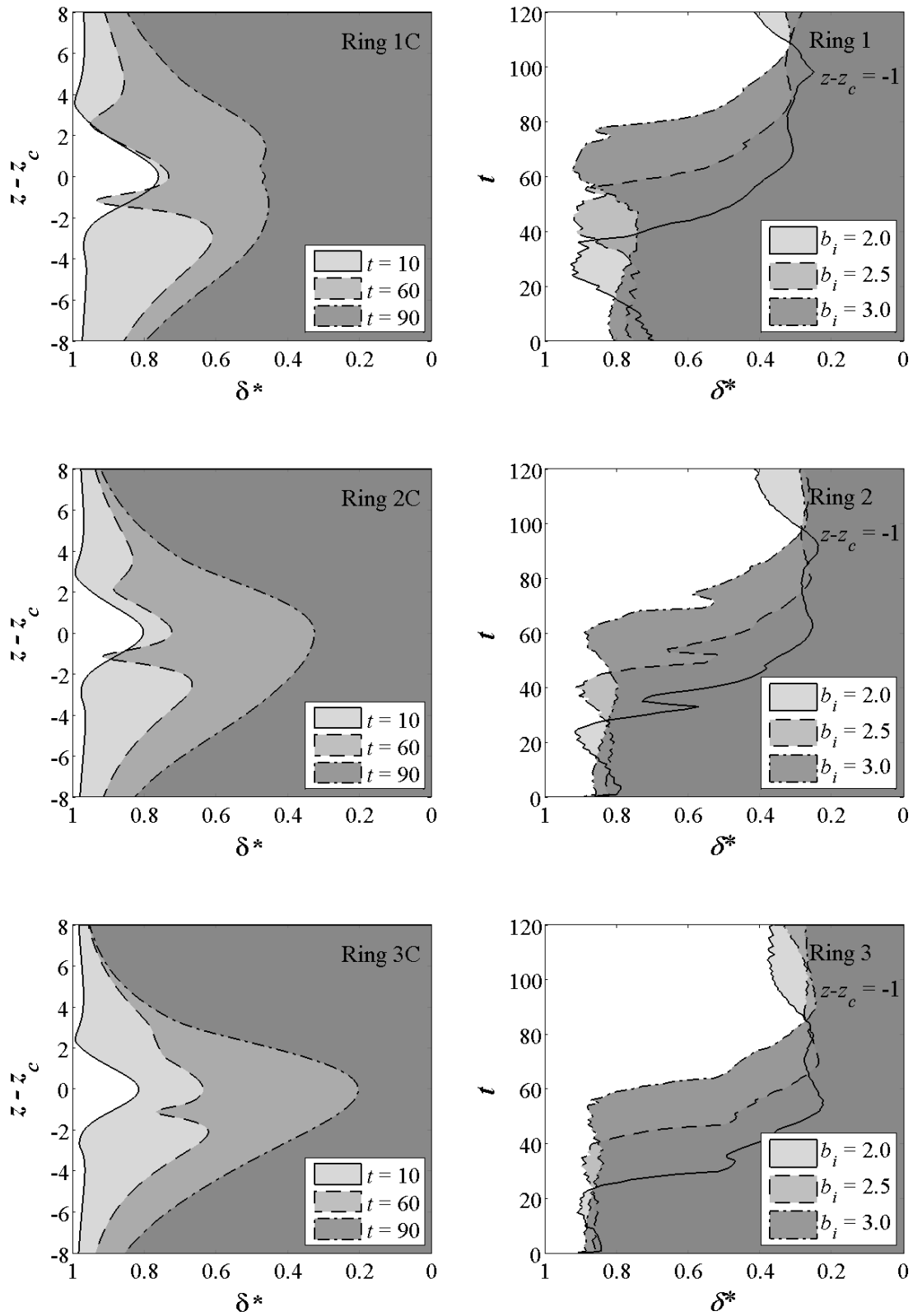
Figure 5-17 – Representation of the boundary layer (δ^*) for the three ring sizes. The left column gives δ^* as a function of z-position for a single wall separation, at 3 different times. The right column gives δ^* as a function of time at a single z-position, for 3 wall separations.

In the vicinity of the core, the motion of the ring in the wall direction decreases the boundary layer thickness over time, due to the increase in magnitude of the velocity field. This is with the exception of a small region downstream of the core, where a tongue of vorticity is drawn out from the wall. This is effectively the boundary layer spire that is observed for a near-wall vortex tube. The vorticity downstream of the vortex core (which would be considered to be upstream for an isolated vortex tube), extends outwards from the wall over time. This process is explored in more detail in Section 5.2.7.

The right hand column of Figure 5-17 follows the development of this approximation of the boundary layer thickness, at a consistent downstream point (a_i behind the vortex core). The three frames correspond to Rings 1, 2, and 3 (from top to bottom). Each shaded region represents a different initial wall separation (the closer wall separations peak earlier). It is clear that for a given ring size, varying the initial separation from the wall simply delays the wall interaction process, and does not have a dominant impact on the eventual development of the boundary layer-vortex ring hybrid structure.

5.2.7. Wall vorticity generation and vorticity twisting

The interaction between the vortex ring and the boundary layer induces the development of vorticity along the wall. An adverse pressure gradient develops on the wall, and vorticity from along the wall advects out into the center of the vortex ring. This vorticity moves as a coherent body of fluid, and the inherent symmetry of the vortex ring causes a reflective symmetry to occur about the $x = 0$ plane of the domain. This manifests as two separate vortices when viewed in terms of the λ_2 field; these reach out from the wall between $t = 60$ and $t = 72$ for Ring 1C (frames D and E in Figure 5-3). The boundary layer vorticity is initially orientated in the y-direction, however this vorticity twists into the z-direction, due to solid body rotation around the vortex core, as it moves into the center of the ring.

Figure 5-l8a shows the strongest region of *z*-vorticity (the red iso-contour within the vortex arm), in addition to the *x*- and *y*-vorticity contours in a slice at $x = $ -0.l, shown by the line and colour contours, respectively. The vorticity along the wall near the connection point of the vortex tongue contains both *x*- and *y*-vorticity, which is twisted into the *z*-direction as it enters the center of the core. This vorticity joins up with the two counter-rotating axial vortices described in Section 5.2.2. Figure 5-l8b shows the local velocity vectors after the vortex arms join up with the counter-rotating axial vortices (frame E in Figure 5-3). The axial vortices have the same rotation orientation as the swirling velocity within the core, however the separation of the two regions results in the flow stagnating at two points within their immediate vicinity.
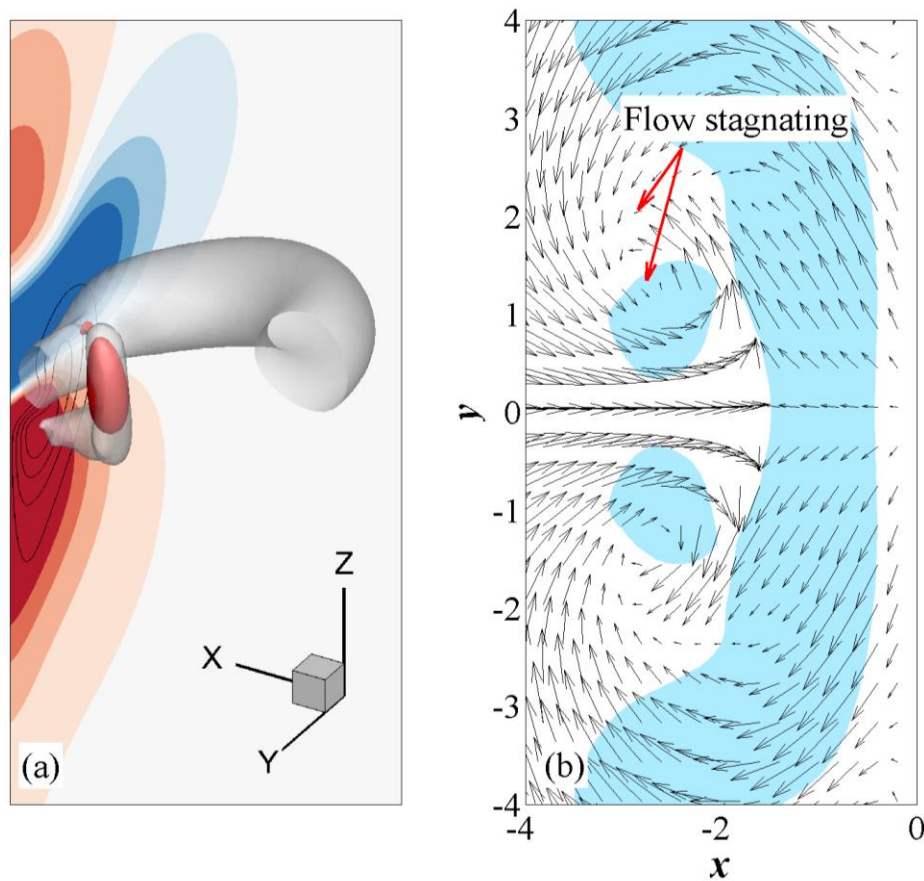
Figure 5-18 – (a) Iso-contour of $\lambda_2 = $ -1 (grey), with an iso-contour of *z*-vorticity (red), in proximity to a slice positioned at $x = $ -0.1, showing coloured contours of *y*-vorticity (red positive, blue negative, contour levels ±[0.05 0.15 0.25 0.35]), and line contours of *x*-vorticity (anti-clockwise rotation, contour levels [0.01 0.02 0.03 0.04]), for Ring 1C at $t = $ 72. (b) Velocity vectors in a plane through the centre of the near-wall core, for Ring 1C at $t = $ 72. A single contour of the λ_2 field ($\lambda_2 = $ -1) is provided to show the position of the vortex arms.

Thicker rings go through a similar experience, as shown for Ring 3C in Figure 5-20. Swirling velocity develops in the core, and moves out and into the center of the vortex ring (frame E in Figure 5-20). However, for this ring, the twin axial vortices that develop do not have the space to move far from the vortex core. They remain joined to the swirl within the core, as shown using z-vorticity iso-surfaces in Figure 5-19a. The boundary layer vorticity that develops at the wall develops at the wall (frame D in Figure 5-20) joins up with the counter-rotating axial vortices much closer to the vortex core (see frame E of Figure 5-20) than in the thin ring case. This simplifies the flow vectors in the plane (Figure 5-19b), as there is no interference between the different swirling regions.

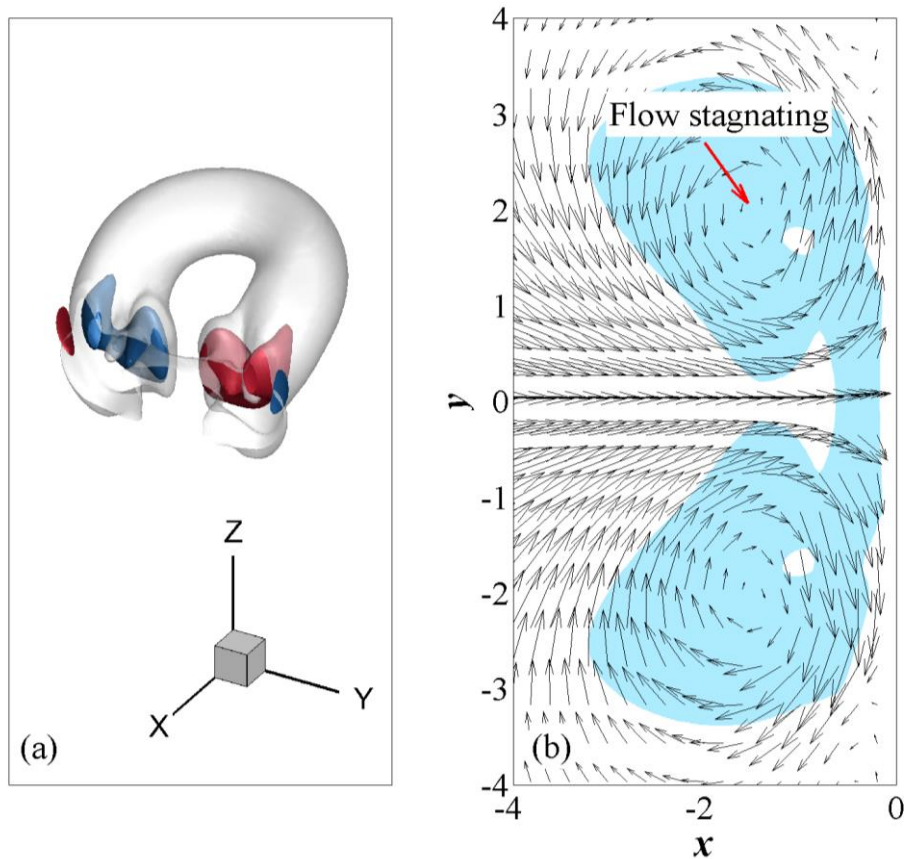Figure 5-19 - (a) Iso-contour of $\lambda_2 = -1$ (grey), with an iso-contour of z-vorticity (red positive, blue negative), qualitatively showing the developing swirl regions, for Ring 3C at $t = 72$. (b) Velocity vectors in a plane through the centre of the near-wall core, for Ring 3C at $t = 72$. A single contour of the λ_2 field ($\lambda_2 = -1$) is provided to show the position of the vortex arms.
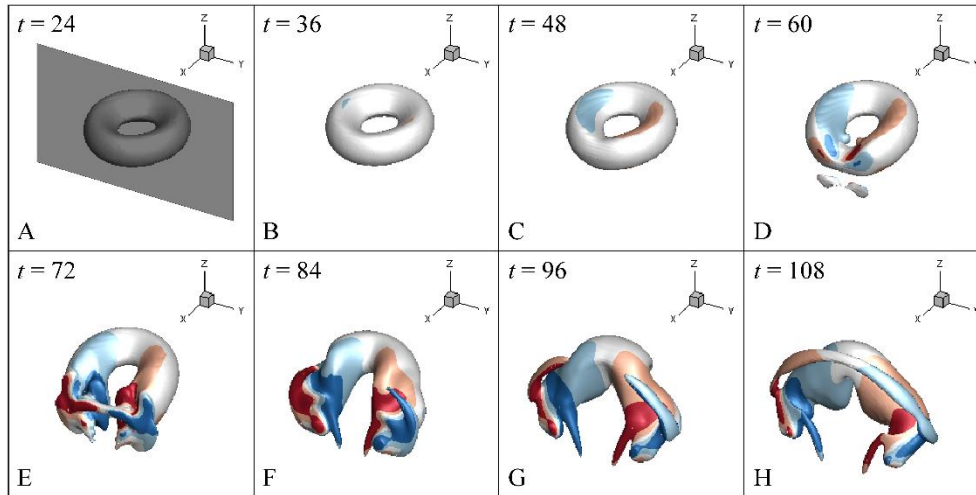
133

Figure 5-20 – Ring 3C - Demonstration of the variation in the ring shape over the course of the near-wall evolution. Contours of z-vorticity [-3,-1,1,3] are overlaid on an iso-contour of the λ_2 field (grey surface). Red represents clockwise rotation (viewed looking down the z-axis), blue represents clockwise rotation. The shaded region in the first frame shows a section of the wall for reference.

The energy required to generate, draw out, and twist the vortex arms from the boundary layer region is provided by the near-wall vortex core, which weakens in strength as the process progresses. Frame G in Figure 5-3 shows the end result of this loss of energy, as the vortex core in the near-wall region has dissipated. The dissipation occurs slightly earlier for the case of the thick ring, and the core is absent from Frame F in Figure 5-20.

For Ring 1C the twin vortex arms continue to move upwards through the ring center, before again moving away from the wall due to the influence of the swirling flow in the region. The swirling flow results in the vortex arms folding back, and aligning with the vortex ring core. This motion is visible when comparing frame F and frame G of Figure 5-3. This folding is driven by the swirling flow field, forcing the arms forward in the center of the ring, but backwards along the core. A similar process occurs for the thicker ring, but is less visible as the arms do not appear as isolated objects once they have entered the vortex core.

The flow fields at $t = 96$ for both Ring 1C and Ring 3C are provided in Figure 5-21. An iso-contour of the λ_2 field is shown in conjunction with a slice through each ring in the yz-plane. The plane contains colour contours of x-vorticity, and line contours of x-velocity. For Ring 1C (Figure 5-21a), the peaks of the arms are entering the region dominated by negative x-velocity (away from the wall), and so are dragged back along the vortex core. As they have the same rotation as the vortex core, the two structures eventually merge (frame H of Figure 5-3). For Ring 3C (Figure 5-21b), the arms have already merged into the vortex ring structure, however the x-velocity field still convects the upper ring region away from the wall. In both cases, the resulting structure at this time resembles a horseshoe vortex, with the ends of the horseshoe connected to the wall.

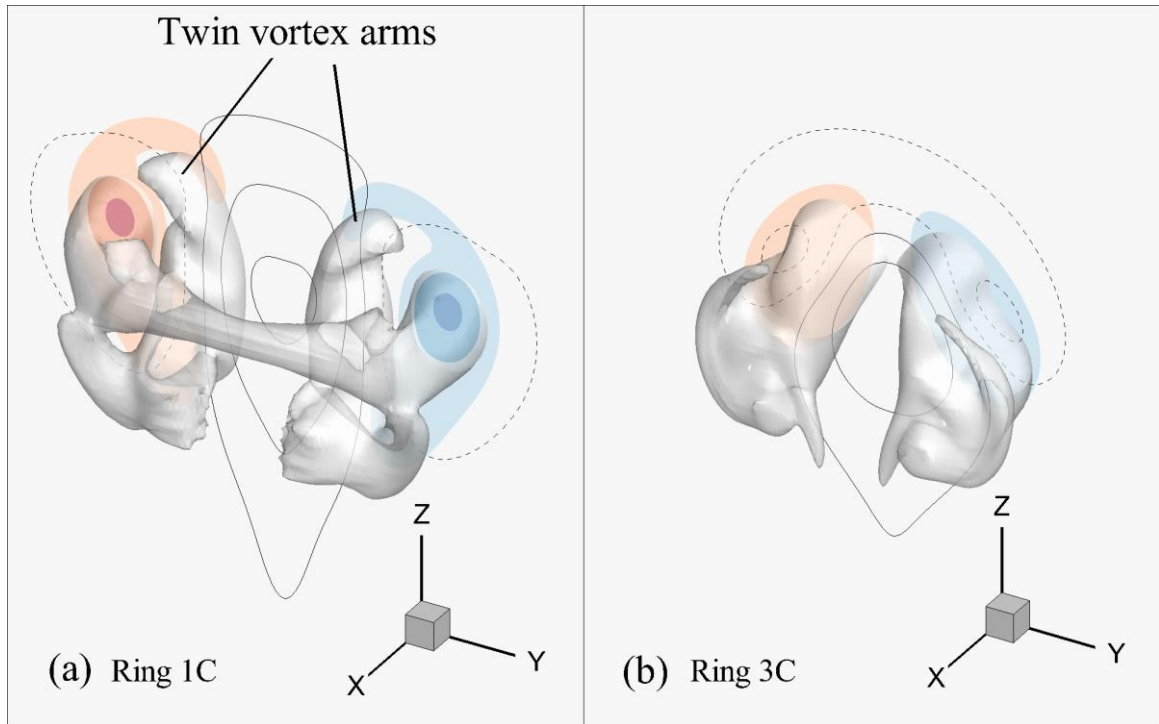Figure 5-21 – (a) Ring 1C and (b) Ring 3C, both at $t = 96$. A transparent iso-contour of λ_2 overlaid on a yz-plane through the centre of the vortex ring, being bent in the wall normal direction by the developed swirling field. Line contours show x-velocity (dashed negative contours) at [-0.15 -0.05 0.05 0.15 0.25], coloured contours show x-vorticity (red anti-clockwise) at [-0.5 -0.3 -0.1 0.1 0.3 0.5].

A key identifiable difference between the two rings is observed at $t = 108$, where the thicker ring has produced an arch of rotating fluid, positioned near the wall and upstream of the other remaining vortex structure (frame H, Figure 5-20). Figure 5-22 presents the difference in y-vorticity contours for Ring 1C (top row) and Ring 3C (bottom row) for $t = 48$ (left column) and $t = 108$ (right column) in the y = 0 plane in the near wall region. At the earlier time, the rotation along the wall near the core opposes the rotational direction of the core, with regions of opposite rotation elsewhere along the wall. At the later time, the far side of each ring is approaching the wall, inducing the opposite rotation. The far side of the thicker ring is closer to the wall at this point, so has a larger influence on the boundary layer. The position of the arch that has formed for the thicker ring is indicated on the figure.
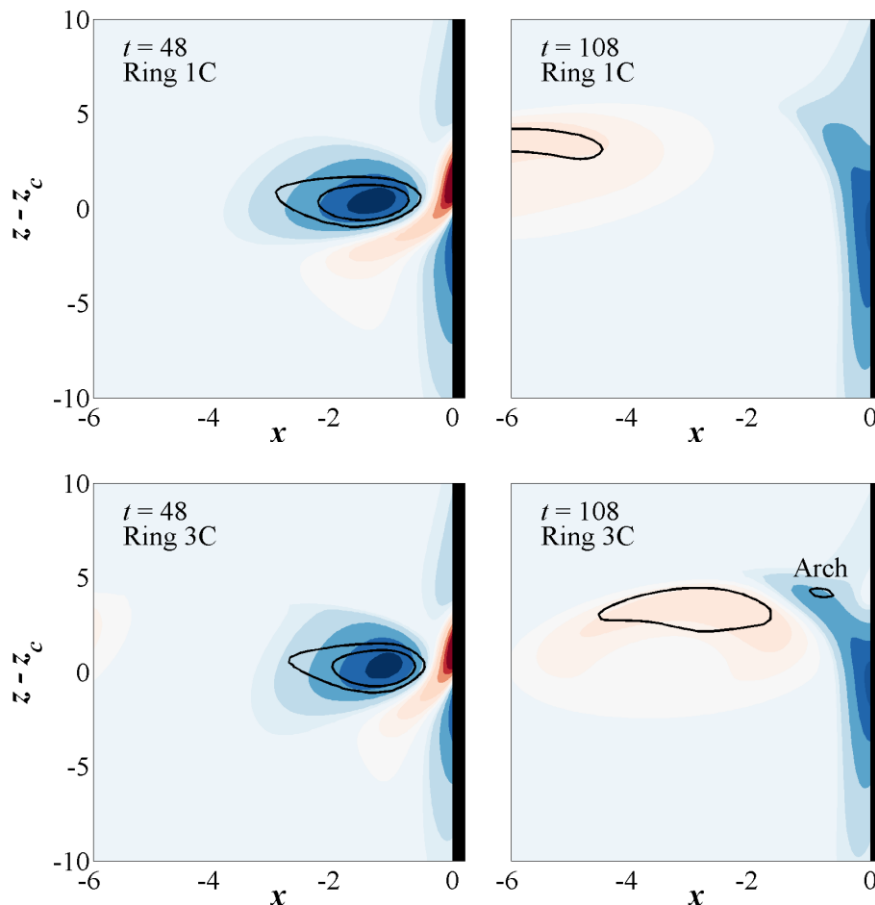
Figure 5-22 – Image showing the difference between a thin and thick ring at two different times. Contours of y-vorticity in the plane at $y = 0$, for Ring 1C (top row) and Ring 3C (bottom row), at $t = 48$ (left column) and $t = 108$ (right column). Red indicates anti-clockwise rotation. Contour levels are [-0.100 -0.075 -0.050 -0.025 -0.010 -0.005 0.005 0.010 0.015 0.025 0.050 0.075 0.100]. Overlaid contour is $\lambda_2 = -1$. The arch observable in Figure 5-20 is labelled for Ring 3C.

5.2.8. Wall-normal velocity

The influence of the vortex rings on the wall normal velocity gives an indication of how effective near-wall vortex rings are at promoting fluid mixing near a boundary. Monitoring the wall-normal velocity over time reveals that the vortex ring reaches a point of peak efficiency midway through its evolution, in terms of effect on the fluid mixing in the near-wall region. The wall-normal velocity can be quantified by considering the area averaged x-velocity over an x-plane. Figure 5-23 presents the magnitude of this average for a plane of size $20a_i$ x $20a_i$ over time for Ring 1C, for $x = -0.5$. The solid line designates the average velocity over the plane, while the dotted and dashed lines represent the wall-normal velocity upstream and downstream of the plane of minimum pressure (i.e. the approximate position of the near-wall core). The flux peaks at approximately the same time as the near-wall core disintegrates, which is immediately followed by a switching in the dominant flux region from downstream to upstream. A similar analysis at $x = -0.1$ reveals the average velocity is an order of magnitude smaller, however the timing is very similar.
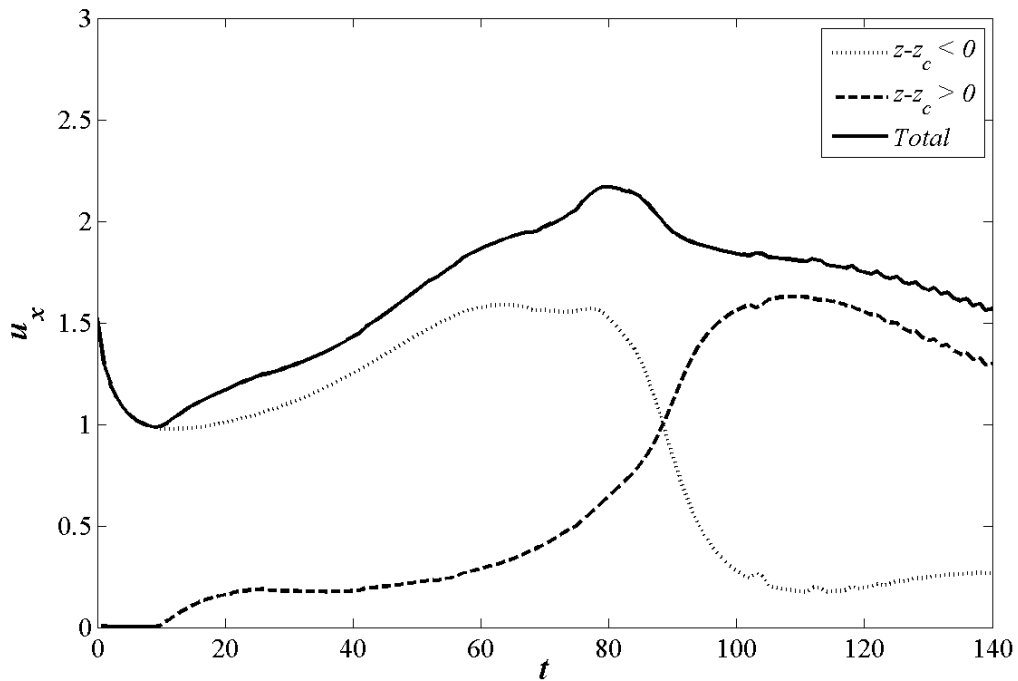

Figure 5-23 – Plot of average u_x, in the direction away from the wall, over the plane located at $x = -0.5$. The plane over which data is sampled is bounded by $-10 < y < 10$ and $-10 < z - z_c < 10$. The inconsistencies at later times are due to the definition of z_c varying slightly after the near-wall core is destroyed.

Figure 5-24a presents a comparison of the average wall-normal velocity for all 9 cases, for a plane at $x = -0.1$. The time axis has been normalized using the "true" wall separation; that is, the initial distance between the wall and the edge of the vortex core as defined by the core radius. Although the magnitude and shape of the curves is different, with this modification all 9 cases evolve at similar rates, peaking in the region $30 < t / (b_i - 1) < 50$. To give a clearer indication of the relationship between cases, the data at $x = -0.5$ is provided for the three wall separations of Ring 1 in Figure 5-24b, while the three rings at a wall separation of $b_i = 3.0$ are presented in Figure 5-24c, also for $x = -0.5$.
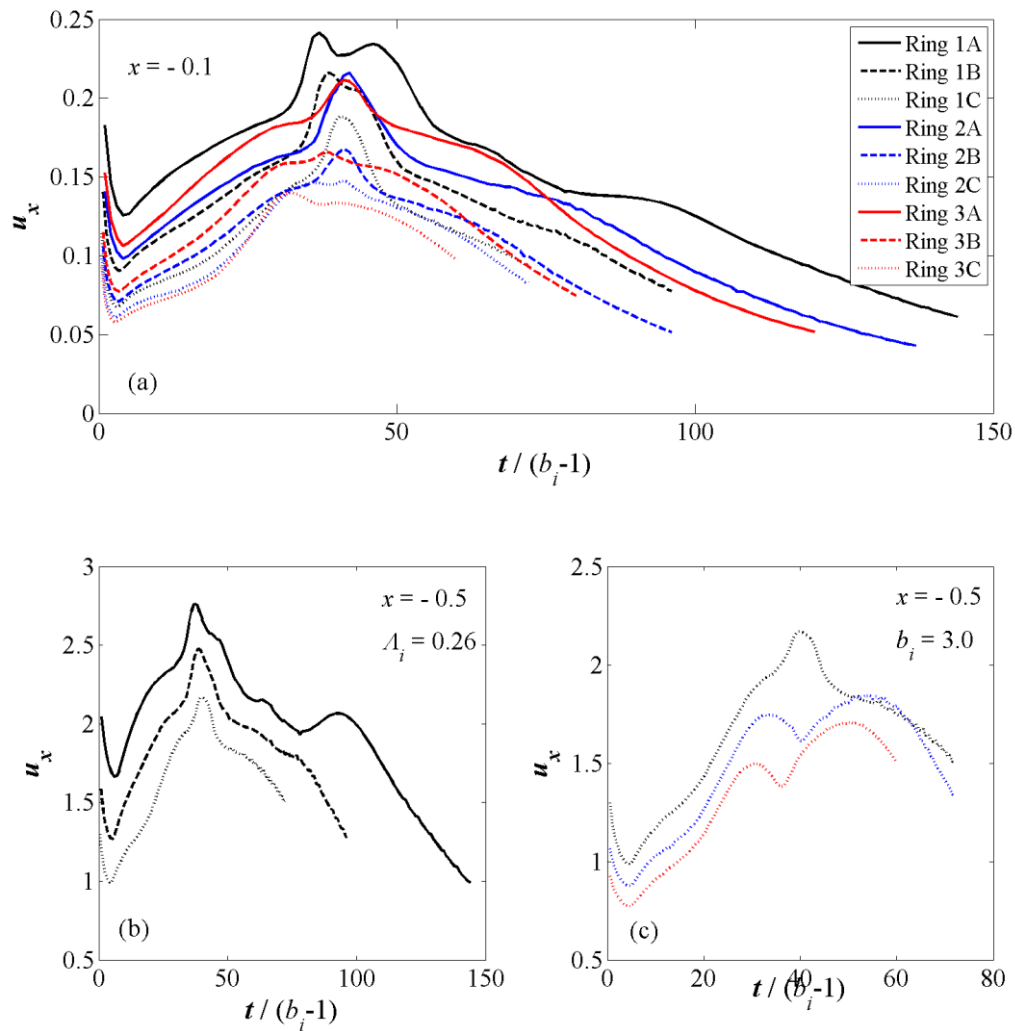
Figure 5-24 – Plot of the average u_x, in the direction away from the wall, in a single x-plane, using a modified time axis. (a) presents the data in $x = -0.1$, comparing all 9 cases, (b) presents the data in $x = -0.5$ for only Ring 1, and (c) presents the data in $x = -0.5$ for $b_i = 3.0$.

138

The cases that are initialized closer to the wall progress further along the evolutionary path, as the interaction occurs sooner. The flow fields for all 9 cases at $t / (b_i - 1) = 40$ are presented in Figure 5-25. Each row represents a differently sized ring, and each column represents a different wall separation. Despite differences in the ring size, and in the interaction between the vorticity arms and the vortex core, the 9 rings are all clearly in a similar stage of their development. This suggests that despite the slightly different physics that is introduced with varying the ring size, a similar evolutionary process is followed by all rings. The success of the alignment demonstrates the validity of the additional time normalization.

Figure 5-25 - Isometric view of the vortex ring in the 9 cases, at a time equivalent to $t / (b_i - 1) = 40$. The graphic shows an iso-contour of the λ_2 field ($\lambda_2 = -1$) overlaid with contours of z-vorticity. Contours are [-3 -1 1 3], red indicates anti-clockwise rotation.

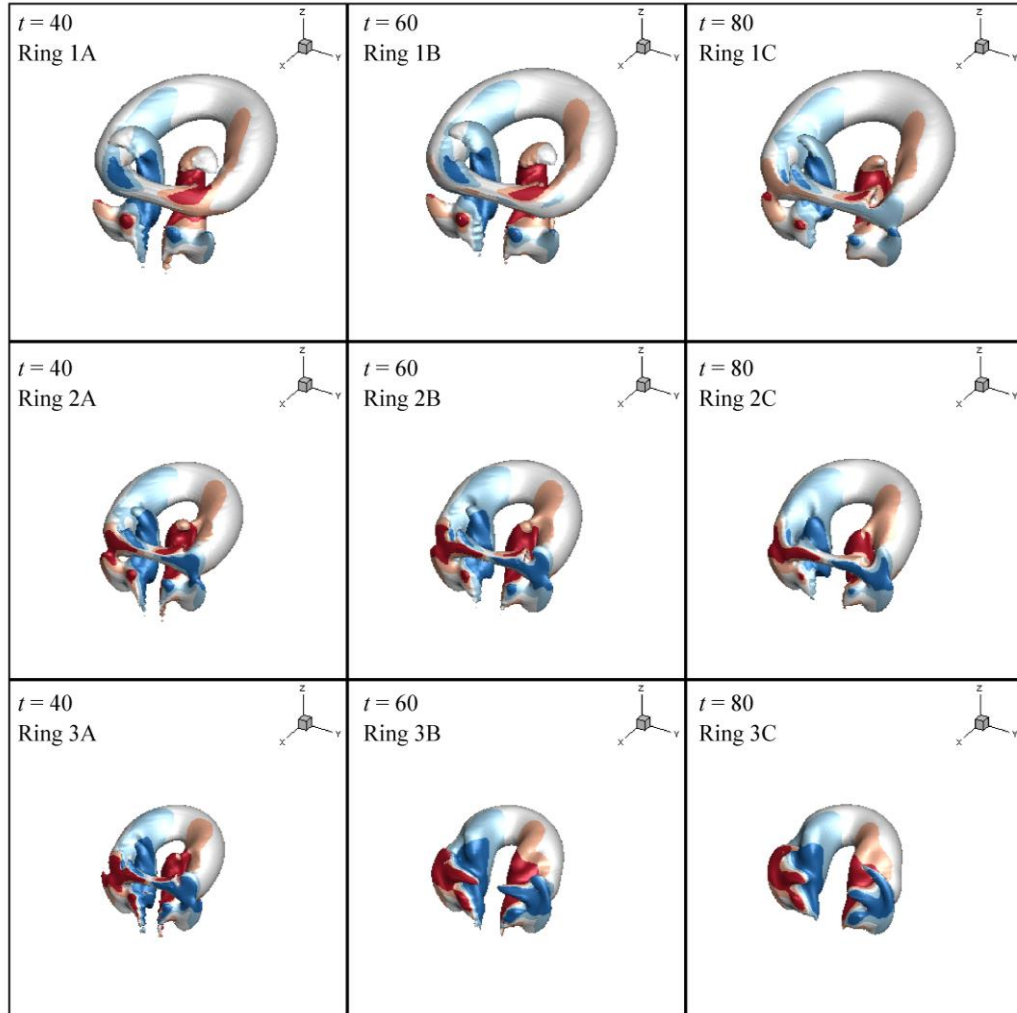The conditions surrounding the double peak in wall-normal velocity in Figure 5-24a, which occurs for Ring 1A, are presented in Figure 5-26, which provides contours of u_x at x = - 0.1. The times for the first three frames have been chosen to lie in the region of $30 < t / (b_i - 1) < 50$. The first spike in the peak, at $t = 38$, corresponds to the core entering the boundary layer region, before weakening. The second spike, at $t = 45$, occurs once the two arms of vorticity take over the role as the primary means of wall-normal fluid transport. The image at $t = 125$ is an example of the flow distribution once the near-wall core has completely broken down, and the ring has a horseshoe like structure. The center of the vortex core is the lowest pressure region in the domain, and therefore the core at this time acts as a conduit for fluid transport in the wall-normal direction. Fluid is taken from the boundary layer and transported to the side of the ring further from the wall. Figure 5-27 presents the same data, but at $x = -0.5$. The main contribution to the peak at this distance from the wall is clearly the vortex core.
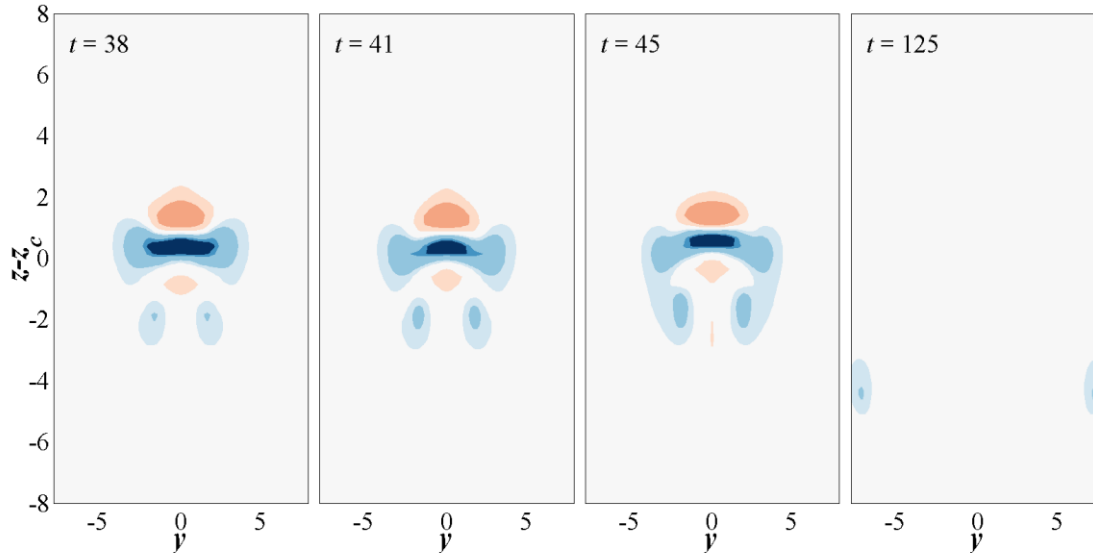

Figure 5-26 – Contours of u_x in the x = -0.1 plane, of Ring 1A. Blue contours indicate flow away from the wall, red indicates contours towards the wall. Contour levels are [-0.002, -0.001, -0.0005, 0.0005, 0.001, 0.002].
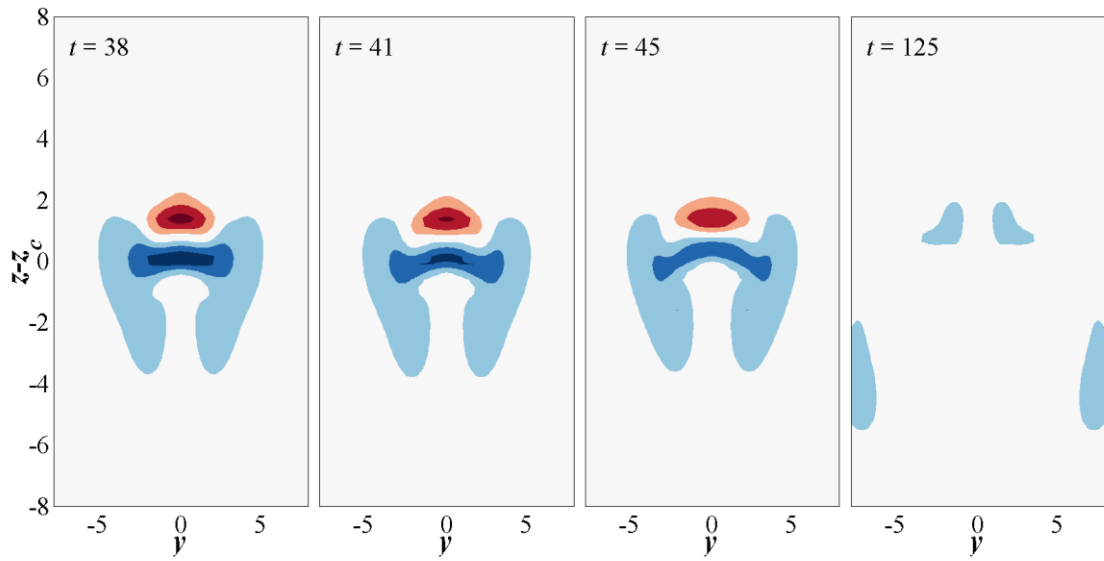
Figure 5-27 - Contours of u_x in the $x = -0.5$ plane, of Ring 1A. Blue contours indicate flow away from the wall, red indicates contours towards the wall. Contour levels are [-0.32, -0.22, -0.12, -0.02, 0.02, 0.22, 0.32, 0.42].

Figure 5-24b suggests that varying the wall separation modifies the timing of the peak flux, due to the delay in the breakdown of the near-wall core. The magnitude is also lower for the rings further from the wall. The modification made to the time axis, however, brings the different wall separations into alignment (a comparison between the flow fields of the three cases is provided in the top row of Figure 5-25, showing that they are qualitatively similar). Figure 5-24b also reveals a secondary peak for the case nearest the wall, which occurs when the far side of the ring moves into the near-wall region, reversing the flow direction in the boundary layer (see Figure 5-22). The same flow reversal occurs for the rest of the cases, however the secondary peak does not appear for all cases (see Figure 5-24b). This suggests that its prominence further from the wall in the single case is due to the strength of that particular vortex core region when it nears the boundary layer. It is not present in Figure 5-24a (at x = -0.1), suggesting that this effect is primarily just outside the boundary layer.

Figure 5-24c compares the influence of ring size at a single wall separation (b_i = 3). The thinnest ring shows a clear peak, however the two thicker rings exhibit a dip at around the same point along the horizontal axis. Monitoring the same rings in Figure 5-24a reveals no peak or dip for these thicker rings, but rather a plateau. The reason for this lack of a peak is investigated in more detail using the flow fields in Figure 5-28. The top row of Figure 5-28 presents the iso-contours of the λ_2 field for the thinnest ring (Λ_i = 0.26), around the time of the formation of the peak in Figure 5-24c.
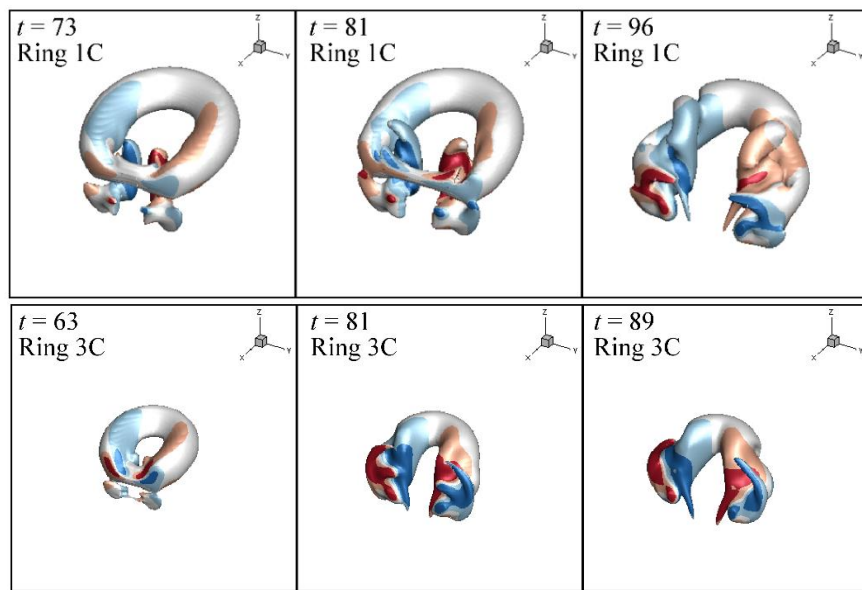
Figure 5-28 – Isometric view of the growth of the boundary layer spire for (top row) Ring 1C, and (bottom row) Ring 3C. The graphic shows an Iso-contour of the λ_2 field (λ_2 = -1) overlaid with contours of z-vorticity in the xy-plane. Contour levels are [-3,-1,1,3], blue represents negative contours.

The peak begins to form at t = 73 (where t / (b_i – 1) = 36.5), when the two arms of vorticity are developing strength. The uppermost point of the peak occurs at t = 81 (40.5), when both the vorticity arms and the core are acting to draw fluid away from the wall region. The peak ends around t = 96 (48), when the dissipation of the near-wall vortex core has completed. The bottom row of Figure 5-28 presents the iso-contours of the λ_2 field for the thickest ring, which exhibits a dip in Figure 5-24c. In this case, the boundary layer vorticity only develops significant strength when the

vortex core near the wall has already dissipated. The conditions for such a peak in the wall-normal velocity field can therefore not be satisfied at any time in the flow. Instead, there is a delay between the destruction of the core and the growth of the arms, leading to the dip seen in the curve.

5.2.9. Extent of surface coverage

The area of the wall surface that is influenced by the vortex ring flow depends on both the distance translated in the z-direction, and the magnitude of the spread in the y-direction. Figure 5-29a presents the z-position of the vortex ring as a function of time, for the 9 different scenarios analysed. The close-wall case of the thick ring moves around 20 spatial units over 120 time units, while the furthest case of the thinnest ring moves around 30 spatial units over the same 120 time units. The remaining cases fall between these two values.

Figure 5-29b presents the same data, but with an additional normalisation on both axes. The vertical and horizontal axes are multiplied by A/b_i, where A is a ratio between cases, such that

$$A = \frac{a_i \ of \ Ring \ 1}{a_i \ of \ Ring \ n} , n = [1,2,3].$$

5-2

This modification collapses the data from all 9 cases into approximate alignment. This reinforces the notion that the evolution of these rings is similar across the different ring sizes and wall separations. Also note the plateauing of all of the curves after $t \ (A/b_i) = 50$, indicating the time at which the vortex rings lose the majority of their forward momentum, and hover near a certain position on the wall. This method of normalisation is only effective for predicting the z-position of the rings, as other variables (such as the tilt angle and the wall-normal velocity magnitude) have different optimal normalisations.
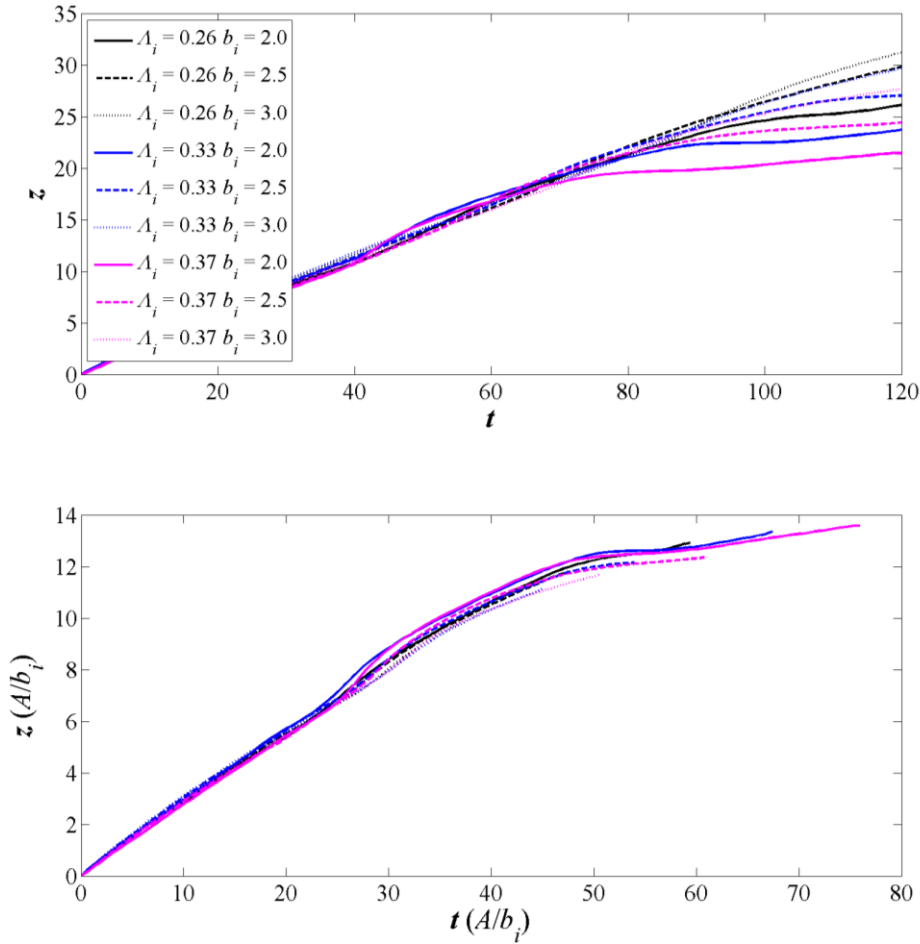
Figure 5-29 – Position of the ring in the z-direction for all 9 cases, as a function of time. The axes in (b) are normalised by the ratio A/b_i, where A itself is the ratio between a_i of each case and a_i of the largest ring.

The spread in the *y*-direction of each case has been compared in Figure 5-30 at $t / (b_i - 1) = 60$ (returning to the normalisation method used in Section 5.2.8). The coverage in this direction is as expected, with the extent determined primarily by the initial ring radius. That is, the more initial coverage the vortex ring has, the more coverage it will have for the majority of its evolution. There is also a slight increase in width with increasing wall separation, as these rings increase in size due to viscous diffusion for longer, before interacting with the wall. Each of the 9 cases present similar contours at the normalised time, suggesting the arrangement of the flow field after reaching the horseshoe-like shape is similar, despite the minor differences in the evolution process to reach this point. The vortex core in the near-wall cases appears to retain more of its size than the equivalent cases further from the wall.
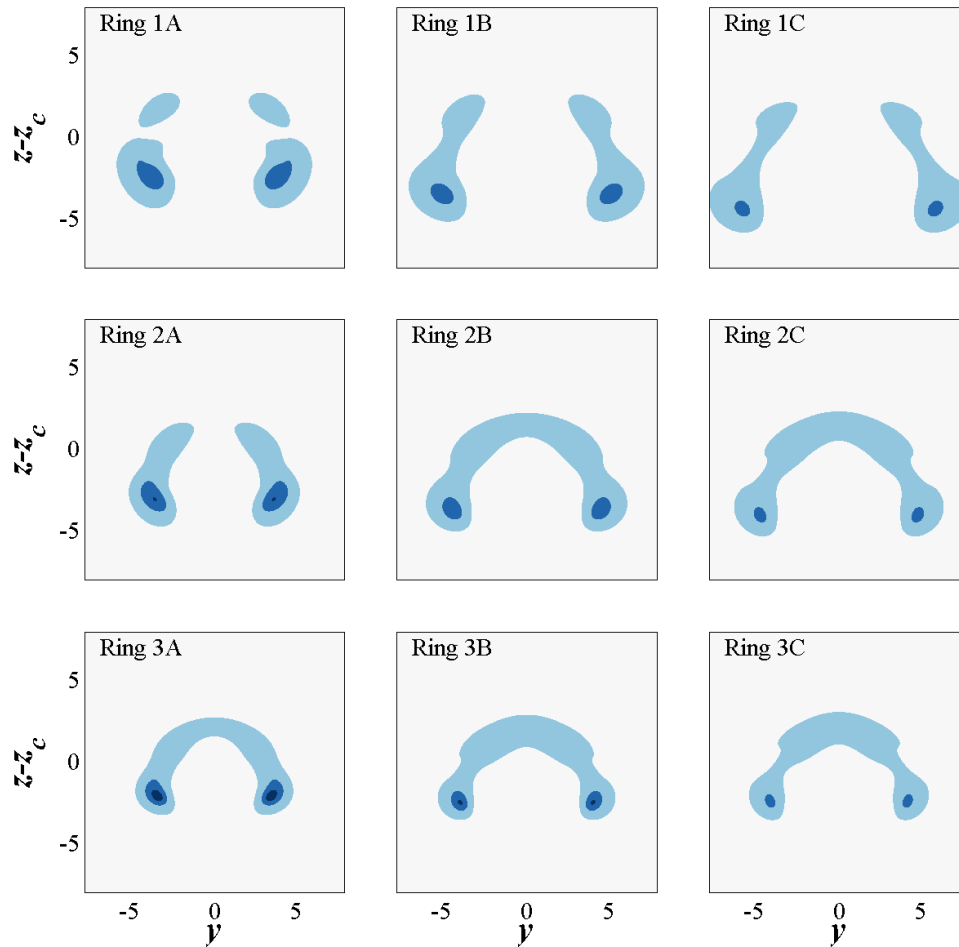
Figure 5-30 – Demonstration of spread in the y-direction, shown using contours of u_x in a plane located $x = -0.5$ at $t / (b_i - 1) = 60$. Contours are [-0.12 -0.02 -0.01 0.01], blue indicates negative contours.

5.2.10. Eventual form of ring

The interaction with the wall eventually removes all circulation from the near-wall vortex ring. The make-up of the vortex rings at late stages in their evolutions is given in Figure 5-31, at $t = 120$. All three cases exist as a series of vortex tendrils, as the remainder of the structure moves towards the boundary layer region. The circulation in the central plane has also drastically reduced. Defining the Reynolds number based on the circulation of the main body vortex in the centre plane, reveals that the rings have reduced from their initial Reynolds numbers of 1000, down to $Re = 735$, $Re = 598$, and $Re = 451$, respectively. All forward momentum has effectively ceased at this time.
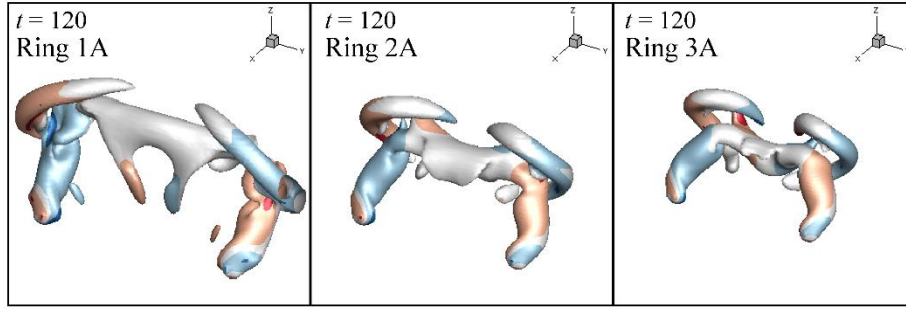
Figure 5-31 – Physical manifestation of the vortex ring late in its evolution, for the three different ring sizes, all with an initial wall separation of b_i = 2.0. Contours of z-vorticity, contours levels [-3,-1,1,3]. Red indicates anti-clockwise rotation.

5.2.11.   Analytical comparison to a developing boundary layer

The effectiveness of Ring 1A at inducing wall normal-flow is quantified in this section. Section 5.2.8 introduced the average wall-normal velocity for the ring, for two 20×20 planes centred on the z-position of the ring, at x = -0.1 and x = -0.5. Averaging each data set over time provides a single value (for each of the two x-positions) with which to quantify the wall-normal velocity. After converting these values to be per unit width of the plane (*i.e.* dividing through by 20), the values are u_x = 0.0073 at x = - 0.1, and u_x = 0.0973 at x = - 0.5. These values are the average wall-normal velocity, per unit time and unit width, over a domain of length 20, centered on the vortex ring. To provide an idea of the magnitude of these values, the propagation velocity of Ring 1A is u_z = 0.35.

Taken in isolation, these values are not particularly meaningful. Therefore, a comparison is provided of the wall-normal velocity induced in a laminar developing boundary layer. The magnitude of the wall-normal flow at a particular height and position along the wall can be obtained by assuming a Blasius solution for the boundary layer velocity distribution. A normalised stream function f is defined as a function of a similarity variable η, allowing the wall-normal velocity component to be obtained through the solution of a differential equation (Blasius, 1908). Conversely, the free-stream velocity required to provide a particular average wall-normal velocity can also be obtained.

146

Using the Blasius solution, the free-stream velocity required to achieve the wall-normal velocities quoted for the vortex ring would be $u_z = 0.4209$ (to be equal at $x = -0.1$) or $u_z = 0.4584$ (to be equal at $x = -0.5$). These values are also per time (assuming a steady flow), and per unit width. However, the key difference between the two flow regimes, is that while the vortex ring requires a single burst of energy at formation, the developing boundary layer case requires continued energy input over time. To quantify the energy difference, the energy of a jet (used to drive a developing boundary layer) is compared to the energy of a vortex ring.

The kinetic energy of a vortex ring of finite thickness is given by

$$KE = \frac{1}{2}\rho\Gamma^2 R \left[\ln\left(\frac{8}{\Lambda}\right) - \frac{7}{4} + \frac{3}{16}\Lambda^2 \ln\left(\frac{8}{\Lambda}\right)\right],$$
<div align="right">C-1</div>

as defined by (Fraenkel, 1972).

The kinetic energy of a jet of fluid produced by a conventional means is given by

$$KE = \frac{1}{2}\rho A U_f^3 t,$$
<div align="right">C-2</div>

where U_f denotes the free stream velocity. The area of the jet is taken as being identical to the area of the vortex ring (πR^2).

Including the appropriate values and taking the ratio of these two energies gives a kinetic energy requirement for the jet 23.6 times larger than the energy required for the ring, for the equivalent development of wall-normal velocity. This is over 140 time units, on a plane of length 20. These two values have been chosen somewhat arbitrarily, and over much longer time or length scales, the jet would take precedence, as the vortex ring eventually ceases its forward momentum, and dissipates. This suggests that vortex rings can be used as efficient cooling mechanisms, providing the desired surface is not too long for the ring to traverse.

5.3 Conclusions

The evolution of near-wall vortex rings has been analysed using numerical simulation, considering three vortex rings of different sizes, each at three different initial wall separations. All rings were found to follow a similar path of evolution. The wall induces a bend in the ring in the near wall region, and rotates the translational axis of the vortex ring towards the wall. This bending induces a swirl component of velocity in the ring, whose direction has opposite signs across the $y = 0$ symmetry plane. The resulting perturbations in the azimuthal vorticity field have the appearance of a resonant Kelvin instability when viewed in the cross-section of the ring, however the 3D form clearly shows that a different mechanism is at work. The swirl results in flow on the inside part of the core moving towards the wall, while flow on the outside part is moved away from the wall. A portion of this swirl advects from each side of y-axis towards the centre of the ring, creating a pair of counter-rotating axial vortices. Vorticity that develops at the surface of the wall is wrapped around and into the vortex ring, reorientates into the z-plane, and joins up with these axial vortices, creating two arms of vorticity. These arms draw fluid out from the wall, increasing the magnitude of the wall-normal velocity.

The motion of the vortex rings into the boundary layer region also influences the wall-normal velocity, as the connection of the vortex core with the wall, though a horseshoe-like structure, provides a low pressure supply line for fluid to be drawn out of the boundary layer and into the free-stream flow. The wall-normal velocity appears to be enhanced for thinner rings, and closer initial wall separations. The magnitude of the wall-normal velocity induced by the vortex rings has been shown to provide an equivalent impact to that of a developing boundary layer, for an energy expenditure of around 20 times less. The vortex rings were shown to cover a distance of between 20 and 30 core radii from the time of initialisation, and expand to at least double their initial ring radii in width. Further investigation is required in order to determine the ideal wall separation of a vortex ring in order to maximise both wall-normal velocity and surface coverage. The influence of modifying the Reynolds number is an additional consideration.

Chapter 6

Convective heat transfer

T he original motivation for considering the interaction of vortex rings with walls is the possibility of using them to effect heat transfer, for example in the cooling of electronics. In this chapter, an additional analysis is performed to cover the final aim of this thesis, which is to determine the effect of these dynamics on the temperature field (Section 1.9.7). In application, a single ring is not a continuous cooling mechanism, and multiple rings are therefore also considered. The results presented in this chapter consist of original work, not previously published in any form.

150

6.1 Introduction

This chapter builds on the work of Chapter 5 by including a temperature field in the simulation of Ring 1A. The temperature field is treated as a passive scalar here, which implies that convection induced by temperature differentials is vanishingly small. Although this is an approximation, ignoring buoyancy forces allows an analyses of the temperature field which is suitable for applications of any orientation. The initial flow field is chosen to be identical to that of Ring 1A from Chapter 5, with the addition of the scalar field. For the purposes of this investigation, the Prandtl number is set to be $Pr = 0.707$, which is similar to that of air at 300 K. This links the study to the eventual application of the work, in which the cooling of micro-scale electrical systems would likely be performed using air as the primary fluid.

6.2 Methodology

6.2.1. Scalar field

The numerical algorithm is identical to that described in Chapter 2, using Fourier expansions to model the z-direction. The temperature field is decoupled from the governing equations, and is treated as a scalar field. The development of a scalar field ϕ over time with an evolving flow field is described by the equation

$$\frac{\partial \phi}{\partial t} + (u \cdot \nabla)\phi = \kappa \nabla^2 \phi \, , \qquad \qquad \text{6-1}$$

where κ is the diffusion coefficient of the scalar field. The algorithm uses an Auxiliary Semi-Lagrangian technique, so that the value of a scalar field can be determined at any point in the domain without the need for interpolation between grid points. The technique integrates Equation 6-1, before finalising the solution with a diffusion step (Sheard and King, 2011). The temperature in the domain is non-dimensionalised, such that the wall has a constant temperature of 1, and the fluid in the domain has an initial temperature of 0. The relative impact of the temperature field can therefore be scaled to whatever physical temperature differential is desired

in the eventual application. The temperature of the wall is constant for the entire simulation, and heat diffuses and convects out into the fluid domain.

Other boundary conditions could be considered for this problem, such as a constant heat flux, however the use of a constant temperature wall greatly simplifies the subsequent analysis.

6.2.2. Multiple rings

In addition, this chapter looks at an array of vortex rings, translating parallel to the wall. The initial flow field consists of 15 axially aligned vortex rings, with the same parameters as Ring 1A from Chapter 5 ($\Lambda_i = 0.26$ and $b_i = 2.0$). Each ring is separated from the preceding ring by a distance of $2R_i$, measured from core centre to core centre. This separation has been chosen so that the influence from the neighbouring rings is roughly equal to the influence of the opposite side of the ring in question. The dynamics influencing the rings in the centre of the array will be similar to those experienced in an infinite array. The evolution is not explored in full detail, however comparisons are made to the isolated ring case. The scalar temperature field is retained for the multiple ring case.

Multiple rings are introduced into the domain by shifting the single ring flow field in the z-direction, summing the new field and the original field, and then repeating this process until the desired number of rings are present in the domain. Although each of the rings equilibrates in the new domain, this is not expected to greatly impact the results as discussed in Section 5.1. For this investigation, the ring at the center of the array (the eighth ring) is monitored over time for comparison to the single ring case. Such an array of rings is idealized, as the fluid drawn into the piston for each pulse in laboratory setup is likely to modify the flow field. However, the approximation is sufficient to identify likely modifications from the isolated ring case. Note that multiple rings are not introduced in this chapter until Section 6.3.2.

6.3 Results

6.3.1. Temperature field of a single ring

The behavior of the scalar temperature field closely follows that of the flow dynamics observed in Chapter 5. Initially, it is the core of the vortex ring that dominates the transfer of fluid in the wall-normal direction. This is evident in Figure 6-1A, which presents the temperature contours in a plane at $x = -0.5$, and a semi-transparent iso-contour of the λ_2 field. The temperature has increased downstream of the ring (where fluid is being moved away from the wall), and decreased upstream of the ring (where fluid is being moved towards the wall). By $t = 40$, the boundary layer vorticity has reached out from the wall, bringing an increased temperature, as seen via the dark red contours in Figure 6-1B. After the near-wall vortex core has dissipated, the horseshoe-like remnant of the vortex ring continues to draw heated fluid away from the wall through the low pressure core centers, while the bulk motion of the ring forces cooler fluid into the near wall region, between the arms of the horseshoe (Figure 6-1C). This process is continuing at $t = 100$, and the area of the lighter contour in Figure 6-1D also reveals the surface area of the plane that has been influenced by the vortex ring. Note that in Figure 6-1, the changing colour of the background is due to the diffusion of the temperature field over time.

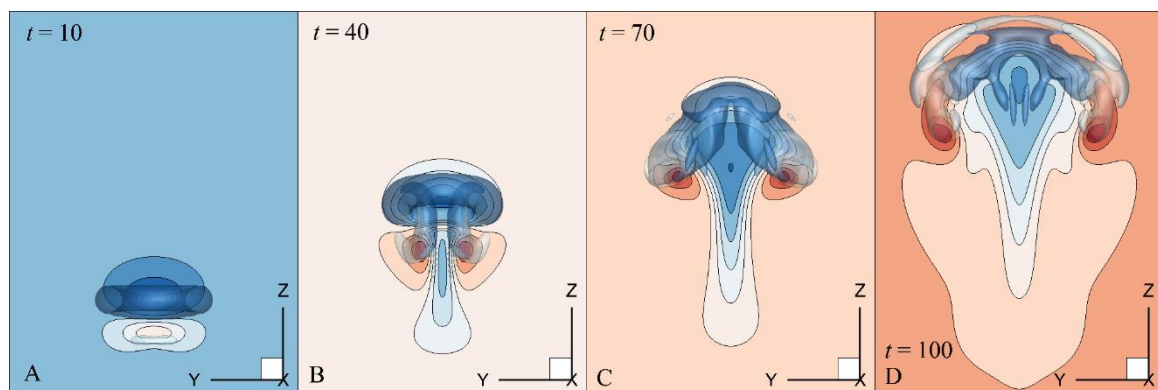Figure 6-1 – An iso-contour of the λ_2 field, with a plane at $x = -0.5$, showing coloured contours of the temperature scalar field for four different times, for Ring 1A. The contour levels start at 0.1 and increase by 0.1. The changing colour of the background is due to the diffusion of the temperature field from the wall. The plane in the images is $20a_i$ in the y-direction, and $30a_i$ in the z-direction.

Figure 6-2 provides the temperature contours in the $y = 0$ plane, accompanied by a 3D visualization of the λ_2 iso-surface overlaid with contours of temperature, at $t = 10$, 40, 70, and 100. At $t = 10$ (first column of Figure 6-2), the vortex core is in the process of advecting the fluid in the thermal boundary layer around itself, as it nears the momentum boundary layer region. The centre of the core retains its low temperature. By $t = 40$ (second column of Figure 6-2), the near-wall core is embedded in heated fluid, while the boundary layer vorticity brings heated fluid in from downstream of the vortex core (note the colour of the iso-contour).

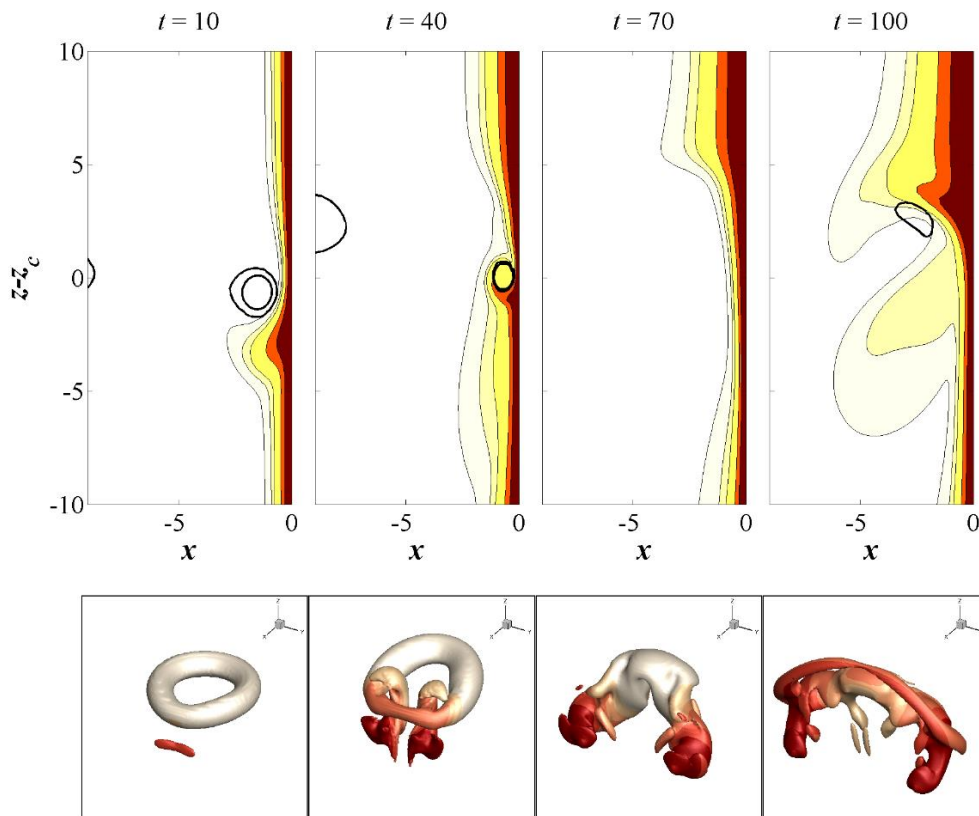Figure 6-2 – Overview of the temperature fields induced by Ring 1A, at (left to right) $t = 40$, 70, 100, 130. The top row provides contours of temperature in the $y = 0$ plane, with a measure of the core position shown with the solid contour. The bottom row provides the same contours, overlaid on an iso-contour of the λ_2 field. The contours are [0.01 0.05 0.10 0.30 0.50], darker contours indicate higher temperatures.

After the core breakdown, at $t = 70$ (third column of Figure 6-2), the arms of the horseshoe like structure are the primary temperature transfer mechanism, visible in the dark red colour of the iso-surface at the ends of the horseshoe. The center plane is relatively uniform, and cool free stream fluid is present close to the heated surface due to the bulk motion of the ring in the x-direction. At $t = 100$ (last column of Figure 6-2), the supply lines provided by the ends of the horseshoe vortex have drawn the heated fluid further into the ring. The raised temperature within the cores of the horseshoe vortex is visible in the yz-plane in Figure 6-1C (and D). This is the primary heat transfer mechanism at later times. The motion of the far-wall core into the boundary layer region also disrupts the contours on the center plane, enhancing mixing between the heated boundary layer and the cool free-stream fluid.

To provide a quantitative measure of the influence of the vortex ring on the temperature field, the effect of diffusion is removed by subtracting the temperature field from an identical domain with the vortex ring absent. The influence that the passage of the ring has on a fixed arbitrary location, placed 10 units upstream of the initial ring position, is monitored over time. Figure 6-3 provides quantitative detail of the influence on the modified temperature field, in the plane at $x = -0.05$, when the center of the ring is at various positions relative to this measuring location.

Each of the lines in Figure 6-3 represents the temperature profile at this arbitrary position, given the relative position of the ring; positive values are before the ring has passed (*i.e.* position is upstream of the ring), negative values are once the ring has passed the position (*i.e.* position is downstream of the ring). The influence of the ring on upstream locations in this plane is minimal; the $z - z_c = 5.0$ curve is only barely deflected from the horizontal. As the ring passes over the sampling point, there is only a slight decrease in the temperature profile. It is only after the ring has passed this point that its full influence is observable, as there is a sharp dip in the temperature profile for the other two sampled times. This is commensurate with the observations made from Figure 6-1 and Figure 6-2, where it is noted that the fluid moving outwards from the boundary layer (forming the twin arms that reach into the ring) takes with it significant amounts of heat.
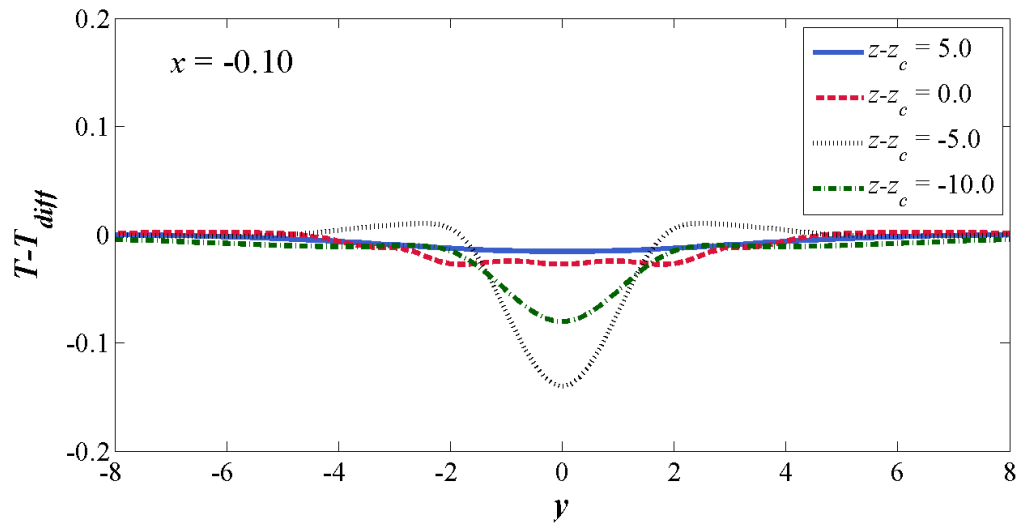
Figure 6-3 - An indication of the temperature profiles at z - z_c as a function of y-position, for x = -0.05, for Ring 1A. The temperature due to diffusion has been subtracted from the value at each point, revealing the true impact of the vortex ring. The sampling location is initially a distance of 10 units upstream of the ring.

Figure 6-4 presents the same plots, but for different x-planes. The influence of the vortex ring on the x = -0.50 plane (Figure 6-4a) is similar to that of the plane closer to the wall; there is only a minor influence as the ring passes over, and a larger influence after it has passed. The upstream influence of the ring is larger here than at the other locations, presumably due to fluid being displaced as the ring enters the boundary layer region. The x = -1.25 and x = -2.00 planes (Figure 6-4b and Figure 6-4c, respectively) exhibit similar profiles to each other, most notably the sharp increase in the temperature either side of y = 0 as the ring passes over the sampling location. This reveals that it is to these regions that the high temperature fluid near the wall is being convected by the action of the ring. This high temperature is retained after the ring has moved 5 units passed the sampling location, although reduces after the ring moves another 5 units.
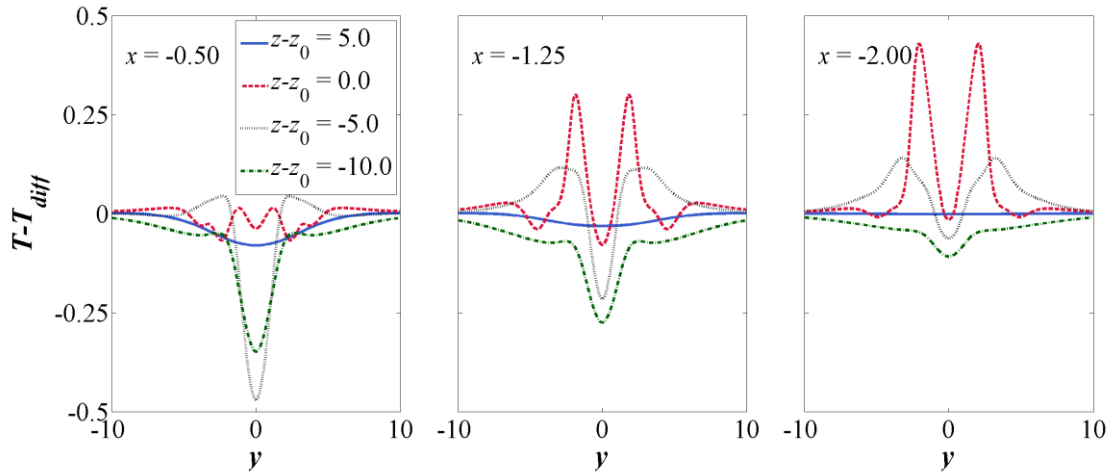
Figure 6-4 – An indication of the temperature profiles $z - z_c$ as a function of y-position, for three additional *x*-positions, for Ring 1A. The termperature due to diffusion has been subtracted from the value at each point, revealing the true impact of the vortex ring. The sampling location is initially a distance of 10 units upstream of the ring.

Although Figure 6-3 and Figure 6-4 give an idea of how the vortex ring influences the temperature of its surroundings, they do not provide a quantitative measure of the overall influence of the ring on the heat transfer. Instead, this is evaluated by averaging the temperature field across *x*-planes for each time step, over a domain centered on the ring with size 20×20. Figure 6-5 shows the results of this process, providing transfer of temperature away from the wall, after removing the effect of diffusion. As the distance from the wall increases (from $x = -0.10$ to $x = -1.00$), the reduction in temperature over that plane increases in magnitude. For the planes within this range, the minimum temperature occurs at around $t = 130$, after much of the vortex ring breakdown process has completed. The planes further from the wall do not follow this trend. The $x = 2.00$ plane has an initial increase in temperature, peaking just after the near-wall core breaks down, before dropping past zero at a similar time to when the closer planes reach their minima. The $x = -5.84$ plane (the location of the center of the ring at $t = 0$) is mostly unaffected until $t = 100$, after which time it experiences a sharp increase in temperature. This suggests that the temperature extracted from the near-wall region by the horseshoe-like vortex is convected out into the free stream by the remaining vortex structure at this time.
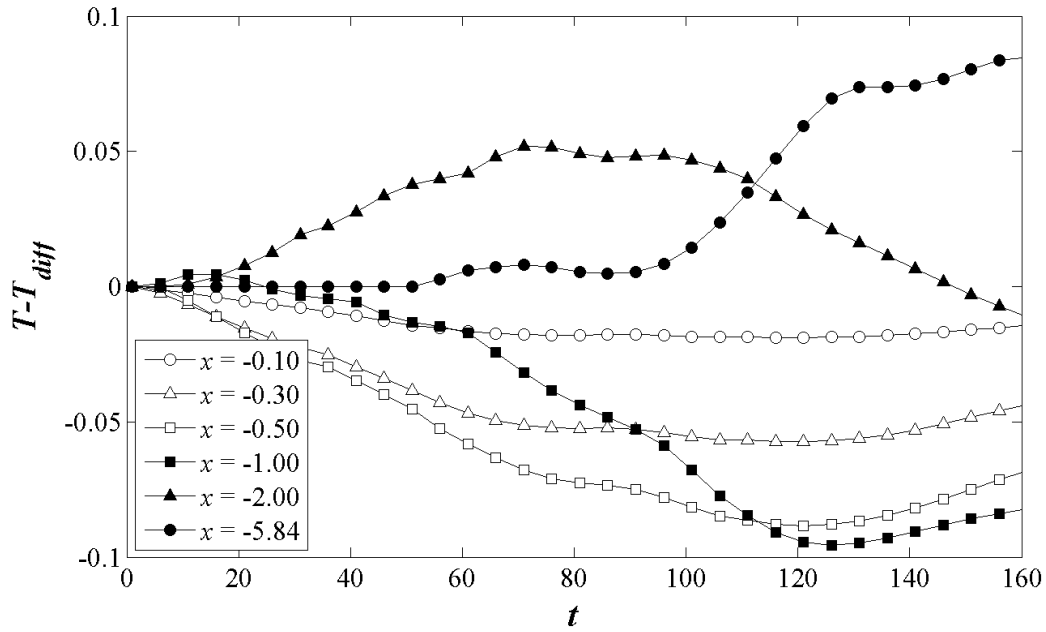
Figure 6-5 – The average temperature over time of various *x*-planes, within a 20x20 plane centred on the vortex ring, for Ring 1A. The temperature due to diffusion has been subtracted from the value at each point, revealing the true impact of the vortex ring.

The changes in the temperature of each plane are related to the changes in the wall-normal velocity magnitude, which is provided in Figure 6-6. At the time of peak wall-normal velocity, the gradient of the temperature curves in the planes close to the wall reaches a maximum. The increase seen in the plane at $x = $ -5.84 appears to align well with the secondary peak in the velocity curves (at around $t = 100$), which occurs due to the far-wall vortex core interacting with the boundary layer. The near-wall planes begin to increase in temperature again at later times, when the average wall-normal velocity is in a steady decline. The flow fields during this later time period are provided in Figure 6-7, in the same style as was used for Figure 6-2. The remaining vortex structure does not change greatly during this time, and consists of an arrangement of vortex tubes.

158
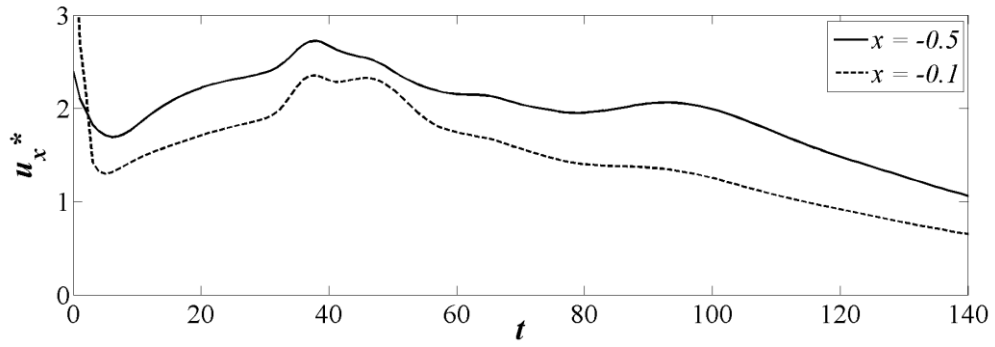
Figure 6-6 - Wall-normal velocity for Ring 1A, at x = -0.5 and x = -0.1, over a plane 20 x 20 in size, centred on the vortex ring. The vertical axis shows u_x^*, which is defined as $u_x^* = u_x$ for x = -0.5, and $u_x^* = 10 u_x$ for x = -0.1.
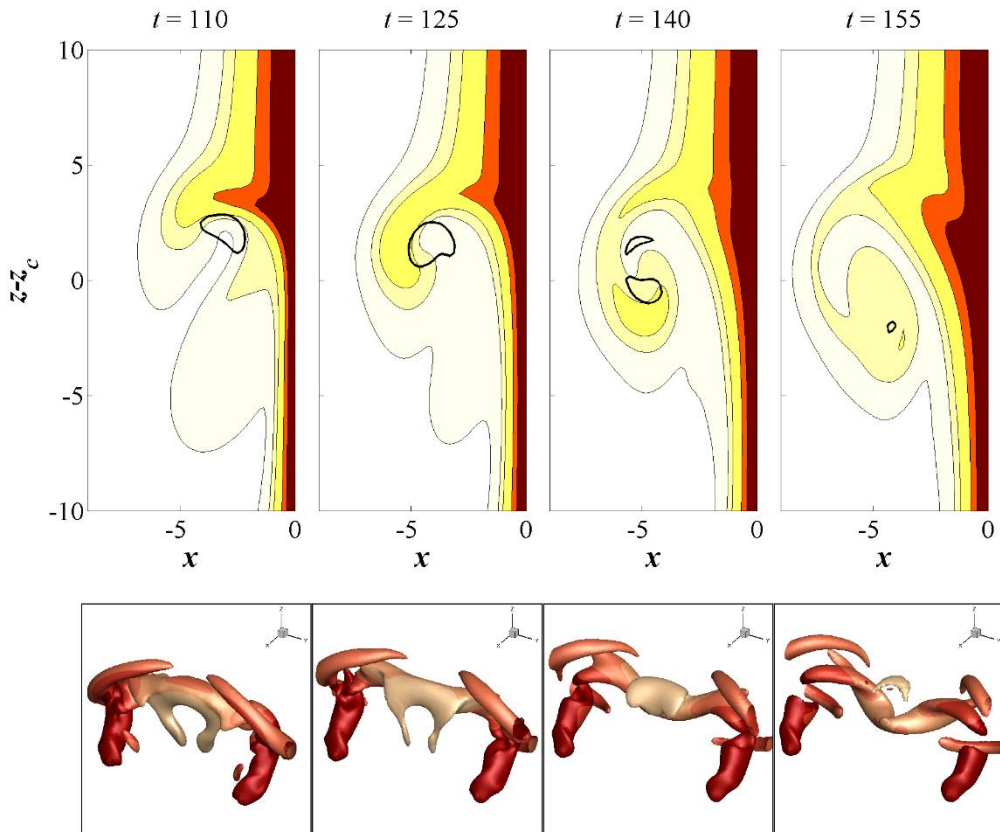
Figure 6-7 - Overview of the temperature fields induced by a near-wall vortex ring (Ring 1A), at (left to right) t = 115, 130, 145, 160. The top row provides contours of temperature in the y = 0 plane, with a measure of the core position shown with the solid contour. The bottom row provides the same contours, overlaid on an iso-contour of the λ_2 field. The contours are [0.01 0.05 0.10 0.30 0.50], darker contours indicate higher temperatures.

159

This analysis shows that the isolated vortex ring has a significant effect on the temperature field. The wall-normal velocity developed by the ring initially transfers temperature from the wall side of the near-wall core ($x < $ -1.00) to the far side of the near-wall core ($x = $ -2.00). The low pressure arms of the horseshoe-like vortex, after the near-wall core dissipation, advect heated fluid further from the wall. The remainder of the vortex structure interacts with the near-wall region at around $t = 100$, moving the heated fluid gathered by the horseshoe further away, and inducing a large increase in temperature at $x = $ -5.84, while the planes near the wall reach their lowest average temperature at this time. The average temperature of the $x = $ -0.1 plane (of size 20×20) is reduced by 10% due to the influence of the ring.

6.3.2. Dynamics of an array of rings

Refer back to Section 6.2.2 for details on the multiple ring simulations. The rings within the array fall into three clear categories of evolution, as can be seen in Figure 6-8. Those at the head of the train undergo leapfrogging, and form a mess of vortex structure at the most upstream point of the array. An additional vortex ring joins this combined vortex region approximately every 30 time steps, so by $t = 105$, the 4 leading vortex rings have been absorbed. Those at the rear of the train, and in particular the last vortex ring, shrink in size due to the action of the above rings. The final ring is pushed away from the wall as the ring above it begins to tilt, and is eventually dissipated far earlier than the rest of the rings (see the very bottom of Figure 6-8D). The rings in the middle of the array are typical of what would occur in a continuous chain of rings, and are therefore the focus of the remainder of the chapter. The behavior of these rings is expected to be qualitatively similar to that of vortex rings being generated constantly from a piston arrangement.
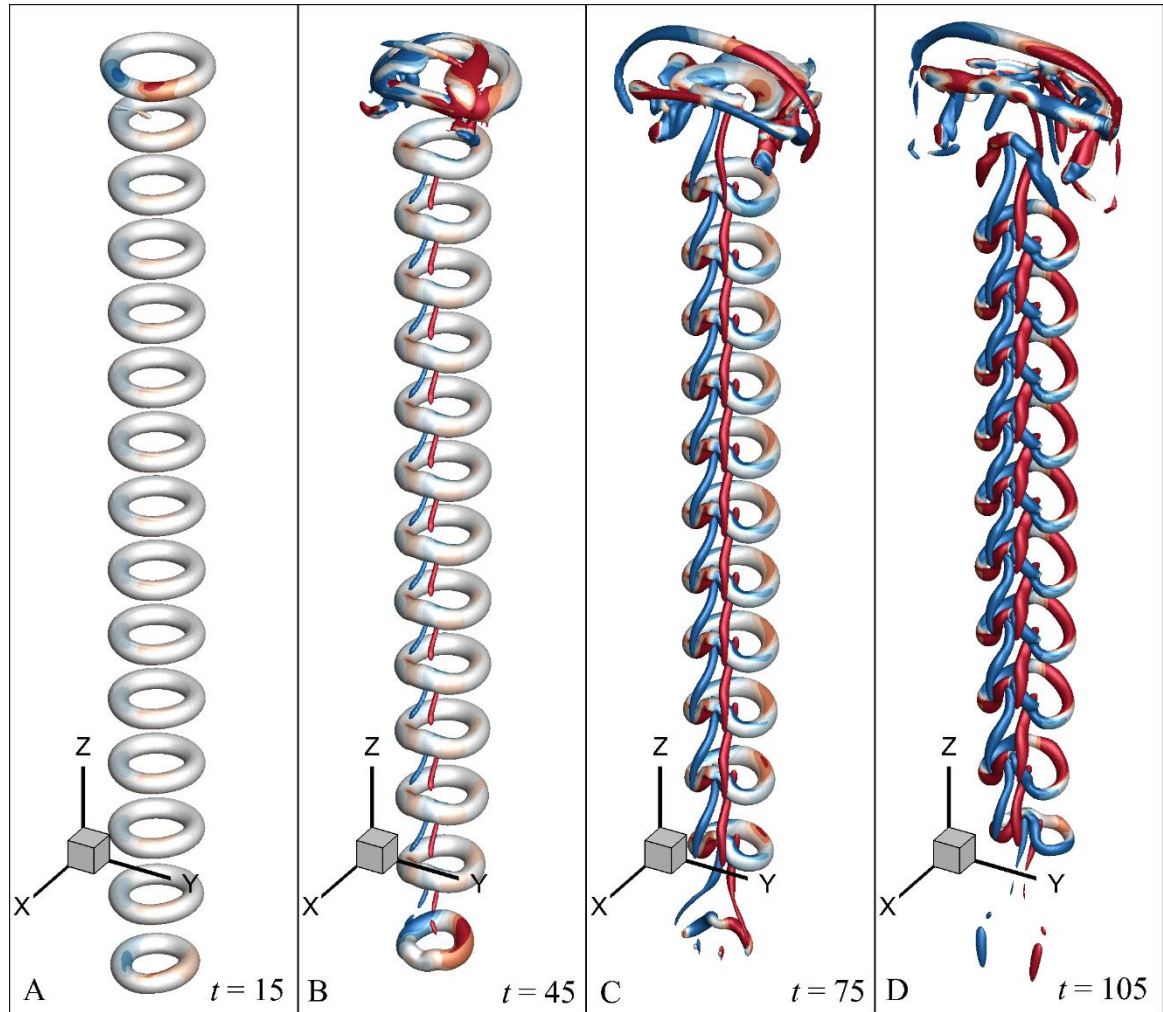
Figure 6-8 – Images of the full array of vortex rings, at t = 15, 45, 75, 105. An iso-contour λ_2 = -1 is overlaid with contours of z-vorticity. Contour levels are [-0.08 -0.05 -0.02 0.02 0.05 0.08]. Red indicates anticlockwise rotation (with the rings approaching the observer).

The rings follow the expected behavior from the previous chapter, experiencing a slight tilt and bend, and developing vorticity along the wall just downstream of the vortex core. The vorticity is advected from the wall and wraps into the center of the vortex core, developing rotation in the xy-plane. However, at this point, the presence of the surrounding rings modifies the evolution, forcing the bending of each individual vortex ring to invert, such that the near wall core moves ahead of the rest of the ring.

The eighth vortex ring in the array (which is initially the middle ring) is followed over time, and compared to the case of the isolated vortex ring. The main difference

in the early stages of the evolution is the effect that the array of rings has on the bending of the near-wall core. Figure 6-9 provides a comparison between the isolated ring case, and the array of rings, when viewed perpendicularly through the wall. The top row shows the evolution of the bend for the isolated ring, which is visible by $t = 6$, and continues to increase in magnitude after that time. However, for the ring within the array, the bending at the early times is not pronounced, and does not increase, instead the ring bends the other way by $t = 48$.
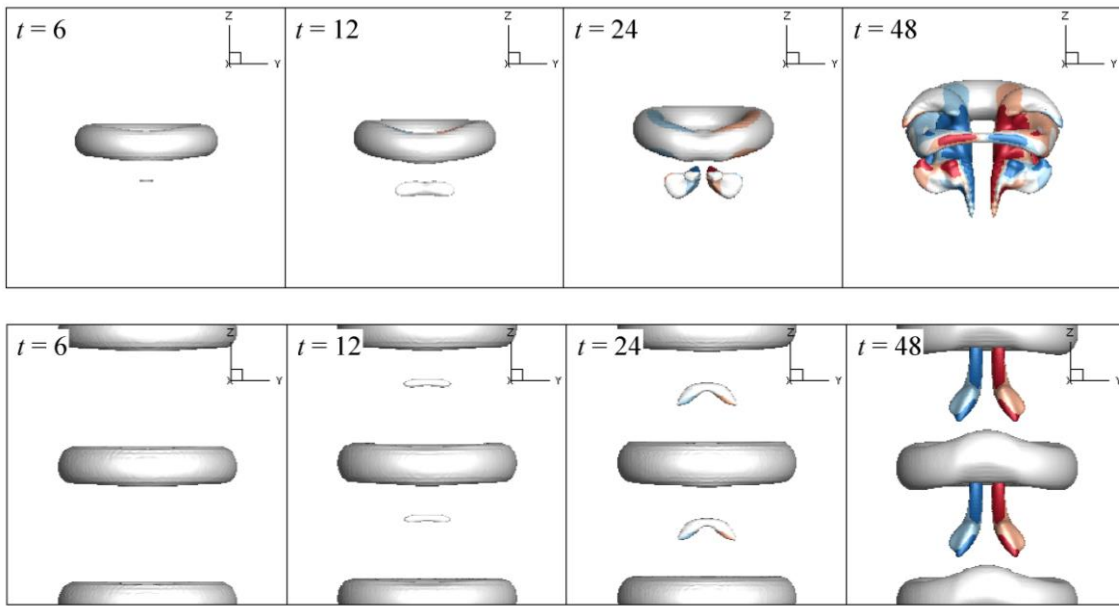
Figure 6-9 – View through the wall of (top row) an isolated vortex ring (Ring 1A) and (bottom row) the array of vortex rings. The graphic shows an iso-contour of the λ_2 field overlaid with contours of z-vorticity. Contours are [-3 -1 1 3], red indicates anti-clockwise rotation (with the rings approaching the observer

The reversal of this bending process is due to the interaction between neighbouring rings, and the boundary layer vorticity created by the ring immediately above it. This vorticity is initially small in magnitude, and therefore the inviscid bending mechanism of the wall is dominant. However, as the boundary layer vorticity develops, and the boundary layer spire begins to form, the x-vorticity that develops acts to pull the centre of the next ring upwards. This is shown in Figure 6-10; a slice through $x = -1.0$ shows coloured contours of x-vorticity, and line contours of z-velocity. The gaps between the rings initially contain positive z-velocity, however the inviscid bending dominates. After the growth of the boundary layer vorticity

from the ring above, the positive velocity region creeps downwards, bringing the near wall core upwards. This opposes the direction of bending initially induced by the wall.

The reversal of the direction of bending also has implications for the azimuthal velocity that develops within the core. Figure 6-11 shows contours of z-vorticity in an xy-plane through the ring, for $t = 6$, $t = 24$, and $t = 42$. The early time shows that the initial rotation direction of this swirl is the same as in the isolated ring case. The majority of the swirl rotation is still in this direction at $t = 16$, and the twin axial vortices have moved towards the center of the ring. However, a small region of oppositely rotating flow has formed, splitting up the swirl contours. By $t = 42$, the reverse bending process is the dominant feature, and the swirl at this time is therefore dominated by the reversed flow.

The reverse bending leads to the resulting dynamics for the multiple ring case being significantly different to the isolated vortex ring. Figure 6-12 provides the flow fields for the eighth ring in the array for a number of times between $t = 10$ and $t = 150$. The vortex rings do not tilt towards the wall, and system breaks down into a complicated mass of vortex tubes. The structure that remains from the rings in the middle of the domain is 40 units upstream of the initial position by $t = 150$.
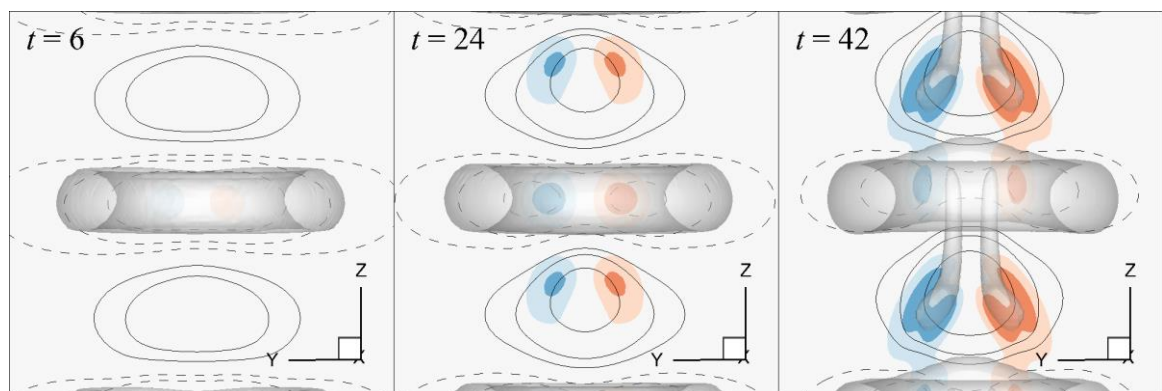
Figure 6-10 – The x-vorticity (colour) and z-velocity (line) contours on a plane at $x = -1.0$, looking into the wall. Red indicates clockwise rotation on the plane as it is viewed here, blue indicates anti-clockwise. Contours are [-0.20 -0.10 -0.05 0.05 0.10 0.20] for both velocity and vorticity. An iso-contour of λ_2 is included to show the ring position.
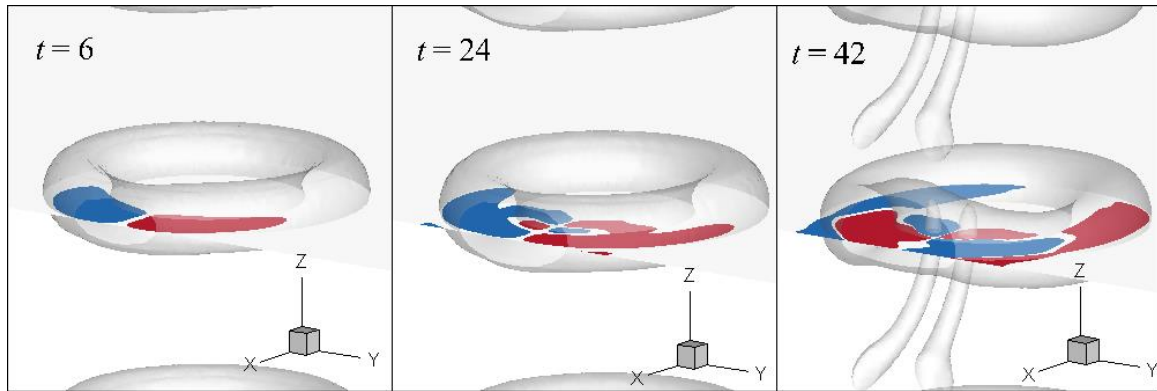
Figure 6-11 – (a) The z-vorticity field in an xy-plane at $z = z_c$, for the 8th ring in the ring array, at three different times. Red indicates anti-clockwise rotation (viewed as the ring approaches the observer). The twin axial vortices can be seen moving toward the centre of the ring, while the direction of rotation of the fluid reverses by $t = 42$. Contour levels are [-0.025 0.025]. The position of the ring is shown using an iso-contour of $\lambda_2 = -1$.
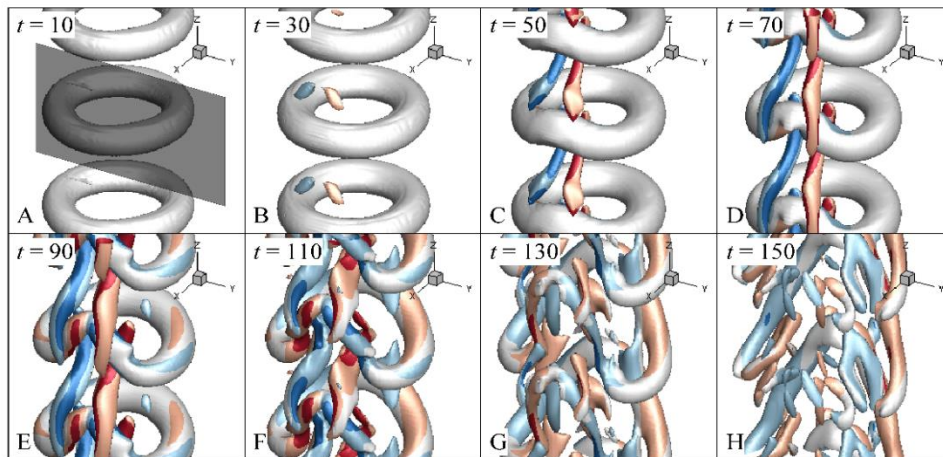
Figure 6-12 - Demonstration of the variation in the ring shape over the course of the near-wall evolution of the array of rings. Contours of z-vorticity [-3,-1,1,3] are overlaid on an iso-contour of the λ_2 field (grey surface). Red represents anti-clockwise rotation (viewed as the ring approaches the observer). The shaded region in the first frame shows a section of the wall for reference.

6.3.3. Temperature field of an array of rings

Given the observed differences between the dynamics of the array of vortex rings and those of a single vortex ring, it is unsurprising that the temperature field is also different. Figure 6-13 presents the temperature contours in a plane at $x = -0.5$, and a semi-transparent iso-contour of the λ_2 field. The primary influence of the vortex ring on the temperature field appears to be along the y-axis and between rings, where a large cooler region forms at $t = 40$, and remains visible at $t = 100$.

Figure 6-14 provides the temperature contours in the $y = 0$ plane, accompanied by a 3D visualization of the λ_2 iso-surface overlaid with contours of temperature, at the same four times. The interaction with the temperature contours occurs more slowly than for the single ring case (in Figure 6-2), although the influence on the $y = 0$ plane is very similar for $t = 10$. At $t = 40$, the near-wall core is still quite strong, unlike in the isolated ring case where the near-wall core has almost disappeared by this time. This suggests that without the tilt angle, the rings are able to keep their distance from the wall more effectively.
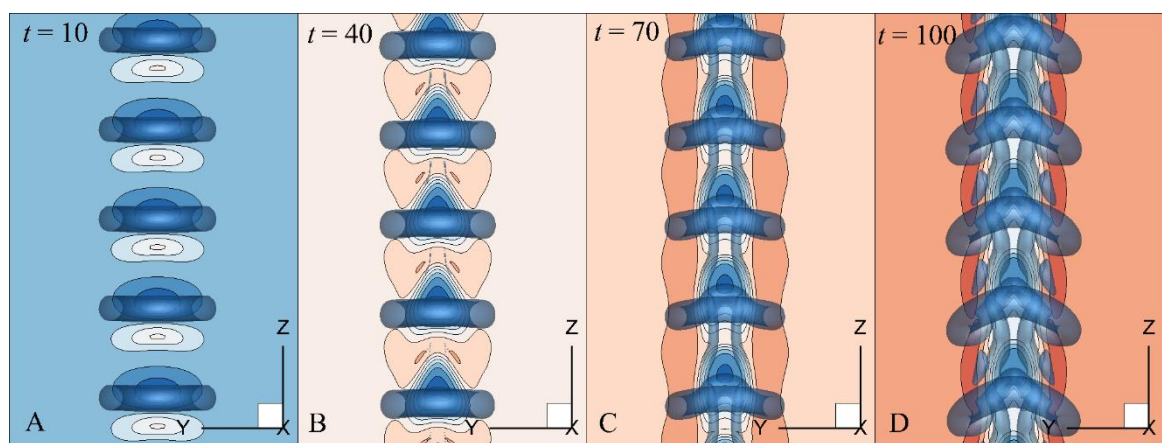
Figure 6-13 – An iso-contour of the λ_2 field, with a plane at $x = -0.5$, showing coloured contours of the temperature scalar field for four different times. The contour levels start at 0.1 and increase by 0.1. The changing colour of the background is due to the diffusion of the temperature field. The plane in the images is $20a_i$ in the y-direction, and $30a_i$ in the z-direction. This figure is analogous to Figure 6-1 in the isolated ring case.
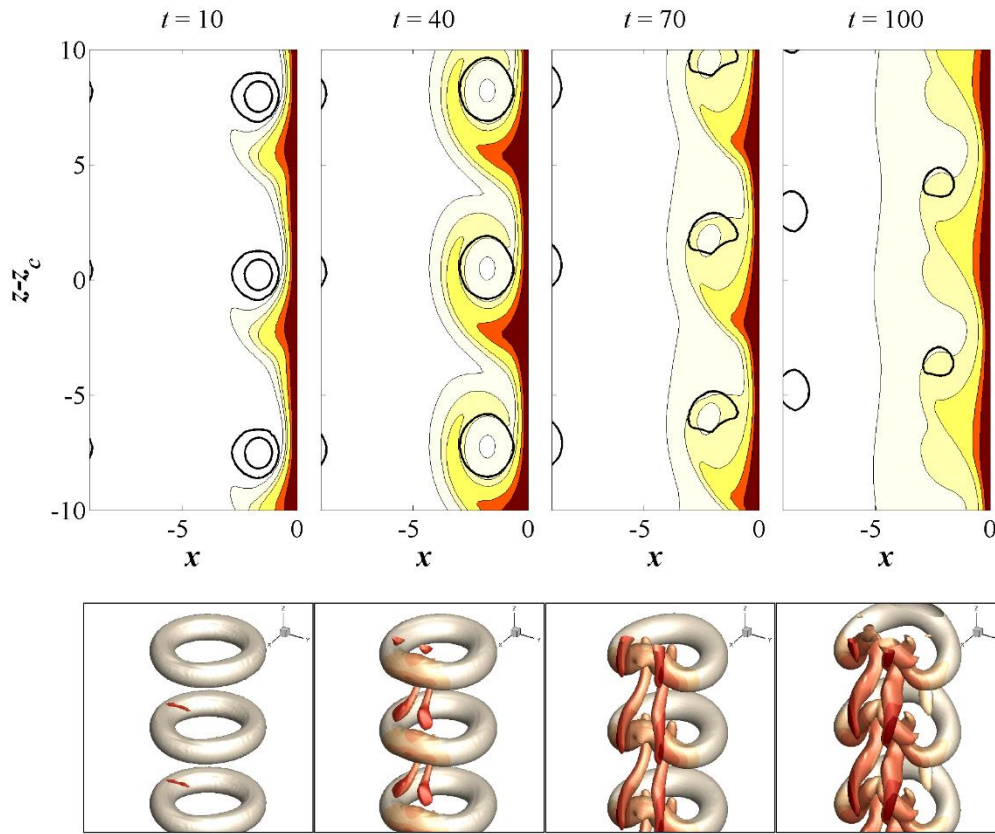
Figure 6-14 - Overview of the temperature fields induced by an array of near-wall vortex rings, at (left to right) t = 10, 40, 70, 100. The top row provides contours of temperature in the y = 0 plane, with a measure of the core position shown with the solid contour. The bottom row provides the same contours, overlaid on an iso-contour of the λ_2 field. The contours are [0.01 0.05 0.10 0.30 0.50], darker contours indicate higher temperatures. This figure is analogous to Figure 6-2 in the isolated ring case.

The quantitative measures of heat transfer used for the isolated ring case are repeated here. Figure 6-15 and Figure 6-16 provide the same information as Figure 6-3 and Figure 6-4, except for the multiple ring case. The primary difference noted is that a fluctuation occurs in the temperature upstream of the observed ring (the eighth in the array) due to the additional rings in the domain. The extra rings actually increase the upstream temperature of the near wall planes (dark blue line), and do not appear to aid in reducing the downstream temperature (black dashed line).
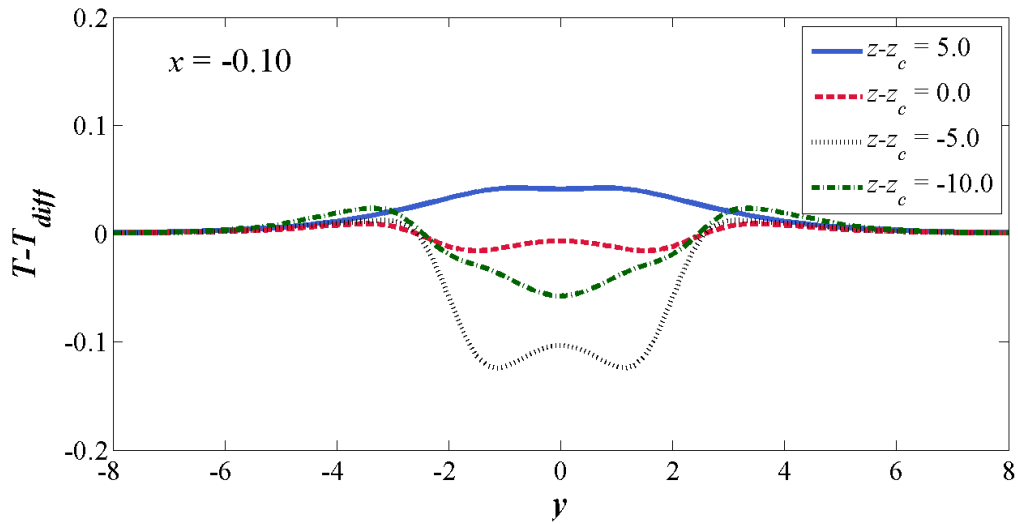
Figure 6-15 - An indication of the temperature profiles at $z - z_c$ as a function of y-position, for $x = -0.05$. The temperature due to diffusion has been subtracted from the value at each point, providing the true impact of the vortex ring. The sampling location is initially a distance of 10 units upstream of the eighth ring in the domain. This figure is analogous to Figure 6-3in the isolated ring case.
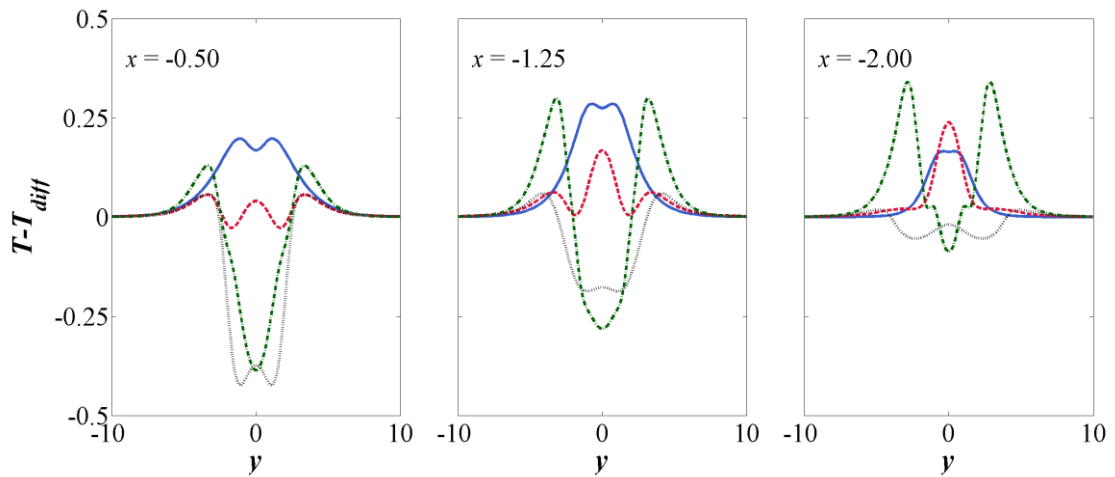
Figure 6-16 – An indication of the temperature profiles at $z - z_c$ as a function of y-position, for three additional *x*-positions. The temperature due to diffusion has been subtracted from the value at each point, providing the true impact of the vortex ring. The sampling location is initially a distance of 10 units upstream of the eighth ring in the domain. This figure is analogous to Figure 6-4 in the isolated ring case.

The spatially averaged temperature field (again over x-planes of size 20×20) is presented in Figure 6-17. The multiple ring case has a slightly larger decrease in temperature in the near wall planes than the single ring case, up to around $t = 40$. After this point, unlike in the case of the isolated vortex ring (see Figure 6-5), the influence it has on the temperature field does not significantly increase. This suggests that the heated fluid is not being transported away from the wall, and is retained within the near-wall region. The temperature of the $x = -2.00$ plane is similar for both cases, suggesting that the multiple rings have no issue with transferring heat to this distance. However, the $x = -5.84$ plane lacks the sharp increase in temperature seen in the isolated ring case, and only experiences a small increase after around $t = 100$. The lack of breakdown into the horseshoe-like vortex appears to be the primary culprit; without the low pressure fluid supply lines provided by the vortex core, no means is provided to transfer heated fluid out to the initial z-location of the ring centre.
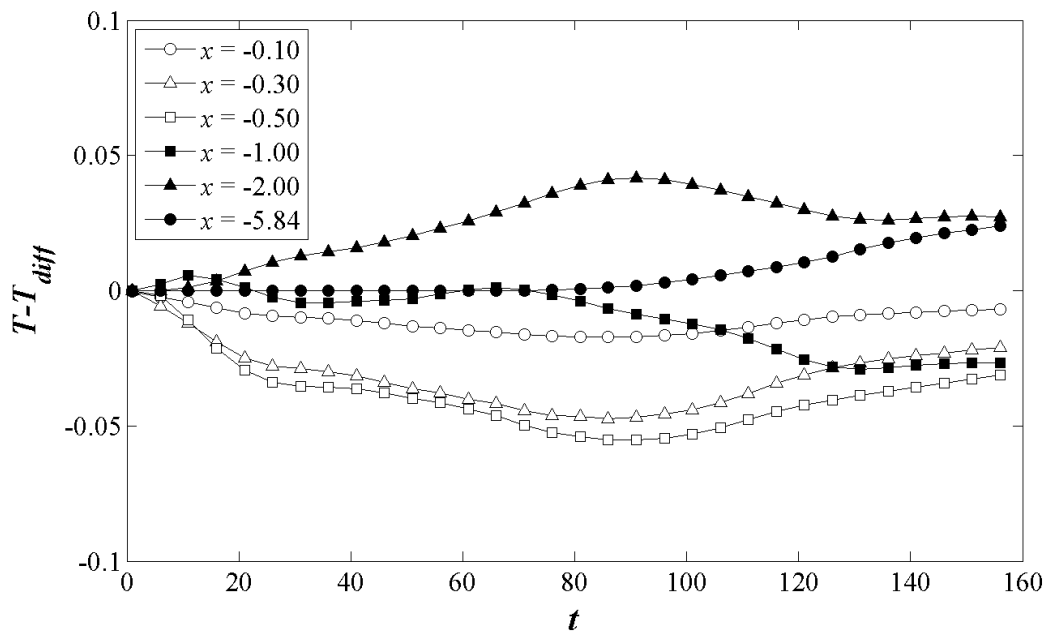
Figure 6-17 – The average temperature over time of various x-planes, within a 20x20 plane centred on the vortex ring. The temperature due to diffusion has been subtracted from the value at each point, providing the true impact of the vortex ring. This figure is analogous to Figure 6-5 in the isolated ring case.

Figure 6-18 shows that, at x = -0.5, the multiple ring case has superior average wall-normal velocity prior to t = 40, roughly equal up to t = 80, and then less for the rest of the evolution. At x = -0.1, it is only superior for $t < 32$. This suggests that, while the multiple ring case is at least initially superior in drawing away heated fluid from the wall boundary layer, it is ineffective at transporting it to the far side of the ring, and the heat remains entrained within the near-wall region. In addition, the wall-normal velocity at x = -0.1 appears to be closely linked to the cooling, as by t = 40, the cooling in the multiple ring case (in Figure 6-17) has diminished significantly.
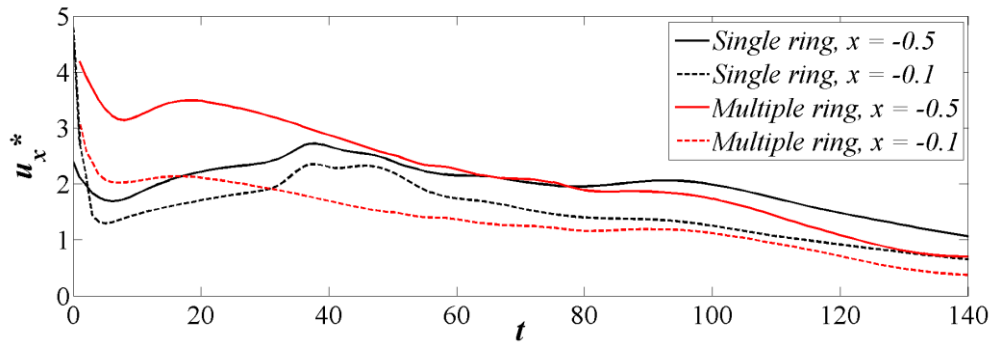
Figure 6-18 – Average wall-normal velocity for Ring 1A, at x = -0.5 and x = -0.1, for both cases, over a plane 20 x 20 in size, centred on either the isolated vortex ring, or the eighth ring in the array. The vertical axis shows u_x^*, which is defined as $u_x^* = u_x$ for x = -0.5, and $u_x^* = 10u_x$ for x = -0.1.

The later times of the multiple ring case, when the temperature is increasing and the average wall-normal velocity is decreasing, are shown in Figure 6-19. The remaining vortex structure breaks apart into a series of vortex tubes (as seen in the iso-surfaces), while the temperature field in the $y = 0$ plane is relatively uniform in appearance.
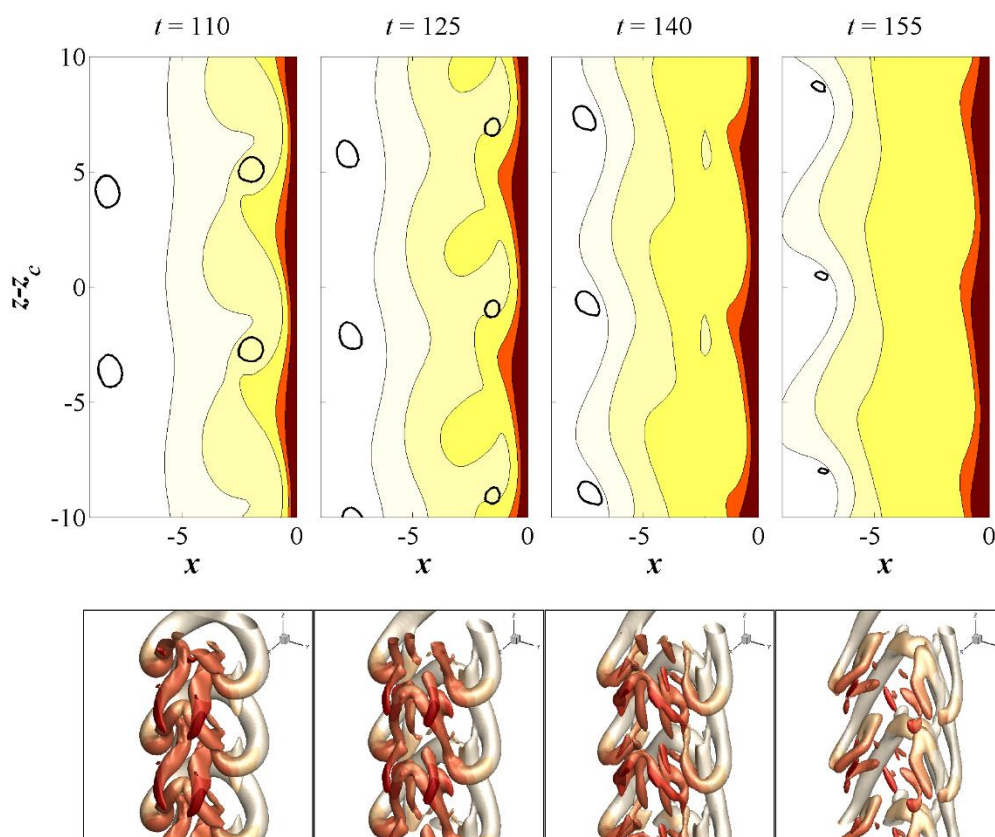
Figure 6-19 - Overview of the temperature fields induced by an array of near-wall vortex rings, at (left to right) t = 110, 125, 140, 155. The top row provides contours of temperature in the $y = 0$ plane, with a measure of the core position shown with the solid contour. The bottom row provides the same contours, overlaid on an iso-contour of the λ_2 field. The contours are [0.01 0.05 0.10 0.30 0.50], darker contours indicate higher temperatures. This figure is analogous to Figure 6-7 in the isolated ring case.

6.4 Conclusions

A scalar temperature field was implemented into the flow domain of Ring 1A from the previous chapter, and monitored over time. The Prandtl number used in the flow was defined to be similar to that of air at 300 K. The results indicate that the motion of the vortex ring near the wall has little initial impact on the temperature field, but begins to influence the field once the ring nears the thermal boundary layer. The vorticity that is generated along the wall contains heated fluid, which is drawn out from the wall as the boundary layer vorticity wraps into the vortex ring. At later times, after the near wall core has ceased to exist, the two horse-shoe like arms of the original vortex ring provide a means to draw heated fluid further away from the wall. This process continues to reduce the temperature in the near-wall region until the supply line is too weak to have a significant effect. The near-wall region reaches its coolest point (neglecting the influence of diffusion) at around $t = 130$, after the far-wall region of the vortex ring has advected this heated fluid even further from the wall, and entered the near-wall region itself.

The dynamics and temperature variations observed for an array of these vortex rings, spaced at intervals of $2R_i$, showed a variety of differences to the isolated ring case. In particular, the bending observed in the single ring case was opposed by the presence of additional rings, and reversed the direction of the generated swirl within the vortex ring. In addition, the magnitude of the temperature reduction in the near-wall region was hampered by the inclusion of multiple rings. The lack of development of the horseshoe-like vortex shape that occurred for the isolated ring appears to be the primary culprit. It should be noted, however, that this particular case only represents the behavior at a single ring separation, wall separation, and ring size. Varying these parameters, particularly the separation between rings, should bring the behavior back towards that of an isolated ring, with enhanced cooling potential. Further work should investigate the parameter space, to determine the wall spacing, ring spacing, and ring size that provide maximum cooling efficiency.

Chapter 7

Contributions and future work

The contributions of this thesis are summarised through the following eight key findings, which correspond to the aims introduced in Section 1.9. The discussion of the contributions is followed by an outline of the limitiations of this research, and suggestions for further study.

7.1 Contributions

7.1.1. Numerical relaxation of swirling vortex rings

Swirling vortex rings, evolved numerically from an initial Gaussian distribution, have been shown to evolve towards an equilibrated core distribution in a similar manner to non-swirling vortex rings. The arrangement of the core vorticity contours at the identified equilibration time is qualitatively similar to that of a piston generated vortex ring at the formation time. The time for this equilibration to occur was found to increase with larger swirl magnitudes, and decrease for rings with a larger initial thickness. A single term in the vorticity Navier-Stokes equations was shown to be the cause of the leading edge shear layer, while various terms in the velocity Navier-Stokes equations were identified as those responsible for the relaxation process. The evolution of the vortex ring following the equilibration process follows the same stages as a piston generated ring. The evidence presented here demonstrates the importance of relaxing swirling vortex rings axisymmetrically before instability growth rates or evolutionary properties are considered.

7.1.2. Development of secondary vortex rings

The shear layer that forms at the leading edge of relaxed swirling vortex ring is subject to an inviscid leading edge shear layer. A shear layer instability, related to the Kelvin-Helmholtz instability, was shown to form within this shear layer, eventually leading to the roll-up of a secondary vortex ring. The secondary vortex ring was observed to only form once the relaxation process had completed, the strength of the shear layer had reached a peak, and excess vorticity from the initial conditions had been convected into the wake. The development of the secondary ring was shown to rely on a sufficiently large shear Reynolds number ($Re_s > 100$) and swirl magnitude ($W_0 > 0.1$). The initial parameters of the vortex rings, including the ring aspect ratio Λ_0, can be related to the shear Reynolds number through the relation $\log_e(W_0\Lambda_0^3)$. Cases with $\log_e(W_0\Lambda_0^3) > -4.9$ all satisfy the relation $Re_s > 100$, and so develop a secondary ring as long as $W_0 > 0.1$. The shear layer weakens over time, and eventually another quasi-steady state is reached.

7.1.3. Primary instability mechanisms for swirling vortex rings

The development of instabilities on swirling vortex rings is fundametally the same as for Batchelor vortex pairs. The introduction of a swirling flow to a vortex ring will modify the Kelvin mode couplings, damping the [–1, +1] mode, and enhancing the growth of the [–2, 0] and [–3, –1] modes. The form of the most amplified mode is dependent solely on the value of the peak azimuthal wavenumber for a particular ring. However, even the most amplified mode does not experience peak growth conditions over the entirety of the ring, as the azimuthal wavenumber varies with the distance from the ring axis. A mode map was constructed in a modified κ-W (wavenumber-swirl magnitude) plane, allowing prediction of the most amplified mode to be made given the initial conditions of a swirling vortex ring. The relative positions of the predicted modes roughly matched those identified in previous work performed on Batchelor vortex pairs.

7.1.4. Growth rate of swirling vortex ring instabilities

The value of κ_c corresponding to the peak growth rate for a particular ring was found to vary with the ring aspect ratio. A similar observation was made for the magnitude of the peak growth rate for each ring. This variation was observed to be due to the aforementioned variation in wavenumber as a function of radius, and a normalisation parameter was derived, which describes this wavenumber variation as a function of the ring aspect ratio. Rings with increased thickness tend to have a lower peak growth rate, as the growth energy is spread over a wider range of wavenumbers.

7.1.5. Evolutionary characteristics of a near-wall vortex ring

The presence of a wall aligned parallel to the translation axis of a vortex ring was found to induce a localised swirling component in the section of the ring nearest the wall, due to bending of the ring in this region via precession. This leads to the development of an instability, similar in nature to resonant Kelvin mode instabilities,

but different in form. The swirl also advects two counter rotating axial vortices towards the ring centre, in a similar manner to that observed for vortex rings with global swirl. Vorticity originating from the boundary layer is advected outwards and into the centre of the vortex ring, wrapping around the vortex core. This is analogous to the boundary layer spire identified for straight vortices. The near-wall region of the ring provides the energy for this process, and dissipates over time. This leaves a horseshoe-like vortex, where the two ends of the horseshoe are attached to the wall; flow continues to be drawn out through the attached cores. The remaining horseshoe structure is continuously drawn towards the wall, and eventually the far-wall section of the ring enters the boundary layer region, creating a new vortex structure. Translation in the wall-parallel direction is reduced over time.

7.1.6. Wall normal velocity variance with ring parameters

The wall-normal velocity induced by the presence of a near-wall vortex ring is enhanced in the early evolution by several factors. The proximity and strength of the near-wall core is the primary contributor, whilst the advecting of the boundary layer vorticity into the ring centre also provides a significant amount of wall-normal velocity. For thinner rings, the boundary layer vorticity joins up with the counter-rotating axial vortices near the centre of the ring, and the contributions from the two separate phenomena combine to produce a peak in the wall-normal velocity, before the vortex core is destroyed. For thicker rings, the near-wall core is dissipated before the boundary layer vorticity provides a meaningful contribution, resulting in a dip in the wall-normal velocity. At later times, the horseshoe-like vortex provides a low pressure supply line for fluid from the wall via the vortex core, which is the sole contributor until the far-wall core enters the boundary layer region. A thin vortex ring has been shown to produce the same wall-normal velocity for less energy expenditure than an equivalent laminar developing boundary layer.

7.1.7. Effect on temperature field

A scalar temperature field was used to highlight the regions of the flow dominated by wall-normal velocity, as high temperature fluid is drawn away from the wall. At small distances from the wall, the results revealed a significant decrease in temperature, while at distances of more than a core radius, some regions showed increases, as heated fluid is transported to these positions. The average temperature of at different distances from the wall showed that the near-wall planes experience a minimum in temperature following the dissipation of the near-wall core. The planes further from the wall begin increasing in temperature at the same time as the low pressure supply lines become the primary wall normal flow mechanism. This suggests that although this period of the interaction occurs with a decrease in wall-normal velocity, the distance at which heated fluid is transported from the wall is largely increased.

7.1.8. Influence of multiple rings

The introduction of an array of vortex rings to the domain was not found to significantly increase the wall-normal velocity magnitude, and even slightly hampered the cooling effect provided by the isolated vortex ring. This was identified as being primarily due to the lack of development of the horseshoe-like vortex after the dissipation of the near-wall core. This does not mean that all such arrays will have the same effect; the particular model parameters chosen to demonstrate this flow were simply found to be less than ideal for the application.

7.1.9. Overall contribution

This thesis has made a significant contribution to the scientific understanding of vortex ring evolution. The numerical equilibration of swirling Gaussian vortex rings, and the properties of the leading edge shear layer that develops, has been shown in detail. The stability characteristics of these equilibrated rings has been compared to those of Batchelor vortex pairs, and the differences explained via the effect of finite

ring size. A near-wall vortex ring has been shown to evolve into a horseshoe-like vortex that provides low pressure supply line for fluid to move away from the wall. Finally, the temperature of boundary layer fluid due to the presence of a near-wall vortex ring is shown to be reduced by a number of different stages in the evolution.

7.2 Future work

Although this thesis has provided a comprehensive look at various aspects of vortex ring evolution, there remain some areas that require further elucidation. Specifically, extending the parameter space used in each section will help provide a more complete understanding.

7.2.1. Reynolds number variation

The primary limitation of the analyses within this thesis is the use of only a single Reynolds number in each parameter space. For Chapter 3, the initial Gaussian flow field is initialised with a Reynolds number of 10 000, although this number varies down to around 8 000 as the different rings go through their axisymmetric equilibration process. Typically, this relaxation is performed at high Reynolds number to reduce the impact on the size of the vortex ring due to viscous diffusion, however for swirling vortex rings it also has an impact on the strength of the leading edge shear layer. Further investigation would determine if the physics observed here are relevant for the development of swirling vortex rings at different Reynolds numbers.

The linear stability discussion in Chapter 4 uses the equilibrated flow fields from Chapter 3. The growth rates and corresponding instability modes are therefore tied to the Reynolds number of the ring at the completion of the equilibration process. As it is known that the Reynolds number has some impact on the growth rates of modes for Batchelor vortex pairs, the results are likely to vary with any modifications made to the Reynolds number of the flow.

The 3D considerations in Chapter 5 are undertaken using non-swirling vortex rings, at an equilibrated Reynolds number of 1 000. The use of 3D simulations necessitated the use of a lower Reynolds number, however returning to the higher Reynolds number used in the axisymmetric study (Re = 10 000) would provide more opportunities for comparison for the development of the near-wall azimuthal velocity. In addition, it is unknown how significantly lower Reynolds numbers would affect the evolution, as the increase in diffusive forces may restrict the initial inviscid development. It is therefore recommended that both higher Reynolds numbers (e.g. Re = 10 000), and lower Reynolds numbers (e.g. Re = 100) be considered to determine the range in which this work is valid.

7.2.2. Additional swirl magnitudes

The growth of the shear layer instability in Chapter 3 was shown to depend on the relation $\log_e(W_0 \Lambda_0^3)$. The largest value investigated in this thesis was $\log_e(W_0 \Lambda_0^3) > -3.5$, however the evolution at larger values would provide a more complete picture. Further increasing Λ_0 is unphysical, as much of the vorticity and ring thickness is already lost in the relaxation process. However, increasing the magnitude of W_0 is justifiable, as the values of swirl used in this thesis are relatively small. Increasing this value risks having the ring tear itself apart before the equilibration process can complete, however this should be confirmed in future work. This would also allow the extension of the mode map developed in Chapter 4.

7.2.3. Modified base flow for instability analysis

The linear stability analysis for the swirling vortex rings was undertaken at a fixed point in time for each ring. This time was chosen using a similar method to that of non-swirling rings, by identifying the time at which numerical relaxation from the initial Gaussian conditions had ceased. However, while non-swirling rings only experience dissipation after this time, swirling rings have additional flow structures (i.e. the axial vortex, the shear layer, the Kelvin-Helmholtz shedding) that continue to influence the flow after this time. Therefore, while this particular time was chosen

as the sweet spot in the evolution (after numerical relaxation but before any Kelvin-Helmholtz shedding), possessing similar flow conditions to that of a newly formed piston-generated ring, attempting the analysis at other times may produce vastly different results. Further research is required to determine the full interaction between the elliptic instability modes and the additional flow structures.

7.2.4. Additional wall separations

The three wall separations implemented in Chapter 5 show various trends induced by varying the wall separation, however these trends are unable to be explored in depth due to a lack of data points. Although it would be ill-advisable to move the rings significantly closer to the wall, adding additional data points in the range $1.0 < b_i < 4.0$ may allow an empirical relationship between wall separation and wall-normal velocity to be derived. The extra data points will also help determine if an optimal wall separation exists for the enhancement of wall-normal velocity.

7.2.5. Additional analysis techniques

The unidentified instability discussed in Chapter 5 may be explored through the use of additional analysis techniques. The use of the Wentzel-Kramers-Brillouin method has the potential to provide more information, while employing a slip condition at the wall could simplify the flow field, allowing a more detailed investigation.

7.2.6. Dynamic temperature field

The method used here to investigate the influence of the wall-vortex ring interaction on a temperature field allowed information only to be transferred in one direction; the change in the temperature field did not influence the flow dynamics. As buoyancy effects may be crucial in real-world applications, additional simulations with a full heat transfer analysis are required. However, the choice for the direction of gravity requires careful consideration, as it could be argued that all directions are plausible in terms of potential applications.

7.2.7. Multiple vortex rings and simulated synthetic jets

The brief look at the multiple vortex ring case revealed that the chosen parameters had a negative impact on the cooling potential of an isolated vortex ring. In order to determine how to improve the development of the flow such that the wall-normal velocity closer matches or even enhances that of an isolated ring, a parameter space study should be undertaken. This is not a small task, as in addition to all the parameters considered in the near-wall section (Re, Λ, W, b), the separation between each ring can be chosen from a wide range of values. In addition, variable ring spacing and different ring aspect ratios could be combined in a single array.

7.2.8. Final thoughts

The work on the axisymmetric evolution of swirling vortex rings and their stability characteristics has been invaluable in relating aspects of the near-wall development back to understood phenomena. However, further exploration of the near-wall case is advisable before any further work is performed on these earlier sections. A full picture of the near-wall evolution, across a more refined parameter space, is required before further understanding of the specific phenomena can be sought. It is suggested that future work focus on the thin ring from this study ($\Lambda_0 = 0.26$) at additional wall separations in the range $1.0 < b_i < 4.0$. This should be performed using the multiple ring scenario, ensuring that larger separations between rings (*i.e.* greater than $2R_i$) are implemented.

References

AHLIN, G. A. & BROWN, R. E. 2009. Wake Structure and Kinematics in the Vortex Ring State. *Journal of the American Helicopter Society,* 54.

AKHMETOV, D. G., LUGOVTSOV, B. A. & TARASOV, V. F. 1980. Extinguishing Gas and Oil Well Fires by Means of Vortex Rings. *Combustion Explosion and Shock Waves,* 16**,** 490-494.

AMITAY, M., HONOHAN, A., TRAUTMAN, M. & GLEZER, A. 1997. Modification of the Aerodynamic Characteristics of Bluff Bodies Using Fluidic Actuators. *AIAA Journal,* 97.

ANDERSON, E. J. & GROSENBAUGH, M. A. 2005. Jet flow in steadily swimming adult squid. *J Exp Biol,* 208**,** 1125-46.

ARCHER, P. J., THOMAS, T. G. & COLEMAN, G. N. 2008. Direct numerical simulation of vortex ring evolution from the laminar to the early turbulent regime. *Journal of Fluid Mechanics,* 598**,** 201-226.

BARKLEY, D. & HENDERSON, R. D. 1996. Three-dimensional Floquet stability analysis of the wake of a circular cylinder. *Journal of Fluid Mechanics,* 322**,** 215-241.

BATCHELOR, G. K. 1967. *An Introduction to Fluid Dynamics,* Cambridge University, Cambridge University Press.

BEGG, S., KAPLANSKI, F., SAZHIN, S., HINDLE, M. & HEIKAL, M. 2009. Vortex ring-like structures in gasoline fuel sprays under cold-start conditions. *International Journal of Engine Research,* 10**,** 195-214.

BLANCO-RODRIGUEZ, F. J. & LE DIZES, S. 2016. Elliptic instability of a curved Batchelor vortex. *Journal of Fluid Mechanics,* 804**,** 224-247.

BLASIUS, H. 1908. Grenzschichten in Flüssigkeiten mit kleiner Reibung. *Zeitschrift für angewandte Mathematik und Physik,* 56**,** 1-37.

BOUSTEAD, N. 2012. *The Haemodynamics of Aneurysms: A Spectral Element Analysis of the Effects of Wall Stiffness,* PhD, Monash University.

CERRA JR, A. W. & SMITH, C. R. 1983. Experimental Observations of Vortex Ring Interaction with the Fluid Adjacent to a Surface. Lehigh University Bethlehem PA Department of Mechanical Engineering and Mechanics.

CHAHINE, G. L. & GENOUX, P. F. 1983. Collapse of a caviating vortex ring. *Journal of Fluid Engineering,* 105**,** 400-405.

CHANG, T. Y., HERTZBERG, J. R. & KERR, R. M. 1997. Threedimensional vortex/wall interaction: Entrainment in numerical simulation and experiment. *Physics of Fluids,* 9**,** 57-66.

CHEN, Z., SWEARINGEN, J. D. & HANDLER, R. A. 1997. *The vortex ring interaction with an inclined wall*, University of Kansas, Mechanical Engineering.

CHENG, M., LOU, J. & LIM, T. T. 2010. Vortex ring with swirl: A numerical study. *Physics of Fluids,* 22.

CROW, S. 1970. Stability theory for a pair of trailing vortices. *AAIA Journal,* 8**,** 2172-2179.

DANAILA, I. & HELIE, J. 2008. Numerical simulation of the postformation evolution of a laminar vortex ring. *Physics of Fluids,* 20.

DANAILA, I., KAPLANSKI, F. & SAZHIN, S. 2015. Modelling of Confined Vortex Rings. *Journal of Fluid Mechanics,* 774**,** 267-293.

DANAILA, I., VADEAN, C. & DANAILA, S. 2009. Specified discharge velocity models for numerical simulations of laminar vortex rings. *Theoretical Computational Fluid Dynamics,* 23**,** 317-332.

DAZIN, A., DUPONT, P. & STANISLAS, M. 2006. Experimental characterization of the instability of the vortex ring. Part 1: Linear phase. *Experiments in Fluids,* 40**,** 383-399.

DEGANI, A. T. & WALKER, J. D. Calculation of unsteady separation from stationary and moving walls. IUTAM Symposium on Bluff-Body Wakes, Dynamics, and Instabilities, 1992 Gottingen, Germany. Springer-Verlag.

DOLIGALSKI, T. L., SMITH, C. R. & WALKER, J. D. 1994. Vortex interactions with walls. *Annual Review of Fluid Mechanics,* 26**,** 573-616.

DOLIGALSKI, T. L. & WALKER, J. D. 1978. Boundary layer induced by a convected two-dimensional vortex. *Journal of Fluid Mechanics,* 139**,** 1-28.

EGELHOFF, C. J. B., R. S., ELGER, D. F., KHRAISHI, T. A. & JOHANSEN, K. H. 1999. Model studies of the flow in abdomainal aortic aneurysms during resting and exercise conditions. *Journal of Biomechanics,* 32**,** 1319-1329.

ELLIOT, J. W., COWLEY, S. J. & SMITH, F. T. 1983. Breakdown of boundary layers: (i) on moving surfaces; (ii) in self-similar unsteady flows; (iii) in fully unsteady flow. *Geophysical and Astrophysical Fluid Dynamics,* 25**,** 77-138.

ELOY, C. & LE DIZES, S. 1999. Three-dimensional instability of Burgers and Lamb-Oseen vortices in a strain field. *Journal of Fluid Mechanics,* 378**,** 145-166.

ERSOY, S. & WALKER, J. D. 1987. The boundary layer due to a three-dimensional vortex loop. *Journal of Fluid Mechanics,* 185**,** 569-598.

FRAENKEL, L. E. 1972. Examples of Steady Vortex Rings of Small Cross-Section in an Ideal Fluid. *Journal of Fluid Mechanics,* 51**,** 119-&.

FUCHIWAKI, M., KUROKI, T., TANAKA, K. & TABABA, T. 2013. Dynamic behaviour of the vortex ring formed on a butterfly wing. *Experiments in Fluids,* 54.

FUKUMOTO, Y. & HATTORI, J. 2005. Curvature instability of a vortex ring. *Journal of Fluid Mechanics,* 526**,** 77-115.

GHARAKHANI, A. & GHONIEM, A. F. 1998. Simulation of the Piston Driven Flow Inside a Cylinder With an Eccentric Port. *Journal of Fluid Engineering,* 120.

GHARIB, M., RAMBOD, E. & SHARIFF, K. 1998. A universal time scale for vortex ring formation. *Journal of Fluid Mechanics,* 360**,** 121-140.

GHOSH, D. & BAEDER, D. 2012. High-order accurate incompressible Navier-Stokes algorithm for vortex ring interactions with solid wall. *AIAA Journal,* 50**,** 2408-2422.

GLEZER, A. 1988. The Formation of Vortex Rings. *Physics of Fluids,* 31**,** 3532-3542.

GLEZER, A. & AMITAY, M. 2002. Synthetic Jets. *Annual Review of Fluid Mechanics,* 34**,** 503-529.

HARVEY, J. K. & PERRY, F. J. 1971. Flowfield produced by trailing vortices in the vicinity of the ground. *AIAA journal,* 9**,** 1659-1660.

HATTORI, Y. & FUKUMOTO, Y. 2003. Short-wavelength stability analysis of thin vortex rings. *Physics of Fluids,* 15**,** 3151-3163.

HATTORI, Y. & FUKUMOTO, Y. 2012. Effects of axial flow on the stability of a helical vortex tube. *Physics of Fluids,* 24.

HETTEL, M., WETZEL, F., HABISREUTHER, P. & BOCKHORN, H. 2007. Numerical verification of the similarity laws for the formation of laminar vortex rings. *Journal of Fluid Mechanics,* 590**,** 35-60.

HU, G., SUN, D. & YIN, X. 2001. A numerical study on vortex rings with swirl. *Journal of Hydrodynamics,* 2.

ISHIZUKA, S., YAMASHITA, T. & SHIMOKURI, D. 2013. Further investigation on the enhancement of flame speed in vortex ring combustion. *Proceedings of the Combustion Institute,* 34**,** 745-753.

JEONG, J. & HUSSAIN, F. 1995. On the identification of a vortex. *Journal of Fluid Mechanics,* 285**,** 69-94.

KAPLANSKI, F., SAZHIN, S. S., BEGG, S., FUKUMOTO, Y. & HEIKAL, M. 2010. Dynamics of vortex rings and spray-induced vortex ring-like structure. *European journal of mechanics. B: Fluids,* 29**,** 195-214.

KARNIADAKIS, G. & SHERWIN, S. 1999. *Spectral/hp Element Methods for Computational Fluid Dynamics*, Oxford University Press.

KARNIADAKIS, G. E., ISRAELI, M. & ORSZAG, S. A. 1991. High-Order Splitting Methods for the Incompressible Navier Stokes Equations. *Journal of Computational Physics,* 97**,** 414-443.

KERSWELL, R. R. 2002. Elliptical instability. *Annual Review of Fluid Mechanics,* 34**,** 83-113.

KHERADVAR, A. & GHARIB, M. 2007. Influence of ventricular pressure drop on mitral annulus dynamics through the process of vortex ring formation. *Annals of Biomedical Engineering,* 35**,** 2050-64.

KOKSHAYSKY, N. V. 1979. Tracing the Wake of a Flying Bird. *Nature,* 279**,** 146-148.

LACAZE, L., RYAN, K. & LE DIZES, S. 2007. Elliptic Instability in a Strained Bachelor Vortex. *Journal of Fluid Mechanics,* 577**,** 341-361.

LAMB, S. H. 1879. *Hydrodynamics,* Cambridge, Cambridge University Press.

LE DIZES, S. & LAPORTE, F. 2002. Theoretical predictions for the elliptical instability in a two-vortex flow. *Journal of Fluid Mechanics,* 471**,** 169-201.

LE DIZES, S. & VERGA, A. 2002. Viscous interactions of two co-rotating vortices before merging. *Journal of Fluid Mechanics,* 467**,** 389-410.

LEWEKE, T. & WILLIAMSON, C. H. K. 1998. Cooperative elliptic instability of a vortex pair. *Journal of Fluid Mechanics,* 360**,** 85-119.

LIFSCHITZ, A., SUTERS, W. H. & BEALE, J. T. 1996. The onset of instability in exact vortex rings with swirl. *Journal of Computational Physics,* 129**,** 8-29.

LIM, T. T. 1989. An experimental study of a vortex ring interacting with an inclined wall. *Experiments in Fluids,* 7**,** 453-463.

LIM, T. T. 1997. On the role of Kelvin-Helmholtz-like instability in the formation of turbulent vortex rings. *Fluid Dynamics Research,* 21**,** 47.

LUNDGREN, T. S., YAO, J. & MANSOUR, N. N. 1992. Microburst Modeling and Scaling. *Journal of Fluid Mechanics,* 239**,** 461-488.

MALLINSON, S. G., HONG, G. & REIZES, J. A. 1999. An experimental and numerical study of synthetic jet flow. *The Aeronautical Journal,* 105**,** 41-49.

MAXWORTHY, T. 1972. The structure and stability of vortex rings. *Journal of Fluid Mechanics,* 51**,** 15-32.

MELANDER, M. V. & HUSSAIN, F. 1994. Topological vortex dynamics in axisymmetric viscous flows. *Journal of Fluid Mechanics,* 260**,** 57-80.

MICHALKE, A. 1964. On the Inviscid Instability of the Hyperbolic-Tangent Velocity Profile. *Journal of Fluid Mechanics,* 19**,** 543-556.

MILNE-THOMSON, L. M. 1962. *Theoretical Hydrodynamics,* London, MacMillan.

MOFFATT, H. K. 1988. Generalized vortex rings with and without swirl. *Fluid Dynamics Results,* 3**,** 22-30.

MOHSENI, K. 2006. A formulation for calculating the translational velocity of a vortex ring or pair. *Bioinspir Biomim,* 1**,** S57-64.

MOORE, D. W. & SAFFMAN, P. G. 1972. The motion of a vortex filament with axial flow. *Philosophical Transcrips of the Royal Society of London,* 272.

MOORE, D. W. & SAFFMAN, P. G. 1973. Axial flow in laminar trailing vortices. *Proceedings of the Royal Society of London,* 333**,** 491-508.

MOORE, D. W. & SAFFMAN, P. G. 1975. The instability of a straight vortex filament in a strain field. *Proceedings of the Royal Society of London,* 346**,** 415-425.

NAITOH, T., FUKUDA, N., GOTOH, T., YAMADA, H. & NAKAJIMA, K. 2002. Experimental study of axial flow in a vortex ring. *Physics of Fluids,* 14**,** 143-149.

NAITOH, T., OKURA, N., GOTOH, T. & KATO, Y. 2014. On the evolution of vortex rings with swirl. *Physics of Fluids,* 26.

NORBURY, J. 1973. A family of steady vortex rings. *Journal of Fluid Mechanics,* 57**,** 417-431.

OOI, A., SORIA, J., LIM, T. T., KOLLMANN, W. & CHONG, M. S. 2001. A Numerical Study of Swirling Vortex Rings. *Casual Productions for Adelaide University***,** 375-378.

ORLANDI, P. & VERZICCO, R. Helical structures in oblique collisions of vortex rings with a wall. *In:* DESHPANDE, P., SREENIVASAN, VISWANATH, ed. Proceedings of the Symposium on Developments in Fluid Dynamics and Aerospace Engineering, 1993a. Elsevier Science Publishing, 70-86.

ORLANDI, P. & VERZICCO, R. 1993b. Vortex rings impinging on walls: axisymmetric and three-dimensional simulations. *Journal of Fluid Mechanics,* 256**,** 615-646.

PANDA, J. & MCLAUGHLIN, R. 1994. Experiments on the instabilities of a swirling jet. *Physics of Fluids,* 6**,** 263-276.

PAVLOVA, A. & AMITAY, M. 2006. Electronic cooling using synthetic jet impingement. *Journal of Heat Transfer,* 128.

PERIDIER, V. J., SMITH, F. T. & WALKER, J. D. 1991. Vortex-induced boundary-layer separation. Part I. The limit problem as Re approaches infinity. *Journal of Fluid Mechanics,* 232**,** 99-131.

RAYLEIGH, L. 1880. On the stability, or instability, of certain fluid motions. *Proceedings of the London Mathematical Society,* 1**,** 474-487.

REYNOLDS, O. 1883. An experimental investigation of the circumstances which determine whether the motion of water shall be direct or sinuous, and the law of resistance in parallel channels. *Philosophical Transcrips of the Royal Society of London,* 174**,** 935-982.

ROBINSON, S. K. 1997. Coherent motions in the turbulent boundary layer. *Annual Review of Fluid Mechanics,* 23**,** 601-639.

ROJANARATANANGKULE, W. A Numerical Investigation of a Vortex Ring in a Rotating Fluid. Recent Advances on Applied Mathematics and Computational Methods in Engineering, 2015.

ROY, C., SCHAEFFER, N., LE DIZES, S. & THOMPSON, M. 2008. Stability of a pair of co-rotating vortices with axial flow. *Physics of Fluids,* 20.

RYAN, K., BUTLER, C. J. & SHEARD, G. J. 2012. Stability characteristics of a counter-rotating unequal-strength Batchelor vortex pair. *Journal of Fluid Mechanics,* 696**,** 374-401.

SAFFMAN, P. G. 1970. The velocity of viscous vortex rings. *Studies in applied mathematics,* 49**,** 371-80.

SAFFMAN, P. G. 1978. The number of waves on unstable vortex rings. *Journal of Fluid Mechanics,* 84**,** 625-639.

SAFFMAN, P. G. 1992. *Vortex Dynamics*, Cambridge University Press.

SALSAC, A.-V. S., S. R., CHOMAZ, J.-M. & LASHERAS, J. C. 2006. Evolution of the wall shear stresses during the progressive enlargement of symmetric abdominal aortic aneurysms. *Journal of Fluid Mechanics,* 260**,** 19-51.

SHARIFF, K. & LEONARD, A. 1992. Vortex Rings. *Annual Review of Fluid Mechanics,* 24**,** U235-U279.

SHARIFF, K., VERZICCO, R. & ORLANDI, P. 1994. A numerical study of three-dimensional vortex ring instabilities: viscous corrections and early nonlinear stage. *Journal of Fluid Mechanics,* 279**,** 351-375.

SHEARD, G. J. 2009. Flow dynamics and wall shear-stress variation in a fusiform aneurysm. *Journal of Engineering Mathematics,* 64**,** 379-390.

SHEARD, G. J. & KING, M. P. 2011. Hoizontal convection: Effect of aspect ratio on Rayleigh number scaling and stability. *Applied Mathematical Modelling,* 35**,** 1647-1655.

SHEARD, G. J., LEWEKE, T., THOMPSON, M. & HOURIGAN, K. 2007. Flow around an impulsively arrested circular cylinder. *Physics of Fluids,* 19**,** 1.

SHEARD, G. J. & RYAN, K. 2007. Pressure-driven flow past spheres moving in a circular tube. *Journal of Fluid Mechanics,* 592**,** 233-262.

SIPP, D. & JACQUIN, L. 2003. Widnall instabilities in vortex pairs. *Physics of Fluids,* 15.

STEWART, K. C., NIEBEL, C. L., JUNG, S. & VLACHOS, P. P. 2012. The decay of confined vortex rings. *Experiments in Fluids,* 53**,** 163-171.

STEWART, K. C. & VLACHOS, P. P. 2012. Vortex rings in radially confined domains. *Experiments in Fluids,* 53**,** 1033-1044.

SWEARINGEN, J. D., CROUCH, J. D. & HANDLER, R. A. 1995. Dynamics and Stability of a Vortex Ring Impacting a Solid Boundary. *Journal of Fluid Mechanics,* 297**,** 1-28.

THOMSON, W. 1867. On Vortex Atoms. *Proceedings of the Royal Society of Edinburgh,* 6**,** 94-105.

THOMSON, W. 1880. Vibrations of a columnar vortex. *Philosopical Magazine,* 5**,** 155-168.

TSAI, C. Y. & WIDNALL, S. E. 1976. The stability of short waves on a straight vortex filament in a weak externally imposed strain field. *Journal of Fluid Mechanics,* 73**,** 721-733.

TURKINGTON, B. 1989. Vortex ring with swirl: Axisymmetric solutions of the Euler equations with non-zero helicity. *Journal of Mathematical Analysis,* 20**,** 57-73.

VERZICCO, R. & ORLANDI, P. 1994. Normal and oblique collisions of a vortex ring with a wall. *Meccanica,* 29**,** 383-391.

VERZICCO, R. & ORLANDI, P. 1996. Wall/vortex-ring interactions. *Applied Mechanics Reviews,* 49**,** 447-461.

VIRK, D., MELANDER, M. V. & HUSSAIN, F. 1994. Dynamics of a Polarized Vortex Ring. *Journal of Fluid Mechanics,* 260**,** 23-55.

VISBAL, M. R. 1991. Structure of laminar juncture flows. *AIAA journal,* 29**,** 1273-1282.

WALKER, J. D. 1978. Impact of a vortex ring on a wall. *Journal of Fluid Mechanics,* 181**,** 99-140.

WEIGAND, A. & GHARIB, M. 1997. On the evolution of laminar vortex rings. *Experiments in Fluids,* 22**,** 447-457.

WIDNALL, S., BLISS, D. B. & ZALAY, A. Theoretical and experimental study of the stability of the vortex pair. Proceedings of Aircraft Wake Turbulence Symposium, 1970 Seattle, USA. Springer.

WIDNALL, S. & TSAI, C. 1977. The instability of the thin vortex ring of constant vorticity. *Philosophical Transcripts of the Royal Society of London,* 287**,** 273-305.

WIDNALL, S. E., BLISS, D. B. & TSAI, C. 1974. The instability of short waves on a vortex ring. *Journal of Fluid Mechanics,* 66.

WIDNALL, S. E. & SULLIVAN, J. P. 1973. On The Stability of Vortex Rings. *Mathematical, Physical, and Engineering Sciences*.

YAGAMI, H. & UCHIYAMA, T. 2011. Numerical simulation for the transport of solid particles with a vortex ring. *Advanced Powder Technology,* 22**,** 115-123.

YAMADA, H., MOCHIZUKI, O., YAMABE, H. & MATSUI, T. 1985. Pressure variation on a flat wall induced by an approaching vortex ring. *Journal of the Physical Society of Japan,* 54**,** 4151-4160.

Appendix A

The detected circulation of the ring at each of the three positions is compared for each different sample. For cases where the step size is halved, Richardson extrapolation is used to predict the mesh independent value. Otherwise, the data is compared to the most resolved case. The discrepancy between each set up and this extrapolated value is given. The data for all cases is provided in Table A-1, while a description of the findings follows.

Test A – Refined region size

The limiting factor for the refined region domain size is the y-direction, as the ring quickly moves away from the edge of the refined region in the x-direction. It can be seen from the data that a refined region length of 14 is acceptable, as there is not much variation between the 14, 16, and 20 values. At later times, however, the vortex rings expands outwards to a large degree. The refined region in the y-direction has therefore been set to be 24, to accommodate this later evolution.

Test B – Refined region step size

It is clear that the step size within the refined region does not have a huge impact on the data, due mainly to the fact that the fine details that require resolving occur in the boundary layer region. A step size of $2a_i$ is likely more than adequate to resolve the typical ring evolution, however a step size of a_i has been chosen for the simulations, in the event that later evolution dynamics require a more refined spacing.

Test C – Boundary layer step size

Clearly, for the behaviour near the wall at $t = 30$, all boundary layer separations provide adequate resolution. However, at later times, the boundary layer thickness be as low as $0.3a_i$. In order to ensure proper resolution of any wall based phenomena at this time, 8 points across this boundary layer is desirable, and so the 1/32 spacing has been selected.

Test D – Boundary layer extent

In a similar vein, it does not matter whether there is a boundary layer mesh or not at this time, however in order to ensure resolution of any subsequent wall based phenomena, the boundary layer thickness has been chosen to be $0.5a_i$.

Test E – Step size in the z-direction

Given the large domains required due to the periodic boundary conditions, having a very small plane separation is computationally expensive. It is thus important to choose the largest plane separation that would provide accurate results. The information given in Table A-1, suggests that four planes per initial core radius are required to provide an error of around 1%.

Test F – Z domain size

The requirement for the z-domain range is that the periodic boundary conditions must have a negligible influence on the vortex ring; otherwise, the condition of isolation is lost. It is more useful in this case to look at the trend of the data, rather than the raw values.

Figure A-1 presents the raw circulation data plotted as a function of the inverse of the domain length. As the inverse goes to zero (so the domain goes to infinity), the circulation goes to its grid independent value.. Extrapolating the data suggests that a z-domain of approximately $400a_i$ is required for a 1% error, or $200a_i$ for a 2% error. Given that this error affects the entire flow field equally, a 2% difference was deemed

190

acceptable. Any larger is not feasible to use in conjunction with the required z-step size of 0.25.

Test G – Final set-up

The final mesh design follows the decisions made in the grid resolution study, with one key addition. A transition region is added between the boundary layer mesh and the refined region mesh in the *x*-direction, to prevent inconsistencies due to the sharp jump in mesh size.
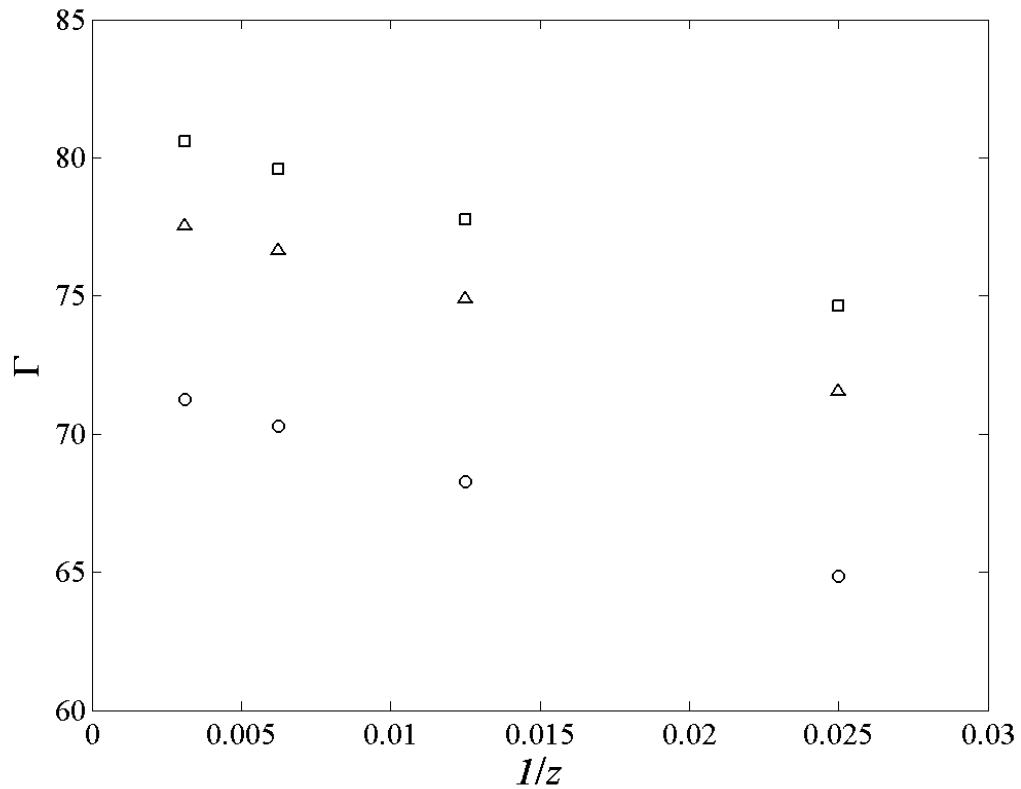

Figure A-1 – Convergence of the circulation parameter with the inverse of the domain size, for the three different θ-angles considered. The symbols refer to the $\theta = 0$ from $y = 0$ (circles), $\theta = 0$ from $y = a_i$ (triangles), and $\theta = \pi$ from $y = 0$ (squares).

Table A-1 – Grid resolution data for the near-wall simulations. Each value is given as a percentage difference between the value found, and either the most resolved case, or the Richardson Extrapolated Value.

	Γ	Γ	Γ	Γ
θ-plane	0	π	0	$\pi/2$
y-centre	0	0	1	0
Test A – Variation due to X_r and Y_r				
10	0.23%	23.35%	94.77%	2.45%
12	0.00%	0.36%	3.16%	0.12%
14	0.00%	0.00%	0.01%	0.02%
16	0.00%	0.03%	0.34%	0.05%
20	64.90	74.59	71.36	74.66
Test B – Variation due to Δ_{xy}				
2.00	0.32%	0.11%	0.32%	0.30%
1.00	0.07%	0.00%	0.06%	0.02%
0.50	0.04%	0.01%	0.02%	0.01%
0.25	0.01%	0.00%	0.01%	0.00%
R.E.V.	64.93	74.60	71.38	74.66
Test C – Variation due to Δ_b				
1/2	0.01%	0.00%	0.01%	0.00%
1/4	0.00%	0.00%	0.00%	0.00%
1/8	0.00%	0.00%	0.00%	0.00%
1/16	0.00%	0.00%	0.00%	0.00%
1/32	0.00%	0.00%	0.00%	0.00%
R.E.V.	64.90	74.59	71.36	74.65
Test D – Variation due to X_t				
0.000	0.01%	0.00%	0.01%	0.00%
0.125	0.02%	0.02%	0.01%	0.00%
0.250	0.03%	0.01%	0.01%	0.00%
0.500	0.01%	0.01%	0.01%	0.00%
0.750	64.90	74.59	71.36	74.65

Test E – Variation due to Δ_z				
0.5000	2.22%	0.12%	0.49%	0.12%
0.2500	0.84%	0.03%	0.12%	0.03%
0.1250	0.21%	0.01%	0.03%	0.01%
0.0625	0.05%	0.00%	0.01%	0.00%
R.E.V.	65.45	74.61	71.44	74.67
Test F – Variation due to Z_R				
0.5000	2.22%	0.12%	0.49%	0.12%
0.2500	0.84%	0.03%	0.12%	0.03%
0.1250	0.21%	0.01%	0.03%	0.01%
0.0625	0.05%	0.00%	0.01%	0.00%
R.E.V.	65.45	74.61	71.44	74.67